UNIVERSITÀ DEGLI STUDI DI BARI
DOCTORAL SCHOOL IN PHYSICS - XXXVI CYCLE

PHD THESIS

Aggregation and Dynamics of Active Particle Systems: From Active Clusters to Chiral Fluids

PhD candidate:
Claudio Basilio Caporusso

supervised by
Prof. Giuseppe GONNELLA

TYPESET 2024-02-12

Contents

Introduction

Active matter is a class of systems composed of self-propelled particles that can convert energy from their environment into directed motion. These systems exhibit a rich variety of collective phenomena that are not possible in thermal equilibrium, such as clustering, swarming, flocking, and self-organization. A major theoretical undertaking is to develop a better understanding of the statistical foundations of active matter, ideally comparable to equilibrium statistical mechanics. While this goal seems to be still far from possible in general, quite some progress has already been made for minimal models that capture the essential features of experimental active systems. Despite the apparent simplicity of these models, many open questions and challenges remain to uncover.

One of the most striking phenomena of active matter is motility-induced phase separation (MIPS), where self-propelled particles aggregate into clusters even in the absence of cohesive forces through a dynamic feedback between speed and density, producing a coexistence between a dense and dilute phase. A class of simple models combining persistent motion with short-range–typically purely repulsive–interactions called active Brownian particles (ABPs) has become a playground to study this phenomenon. Numerical simulations have been used to determine the full phase behaviour of ABPs, and much work has been devoted to establishing a general framework that permits the prediction of the phase boundaries in the spirit of liquid-solid demixing, e.g. through dynamical mean-field theories, treating MIPS like an equilibrium phase separation.

The first major topic this thesis deals with is a full and deep characterization of the aggregation of ABPs. In particular, we focus with MIPS in two dimensions, highlighting the differences with respect to an equilibrium phase separation, using state-of-the-art numerical simulations. In particular, we will answer the following questions: how do particles aggregate and grow over time, what characterize the morphology of the dense phase of the aggregation, and how does the active cluster diffusivity influence the aggregation process. Moreover, we also analyze the role of inertia and hydrodynamic interaction between particles and the solvent in modify active topological phase transitions, which ABPs undergo at high packing fractions.

The second topic we tackle in the thesis are the effects of the morphology of the constituent to the aggregation. Indeed, biological and experimental realization of active particles have often an elongated shape. To this end, we study the universality and robustness of MIPS by considering variants of the ABP model that incorporate different intrinsic features, such as the particles' shape or dimensionality.

The third topic we address in this thesis is the study of the emergence of anomalous flow and edge states 'classical' equilibrium systems when driven out of equilib-

rium. We will use numerical simulations of a model of Lennard-Jones disks in two dimensions, for which the phase diagram is well understood, and add continuous non-conservative transverse forces among colloids: we will call this model Chiral Active Particles. The transverse interaction is motivated by the behaviour of magnetic colloids in experiments, which can spin under the influence of an external magnetic field, and allow for breaking parity and time-reversal symmetry, defying our fundamental description of soft materials.

Finally, a few words about the global motivation we pursue in this thesis are needed. First, as stated before, by understanding specific models of active matter we hope to gain a deeper understanding of the physical mechanisms and the universal features of active matter, eventually leading to a comprehensive theoretical framework on par with the completeness and elegance of equilibrium statistical mechanics. Second, the characterization of minimal models paves the possibility of controlling and tuning the aggregation behaviour of experimental active particles, which could help the design of smart materials and devices with interesting and helpful applications.

The thesis is organized as follows:

- Chapter 1 provides a general introduction to the field of active matter and reviews the main models and methods, with a particular mention to the Active Brownian Particle model.
- Chapter 2 introduces the general theoretical background to describe aggregation in passive and active colloidal systems.
- Chapter 3 presents our findings on MIPS in the ABPs model in two dimensions. We determine that the morphology of the dense phase of the MIPS is more complex than an equilibrium one, as it exhibits, on top of the macroscopic phase separation, a microscopic phase separation of domain with the same lattice orientation, whose size can be controlled by the activity. We further uncover the differences between MIPS and equilibrium in the differences of the growth mechanism.
- Chapter 4 deals with the high-density low-activity region of the ABPs phase diagram in two dimensions, where topological phase transitions arise. In particular, we investigate how these are affected by the inertia of the active particles and by hydrodynamic interactions with the solvent. To address this question, we will introduce a generalization of the ABP model that takes into account hydrodynamics, which we call the Active Hydrodynamic Particles (AHPs) Model.
- in Chapter 5 we explore the role of the particle shape in the MIPS aggregation process. We use a minimal model of elongated particles - the dumbbells - which consist of a diatomic molecule with two rigidly connected circular beads. We show the differences in the morphology of the MIPS with respect to the standard ABPs model. In three dimensions, on the other hand, MIPS is suppressed and we analyze the rich phase behaviour that active dumbbells have adding the attractive interaction.
- Chapter 6 deals with our findings on Chiral Active Particles. We derive the non-equilibrium extension of the Lennard-Jones phase diagram introducing a transverse force between beads. We show how chiral particles show edge currents and we validate the measurements of such states using the hydrodynamic theory.

Part I

Background

1

Active Matter

This chapter is divided into three sections. In the first one, we will introduce what is Active Matter with some examples taken from the technological and biological world; in the second section, we will introduce the most relevant models used for understanding active matter systems on different scales. The third section deals with the main topic of this thesis, the Active Brownian Particle model.

1.1 Active Systems

Active matter is a novel class of nonequilibrium systems composed of a large number of self-driven agents. These agents can range in size from nanometers to meters and include both artificial and biological elements, such as molecular motors, biological tissues, artificial self-propelling particles, insects, fish, and humans.

Active systems are intrinsically out of equilibrium due to the continuous energy conversion within an internal reservoir. This distinguishes them from other nonequilibrium systems, in which energy is typically supplied from external sources. As a result of their nonequilibrium nature, active systems lack equilibrium concepts such as detailed balance and free energy that govern the system's evolution. On the other hand, this allows them to exhibit complex and fascinating behaviours, which include phase separation induced by activity, unusual mechanical and rheological properties, and collective phenomena such as swarming, flocking, and pattern formation. The understanding of these phenomena requires an interdisciplinary approach involving biology, chemistry, ecology, engineering, mathematics, and physics.

In particular, from a physical viewpoint, active systems can be studied using the tools of condensed matter physics and statistical mechanics. However, the theory of active matter is still under development, being specifically system-wise rather than general, and thus lacks the unifying elegance reached by equilibrium statistical mechanics. Recent and future developments in experiments, simulations, and theory promise to lead to a deeper understanding of active matter systems and their potential applications; for example, active agents could be used to create new intelligent materials that are capable of self-assembly, self-repair, and autonomous movement.

Now we will discuss some examples of these systems and of the collective phenomena which they present.

Biological microswimmers

Biological microswimmers, such as sperm cells, bacteria, and algae, are a classical example of active matter. While their propulsion mechanisms may differ, they all share the common strategy of swimming in a fluid. Dense swarms of bacteria exhibit a rich phenomenology due to the combination of their self-propulsion, alignment interaction due to their rod-like shape, and hydrodynamic coupling with the medium. Under the right conditions, new phases can arise, such as, for example, the zooming bionematic phase [DCC$^+$04b], which is a collectively ordered phase in which domains of bacteria move in the same direction at much greater speeds than those of the individual organisms. Bacteria show also incredible cluster phases: experiments with *Bacillus subtilis* involving up to a thousand individuals revealed a wide distribution of cluster size, giant density fluctuations, and highly ordered, scale-invariant clusters [CDB$^+$12, ZBFS10]. Clustering of myxobacteria exhibits, at a critical cell volume fraction, a scale-free size distribution [PDB06b].

Synthetic swimmers

Artificial self-propelled particles, or synthetic swimmers, are a promising class of active matter with potential applications in nanomedicine, environmental protection, and other fields [WM13, YSCP17, LFWG18, WSS$^+$16]. These particles propel themselves by exploiting chemical, thermal, or electrical gradients. One popular type of synthetic swimmer is the Janus particle, which is partially coated with a catalytic material. Janus particles are immersed in a solution containing a fuel source, which is decomposed locally by the catalyst, creating a concentration gradient and driving the particle forward. Other methods for propelling synthetic swimmers include using light to create thermal gradients or exploiting a local the phase separation. Artificial swimmers can be synthesized using various methods [SPJ$^+$19], but evaporative deposition is the most common and economical technique. In this technique, the particles are arranged in such a way as to expose only one hemisphere to the outside. They are then placed in an evaporator through which the material is deposited only on the exposed hemisphere.

2D experimental system of self-propelled Janus colloids shows dynamical clustering, with living clusters that continuously aggregate and fragmentate, increasing overall their average size over time [vdLAAD19], as shown in Fig. 1.1. Several groups have developed ways to analyze large spatial structures formed by thousands of self-phoretic colloids, measuring their size distribution and the aggregation-fragmentation rate [PSS$^+$13, TCBP$^+$12b, GTD$^+$18].

Cell and tissues

Fundamental biological processes, such as tissue repair and morphogenesis, require collective cell motions. This gives rise to a variety of collective phenomena in cells and tissues, such as the super-elasticity of cytoskeletal active polymerization dynamics [BCH09] and the rheological properties of tissues mediated by activity [MFAB$^+$17]. The Nédélec group have developed computational active models that have shown that

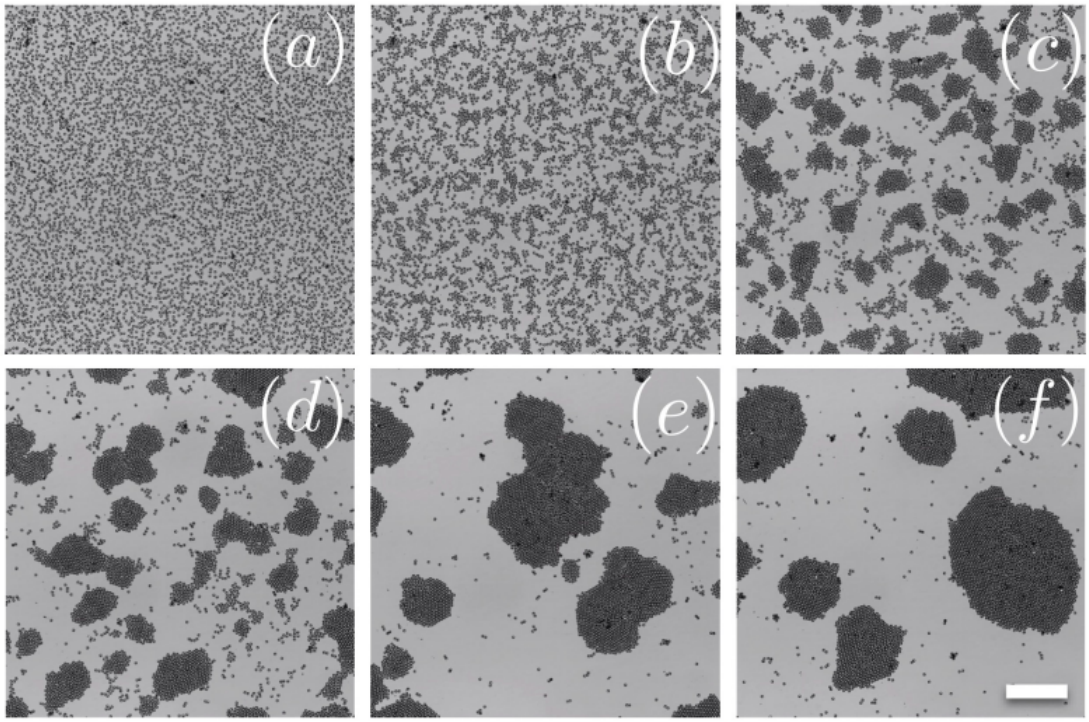

Figure 1.1: Aggregation kinetics in a system of electrophoretic self-propelled Janus colloids at times $t = 0.02, 0.4, 2, 5, 20, 68s$. The scale bar corresponds to $100\,\mu m$. Adapted from [vdLAAD19].

the collective behaviour of cytoskeletal filaments and motors can give rise to complex patterns and dynamics, such as aster formation, spindle assembly, and contractile ring formation [NSML97, NS01, NSK03, NF07]. These processes are essential for cell division, differentiation, and development.

Swarming in macroscopic biological systems

Swarming is a collective behaviour exhibited by many macroscopic biological systems, such as birds, locusts, and fish. Swarming systems are characterized by a few key features: i) They are large and cohesive groups without a leader or global coordination, ii) Individuals only interact with their neighbours. These two simple rules result in emergent global patterns that help the group survive and rapidly adapt to environmental changes. In the following we report some examples of such systems.

The STARFLAG project studied how birds form flocks by analyzing videos of European starlings. They found that each bird adjusts its speed and direction based on the 6-7 birds topologically closest to it, regardless of their distance [BCC$^+$08]. This ensures the compactness and cohesion of the flock, even when the density or shape changes.

The desert locust, *Schistocera Gregaria*, can switch from solitary to gregarious behaviour depending on the population density. When they are gregarious, they form bands of marching nymphs and swarms of flying adults. Couzin et al. studied how this transition occurs by tracking individual locusts and comparing them to simple models [BSC$^+$06]. They found that the locusts align their movement with the ones in

front of them, and avoid being bitten by the ones behind them. This creates a "living fluid" that flows in a common direction [BBH+08].

Makris *et al.* used a new technique to monitor fish populations on a continental scale using sound waves [MRS+06]. This allowed them to understand the structure and dynamics of large-scale fish schools, consisting of millions of individual fish. The experiments also showed the formation of "fish waves" at fairly regular intervals, which are perturbations within the school that propagate at much faster speeds than a single fish.

1.2 Relevant Active Matter models

To capture the essential features of active systems, minimal models have been developed that explicitly incorporate the effects of constituents' activity. As we pointed out in the introduction, the theory has not reached yet the elegance of a unified framework, but rather that a set of different models which describe a quite specific experimental system. However, a general way to classify these models can still be found: the scale of the systems studied, the symmetries of the system, and the type of interaction with the surroundings.

A way to classify active matter models regards the total momentum conservation. *Dry active matter* systems are those for which hydrodynamic interactions are absent and total momentum between agents and fluid is not conserved. *Wet active matter* systems are those, on the contrary, in which hydrodynamic interactions are present and momentum is conserved. Another way to classify active matter models is according to the scale and the resolution the models operate. On the microscopic scale, usually models describe the behaviour of single agents or particles. Models on a coarse-grained level do not rely on the microscopic details of the interactions between individual particles and use continuum fields, which describe the evolution of relevant slow variables of the system, to describe its large-scale behaviour.

We will now review some of the most widely used models and discuss their main applications. A summary of the models and the relations between them is shown in Fig. 1.2.

Dry models

Dry active systems are a class of active matter systems that do not conserve momentum. This is typically the case in mesoscopic models, where the hydrodynamic is integrated into an effective interaction and the particles lose momentum with the medium through friction; another case is in for large-scale systems, such as bird flocks, where hydrodynamic interactions are not significant at all and can be neglected. The most widespread examples of dry models we focus on are two paradigmatic minimal models: Vicsek-type models and Active Brownian Particles (ABPs).

The Vicsek model is an agent-based minimal model for flocking, accounting for the interplay between fluctuations and simultaneous interactions of multiple agents [VCBJ+95]. This model is used to describe various living organisms and elongated particles, which all share an alignment interaction type. The model describes an ensemble of N particles, in which particle i move in a plane with constant velocity v_0 and

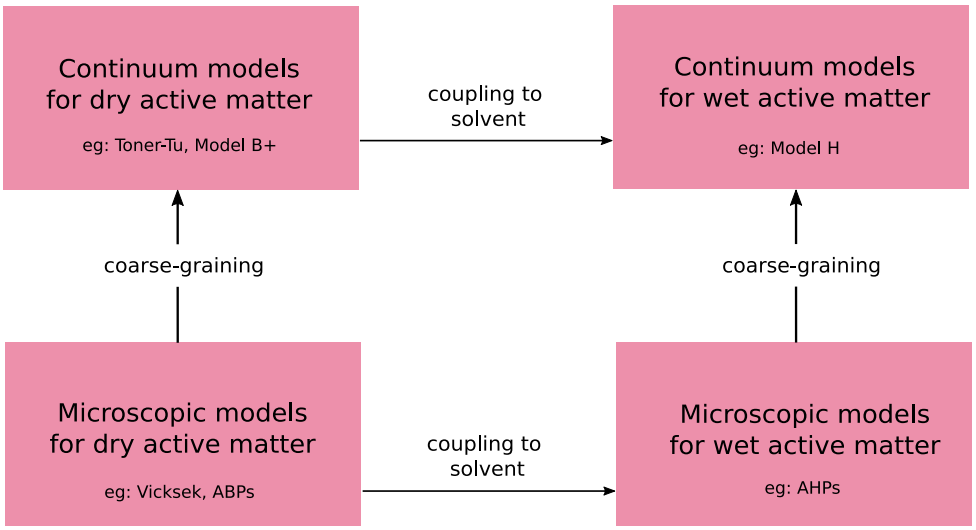

Figure 1.2: Schematic view of the different scales and interaction of active models. Adapted from [SWW+20a]

align it with their neighbours adjusting their velocity angle θ_i according to the rule

$$\theta_i(t+1) = \langle\theta(t)\rangle + \xi_i(t) \tag{1.1}$$

where $\langle\theta(t)\rangle$ is the average velocity angle of particles located in a radius R surrounding particle i, and $\xi_i(t)$ is a noise term, practically an angle extracted from the uniform distribution $[-\sigma\pi, \sigma\pi]$. Since hydrodynamic interaction is neglected, momentum is not conserved. A continuous transition from a disordered to an ordered state occurs on increasing the particle density or decreasing σ. Despite this being a non-equilibrium phase transition, various notions of equilibrium statistical mechanics can be applied to it, owing to spontaneous symmetry breaking and the emergence of well-defined macroscopic states [SCT15, CGG+08].

The Active Brownian Particle model describe microscopic disks moving in a solvent at a given temperature with a dynamics alike Brownian motion (hence the name) which includes a self-propulsion [FM12b]. The interaction of the solvent is integrated into a stochastic noise, which represents the collisions among fluid particles and the colloids. Since this model is the starting point of a big part of the results in the thesis, it will be described in full detail in Section 1.3. The model presents intriguing collective behavior [MJR+13a, SWW+20b]. One such peculiarity is that, at sufficiently high activity, their constituents cluster in the absence of attractive interactions, forming a steady state with a dense droplet immersed in a dilute background, alike a classical phase separation, a phenomenon called Motility-Induced Phase Separation (MIPS) [CT15a, RHB13a]. Extension of this model includes adding additional torques to the dynamical equations or using particles with asymmetric shapes. In particular, we will show in Chapter 5 an example of an extension of the ABP model using particles with an elongated shape, the dumbbells [CDGS17c, SMGO14].

On larger scales, the behaviour of many particles' active systems can be captured by continuous models, which describe the evolution of the slow variables, such as the density $n(\boldsymbol{r},t)$ or the velocity $v(\boldsymbol{r},t)$, obtained from coarse-graining the microscopic equations, or adopting symmetry arguments to derive the field equations. An example is the continuum description of the Vicsek model, obtained using symmetry considerations, called *Toner-Tu* model [TT95, TT98]. The theory describes particles that have a polarization field $\boldsymbol{p}(\boldsymbol{r},t)$. The conservation of the number density $n(\boldsymbol{r},t)$ leads to a continuity equation that includes the active contribution $v_0 n\boldsymbol{p}$, to the particles flux:

$$\rho(\boldsymbol{r},t) = \sum_n \delta(\boldsymbol{r} - \boldsymbol{r}_n(t)), \tag{1.2}$$

$$\boldsymbol{p}(r,t) = \frac{1}{\rho(\boldsymbol{r},t)} \sum_n \boldsymbol{\nu}_n(t)\delta(\boldsymbol{r} - \boldsymbol{r}_n(t)), \tag{1.3}$$

where $\boldsymbol{r}_n$ are the particles' position vectors with $\boldsymbol{\nu}$ their unit vectors. The equations of motion can be written in a way that one can separate the contribution arising from a free energy functional $\mathcal{F}_p$ (hence the equilibrium part) from the non-equilibrium ones [MJR$^+$13b]:

$$\partial_t\rho + v_0\boldsymbol{\nabla}\cdot(\rho\boldsymbol{p}) = -\boldsymbol{\nabla}\cdot\left(-\frac{1}{\gamma_p}\boldsymbol{\nabla}\frac{\delta F_p}{\delta\rho} + \boldsymbol{f}_p\right) \tag{1.4}$$

$$\partial_t\boldsymbol{p} + \lambda_1(\boldsymbol{p}\cdot\boldsymbol{\nabla})\boldsymbol{p} = -\frac{1}{\gamma}\frac{\delta F_p}{\delta\boldsymbol{p}} + \boldsymbol{f}. \tag{1.5}$$

where v_0 is the self-propulsion speed of the individual active particles, γ_p and γ kinetic coefficients, λ_1 a phenomenological parameter determined by the microscopic proprieties of the systems, $\boldsymbol{f}$ and $\boldsymbol{f}_p$ are zero-mean white Gaussian noises. The equilibrium relaxation dynamics is controlled by the effective free energy

$$\mathcal{F}_p = \int_{\boldsymbol{r}} \Big[\frac{\alpha(\rho)}{2}|\boldsymbol{p}|^2 + \frac{\beta}{4}|\boldsymbol{p}|^4 + \frac{K}{2}(\partial_\alpha p_\beta)(\partial_\alpha p_\beta) + \tag{1.6}$$

$$\frac{w}{2}|\boldsymbol{p}|^2\boldsymbol{\nabla}\cdot\boldsymbol{p} - \frac{w_1}{2}|\boldsymbol{p}|^2\nabla\cdot\boldsymbol{p}\frac{\delta\rho}{\rho_0} + \frac{A}{2}\left(\frac{\delta\rho}{\rho_0}\right)^2\Big], \tag{1.7}$$

where ρ_0 is the average density and $\delta\rho = \rho - \rho_0$ is the fluctuation in the density around the average. The model exhibits giant number fluctuations and long-range order in 2D [TTR05].

To explore the large-scale behaviour of Active Brownian Particles and their aggregation proprieties (MIPS), a similar coarse-grained procedure to obtain the evolution of the fields is desired. In this case, the passive model B [HH77], which is a field-theoretical model for accounting for diffusive phase separation processes characterized by a conserved order parameter ϕ, has been used as a starting point. The model has been extended to the active case by adding an active chemical potential, $\mu_{\text{active}} = \lambda(\boldsymbol{\nabla}\phi)^2$, to the equilibrium chemical potential $\mu_{\text{eq}} = -\phi + \phi^3$, with the active term breaking the time-reversal symmetry at leading order in the density gradient expansion. The resultant model has been called Active Model B. A generalization of Acitve Model B that allows for circulating currents to appear has been also proposed [WTS$^+$14, STA$^+$13b]. The model, called Active Model B+, displays rich and complex dynamics such as microphase separation (bubbles of a finite length scale) and a reverse

Ostwald process [TNC18] (an increase of the number of vapour bubbles inside the gas phase). We redirect the reader to Section 2.4 for a detailed description of Model B and Model B+.

Wet models

Wet models are characterized by the conservation of the total momentum of the system, which ensures Galilean invariance. Depending on the specific system, this can be achieved in different ways. As in the dry case, there are two possible approaches: a mesoscopic description or a large-scale one. In the mesoscopic approach, one needs to solve the Navier-Stokes equations for the fluid and couple it with the microswimmer dynamics, in order to take into account the momentum exchange between the two components. There are several methods that have been developed to solve the fluid equations in alternative and efficient ways, such as Lattice-Boltzmann (LB) methods [MZ88, DL09], Dissipative Particle Dynamics (DPD) [PF01, EW95], and Multiparticle Collision (MPC) [GIKW09, LGIK01, Kre09]. These methods are combined with the equation describing the microswimmers, which in turn depends on the nature and degree of coarse-graining of the latter. For instance, one can have high-resolution models of all the body structure of *E.coli* where no-slip boundary conditions are applied both to the cell body and the flagella [HYGW15], or one can have a less detailed model, like the squirmers [Lig52, Bla71, LP10, Ped16], where microswimmers are modelled as point-like colloids with a given fluid velocity at the surface. In particular, we will discuss in Chapter 4 the coupling between Active Brownian Particles and the fluid using the MPC method, which leads to the Active Hydrodynamics Particles model (AHPs).

On the other hand, one can directly formulate continuum descriptions that intrinsically conserve momentum and thus are hydrodynamically accurate. This is done using modified hydrodynamic equations with additional terms that arise from the self-propulsion of the particles. There are several ways to obtain these modified hydrodynamical equations: one is to start from a microscopic model of the system, and then obtain a large-scale description by coarse-graining the microscopic degrees of freedom into a continuous macroscopic field. This way is often not very practical due to the complexity of the interactions that occur at the microscopic level, and it requires some approximations, such as considering the dilute systems or weak-interaction limit, but this approach has a clear advantage that it allows to link microscopic parameters to macroscopic quantities - which are the ones usually measurable in experiments. Other ways to obtain the hydrodynamic equations, more phenomenological, are to write directly the equations for the fields including all the terms required by the symmetry of the system, or to consider the non-equilibrium steady state as obtained from an equilibrium state perturbated by some forces. In this way, it is possible to obtain the description of the non-equilibrium state as a series expansion of the fields around the equilibrium state.

As an example of a continuum model that considers interaction with the fluid, we cite Active Model H [TWMC15, Cat19]. The model describes scalar active matter and it is a direct extension of Active Model B, intended to account for the momentum-conserving solvent. The dynamics of the order parameter $\phi(\boldsymbol{r}, t)$ obeys the same equation of Active Model B, with an additional advective term $\boldsymbol{v} \cdot \boldsymbol{\nabla}\phi$ that couples the order parameter to the velocity field of the fluid, whose dynamics is governed *via* the Naver-

Stokes equations. Activity gives a contribution to the deviatoric stress $\boldsymbol{\sigma}$, leading to an unusual arrested MIPS in some cases [SWW$^+$20a, TSGL09].

1.3 Active Brownian Particles

The Active Brownian Particle (ABP) model is a minimal microscopic active matter model that captures the essential features of self-propelled microscopic spheres (such as Janus particles) that undergo rotational diffusion and interact only through excluded volume effects. The model displays a rich phase diagram, with phenomena such as clustering without any attractive forces, especially in two dimensions ($2d$) [RBE$^+$12, BSL12, FM12a, SMAC14a, LCP17a, SMBL15, RHB13b, DLS$^+$18a, KKK18, DLC$^+$19, PD20, MLL19, CMP20b], which is the dimensionality we focus on in this thesis, unless otherwise specified. This model serves as the basis for many of the subsequent results, and we will describe it in detail in this section.

Equations of motion

The Active Brownian Particles model described N particles at positions $\boldsymbol{r}_i$ moving in a solvent at temperature T, in a box of dimension $L_x \times L_y$ with periodic boundary conditions. The particles evolve according to an overdamped Langevin stochastic equation, with an additional term representing the self-propulsion:

$$\begin{array}{rcl} \gamma\dot{\boldsymbol{r}}_i & = & F_{\mathrm{act}}\boldsymbol{n}_i - \sum_{j(\neq i)} \boldsymbol{\nabla}_i U(r_{ij}) + \sqrt{2\gamma k_B T}\boldsymbol{\xi}_i \ , \\ \dot{\theta}_i & = & \sqrt{2D_\theta}\eta_i \, . \end{array} \tag{1.8}$$

Here, $\boldsymbol{r}_i$ is the position vector of the particles, γ is the damping coefficient, $U(r_{ij}$ is the pair potential of the steric interaction, F_{act} is the self-propulsion force acting along the particle's axis,

$$\boldsymbol{n}_i = (\cos\theta_i(t), \sin\theta_i(t)), \tag{1.9}$$

and the components of $\boldsymbol{\xi}$ and η are independent white Gaussian noises with zero mean and unit variance, verifying the equations

$$\langle \xi(t)\xi(t')\rangle = \delta_{ij}\delta_{\alpha\beta}\delta(t-t') \tag{1.10}$$

$$\langle \eta(t)\eta(t')\rangle = \delta_{ij}\delta(t-t'), \tag{1.11}$$

where Greek letters indicate Cartesian components. The two noises represent the interaction of the particle with the fluid which randomizes the particle's position and orientation. Indeed, in addition to the contribution to the translational dynamics, the particles' axis rotates through a diffusive process with constant D_θ. The angular diffusion coefficient D_θ is an independent parameter of the model, but it can be related to the temperature of the bath to $D_\theta = 3k_BT/\gamma\sigma_d^2$, assuming that rotational diffusion is of thermal origin. This follows from the Navier-Stokes equations assuming Stokes flow in the solvent and stick boundary conditions on the particle surface [HM13]. It is also worth noticing that dynamics of Eq. (1.8) is explicitly out of equilibrium due to the active force term, which also couples the evolution of the velocity $\dot{\boldsymbol{r}}$ to the angular diffusion. In the passive limit $F_{\mathsf{act}} \to 0$, we indeed recover the classical Brownian particle model.

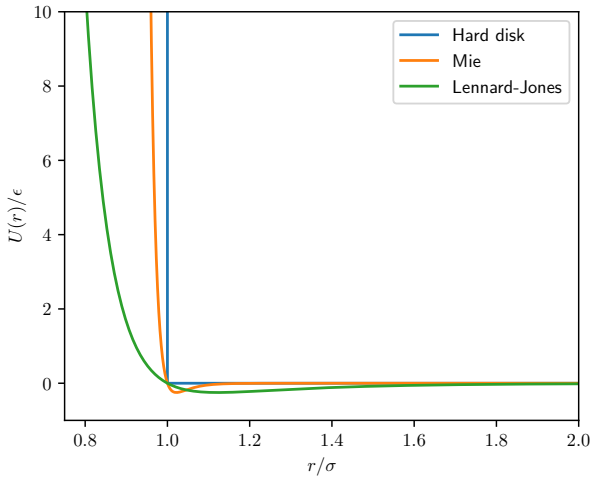

Figure 1.3: Differences between the Hard Disk potential (blue), the Mie potential with $n = 32$ (orange), and the Lennard-Jones potential (with $n = 6$) (green)

As anticipated, the particles interact only through volume exclusion. In theory, this is represented by the hard disk potential, $U(r) = 0$ if $r > \sigma_d$ and $U(r) = \infty$ if $r <= r_c$. In practice, this choice is computationally inefficient and several alternatives have been used. A common one is to use a standard pair potential and truncate it to remove the attractive part. One can choose between stiffer or softer potential, which would allow or not particles to overlap. A widely used potential is the Mie potential [Mie03]

$$U(r_{ij}) = \begin{cases} 4\varepsilon \left[\left(\frac{\sigma}{r}\right)^{2n} - \left(\frac{\sigma}{r}\right)^{n} \right] + \varepsilon, & \text{if } r < \sigma_d, \\ 0, & \text{otherwise,} \end{cases}$$

with $r_{ij} = |\boldsymbol{r}_i - \boldsymbol{r}_j|$ is the distance between interacting particles i and j and $\sigma_d = 2^{1/32}\sigma$, such that the potential minimum results $\epsilon = U(\sigma_d)$. This potential is a generalization of the famous Lennard-Jones one, which is obtained for $n = 6$. However, higher values of n increase the potential stiffness, as shown in Fig.1.3 in comparison with the hard disk potential. Typically, our choice is to use $n = 32$, which is a good trade-off between potential stiffness and computational complexity. One motivation to opt for a potential that closely resembles the hard-disk one is that in that case the equilibrium limit ($F_{\text{act}} = 0$) is well-known and studied, as we will explain in more detail in Sec. 1.3

Single particle dynamics

Active Brownian particles (ABPs) exhibit persistent motion, which is the tendency of a particle to continue moving in the same direction for a prolonged period of time. This feature makes the model suitable for describing many active systems, particularly the self-propelling microscopic particles described in Sec. 1.1. The origin of the persistence is twofold: the presence of the self-propulsion force and a memory in the direction of this force. The latter can be seen explicitly calculating the time-correlation of θ, the direction of the axis of the particle [BMRS18]. It can be seen easily that

$$\langle \boldsymbol{n}(t) \cdot \boldsymbol{n}(t_0) \rangle = \langle cos[\theta(t) - \theta(t_0)] \rangle, \tag{1.12}$$

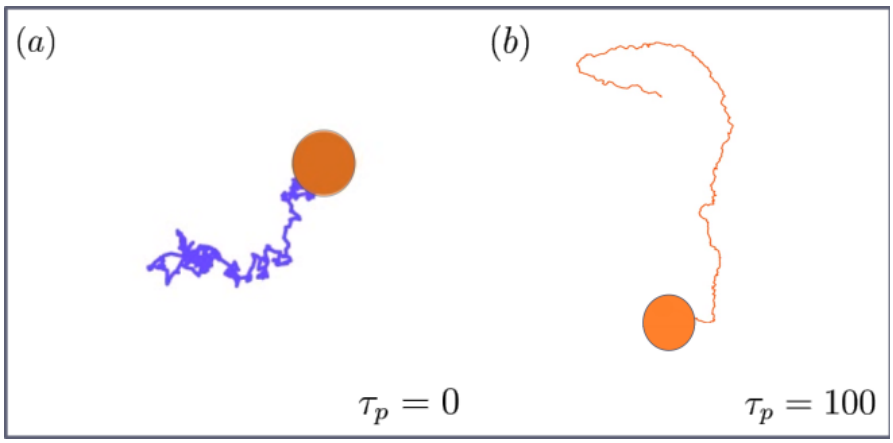

Figure 1.4: Trajectories of an Active Brownian Particle with (a) $\tau_p = 0$ and (b) $\tau_P = 100$.

where t_0 is the initial time for the measurements. Using the fact that $d\theta$ is a Wiener process with amplitude D_θ, we then obtain[1]

$$\langle \boldsymbol{n}(t) \cdot \boldsymbol{n}(t_0) \rangle = e^{-(t-t_0)/\tau_p}, \tag{1.13}$$

where we have introduced the persistence time $\tau_p = 1/D_\theta$. Eq. (1.13) implies that the angular orientation decays exponentially, and the active force (hence, the particle's velocity) points in the same direction for a time proportional to τ_p. The difference between a classical Brownian motion - which corresponds to the limit of totally uncorrelated angular orientations, $\tau_p \to 0$, and a persistent motion, is illustrated in Fig. 1.4

The mean square displacement can be derived by integrating the equation of motion Eq. (1.8)

$$\begin{aligned} \langle (\boldsymbol{r}(t) - \boldsymbol{r}(t_0))^2 \rangle &= \int_0^t dt' \int_0^t dt'' \langle (\dot{\boldsymbol{r}}(t) - \dot{\boldsymbol{r}}(t_0)^2 \rangle \\ = \frac{4k_BT}{\gamma}(t-t_0) + \left(\frac{F_{\text{act}}}{\gamma}\right)^2 &\int_{t_0}^t dt' \int_{t_0}^t dt'' e^{-D_\theta(t'+t''-2\min(t',t''))} \\ = \frac{4k_BT}{\gamma}(t-t_0) + 2\left(\frac{F_{\text{act}}}{\gamma}\right)^2 &\frac{1}{D_\theta^2}\left[D_\theta(t-t_0) + e^{-D_\theta(t-t_0)} - 1\right]. \end{aligned} \tag{1.14}$$

From that, one can extract the diffusion coefficient as $D = \lim_{t\to\infty} \langle (\boldsymbol{r}(t) - \boldsymbol{r}(t_0))^2 \rangle / 4t$. In the passive limit ($F_{\text{act}} = 0$), $D = k_BT/\gamma$, which agrees with the value expected by the Green-Kubo relation,

$$D_0 = \frac{1}{2}\int_0^\infty \langle \dot{\boldsymbol{r}}(t) \cdot \dot{\boldsymbol{r}}(0) \rangle = \frac{k_BT}{\gamma}. \tag{1.15}$$

Let us now analyze the Mean Square Displacement and the diffusion coefficient in the presence of activity. In the limit of small times, $t - t_0 \ll \tau_p$, we can expand the exponential in Eq. (1.14), obtaining

$$\langle (\boldsymbol{r}(t) - \boldsymbol{r}(t_0)^2 \rangle \sim \left(\frac{F_{\text{act}}}{\gamma}\right)^2 (t-t_0)^2, \tag{1.16}$$

[1]Note that here we use the Ito prescription for the calculations.

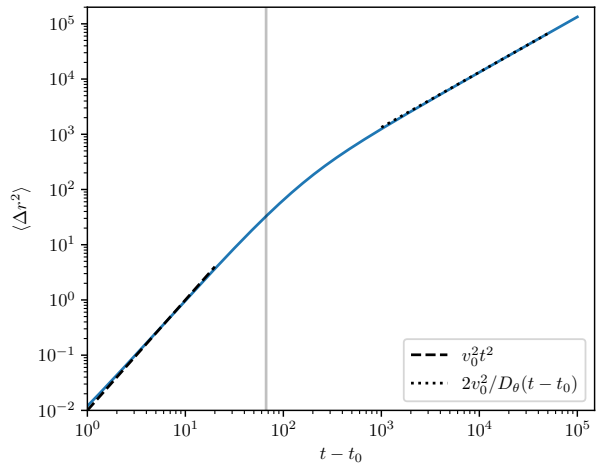

Figure 1.5: Time evolution of the Mean Square Displacement $\langle \Delta r^2 \rangle$ of a single Active Brownian Particle obtained through a numerical simulation. The dashed line represent the low time regime, Eq. (1.16) and the dotted line represent the long time limit of Eq. (1.14). The vertical gray line is placed at $t = \tau_p$.

which corresponds to a ballistic regime with persistent velocity $v_0 = F_{\text{act}}/\gamma$. At long times, on the contrary, only the linear terms remain and we recover a diffusive motion with an enhanced diffusion constant

$$D_{\text{eff}} = D_0 + \frac{2v_0^2}{D_\theta}, \tag{1.17}$$

which depends directly on the self-propulsion strength. The two dynamical regimes are separated by the persistence time τ_p, as shown in Fig. 1.5.

Phase Behaviour

In the previous section, we considered a single Active Brownian Particle and captured its fundamental properties. However, self-propelled motion usually occurs at finite densities, where short-range repulsive interactions between particles play a significant role. It is convenient, therefore, to introduce the non-dimensional parameter of the global surface ϕ defined as

$$\phi = \frac{\pi \sigma_d^2}{4V} \tag{1.18}$$

where $V = L_x \times L_y$ is the total surface available to the system. In addition to the surface fraction, another non-dimensional parameter is needed to account for self-propulsion in many-particle systems. This parameter is known as the Péclet number,

$$\text{Pe} = \frac{F_{\text{act}} \sigma_d}{k_B T}, \tag{1.19}$$

and it expresses the ratio between the work done by self-propulsion and the thermal energy.

The full phase diagram of ABPs in the $(\phi - \text{Pe})$ plane has been numerically determined by Digregorio *et al.* in [DLS+18a], and it is reported in Fig. 1.6.

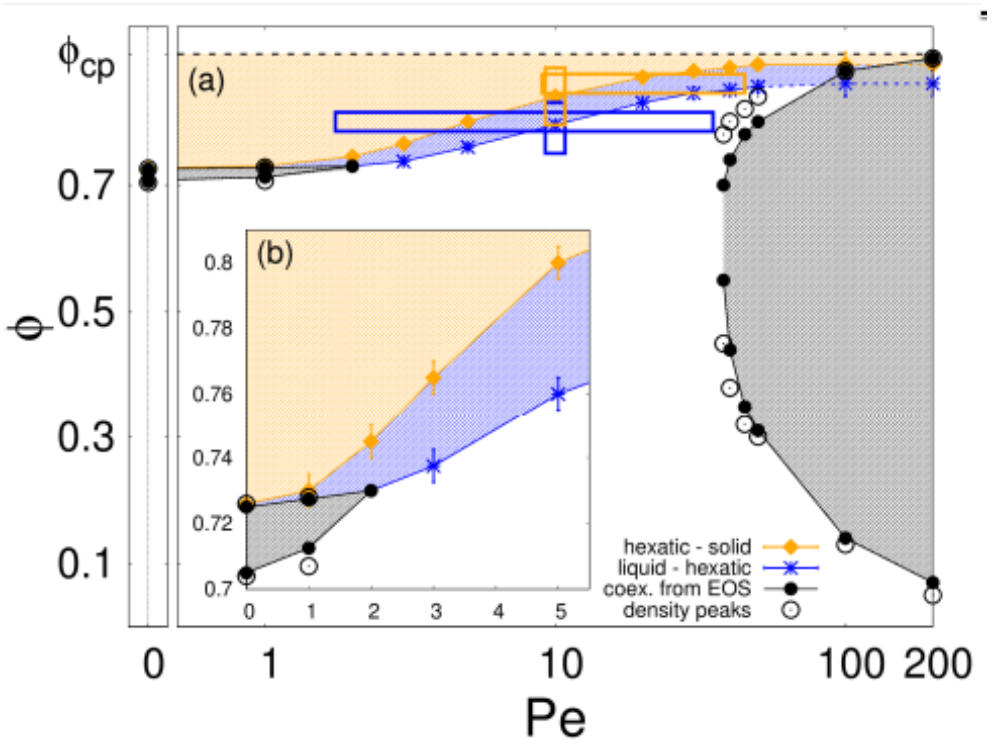

Figure 1.6: Pe-ϕ phase diagram of ABP. In the inset, zoom over the low Pe - high ϕ regime highlights the connection with 2D hard disk melting. In the black area there is MIPS coexistence, in the blue hexatic order and the orange one is an active solid phase. Adapted from [DLS+18a]

In the equilibrium limit ABPs behave like passive hard disks that undergo the 'two-step' scenario [BK11]: decreasing the packing fraction from the solid phase, they undergo a continuous Berezinski-Kosterlitz-Thouless (BKT) melting transition from solid to hexatic, characterized by the emergence of topological defects in the hexagonal lattice of the solid phase, followed by a first-order transition with coexistence between a liquid phase and a hexatic phase [KSK18]. The different phases are characterized by a different behaviour of the positional and orientational correlation functions (that we will formally introduce in Section 2.3); solid phase has quasi-long-range (QLR) positional and long-range (LR) orientational order, the hexatic phase has short-range (SR) positional and QLR orientational order, while the liquid phase is homogeneous and has SR positional and orientational order. It is worth mentioning that the size of the coexisting region is strongly affected by the shape and the stiffness of the pair interactions [KK15]. Varying the exponent in a power-law repulsive pair interactions, the coexistence region spreads or shrinks, eventually disappearing for low powers - and thus soft enough - potentials.

Digregorio *et al.* found that the equilibrium two-step scenario of hard disks is still maintained in ABPs at finite but small activities (Pe $\leq$ 2, with a coexistence region between active liquid and hexatic phase (black area in Fig.1.6). At higher densities, an active hexatic phase (blue area) and an active solid phase (orange area) exist. A thoughtful measurement of lattice defects [DLC+19] is consistent with these measurements, with the solid-hexatic transition driven by unbinding of dislocations, while the hexatic-liquid transition is generally accompanied by percolation of clusters of defects.

The liquid-hexatic and hexatic-solid transitions shift towards higher densities with Pe, meaning that activity destabilizes the ordered phases. Finally, at $\mathrm{Pe} > 2$, the first-orded transition disappears, leaving only an active hexatic phase.

At high enough activity ($\mathrm{Pe} \geq 35$), the system undergoes a new type of phase transition, where particles cluster together forming a dense phase that coexists with a dilute phase, like a classical phase-separation, even if this happens in complete absence of any attractive interactions among particles. The clustering indeed stems from an intrinsic nonequilibrium mechanism, called motility-induced phase separation (MIPS), which arises from an interplay between self-propulsion and the excluded volume interaction of the particles: particles accumulate when they go slower and they slow down when they crowd, causing a positive feedback resulting in a macroscopic aggregation. A mathematical description of this self-trapping mechanism can be found in appendix B.

Although driven by the activity, MIPS quite resemble a spinodal decomposition, which occurs in equilibrium across first-order phase transitions. As in equilibrium, the pressure drops for values of the density well above the spinodal and then reaches constant values within the MIPS, as shown in Fig. 1.7(a). This behaviour mimics the mechanism of Maxwell construction for the van der Waals loop and allows for the estimation of the binodal of the MIPS region, reported as black points in Fig. 1.6. An analogous measurement of the binodal can be independently obtained by measuring the local density of the distributions, which shows a bimodal shape with two peaks corresponding to the coexisting densities, Fig. 1.7(b). The peaks' density values are reported in Fig. 1.6 as white dots. The two measurements of the binodals give consistent results and allow for global delimiting of the MIPS region, represented as a dark area in Fig. 1.6. The region broadens as activity increases, eventually crossing the hexatic and solid transition lines. Such results show that (i) MIPS prevails over the hexatic and solid phases, and (ii) MIPS generates a phase separation between a dilute and a high-density phase, which can either be liquid, hexatic, or solid, as activity is increased; in general, it is a polycristal composed of different hexatic patches, as we will see in Chapter 3.

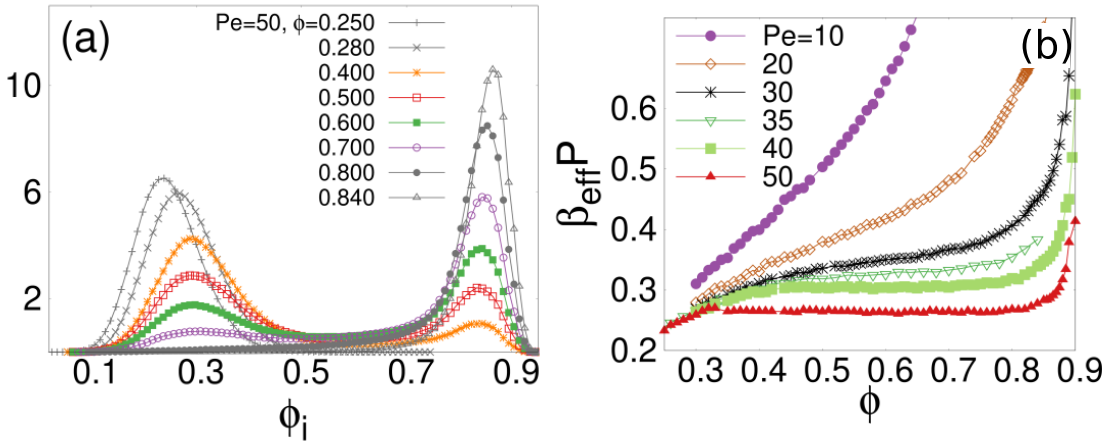

Figure 1.7: (a) Local density distribution in the MIPS region at $\mathrm{Pe} = 50$ and different densities reported in the legend. (b) Pressure normalized to the effective temperature of the bath $k_B T_{\mathrm{eff}} = 1/\beta_{\mathrm{eff}} = T(1 + v_0^2/2D_0D_\theta)$ for different Péclet numbers; once the critical activity ($\mathrm{Pe} \sim 35$) is reached, the pressure becomes flat. Both figures are adapted from [DLS+18a]

2

Aggregation Kinetics and Phase Ordering dynamics

This chapter delves into the theoretical foundation of the central theme of this thesis: aggregation. We will first describe equilibrium phase separation and then move to the phenomenology of aggregation observed in active systems, where traditional equilibrium theories often fall short of capturing the dynamics observed in numerical simulations.

The first section provides a concise introduction to aggregation theory within the well-studied context of first-order phase separation. This section serves as a stepping stone for the more complex aggregation phenomena in active systems. The second section introduces another perspective of first-order phase transition from the point of view of cluster dynamics. This approach will be, in particular, of use in Chapter 3, where we will study active cluster dynamics. The third section introduces the essential tools for measuring and tracking ordering processes over time. Correlation functions and their Fourier transforms, known as structure factors, play a pivotal role in this analysis. Finally, the fourth section provides a brief overview of the existing literature on the aggregation of Active Brownian Particles (ABPs) and the kinetics of the MIPS process. This section establishes a necessary foundation for Part II of the thesis, where we will present the results obtained during the PhD project.

2.1 Phase separation in passive systems

Here we review the theory of the dynamics of the phase separation of first-order phase transition in passive[1] (equilibrium) systems. We will follow the discussion of [Dom00] and [Jon02].

The dynamics of phase transitions describe the evolution of a system that becomes unstable due to a sudden change in its thermodynamic parameters, a process called *quenching*. The evolution of a quenched system depends on its final position in the phase diagram. As shown in Fig. 2.1, which illustrates the phase diagram of the system

[1] We will use the terms *passive* and *equilibrium* interchangeably throughout the thesis.

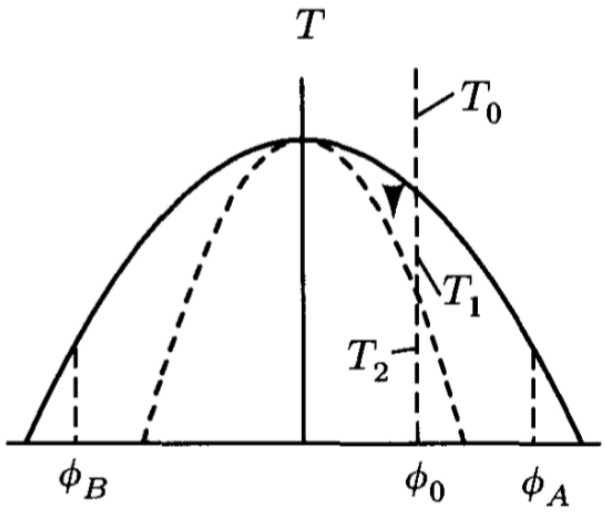

Figure 2.1: Schematic representation of phase diagram and effects of quenching. On the x-axis is plotted density ϕ and on y-axis temperature T. The curve divides the region where there is only one phase (outside) from that where there is coexistence of phases (inside), while the dashed line is the spinodal curve. At T_0, the system is outside both curves and all in one single phase. Moving vertically along the diagram at T_1, we enter an external region to coexistence where nucleation occurs. Lowering further temperature at T_2, we find ourselves inside the spinodal region.

at equilibrium as a function of density ϕ and temperature T, the system can pass from a single phase to a coexistence of two different phases below a certain point, called the critical point. The entrance into the coexistence region is usually controlled through an order parameter, which is a quantity defined to vanish before the critical point and suddenly increase once the critical point is reached. In the case of a liquid-gas transition, for example, the order parameter is the density difference between the two phases.

Such a quenched system gradually evolves from a non-stable state towards a thermodynamically stable one, where two different phases coexist. In the classical theory of first-order phase transitions, one can distinguish two different regimes in which this state is reached: nucleation and spinodal decomposition. The nucleation regime is characterized by the aggregation of small droplets of the denser phase, which gradually grow in size over time. On the other hand, in the spinodal decomposition, the system evolves by the formation of structures that span uniformly throughout space. These two regimes are separated by a line in the phase diagram called the spinodal line; if the quench put the system outside the coexistence region relative to the spinodal line, then it evolves by nucleation; in contrast, if the system is located inside the spinodal line, then it evolves by spinodal decomposition.

After some time, a late stage of the phase separation process takes place, independently from the original regime, in which the domains grow in time through a process called *coarsening*. The laws governing this phenomenon are still a case of study, and a theory has been developed only in certain limited cases.

We will now give a quick overview of the theory behind these processes.

Semi-phenomenological theory of phase separation

We turn to a field theoretical description of the dynamics of the evolution of the system. In order to describe the macroscopic evolution through a coarse-grained field, we focus on the evolution of the order parameter $\psi(\boldsymbol{r}, t)$, which is a function of space and time. The dynamics can be described in terms of a dissipative Langevin equation

$$\frac{\partial \psi}{\partial t} = -M \frac{\delta \mathcal{F}}{\delta \psi} + \eta(\boldsymbol{r}, t), \tag{2.1}$$

where $\mathcal{F}$ is the free energy functional of the system, M is the mobility coefficient and $\eta_i(\boldsymbol{r}, t)$ is a Gaussian noise with mean and correlation

$$\langle \eta(\boldsymbol{r}, t) \rangle = 0, \tag{2.2}$$

$$\langle \eta(\boldsymbol{r}, t) \eta_j(\boldsymbol{r}', t') \rangle = 2 k_B T \, M \, \delta(\boldsymbol{r} - \boldsymbol{r}') \delta(t - t'). \tag{2.3}$$

The free energy functional $\mathcal{F}[\rho]$ is given by the spatial integral of the free energy density $f(\{\psi)\}, \boldsymbol{r})$, which is a function of the order parameter and its derivatives. An essential feature of the free energy density is that it has a double well shape, with the appearance of two (or more) minima below the critical temperature T_c.

In this model, the order parameter ψ is non-conserved over time. It is generally called Model A in the Halperin and Hoenberg classification [HH77], which distinguishes the dynamics with non-conserved order parameters (Model A) from the one where the order parameter is conserved over time (Model B). The conservation of ψ in Model B is obtained through a continuity equation

$$\frac{\partial \psi}{\partial t} = -\boldsymbol{\nabla} \cdot \boldsymbol{J} + \eta(\boldsymbol{r}, t), \tag{2.4}$$

where the current $\boldsymbol{J}$ is given by

$$\boldsymbol{J} = -M \boldsymbol{\nabla} \frac{\delta \mathcal{F}}{\delta \psi} = -M \boldsymbol{\nabla} \mu; \tag{2.5}$$

in the last equation, we introduced the chemical potential $\mu \equiv \delta \mathcal{F} / \delta \psi$.

Let us now consider a practical example: a simple binary alloy consisting of two atomic species A and B. This system, under a critical temperature, separates into two phases, one with the majority of phase A and the other with phase B. In this case, the order parameter is the difference in the concentration of the two species, $c = c_A - c_B$. The dynamic is conserved and the equations of motion are given by Eqs. (2.4) and (2.5):

$$\frac{\partial c}{\partial t} = -\boldsymbol{\nabla} \cdot M \boldsymbol{\nabla} \frac{\delta \mathcal{F}}{\delta c} + \eta(\boldsymbol{r}, t). \tag{2.6}$$

One can phenomenologically write a Ginzburg-Landau free energy functional for the system in this way:

$$\mathcal{F} = \int d\boldsymbol{r} \left[\frac{K}{2} (\boldsymbol{\nabla} c)^2 + f(c) \right], \tag{2.7}$$

where $f(c)$ has the expression (ϕ^4 model)

$$f(c) = \frac{1}{2} a c^2 + \frac{1}{4} b c^4, \tag{2.8}$$

with a proportional to the distance from the critical point, and b a positive constant. In this way, the free energy has the double well structure under the critical point T_C. Expliciting Eq.2.6[2], we obtain a nonlinear diffusion equation

$$\frac{\partial c}{\partial t} = M\nabla^2 \left[-K\nabla^2 c - ac + bc^3\right] + \eta(\boldsymbol{r}, t). \tag{2.9}$$

Equation 2.9 is known as Cahn-Hilliard equation.

Early stages of phase separation

As anticipated in the introduction, after a quench in an unstable point of the system, two mechanisms are possible for phase separation to take place: spinodal decomposition and nucleation. The first mechanism takes place through a continuous change in composition, by a process in which concentration fluctuations are amplified. On the other hand, nucleation happens when a mixture is in a metastable region of the phase diagram, and the systems phase-separate around large composition fluctuations.

Spinodal decomposition The characterization of spinodal decomposition is obtained using the Cahn-Hilliard theory we sketched in the previous section. The validity of this theory is considered to be limited to very short times following the quench, nevertheless, it provides an intuitive picture of the process. We start dropping the noise term in Eq. (2.9). This is done for two reasons: because it is usually small with respect to the other terms, and because this makes the equations more manageable analytically. We thus obtain:

$$\frac{\partial c}{\partial t} = M\nabla^2 \left[-K\nabla^2 c + \frac{\partial f}{\partial c}\right]. \tag{2.10}$$

The idea is to linearize this equation around the average concentration c_0

$$\frac{\partial u(\boldsymbol{r})}{\partial t} = M\nabla^2 \left[-K\nabla^2 + \left(\frac{\partial^2 f}{\partial c^2}\right)_{c_0}\right] u(\boldsymbol{r}), \tag{2.11}$$

where $u(\boldsymbol{r}) = c(\boldsymbol{r}) - c_0$. Note that this linearization is valid only for short times after the quench, when the concentration fluctuations are small. In absence of the term $K\nabla^2$, one recovers the diffusion equation, with a diffusion constant

$$D = M\left(\frac{\partial^2 f}{\partial c^2}\right)_{c_0}. \tag{2.12}$$

Being M is always positive, the sign of D depends on the sign of the second derivative of the free energy density. Since the definition of the spinodal line is given in general by the condition $d^2 f/dc^2 = 0$, inside the spinodal region the effective diffusion coefficient is negative: material is diffused from regions of low concentration to regions of high concentration.

Taking the Fourier transform of the equation, we have

$$\frac{\partial \hat{u}(\boldsymbol{q}, t)}{\partial t} = -Mq^2 \left[Kq^2 - \left(\frac{\partial^2 f}{\partial c^2}\right)_{c_0}\right] \hat{u}(\boldsymbol{q}, t) = -\omega(q)\hat{u}(q). \tag{2.13}$$

[2]Here we are considering that the motility coefficient has no dependence on $\boldsymbol{r}$.

Inside the spinodal region the constant $\left(\frac{\partial^2 f}{\partial c^2}\right)_{c_0}$ is negative, and thus $\omega(q)$ is also negative for $q < q_c$, with $q_c^2 = K^{-1}\left|\left(\frac{\partial^2 f}{\partial c^2}\right)_{c_0}\right|$. This wavelength will grow exponentially in time, while the others will decay. This is the mechanism of spinodal decomposition. The structure factor of the system - which is a quantity related to the scattered radiation in experiments, see the next Section - using this prediction should behave as

$$S(q,t) = \langle|\hat{u}(\boldsymbol{q},t)|^2\rangle = S(q,0)e^{-2\omega(q)t}. \tag{2.14}$$

Thus, the initial stages of spinodal decomposition should produce an exponential growth in the scattering intensity for $q < q_c$, with a peak at $q_m = q_c/\sqrt{2}$.

Nucleation A system quenched into the metastable part of the phase diagram is stable for small fluctuations in concentration, and thus the continuum process of spinodal decomposition cannot take place. Instead, in this region, a formation of a drop of material at the coexisting density must occur despite causing an increase to the free energy, and then subsequentially grows until the free energy does not start to decrease again. This process is called nucleation: a droplet must be nucleated by thermal fluctuations and be large enough to be stable. Let us compute the free energy cost of a droplet of radius R in a metastable state. There would be a negative contribution proportional to the volume of the droplet; this is because the system is globally in an unstable state so if it does succeed in phase separating it will lower its free energy by an amount ΔF_v per unit of volume. On the other hand, to make a droplet of radius R one has to create a surface of area $A = 4\pi R^2$, which has a positive contribution to the free energy proportional to the surface tension γ. Thus, the total free energy cost of a droplet of radius R is

$$\Delta F(R) = \frac{4}{3}\pi R^3 \Delta F_v + 4\pi R^2 \gamma. \tag{2.15}$$

The energy variation has a maximum for the critical size R_c solution of $d\Delta F/dR = 0$. Droplets of a size below R_c are unstable, and once created the free energy will increase if they grow any further. Droplets of a size above R_c are stable, and their growth will lower the free energy of the system. The energy needed to form a droplet of size R_c is called the nucleation barrier ΔF_c. The nucleation barrier is given by

$$\Delta F_c = \frac{16\pi}{3}\frac{\gamma^3}{\Delta F_v^2}. \tag{2.16}$$

Thus nucleation can only occur if a fluctuation of the order parameter is large enough to produce a droplet of size R_c, increasing the local free energy of the system by an amount ΔF_c. The probability of such a fluctuation is given by the Boltzmann factor, and thus the nucleation rate is proportional to $\exp(-\Delta F_c/k_B T)$. Different theories have been developed for precise calculations of the nucleation rate, whose description goes beyond the simple picture we have described here.

Late stages of phase separation

Once a first-order phase separation has proceeded and clusters of the dense phase are formed, whether by spinodal decomposition of homogeneous nucleation, the domains

grow in a process called *coarsening*. As already mentioned, a theory of the process exists only in limited cases. One such case is when the system is composed of small droplets of the minority phase, with a distribution in size. The effect of the curvature of the droplets is that the local solubility of the minority component is higher near the smaller particles than the larger ones; this gradient drives diffusive mass transport, where the smaller particles dissolve and the material is absorbed by the larger ones. This process is known as Ostwald ripening and it is theoretically described by the Lifshitz-Slyozov-Wagner (LSW) theory, the main result being that the growth law of the average droplet size obeys $R(t) \propto t^{1/3}$.

Here we report a sketch of the derivation of the LSW theory. The starting equation arises from the consideration that, since coarsening occurs only after a near-equilibrium volume fraction of the coexisting phases has formed, diffusion gradients are quite small, and change in concentration occurs quite slowly. As a first approximation, we can write the time-dependent diffusion equation for the concentration as

$$\nabla^2 c \sim 0. \tag{2.17}$$

This gives a well-known result for the instantaneous diffusion field in the neighbourhood of a spherical droplet of radius R [RC75]:

$$c(r) \simeq c_0 - R\frac{\delta c}{r}\left(1 - \frac{R_c}{R}\right), \tag{2.18}$$

where δc is the difference in concentration between $c - c_A$ (supersaturation), c_0 is the initial concentration, $r > R$ is the distance from the center of the droplet and R_c is the critical radius for the droplet nucleation introduced in the previous section. The diffusion flux into the droplet is given by Fick's law:

$$J = D\frac{dc}{dr}\bigg|_{r=R} = \frac{\delta c}{R}\left(1 - \frac{R_c}{R}\right). \tag{2.19}$$

The flux is directly responsible for the droplet growth rate, $dR/dt \sim J$, and thus finally we obtain the equation of motion

$$\frac{dR}{dt} = \frac{D\delta c}{R}\left(1 - \frac{R_c}{R}\right). \tag{2.20}$$

For every value of the supersaturation $\delta c(t)$, there is a critical radius R_c for which a droplet is in equilibrium with the surrounding solution. Droplets grow or dissolve, whether their radius R is larger or smaller than R_c (which gives, respectively, a positive or negative rate). This is the mechanism of the Ostwald ripening, in which smaller droplets dissolve and the material is absorbed by the larger ones. The asymptotic solution of Eq.(2.20) [LS61, Wag61] is

$$R(t)^3 = \frac{4}{9}D\alpha t, \tag{2.21}$$

where α is a constant. From this equation, we obtain the growth law $R \propto t^{1/3}$.

In general, even if the exact growing mechanism is not known, some assumptions can still be made in the late stages of aggregation, where the only important length

scale is the average size $R(t)$ of the domains; this is called the *dynamical scaling hypothesis* and it is verified in experiments and simulations. The implications are that if one measures a quantity which statistically characterizes the systems, such as the two-point correlation function $G(r,t)$, it can be rewritten as

$$G(r,t) = G(x), \tag{2.22}$$

where $x = r/R(t)$ and G is an universal function. The physical meaning of this is that statistically the pattern at any later time is simply a *magnification* (in a statistical sense) of the pattern at an earlier time. This integrates out the time dependence of the problem, leaving only to determine the single-scaled pattern $G(x)$. However, obtaining a theory to predict the scaling function $G(x)$ is difficult, and often the dynamical scaling hypothesis can be only tested against numerical simulations.

2.2 The Structure Factor

Insights about the phase separation process in experimental systems are obtained through the study of the correlation functions of the systems. We already introduced in Section 1.3 the pair correlation function $g(r)$, which is the probability of finding a particle at a distance r from another particle.

A quantity easier to access by scattering experiments is instead the structure factor $S(q)$, related to the Fourier transform of the pair correlation function. This quantity is particularly helpful in the study of the kinetics of phase separation since it can be related to the growth of the characteristic length scale of the system.

The intensity of the scattered radiation can be expressed as

$$I(\boldsymbol{q},t) \propto P(\boldsymbol{q})S(\boldsymbol{q},t). \tag{2.23}$$

The term $P(\boldsymbol{q})$ is called the form factor and is related to the geometric structure of the constituents of the system, while the term $S(\boldsymbol{q},t)$ is called the structure factor,

$$S(\boldsymbol{q},t) = \langle \frac{1}{N} \rho_{\boldsymbol{q}} \rho_{-\boldsymbol{q}} \rangle, \tag{2.24}$$

where $\rho_{\boldsymbol{q}}$ is the Fourier transform of the microscopic density $\rho(\boldsymbol{r})$,

$$\rho_{\boldsymbol{q}} = \int d\boldsymbol{r} \rho(\boldsymbol{r}) e^{-i\boldsymbol{q}\cdot\boldsymbol{r}}. \tag{2.25}$$

Since in experiments one deals with particles, it is useful to define the structure factor supposing that the system is composed of N colloidal particles in the positions $\boldsymbol{r}_i$, $i = 1, ..., N$. In order to do that, we write the density operator as a superposition of delta functions centered at the positions of the particles:

$$\rho(\boldsymbol{r}) = \sum_i \delta(\boldsymbol{r} - \boldsymbol{r}_i). \tag{2.26}$$

Using the latter expression, the structure factor in Eq. (2.24) can be rewritten as

$$\begin{aligned} S(\boldsymbol{q},t) &= \langle \frac{1}{N} \int d\boldsymbol{r}\, d\boldsymbol{s} \sum_i \delta(\boldsymbol{r} - \boldsymbol{r}_i) \sum_j \delta(\boldsymbol{s} - \boldsymbol{r}_j) e^{-i\boldsymbol{q}\cdot\boldsymbol{r}} e^{i\boldsymbol{q}\cdot\boldsymbol{s}} \rangle \\ &= \frac{1}{N} \sum_{i,j}^{N} \langle e^{i\boldsymbol{q}\cdot(\boldsymbol{r}_i - \boldsymbol{r}_j)} \rangle. \end{aligned} \tag{2.27}$$

It can be shown that the structure factor is related to the correlation function of the spatial density through a Fourier transformation. The spatial density correlation function is defined by

$$\rho_2(\boldsymbol{r}, \boldsymbol{s}) = \langle \sum_{i \neq j} \delta(\boldsymbol{r} - \boldsymbol{r}_i)\delta(\boldsymbol{s} - \boldsymbol{s}_j) \rangle, \tag{2.28}$$

the interpretation of this function is that $\rho_2(\boldsymbol{r}, \boldsymbol{s})d\boldsymbol{r}d\boldsymbol{s}$ is the probability that a particle is located in $\boldsymbol{s}$ within a radius $d\boldsymbol{s}$, given that another particle is located in $\boldsymbol{r}$ within a radius $d\boldsymbol{r}$. In a homogeneous and isotropic two-dimensional system, the function depends only on the modulus of the distance between the two points, and we can define the pair correlation function

$$\rho_2(\boldsymbol{r}, \boldsymbol{s}) = \rho_0^2 g(|\boldsymbol{r} - \boldsymbol{s}|), \tag{2.29}$$

so that $2\pi r g(r)dr$ is the probability of finding a particle in a circular section of radius r and thickness dr, conditioned on the fact that another particle is located at the origin. One can straightforwardly verify that

$$S(\boldsymbol{q}, t) = 1 + \rho_0 \int d\boldsymbol{r}\ [g(\boldsymbol{r}, t) - 1]\ e^{i\boldsymbol{q}\cdot\boldsymbol{r}} = 1 + 2\pi\rho_0 \int_0^\infty dr\ r\ h(r, t) J_0(qr), \tag{2.30}$$

where J_0 is the spherical Bessel function of order zero and we have introduced $h(r) = g(r) - 1$.

The structure factor for a system of non-interacting colloids can be calculated analytically using the Ornstein-Zernike equation

$$h(r) = c(r) + \int dr' c(r') h(|r - r'|), \tag{2.31}$$

where the total correlation is obtained through a direct correlation function between two particles $c(r)$ and a spatial convolution of the indirect correlations through all the other particles. The Percus-Yevick approximation [PY58], provides the closure of eq. (2.31) for the determination of $c(r)$ and $h(r)$. The structure factor calculated analytically with this method is shown in fig. (2.2). As can be seen, in the limit of dilute systems ($\phi \to 0$), it is constantly equal to one. For higher concentrations, instead, a peak appears for $q \neq 0$. This peak grows in intensity and shifts to the right as the density increases and is associated with the average distance between the colloidal particles.

We now analyze the information that the structure factor gives about the state of aggregation of a system. The presence of organized structures among the particles within the system corresponds to the appearance of a peak in the structure factor at a certain value of the wave vector q_q, which corresponds to the spatial scale L probed by the elastic scattering from the relation

$$L \approx \frac{2\pi}{q}. \tag{2.32}$$

During coarsening, the value of q_m shifts to smaller and smaller values as time passes, and the peak increases in intensity. This represents the fact that the characteristic length scale of the system L grows over time.

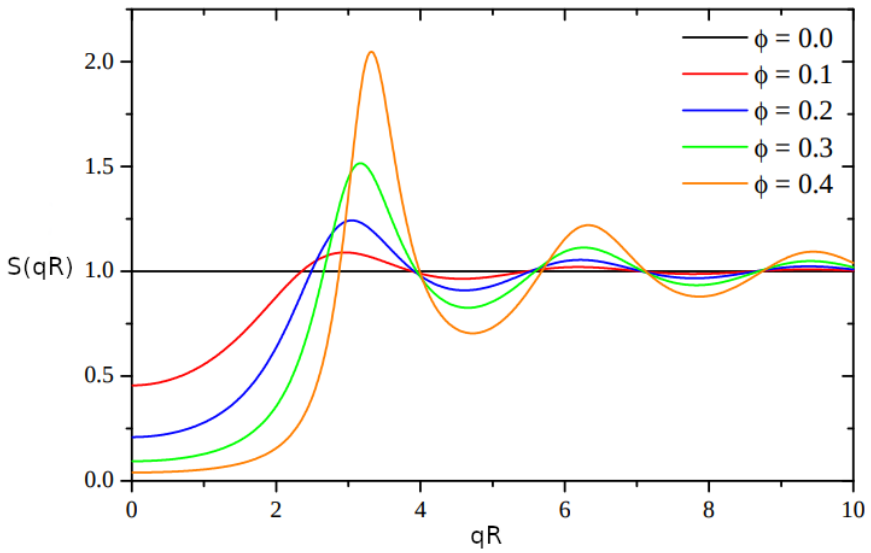

Figure 2.2: Simulated structure factor for a system of non-interacting spheres with excluded volume interaction as a function of density. As the density increases, a peak appears at $qR \neq 0$, and for $q \to 0$ the value goes to zero. From [Wes16].

2.3 Cluster Models

Another perspective on first-order phase transition is the one in terms of cluster models. Theories of cluster dynamics were first introduced by Binder and collaborators [BS76], and are based on kinetic equations that model the detailed mechanism leading to clusters' formation and evolution. These models are more useful compared to continuum theories when dealing with particle-based systems, such as the one we will study in Part II of the thesis. The system is described in terms of the average concentration of clusters of size l at time t, $n_l(t)$. Atomic exchanges with a substrate, or breaking and merging events with other clusters, lead to the evolution of the distribution. This evolution is modeled by a stochastic process which does not take into account the complications of real systems. However, it is thought to contain the essential physics of the phase separation process.

Kinetic equations

We now develop the dynamical theory of cluster formation, following the discussion of the reviews [DCC+04a, BS76]. The processes that can lead to a cluster mass change are the following: evaporation and condensation, dissociation and coagulation and diffusion. The first two mechanisms imply a change in the size l of the clusters; diffusion instead refers to the process in which the position of the center of mass of the cluster

changes with time. If we ignore the latter, we can write a master equation

$$\frac{d}{dt}n_l(t) = \sum_{l'=1}^{\infty} S_{l+l',l'}n_{l+l'}(t) - \frac{1}{2}\sum_{l'=1}^{l-1} S_{l,l'}n_l(t) + \\ + \frac{1}{2}\sum_{l'=1}^{l-1} C_{l-l',l'}n_{l'}(t)n_{l-l'}(t) - \sum_{l'=1}^{\infty} C_{l,l'}n_l(t)n_{l'}(t). \quad (2.33)$$

The first term of the equation gives the increase in the number of l-clusters due to dissociation reaction $(l+l') \implies (l,l')$. The second term represents the decrease of l-clusters caused by dissociation reaction $l \implies (l-l',l')$. The third term represents the increase of l-clusters by coagulation of clusters of size l' and $l-l'$. Finally, the fourth term represents the decrease of l-clusters by the coalescence reactions $(l,l') \implies (l+l')$. The next step is to assume the validity of detailed balance. This yields the correct equilibrium solution and allows to have a single rate W instead of the two different rates C and S for the opposite processes. We then have

$$\frac{d}{dt}n_l(t) = \sum_{l'=1}^{\infty} W_{l',l'}\frac{n_{l+l'}(t)}{n_l+l'} - \frac{1}{2}\sum_{l'=1}^{l-1} W_{l-l',l'}\frac{n_l(t)}{n_l} + \\ + \frac{1}{2}\sum_{l'=1}^{l-1} W_{l-l',l'}\frac{n_{l'}(t)}{n_{l'}}\frac{n_{l-l'}(t)}{n_{l-l'}} - \sum_{l'=1}^{\infty} W_{l,l'}\frac{n_l(t)}{n_l}\frac{n_{l'}(t)}{n'_l}, \quad (2.34)$$

where we used the notation $n_l(t)$ to denote the time-depending cluster distribution and n_l for the equilibrium one. Moving to a continuum description and arranging terms to make explicit the different processes contributing to the evolution of cluster density, we obtain

$$\frac{\partial n_l(t)}{\partial t} = \frac{\partial}{\partial l}\left(R_l n_l \frac{\partial}{\partial l}\frac{n_l(t)}{n_l}\right) \\ + \frac{1}{2}\int_{l_c}^{l} dl' W(l-l',l')\frac{n_{l'}(t)}{n_{l'}}\frac{n_{l-l'}(t)}{n_{l-l'}} - \frac{n_l(t)}{n_l}\int_{l_c}^{\infty} dl' W(l,l')\frac{n_{l'}(t)}{n_{l'}}, \quad (2.35)$$

with the kinetic coefficient

$$R_l = \frac{1}{n_l}\sum_{l'=1}^{l_c}(l')^2 W(l-l'). \quad (2.36)$$

From Eq. (2.35), we can derive the analogous of all the processes we described in Sec. 2.1, i.e., the nucleation theory and Lifshitz-Slyozov mechanism, yielding similar results. As an example, we sketch the derivation of the latter in the next subsection.

Lifshitz-Slyozov theory from a cluster perspective

We can use Eq. (2.35) to derive the Lifshitz-Slyozov theory for the late-time behavior of the phase separation process. The LSW theory is based on the assumption of the growth of large spherical droplets through the diffusive exchange of material. We can thus neglect in the master equation i) the coagulation events between droplets, and ii)

the diffusive part of the master equation proportional to $(\partial^2 n/\partial l^2)$ with respect to the drift part $(\partial n/\partial l)$. The latter approximation is valid if one is interested in describing the growth or shrinking of droplets with size sufficiently differing from the critical size R_c [BS76]. The resultant equation is the continuity equation

$$\frac{\partial n_l(t)}{\partial t} = -\frac{\partial}{\partial l}(v_l n_l(t)), \tag{2.37}$$

with the drift velocity

$$v_l = 2H(t)R_l \tag{2.38}$$

Where we introduced a time-dependent field H in order to satisfy the conservation law for the number of particles. We now must specify R_l to determine the drift velocity. We use the solution of [PL79] for the diffusion-limited growth of large spherical droplets, $R_l = l^{1-2/d}$, where d is the dimension of the system. In three-dimension, the drift velocity is then

$$v_l \sim \left[\left(\frac{l}{l_c}\right)^{1/3} - 1\right]. \tag{2.39}$$

We can introduce a time-dependent scaling solution for the cluster distribution:

$$n_l(t) = t^{\gamma}\tilde{n}(lt^{-x}), \tag{2.40}$$

where γ and x are two unknown exponents. Using the mass conservation law

$$\frac{d}{dt}\sum_l l n_l(t) = 0 \tag{2.41}$$

and Eq. (2.40), we obtain $\gamma = -2x$. Substituting now Eq. 2.40 into Eq. (2.37), then we obtain $x = 1/3$. The scaling solution becomes

$$n_l(t) = t^{-2/3}\tilde{n}(lt^{-1/3}), \tag{2.42}$$

and, in particular, from the argument of the scaling function, $l \sim t^{1/3}$, which is exactly the exponent predicted by LSW theory.

The Smolukowski Equation

The master equation in Eq. 2.33 can be rewritten in a simplified form ignoring the fragmentation terms:

$$\frac{dn_k}{dt} = \frac{1}{2}\sum_{i+j=k} K_{ij} n_i n_j - c_k \sum_{i\leq 1} K_{ik} n_i. \tag{2.43}$$

This is the Smolukowski equation [Smo16], which has some interesting properties and can be used to estimate the growth laws when the dominant mechanism is cluster-cluster collisions. There are several solutions to this infinite set of equations, according to the type of kernel. We will illustrate some results in the case of the constant kernel and the diffusive kernel.

Constant Kernel

The easiest case is the one with a constant kernel, with $K_{ij} = K$ constant numbers. In this case, Eq. 2.43 become

$$\frac{dn_k}{dt} = K\left(\frac{1}{2}\sum n_i n_k - n_k \sum n_i\right). \tag{2.44}$$

Let us consider a monodisperse system as the initial state. In this case, $n_0 = N$ and $c_k = 0$, for $k > 0$. Let us write $c_k = \phi(t)\psi(t)^{k-1}$, where ϕ and ψ are two functions of time. The initial condition is $\phi(0) = N$ and $\psi(0) = 0$. Substituting this ansatz in the Smolukowski equation, we obtain

$$\psi^{k-1}\frac{d\phi}{dt} + (k-1)\phi\psi^{k-2}\frac{d\psi}{dt} = K\phi^2\psi^{k-2}\left(\frac{k-1}{2} - \frac{\psi}{1-\psi}\right). \tag{2.45}$$

Identifying then the terms with the same power of ψ, we obtain a set of equations:

$$\frac{d\phi}{dt} = -k\frac{\phi^2}{1-\psi} \tag{2.46}$$

$$\frac{d\psi}{dt} = K\frac{\phi}{2}. \tag{2.47}$$

Upon variable substitution, one gets (taking care of the initial conditions):

$$\phi = N(1-\psi)^2. \tag{2.48}$$

We can now solve the equation for ψ, finding

$$\psi = \frac{KN}{2}\frac{t}{1+KNt/2}, \tag{2.49}$$

and finally

$$c_k = N\left(\frac{KNt}{2}\right)^{k-1}\left(1+\frac{KNt}{2}\right)^{-k}. \tag{2.50}$$

The total number of clusters is easily calculated as

$$N_c = \sum_{k=1}^{\infty} c_k = \frac{N}{1+KNt/2}. \tag{2.51}$$

Kernel in the Diffusive case

Let us consider the case of the Brownian diffusion of the aggregates. In this case, the aggregation causes the formation of fractal structures with a fractal dimension $d_f < d$, where d is the dimensionality of the system and d_f verifies the relation $M \sim R^{d_f}$, where M is the mass of the aggregates and R their radius.

The rate of collision between a given i aggregated supposed to be fixed, centered on the origin, and all the other j clusters, can be calculated assuming that, for sufficiently large times, a steady state is established in which all j aggregates diffuse radially from a region far away from the origin, where concentration c_j is constant and equal to n_j/V (the mean value in the solution) to a region close to the aggregate where they disappear,

i.e. $c = 0$. Introducing a mean hard core radius R for clusters i, and assuming a spherical geometry, this reduces to a trivial steady-state diffusion problem in which c_j depends on the distance from the origin, with $c_j = n_j/V$ for $r = \infty$ and $c_j = 0$ for $r = R_i + R_j$. The radial current of j clusters, J_j, is given by:

$$J_j = -\frac{K_{ij} n_j}{4\pi r^2}. \tag{2.52}$$

Considering that Flick's law relates the concentration gradient to the radial current through the diffusion coefficient, $J_j = -D_{ij} dc_j/dr$, this gives

$$c_j(r) = c(\infty) - \frac{K_{ij} n_{ij}}{4\pi D_{ij} r}, \tag{2.53}$$

Taking one of the two clusters as a reference frame, for example, cluster i with a diffusion coefficient D_i, it can be shown that the other cluster diffuses with an effective diffusion constant $D_{ij} = D_i + D_j$. Now, using this fact and the limiting conditions on c_j, one obtains

$$K_{ij} = 4\pi D_{ij}(R_i + R_j) = 4\pi(D_i + D_j)(R_i + R_j). \tag{2.54}$$

Now we use the relation between the mass of the cluster and the diffusion coefficient. For spherical particles, the diffusion coefficient decreases with the inverse of the radius, $D_i \sim R_i^{-1}$. In the case of a cluster which departs from the spherical symmetry, this relation does not hold anymore, but we can still use a general relation $D_i \sim R_i^{-\alpha}$. Using the latter expression, reasoning in d dimensions, and using the fact that our clusters are fractal with fractal dimension d_f, we obtain

$$K_{ij} \sim (i^\alpha + j^\alpha)(i^{1/d_f} + j^{1/d_f})^{d-2}. \tag{2.55}$$

This expression verifies a homogeneity propriety, $K_{\lambda i, \lambda j} = \lambda^{2\omega} K_{ij}$, with

$$2\omega = \alpha + \frac{d-2}{d_f}. \tag{2.56}$$

From the homogeneity propriety, we can derive a scaling solution for the cluster distribution. In the case of $\omega < 1/2$, also called flocculation regime, one can define a regular cluster size distribution function. For large times, the mean cluster size $\langle k \rangle$ increases with time as a power law,

$$\langle k \rangle \sim t^\gamma, \tag{2.57}$$

with $\gamma = 1/(1 - 2\omega)$. Finally, using Eq. 2.56, we can derive the exponent γ in terms of the fractal dimension d_f and the exponent α of the cluster diffusion:

$$\gamma = \frac{1}{1 - \alpha - \frac{d-2}{d_f}}. \tag{2.58}$$

In particular, this expression will come in hand when we will estimate the growing coefficient of ABPs clusters in Chapter 3.

2.4 Aggregation in MIPS

The theory of phase separation considered previously has a great advantage, it correctly predicts the universality class of the coarsening exponent and the static proprieties of the phase-separated system, such as the phase diagram. However, the theory is based on the thermal equilibrium assumption, which is not valid for active systems.

As stated in the first chapter, ABPs are the minimal model of active systems and, therefore, have been the standard tool for testing and studying aggregation phenomena in non-equilibrium settings. ABPs phase separation is strikingly reminiscent of equilibrium vapour-liquid demixing, with the role of the temperature played by the activity of the particles: after a critical Péclet number, the particles separate in a dilute and dense phase, with the densities of the two falling along a binodal. However, the phase separation is not driven by an attractive interaction among particles, but solely by the activity itself: this is the MIPS phenomenon we already introduced in the first chapter. Simply speaking, this is a consequence of the interplay between self-propulsion and steric repulsion, which leads to active particles accumulating where they move slowly. This follows directly from the master equation for the local density of particles ρ [GMST15a] (see Appendix B for a complete derivation)

$$\partial_t \rho(\boldsymbol{r}, t) = \frac{\tau}{2} \boldsymbol{\nabla} \cdot \left[v(\boldsymbol{r}, t) \boldsymbol{\nabla} (v(\boldsymbol{r}, t) \rho) \right], \tag{2.59}$$

whose steady-state solution implies $v(\boldsymbol{r}, t) \propto 1/\rho(\boldsymbol{r}, t)$, that is, the local velocity field v results inversely proportional to the local density ρ.

The non-equilibrium nature of active phase separation stems directly from the lack of microscopic time-reversal symmetry, which also implies that their steady states do not obey detailed balance. For all the reasons above, all the knowledge and tools derived from the standard thermodynamic approach cannot be directly applied to analyze MIPS. This seems unfortunate since numerical experiments report numerous similarities between MIPS and an *ordinary* phase separation. Therefore, a question the active matter community has been asking is whether there exists a mapping from equilibrium to active phase separation, and to what extent the concepts and tools of the classical theory can be adapted or generalized to describe MIPS. The attempts of various researchers culminated in deriving a general thermodynamic framework suitable also out of equilibrium that successfully predicts the phase equilibria of MIPS.

Apart from a possible mapping with equilibrium, another question puzzling researchers is about the aggregation mechanism and coarsening behaviour of MIPS. We have seen that in the phase separation, an initially homogeneous fluid gives rise to a system of droplets of the dense phase immersed in a dilute phase. The droplets grow in time, and the system evolves towards a state of complete phase separation, and at late times their length scale grows as a power law in time, $R(t) \sim t^{\alpha}$. LSW theory predicts an exponent $\alpha = 1/3$, regardless of the dimension of the system. Even if there is no reason *a priori* to expect that this universality class is preserved in the case of MIPS, analytical models of active aggregation are built starting from the equilibrium counterpart and thus predict by constructions the same coarsening exponents for late time of the phase separation process. However, numerical experiments have shown a coarsening exponent close to the equilibrium case but slightly slower in $2d$, leaving open the question about the actual nature of the aggregation mechanism in ABPs.

We will now review in more detail these results about MIPS and active aggregation. We will mostly follow the discussion of the review [CT15c]

Active Multibody dynamics

The first approach one could use to have a theoretical understanding of MIPS is to coarse-grain the dynamics of a single ABP, as done for example in [TC08, CT13]. One obtains the equation of motion for the probability density $\phi(\boldsymbol{r})$ of finding a particle at position $\boldsymbol{r}$ at time t,

$$\partial_t \phi = -\boldsymbol{\nabla} \cdot \boldsymbol{j}, \tag{2.60}$$

$$\boldsymbol{j} = -D\boldsymbol{\nabla}\phi + \boldsymbol{V}\phi, \tag{2.61}$$

where $D(\boldsymbol{r}) = v(\boldsymbol{r})^2\tau(\boldsymbol{r})/d$ is the diffusion coefficient, d is the dimensionality of the system, $\boldsymbol{V}(\boldsymbol{r})$ is the drift velocity, and $\tau(\boldsymbol{r})$ is the persistence time. The drift velocity is related to the persistence time through the relation

$$\frac{\boldsymbol{V}(\boldsymbol{r})}{D(\boldsymbol{r})} = -\boldsymbol{\nabla} \ln v(\boldsymbol{r}). \tag{2.62}$$

These equations are formally equivalent to a passive Brownian particle in an external potential $\beta U(\boldsymbol{r}) = \ln v(\boldsymbol{r})$. One can thus use standard tools to derive the coarse-grained density $\rho(\boldsymbol{r})$ in a system of many interactive ABPs. We only report the results of the calculations that can be found in [TC08]. In the case of noninteracting ABPs, the equation of motion for the density is

$$\partial_t \rho = \boldsymbol{\nabla} \cdot \boldsymbol{J}, \tag{2.63}$$

$$\boldsymbol{J} = -D\boldsymbol{\nabla}\rho + \boldsymbol{v}\rho + \rho\boldsymbol{\nabla}\frac{\delta}{\delta\rho}D([\rho], \boldsymbol{r}) + \sqrt{2D\rho}\boldsymbol{\Lambda}, \tag{2.64}$$

where we generalized the expression allowing for a density-dependent diffusion coefficient $D([\rho], \boldsymbol{r})$. This equation can be converted to a Fokker-Plank equation for the many-body probability $P[\rho]$, which reads

$$\partial_t P = -\int d\boldsymbol{r} \left(\boldsymbol{\nabla}\frac{\delta}{\delta\rho}\right) \left[\boldsymbol{V}\rho - D\boldsymbol{\nabla}\rho - D\rho\left(\boldsymbol{\nabla}\frac{\delta}{\delta\rho}\right)\right] P. \tag{2.65}$$

We can find the steady state solution of the equation by setting $\partial_t P = 0$, which gives

$$\left[\boldsymbol{V}\rho - D\boldsymbol{\nabla}\rho - D\rho\left(\boldsymbol{\nabla}\frac{\delta}{\delta\rho}\right)\right] P_{\mathrm{eq}} = 0. \tag{2.66}$$

Using the ansatz $P_{\mathrm{eq}} = \exp\left(-\mathcal{F}[\rho]\right)$, one can obtain the condition for the equilibrium free energy $\mathcal{F}[\rho]$ to exist:

$$\frac{V([\rho], \boldsymbol{r})}{D([\rho], \boldsymbol{r})} = -\beta\boldsymbol{\nabla}\frac{\delta\mathcal{F}}{\delta\rho}, \tag{2.67}$$

which can also be written as

$$k_B T \ln v([\rho], \boldsymbol{r}) = \frac{\delta\mathcal{F}_{\mathrm{ex}}}{\delta\rho}. \tag{2.68}$$

This equivalence reveals a crucial point: the existence of a well-defined free energy functional $\mathcal{F}_{\rm ex}$ hinges on the system's ability to satisfy detailed balance, a principle ensuring microscopic reversibility under specific conditions. In general, active systems violate detailed balance due to their non-equilibrium nature, which implies the absence of $\mathcal{F}_{\rm ex}$ that satisfies Eq. (2.68). However, if under specific circumstances the "excess" free energy functional exists, the active system becomes formally equivalent to a passive system with a total free energy functional:

$$\mathcal{F}[\rho] = k_B T \int d\boldsymbol{r} \rho(\ln \rho - 1) + \mathcal{F}_{\rm ex}[\rho], \tag{2.69}$$

with

$$\mathcal{F}_{\rm ex}[\rho] = \int_0^\rho ds\ \ln v(s). \tag{2.70}$$

Equivalently, introducing the free energy density $f(\rho)$, one has $\mathcal{F}[\rho] = \int d\boldsymbol{r}\, f(\rho)$, with[3]

$$f(\rho) = \rho(\ln \rho - 1) + \int_0^\rho ds\ \ln v(s). \tag{2.71}$$

As said, the existence of the "excess" free energy functional $\mathcal{F}_{\rm ex}[\rho]$ does not hold in general, and this causes the striking difference between passive and active systems: that detailed balance is not satisfied at all scales. Suppose, however, that ρ is a slowly varying field, and that the speed $v([\rho], \boldsymbol{r})$ depends isotropically on the density within some finite range from the point $\boldsymbol{r}$. In this case, one can write

$$v([\rho], \boldsymbol{r}) = v[\rho(\boldsymbol{r})] + \mathcal{O}(\nabla^2 \rho). \tag{2.72}$$

Suppressing the gradient terms is equivalent to assuming a local dependence of swim speed on density $v = v(\rho)$. In this case, the condition for the existence of the functional $\mathcal{F}_{\rm ex}$ is always satisfied, and the system can be mapped onto equilibrium. However, this assumption means that the interfacial tension of this equivalent passive system is zero, because of the absence of the gradient terms. The interfacial tension is at the same time the driving force of phase separation, thus a theory that neglects it cannot describe the phase separation process satisfyingly.

A phenomenological ansatz to solve this issue is to add a square gradient term with constant coefficient κ to the free energy functional of the equivalent passive system,

$$\mathcal{F}[\rho] = \int d\boldsymbol{r} \left[\frac{\kappa}{2} (\boldsymbol{\nabla}\rho)^2 + f(\rho) \right], \tag{2.73}$$

where $f(\rho)$ obeys Eq.(2.71). From the latter equation, the non-equilibrium chemical potential reads

$$\mu = \frac{\delta \mathcal{F}}{\delta \rho} = -\kappa \nabla^2 \rho + \ln \rho + \ln v(\rho). \tag{2.74}$$

In order to solve the MIPS theory declined above, one must provide as an input the expression for the velocity of the particles as a function of the density, $v(\rho)$. Numerical experiments find it to decrease with good approximation linearly with density [FM12a, RHB13a, STA$^+$13a, SMAC14b]:

$$v(\rho) = v_0 \left[1 - \rho/\rho^*\right], \tag{2.75}$$

[3]Here and in the following we used, without loss of generality, $\beta = 1$

where v_0 is the swim speed of the active particles in the dilute region, and ρ^* is the close packing limit of the system. This theory, however, has a big limitation: it always predicts a spinodal decomposition and thus a phase separation for $\rho > \rho^*/2$, regardless of the Péclet number of the particles. This contradicts numerous numerical simulations which have found with great accuracy the critical point of MIPS at $\mathrm{Pe_c} \approx 55$ (in $d = 2$). The existence of a critical point for MIPS is also predicted by numerous kinetic approaches [FM12a, RHB13a, BLS13].

Scalar theory of active aggregation

A more general study requires a gradient expansion of the swim speed v. A simple way to do this [SMAC14b] is to consider only the gradient contribution coming from the non-equilibrium chemical potential $\mu = \mu_{\mathrm{id}} + \mu_{\mathrm{ex}}$, where $\mu_{\mathrm{id}} = \ln \rho$ is the ideal chemical potential and $\mu_{\mathrm{ex}} = \ln v([\rho], \boldsymbol{r})$ is the excess chemical potential. Then one assumes

$$\mu_{\mathrm{ex}} = \ln v[\hat{\rho}(\boldsymbol{r})], \tag{2.76}$$

where $\hat{\rho}(\boldsymbol{r})$ is a smoothed density field by a convolution with an isotropic kernel whose range is comparable with the persistence length $\ell = v(\rho)\tau$. This is the length scale that the particles sample before changing direction. Assuming a slowly varying ρ, one can expand it as

$$\hat{\rho} = \rho + \gamma^2 \nabla^2 \rho, \tag{2.77}$$

where $\gamma = \gamma_0 v(\rho)$ and γ_0 is a constant of order unity. The chemical potential can be then written as

$$\mu = \ln \rho + \ln v(\rho) - \kappa(\rho) \nabla^2 \rho, \tag{2.78}$$

where $\kappa(\rho) = -\gamma_0^2 \tau^2 v(\rho) v'(\rho)$. Since $\kappa(\rho)$ is non-constant, this chemical potential is not integrable: the theory therefore does not obey detailed balance at this coarse-grained level, and no mapping with an equilibrium system can be done. However, one can still define the *nearest integrable model* as

$$\mathcal{F} = \int d\boldsymbol{r} \left[f(\rho) + \frac{\kappa(\rho)}{2} (\boldsymbol{\nabla}\rho)^2 \right], \tag{2.79}$$

with a chemical potential

$$\frac{\delta \mathcal{F}}{\delta \rho} \equiv \mu_{DB} = \ln \rho + \ln v(\rho) - \kappa(\rho) \nabla^2 \rho - \frac{\kappa'(\rho)}{2} (\boldsymbol{\nabla}\rho)^2. \tag{2.80}$$

Compared to Eq.(2.78), now an additional term appears, $\kappa'(\rho)(\boldsymbol{\nabla}\rho)^2/2$, which is needed to restore detailed balance. The model is completed with the functional expression for $v(\rho)$ of (2.75) as the only external parameter. The results of the integration of the model using both the explicit break of detailed balance, Eq.(2.78), and the expression with restored detailed balance, Eq.(2.80), are shown in Fig.2.3. In particular, the average size of the dense phase $L(t)$ for spatial dimension $d = 2, 3$ is compared against particle-based simulations of ABPs. Even if particle-based simulations and continuum theories show a good agreement, in $d = 2$, the coarsening exponent appears to be below the $1/3$ observed in equilibrium phase separation. This shift is independent of the presence or not of detailed balance.

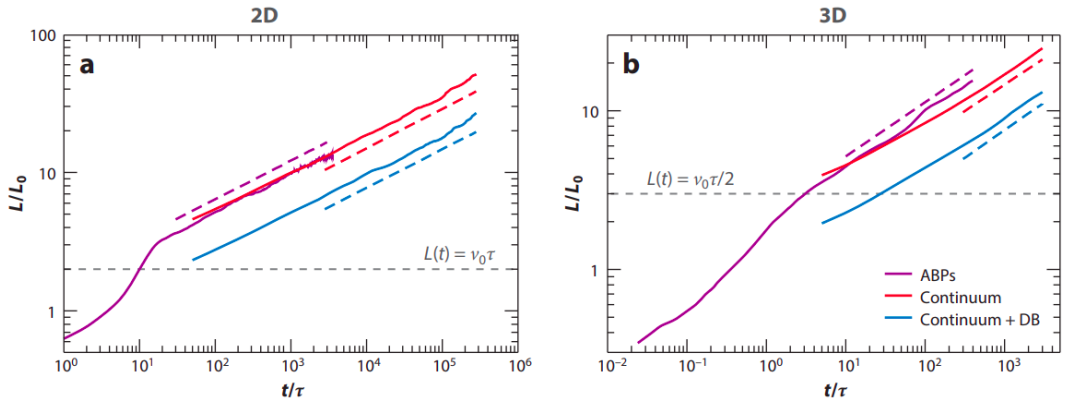

Figure 2.3: Coarsening dynamics of (a) the continuum model violating detailed balance (DB), ABPs simulations, and (shifted downward for clarity) the nearest integrable model in $d = 2$. (b) Same for $d = 3$. Dashed lines correspond to exponents $\alpha \approx 0.28$ in $d = 2$ and $\alpha \approx 0.33$ in $d = 3$. Adapted from Reference [SMAC14b].

Active Model B

In the same spirit of the previous section, an active extension of the Cahn-Hilliard equations of Model B, Eq.(2.9), has been proposed in [STA$^+$13a, WTS$^+$14, SBML14, SMBL15]. The idea is to add the minimal 'non-integrable' gradient term to the equations; the resulting theory, Active Model B (AMB), cannot be obtained therefore by any free-energy functional. The equation of motion for the scalar field $\phi(\boldsymbol{r}, t)$ are

$$\frac{\partial \phi(\boldsymbol{r}, t)}{\partial t} = -\boldsymbol{\nabla} \cdot \boldsymbol{J}(\boldsymbol{r}, t), \tag{2.81}$$

$$\boldsymbol{J}(\boldsymbol{r}, t) = -\boldsymbol{\nabla} \cdot \mu + \Lambda, \tag{2.82}$$

$$\mu = -\phi + \phi^3 - \nabla^2 \phi + \lambda (\boldsymbol{\nabla} \phi)^2, \tag{2.83}$$

where the order parameter ϕ is related to the number density as $\phi = (2\rho - \rho_H - \rho_L)$, with ρ_H e ρ_L the coexisting densities. The vector $\boldsymbol{\Lambda}$ is a Gaussian white noise with zero mean and variance, and μ is the chemical potential. One can write Eq.(2.83) as $\mu = \mu_0 + \mu_1$, where the first term is chosen to be equal to the usual Model B form, $\mu_0 = -\phi + \phi^3$, so that at zeroth-order the model has the same free-energy of the equilibrium case. The gradient term $\mu_1 = \mu_1^P + \mu_1^A$ is the sum of an integrable 'passive' piece, which can be written as the functional derivative of a free-energy functional, and a non-integrable 'active' piece, which instead cannot. The passive piece is given by $\mu_1^P = -\nabla^2 \phi$, which implies it comes from a free-energy functional of the form $f_1 = (\nabla \phi)^2/2$ (same as equilibrium). For the active and non-integrable term, the usual choice is $\mu_1^A = \lambda (\boldsymbol{\nabla} \phi)^2$, with the constant λ a parameter of the model. This is the simplest addition to μ at second order in the gradient expansion that is not integrable.

From this model, analytical predictions about the phase diagram can be derived utilizing a modified common tangent construction to find the coexisting phases, although we will postpone the discussion to the next section. On the other hand, the coarsening behaviour can be studied numerically, although it shows no significant differences from passive coarsening. However, also in this case, numerical evidence suggests that the exponent governing the growth of domain size R(t) exhibits a subtle slowing down.

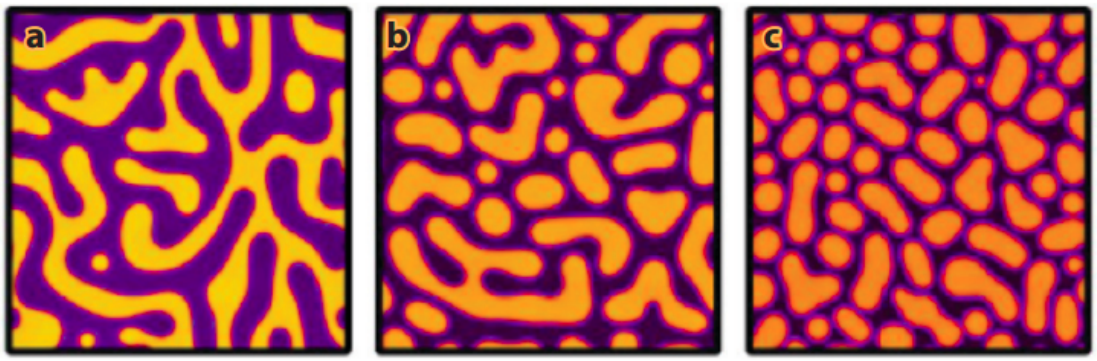

Figure 2.4: Coarsening dynamics of Active Model B for different values of $\lambda = 0, -1, -2$ (for a, b, c, respectively) at $\phi = \phi_0 = 0$ in $d = 2$

In Fig.2.4 snapshots of the system during the coarsening process at different λ are reported.

A generalization of Active Model B, called Active Model B+ (AMB+), has been proposed in [TNC18]. The model is obtained from Model B by adding all therm to order $\mathcal{O}(\nabla^4\phi^2)$ in the gradient expansion. This is because these terms allow to break of the time-reversal symmetry, which is necessary to allow for circulating real-space currents, which in turn are directly involved in the nonlocality of the chemical potential $\mu = \mu[\phi]$, and have a direct effect in the phase ordering and phase equilibria. AMB+ thus can describe a more complex phenomenology of phase separation, such as the reversing of the Ostwald ripening process. These phenomena are not captured by AMB, which for construction has a similar behaviour to the passive model B.

Practically speaking, the breaking of time-reversal symmetry is obtained in Active Model B+ by adding these terms without altering the relation between mobility and noise in the equation of motion for the order parameter. The model can be written as

$$\partial_t \phi = -\boldsymbol{\nabla} \cdot \boldsymbol{J} + \sqrt{2DM}\Lambda, \tag{2.84}$$

$$\boldsymbol{J}/M = -\boldsymbol{\nabla}\left[\frac{\delta \mathcal{F}}{\delta \phi} + \lambda|\boldsymbol{\nabla}\phi|^2\right] + \xi(\nabla^2\phi)\boldsymbol{\nabla}\phi, \tag{2.85}$$

where the terms λ and ξ are responsible for the breaking of time-reversal symmetry, plus a modification in the structure of the gradient term in the free energy. The case of $\lambda \neq 0$ and $\xi = 0$ is Active Model B we cited before. The phenomenology of the model is related to the activity model parameters, λ and ξ. When both are small, Ostwald ripening operates normally as a late-time aggregation mechanism. The same is obtained at large activity when λ and ξ have opposite signs. The most interesting regime is obtained however when the parameters are large and positive. For such parameters, numerical simulations find a regime of *reverse* Ostwald ripening for vapour bubbles in a dense liquid, meaning that small droplets grow at the expense of larger droplets; and when both the parameters are large and negative, one finds the same for dense droplets in a dilute vapour. The reverse Ostwald ripening phenomenon is rationalized analytically by the appearance of a negative pseudotension, which plays the role of the surface tension for the phase separation in this system. Some snapshots of the coarsening of AMB+ in the different regimes are reported in Fig.2.5.

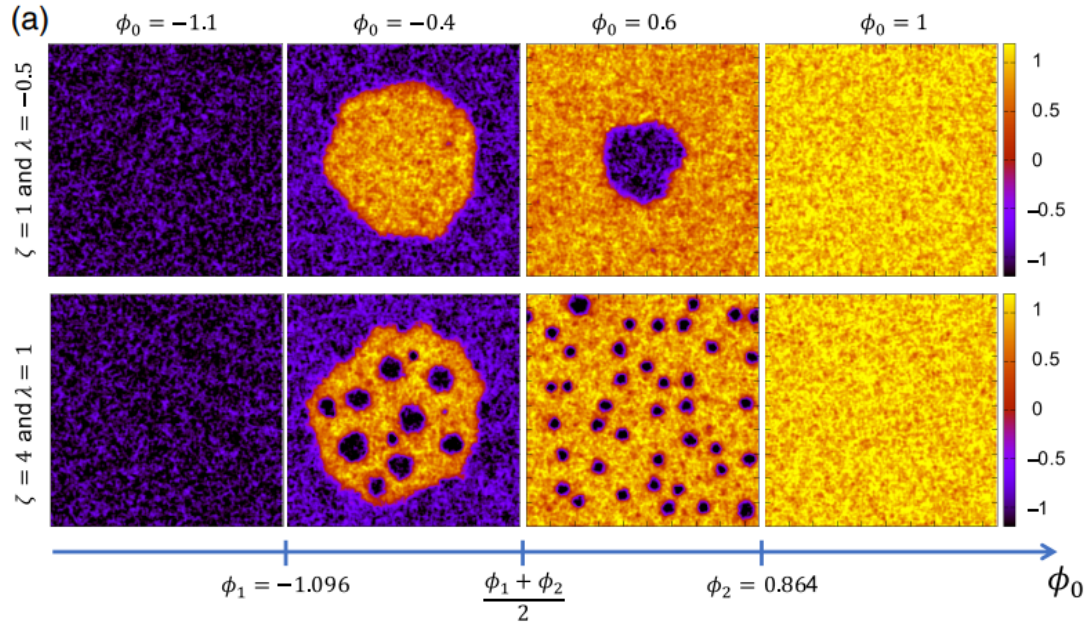

Figure 2.5: Steady-state phase diagram as a function of global density ϕ_0 for two different sets of activity parameters: $\xi = 1$, $\lambda = -0.5$, and $\xi = 4$, $\lambda = 1$. For the former parameters, the steady-state phase diagram resembles equilibrium Model B with full phase separation into dense (yellow) and dilute (blue) phases. The latter parameters instead, besides the low- and high-density uniform phases, produce a either bubbly phase separation or a homogeneous bubble phase. Adapted from Reference [TNC18].

The studies above do not take into account hydrodynamic interactions. The first attempt in this direction is done in [TWMC15], where the Active Model H is introduced. The model is the active extension of equilibrium Model H, by including two terms that break time-reversal symmetry: one in the diffusive current and one in the deviatoric stress tensor. These terms have different effects on the coarsening behaviour of the systems, depending on the type of active particles: extensile or contractile. The former have a tendency to align with the local velocity field, while the latter have a tendency to align against it. For extensile particles, the coarsening follows a similar behaviour as in the passive case, with a crossover from a diffusive to a viscous hydrodynamic regime. For contractile particles, instead, the coarsening can be arrested at a finite length scale, due to a balance between diffusive and mechanical stresses.

Generalized thermodynamic approach for phase equilibria

The fundamental aspects of the phase equilibrium can then be inferred from a generalized thermodynamic treatment, as shown in [SSW$^+$15a, SSC$^+$18a, SSC$^+$18b]. The active counterpart of the Cahn-Hilliard equation can be written in a generalized form as

$$\partial_t \rho = \boldsymbol{\nabla} \cdot (M \boldsymbol{\nabla} g[\rho]), \tag{2.86}$$

$$g[\rho] = g_0(\rho) + \lambda(\rho) |\boldsymbol{\nabla}\rho|^2 - \kappa(\rho) \nabla^2 \rho, \tag{2.87}$$

where $g_0(\rho)$ is the equilibrium free energy density, and $\lambda(\rho)$ and $\kappa(\rho)$ are the kinetic coefficients. It can be shown that the equilibrium dynamics is obtained if the coeffi-

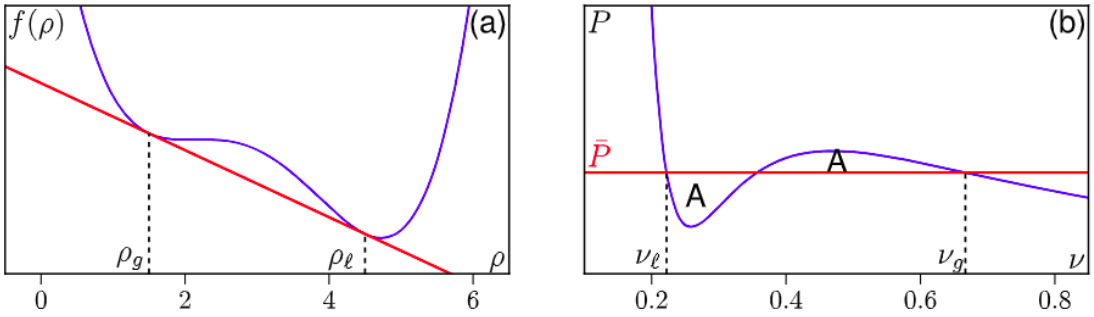

Figure 2.6: Illustration of the thermodynamic constructions of coexisting densities. (a) Common tangent construction on the free energy density $f(\rho)$. (b) Maxwell equal-area construction on the pressure. From reference [SSC+18a].

cients verify the relation $2\lambda + \kappa' = 0$. In this case, $g[\rho]$ becomes the derivative of the free energy functional

$$g[\rho] = \frac{\delta \mathcal{F}}{\delta \rho} = \frac{\delta}{\delta \rho} \int d\boldsymbol{r} \left(f(\rho) + \frac{\kappa(\rho)}{2} (\boldsymbol{\nabla} \rho)^2 \right). \tag{2.88}$$

This ensures that at equilibrium, one can extract the coexisting densities for the phase separation from the common tangent construction of the bulk free energy $f(\rho)$ (see, for instance, [Bra02]). The extracted two coexisting densities fulfil the equal-area Maxwell construction,

$$\int_{v_g}^{v_l} dv \left[P(v) - \overline{P} \right] v = 0, \tag{2.89}$$

where v is the inverse of the density, $P(v)$ is the pressure, defined as $P(\rho) = \rho f'(\rho) - f(\rho)$, and $\overline{P}$ is the equilibrium bulk pressure. The method is schematically shown in Fig.2.6.

In the non-equilibrium generalization of Eq.(2.86), there are no guarantees about the existence of a free energy functional that can govern the system's dynamics. However, is it possible to write g as a functional derivative of a generalized free energy $\mathcal{G}$, with respect to a new variable R defined through the relation

$$\kappa R'' = -(2\lambda + \kappa') R'. \tag{2.90}$$

Here we denoted with the prime symbol the derivative with respect to the field ρ. Now, Eq. (2.86) can be written as

$$\partial_t \rho = \boldsymbol{\nabla} \cdot \left(M \boldsymbol{\nabla} \frac{\delta \mathcal{G}}{\delta R} \right), \tag{2.91}$$

with

$$\mathcal{G} = \int d\boldsymbol{r} \left[\phi(R) + \frac{\kappa}{2R'} (\boldsymbol{\nabla} R)^2 \right], \quad \frac{d\phi}{dR} \equiv g_0. \tag{2.92}$$

Although dealing with a non-conserved order parameter R and with a generalized thermodynamic functional $\mathcal{G}$, one can recover the common tangent construction for the generalized free energy ϕ. In particular, in the case $2\lambda + \kappa' = 0$, one has from Eq. (2.90) that $R = \rho$ and the equilibrium situation is recovered.

This framework can be tested on active particles. In this case, one can use a fluctuating hydrodynamic expression for the stochastic density $\hat{\rho}(\boldsymbol{r}) = \sum \delta(\boldsymbol{r} - \boldsymbol{r}_i(t))$ [SSC$^+$18a, FMMT12], where $\boldsymbol{r}_i(t)$ is the position of the i-th particle at time t. The deterministic limit of the equation of motion for $\hat{\rho}$ gives the coarse-grained equation for the mean-field density. Considering a phase-separated setup with the interface parallel to the y axis, the equation of motion for the density reads $\dot{\rho} = \partial_x^2 g$, with

$$g = D_t \rho + \frac{v_0^2}{2D_r}(\rho + m_2) + \hat{I}_2 - \frac{v_0 D_t}{D_r}\partial_x m_1 + P_D, \tag{2.93}$$

$$P_D = \int_{-\infty}^{x} dx \int d^2\boldsymbol{r}\partial_x V(\boldsymbol{r} - \boldsymbol{r}')\langle\rho(\boldsymbol{r})\rho(\boldsymbol{r}')\rangle, \tag{2.94}$$

$$\hat{I}_2 = \frac{-v_0}{D_r}\int d^2\boldsymbol{r}\partial_x V(\boldsymbol{r} - \boldsymbol{r}')\langle\rho(\boldsymbol{r})\hat{m}_1\rangle, \tag{2.95}$$

where $\hat{m}_n = \sum_i^N \delta(\boldsymbol{r} - \boldsymbol{r}_i(t))\cos(n\theta_i(t))$ is the n-th moment of the density, D_t is the translational diffusion coefficient, D_r is the rotational diffusion coefficient, v_0 is the self-propulsion speed, $V(\boldsymbol{r})$ is the interaction potential, and P_D is the direct interaction pressure. The term $\hat{I}_2$ is the contribution of the interaction to the pressure. The term P_D is the direct interaction pressure, and it is the only term that depends on the microscopic details of the system.

For homogeneous systems, the expression for g reduces exactly to the equation of state for the mechanical pressure [SSW$^+$15b]. Eq.(2.93) can therefore be seen as a generalization of the pressure to the inhomogeneous case, where contributions from interfacial terms are also present. We can separate the homogeneous contribution from the inhomogeneous one, $g = g_0(\rho(x)) + g_{\text{int}}([\rho], x)$, where $g_{\text{int}}([\rho], x)$ gives a non-local contribution the pressure. This separation is done in [SSC$^+$18a] utilizing an empirical expression for g_0 and inferring the expression for g_{int} numerically.

Then they can proceed to apply the common tangent construction to the generalized free energy. Concretely, this is done by solving the equation

$$\int_{v_l}^{v_g} d\,v\,[g_0(v) - \overline{g}] = \int_{x_g}^{x_l} g_{\text{int}}\partial_x v dx, \tag{2.96}$$

which correspond to a modified Maxwell construction: the binodals correspond to the intersection between the function $g_0(v)$ and the horizontal line $\overline{g}$. which gives the coexisting densities v_l and v_g and $\overline{g}$. The resultant coexisting densities for the MIPS are shown in Fig.2.7 and match very well the measured ones. However, it is important to note that the equilibrium Maxwell construction (blue line in Fig.2.7) fails to account for the phase diagram of Active Brownian Particles.

Particle-based numerical evidence of coarsening behaviour

Continuum models of active aggregation are based on modifications of the equilibrium Cahn-Hilliard equation, which describes the phase separation of a binary mixture. These models can provide some understanding of the physical principles that govern the aggregation process, but they have inherent limitations. Specifically, they assume a predefined mechanism of aggregation that depends on the equilibrium free energy functional, and they neglect the effects of fluctuations, interactions, and heterogeneities that may arise in the system. To capture the full complexity and diversity of

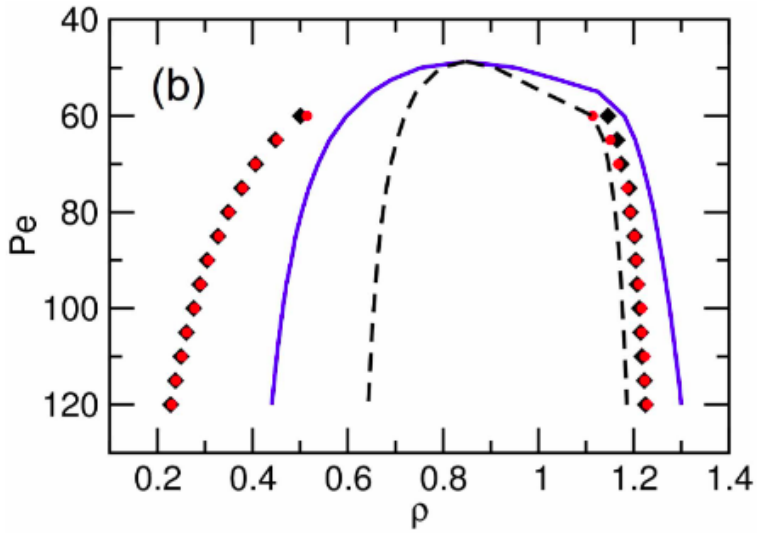

Figure 2.7: Phase diagrams of ABPs, measured numerically (diamonds), through the predictions of equation (2.96) (red circles), and from the equilibrium Maxwell construction with (blue line). The dashed line corresponds to the boundaries of the spinodal region. Adapted from Reference [SSC$^+$18a].

the aggregation phenomenon, one needs to resort to particle-based simulations, which can account for the microscopic details and dynamics of the system. However, these simulations are computationally demanding and require enormous statistics to obtain reliable results and avoid finite-size effects.

The first kinetic study with particle-based simulation for a model of ABPs is from Redner et al. [RHB13c]. They simulated around 5×10^4 ABPs and measured a growth exponent for the cluster mean size equal to $\alpha = 0.272$ in 2D. A second numerical study of ABPs [SWMC15] is [SMAC14b], where ABPs simulations with 5×10^5 particles were performed in $2d$ and 4×10^7 particles in $3d$. The authors found a coarsening exponent of $\alpha \approx 0.28$ in $2d$ and $\alpha \approx 0.34$ in $3d$ (see Fig.2.3).

In summary, we have reviewed the main results and challenges of studying MIPS in Active Brownian Particles. We have seen that both continuum models and particle simulations report a slightly smaller coarsening exponent in $2d$ than that of equilibrium phase separation, which is $\alpha = 1/3$. These results have generally been interpreted as consistent with the $\alpha = 1/3$ exponent, assuming that the lower exponent in $2d$ is a transient regime that would eventually converge to the real exponent at very long times. However, this interpretation is under debate, and large particle-based simulations are required to i) study the growth mechanism of the MIPS domains and ii) obtain a reliable measurement of the asymptotic coarsening exponent. These questions are part of the broader question about the mesoscopic phenomenological differences between MIPS and equilibrium phase separation, which is still to be investigated further. We addressed these questions in my PhD project, and we will report the results we found in the next part of the thesis.

Part II

Results

3

MIPS Dynamics and Morphology

We closed the first part of the Thesis with the debate about the aggregation mechanism of MIPS and, in a broader sense, about the differences with an equilibrium phase separation. In this chapter, we explore some of these open questions, in particular regarding the properties of the aggregated structures formed by (hard) active Brownian particles (ABPs) in two dimensions, using state-of-the-art numerical simulations.

The chapter is organized as follows. In the first section, we study the aggregation dynamics of motility-induced phase separation (MIPS) and the structure of the dense phase. We identify several dynamic regimes of ABP aggregation, provide the most accurate estimate of the coarsening exponent (at date), and show that the dense phase consists of hexatic micro-domains separated by clusters of topological defects and regions of lower density. In the second section, we focus on studying the aggregation mechanism of MIPS and unveil the role played by active clusters in it.

3.1 Motility-induced micro and macro phase separation

As extensively presented in the introduction, the simplest microscopic active matter model is the Active Brownian Particles (ABPs) model. It exhibits a very rich phase diagram, including MIPS in two dimensions ($2d$) [RBE$^+$12, BSL12, FM12a, SMAC14a, SMBL15, RHB13b, PD20, MLL19, CMP20b]. In particular, the special role played by hexatic order in these systems was discussed in [RHB13b, KKK18, PD20], and the existence of a phase with such order was exhibited [DLS$^+$18a]. The large-scale and long-time behaviour of systems exhibiting MIPS was addressed with adaptations of the Cahn-Hilliard approach, the Active Model B, with few approaches using particle-based models.

Although the non-equilibrium phase diagram of (hard) ABP has been well established [DLS$^+$18a], the dynamics across the various phase transitions, how the dense droplets are formed via MIPS, and which is its actual nature, still need clarification. Using extensive Molecular Dynamics (MD) simulations[1], we were able to identify and

[1]Details on the numerical integration of the equations of motion and the units can be found in Appendix A.

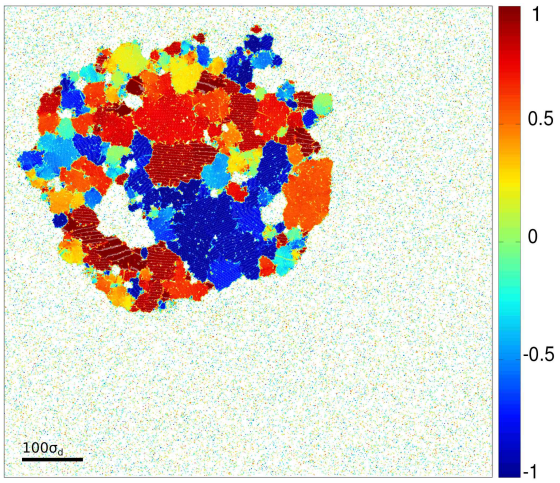

Figure 3.1: **Hexatic domains and bubbles in a MIPS droplet.** A steady-state snapshot of 512^2 ABP at moderate density ($\phi = 0.25$) and high activity (Pe = 200) showing a *macro*-droplet made of a mosaic of hexatic *micro*-domains, delimited by clusters of topological defects from which *micro*-bubbles arise. Colors indicate the projection of the particles' hexatic parameter $\psi_{6,j}$ (see the definition in the text) onto the direction of its global average $\Psi_6 = \frac{1}{N}\sum_j \psi_{6,j}$.

characterise several dynamic regimes and the growth exponent of ABP aggregation. More interesting, we found that MIPS morphology significantly differs from equilibrium: on top of the *macro* phase separation of the dense phase akin to gas-liquid demixing, there is a *micro* phase separation of hexatic domain Fig. 3.1, which do not coarsen indefinitely but saturates to a characteristic size can be directly controlled by self-propulsion. Moreover, the hexatic domains are delimited by clusters of topological defects, which leave space for vapour cavitation bubbles, whose size is also controlled by the single ABP activity.

Macro phase aggregation dynamics

The aggregation is started quenching the system by suddenly turning on activity, quantified by the Péclet number, deep in the MIPS coexistence region [2], starting from a homogeneous configuration at a given packing fraction ϕ. After the quench, the system destabilizes and particles start to aggregate and demix in a dense and dilute phase. Usually, in our simulations, we start from a density ϕ lying on the 50:50 curve, which is defined as the set of points for which the system de-mixes into equally distributed dense and dilute portions.

In order to track the evolution of the dense phase, we measure the time-dependent structure factor

$$S(\boldsymbol{k}, t) = N^{-1}\langle \sum_{i=1}^{N} e^{i\mathbf{k}\cdot(\boldsymbol{r}_i - \boldsymbol{r}_j)} \rangle. \tag{3.1}$$

We compute the spherical average over shell in the reciprocal space, obtaining a spherically average structure factor $S(k, t)$, at several times t after the quench, which is shown in Fig. 5.4. The increase in the magnitude of the short wavelength peak as a function of

[2] Here, the MIPS critical point is located at (Pe, ϕ) $\approx (32, 0.6)$

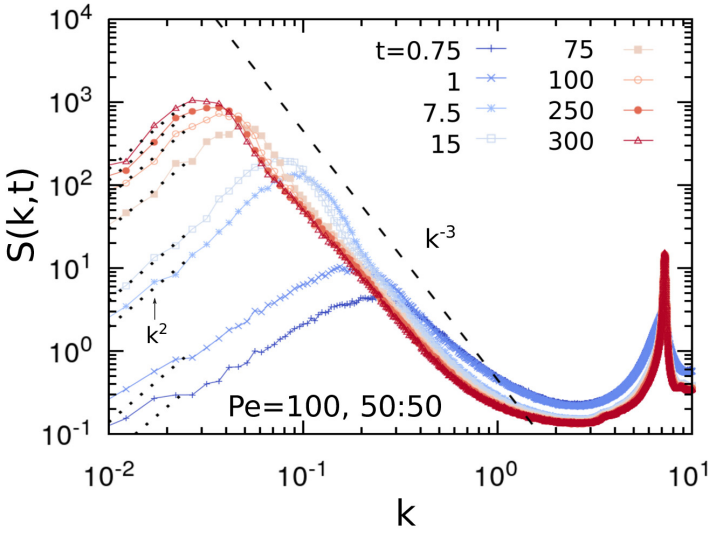

Figure 3.2: Structure factor $S(k,t)$ calculated from simulations of $N = 1024^2$ ABP at Pe $= 100$ (using a 50:50 mixture) and for the different times after the quench reported in the key. The dotted lines are the k^2 growth for a very small wavevector expected in the long-time scaling limit. The first peak is at $\hat{k}(t) = \pi/R(t)$ with $R(t)$ the typical growing length of the dense phase. The dashed line $\sim k^{-3}$ is shown as a reference for the decay on the long-wavelength side of the peak, according to Porod's law. The second peak is located at $k \sim 2\pi/\sigma_d$ and it does vary with time.

time and its shift towards lower wave-vector values follow the large-scale ordering kinetics of the system after being quenched to high activity from a randomly disordered state. The location of the first peak, $\hat{k}(t)$, corresponds to the characteristic length scale in the system, the dense cluster(s) mean size, by the relation $R(t) = \pi/\hat{k}(t)$. This peak shifts toward smaller wavelengths as time goes on, meaning that the associated length scale is growing. The structure factor also shows a second peak at a time-independent wavelength, $k \sim 2\pi/\sigma_d$, related to the short-distance hexatic structure of the particles in the lattice. After the time scale associated with the nucleation of small aggregates from the homogeneous disordered phase, the position of this peak does not vary. This time-independence suggests that the local structure of the system does not significantly change over the scale of the first neighbor shells, while the size of the dense clusters grows. The large-scale behaviour, in between the first and second peak, is in agreement with Porod's law, $S(k,t) \sim k^{-(d+1)}$, with $d = 2$ the dimensionality of the system, as expected for segregated systems with smooth interfaces between the phases [Bra02]. Finally, the wave-vector structure factor of the ABP behaves like conserved scalar order parameter dynamics (model B continuous field theory), where the small k behavior of the scaling function $\mathcal{F}(kR(t) = x) \sim x^2$ grows from zero as k^2, if thermal fluctuations are effective [Fur89], as shown with the dotted lines added close to the data at different times in Fig. 5.4. Already at $t = 15$ the long-time behaviour is attained. (Note that in the particle system $S(\mathbf{0}, t) = N$. The first data-points in Figs. 5.4 correspond to the first wave-vector available, with components $2\pi/L$.)

A precise estimation of the dense phase size is obtained through the inverse of the

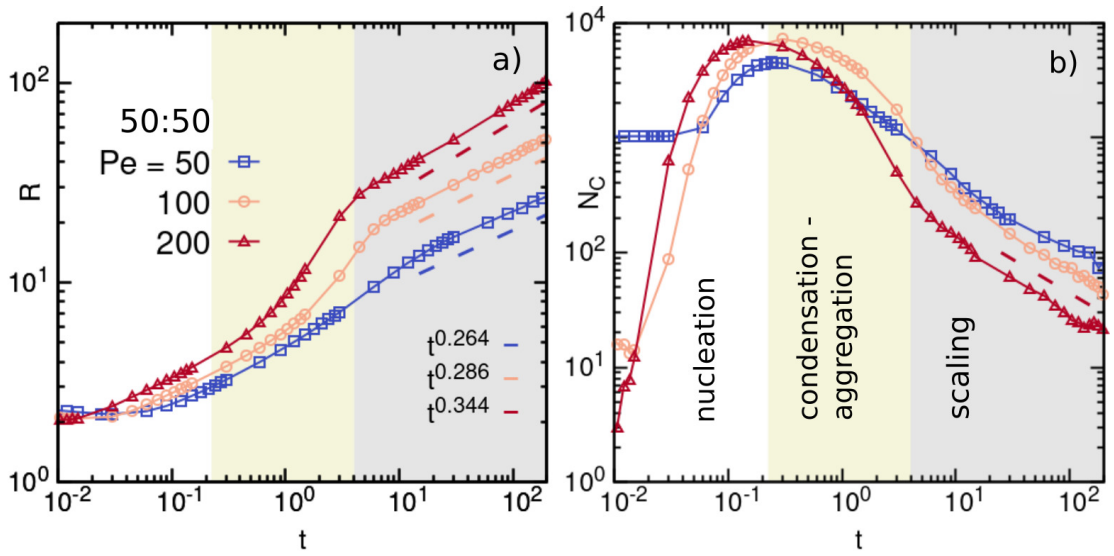

Figure 3.3: **Dense phase formation.** (a) Typical dense phase size from $S(k,t)$ and (b) the number of clusters, both as a function of time, after a quench into the MIPS coexistence region, in a system with $N = 1024^2$ particles at different Pe on the curve with equal surface fraction of dense and dilute phases. Three time regimes are discerned: nucleation, condensation and aggregation, and scaling.

first moment of the structure factor,

$$R(t) = \pi \left(\frac{\int dk\, k\, S(k,t)}{\int dk\, S(k,t)} \right)^{-1}. \tag{3.2}$$

The resulting value of $R(t)$ over time obtained from the structure factor is plotted in Fig. 3.3(a) for three Pe lying on the 50:50-curve. From the time behaviour of $R(t)$, together with the one of the total number of particle clusters, N_C in Fig. 3.3(b), we are able to identify several dynamical regimes. First, there is multi-nucleation of tiny droplets and R is small and roughly independent of Pe. During nucleation, N_C grows fast until a maximum due to the formation of small clusters. A crossover to a regime in which small droplets evaporate while larger ones grow by condensation and aggregation of particles from the gas is favoured by increasing Pe. Last, a scaling regime establishes next and R is algebraic with a universal exponent $1/z$ that is closer to the expected $z = 3$ of phase separation than the values estimated in previous works [RHB13b, SMAC14a, MLL19]. These different regimes can be appreciated in the movie[3]. Moreover, from the mass conservation, one expects that

$$N_C \sim R_C^{-2z}. \tag{3.3}$$

In the scaling regime a fit to the Pe = 200 data yields $N_C \sim t^{-0.59}$, consistently with the growth of R. This last regime takes its name from the fact that the dynamic scaling hypothesis is fulfilled. The dynamical scaling propriety was introduced in Section 3.1 and comes from equilibrium phase separation. It states that the structure factor can be

[3] https://www.dropbox.com/scl/fi/f4eikmjuzduh6no69doe0/Movie1_heavy.mp4?rlkey=i8lhawefmxjlzormmt62qgfxo&dl=0

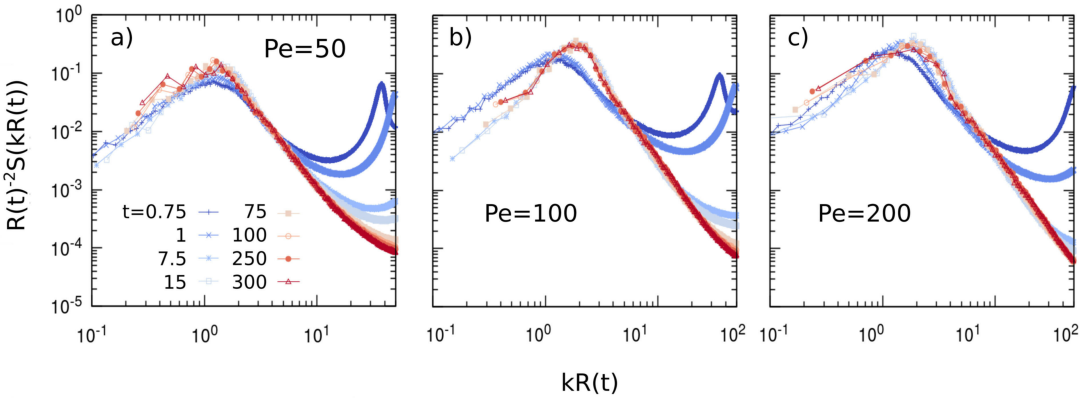

Figure 3.4: Scaling of the structure factor according to the form in Eq. (3.4). Data obtained from simulations of a system of $N = 1024^2$ ABP with equal fraction of the system in the dilute and dense phase. The measuring times are reported in the key in (a), and the different Pe values are indicated as labels. The data points fall on top of each other for $t > 7.5$ in all cases, showing that dynamical scaling holds at all Pe.

expressed by a universal function independent of time. The scaling reflects the fact that the system, from a statistical point of view, evolves in time only through a scale change by $R(t)$. Numerical simulations [SMAC14a] suggested that MIPS in ABP verifies dynamical scaling, meaning that at the late stages of phase separation, the evolution of the structure factor is characterized by a single length scale:

$$S(k,t) = R(t)^d \, \mathcal{F}(kR(t)). \tag{3.4}$$

We extensively tested this hypothesis in our simulations, in the systems made of an equal fraction of dense and dilute phases (50:50 fraction), for different Pe values. In Fig. 3.4 we show scaled data using Eq. (3.4) and $R(t)$ extracted from the numerical data (see Sec. A.2 below). The data collapse at late times ($t \gtrsim 7.5$ in units of $1/D_\theta$), which thus allows us to define the "scaling regime". At early times dynamical scaling is not satisfied, meaning that several length scales are present in the initial growing kinetics. The evolution of the dense phase continues until the size of the dense cluster saturates to a value that grows with the system size L.

Another measure of the dense phase size is provided by the average radius of gyration of the clusters,

$$R_G^2 = \frac{1}{N_d} \langle \sum_{i \in d} (\mathbf{r}_i - \mathbf{r}_d^{\mathrm{cm}})^2 \rangle, \tag{3.5}$$

with $\mathbf{r}_i$ the position of the ith particle among the N_d ones in the cluster, and $\mathbf{r}_d^{\mathrm{cm}}$ the position of the cluster center of mass. $\langle \dots \rangle$ is an average over all clusters. Its behaviour, in Fig. 3.5(a), is analogous to the one of R. The dotted vertical lines locate the crossovers between the time-regimes in Fig. 3.3, with a slightly more extended intermediate one in which R_G raises with the $t^{1/2}$ of Brownian aggregation [Ley03] to later accelerate pushed by activity, and then crossover to $t^{1/3}$ when the mass of the gas reaches its constant target value. R_G saturates to $R_G^s \propto L$ after the relaxation time $N^{z/2}$. For the largest system, $N = 1024^2$, z is very close to $z = 3$. At fixed N and t, R_G increases monotonically with ϕ and Pe, since the fraction of the system in the dense phase also does, see Fig. 3.6(a), (c).

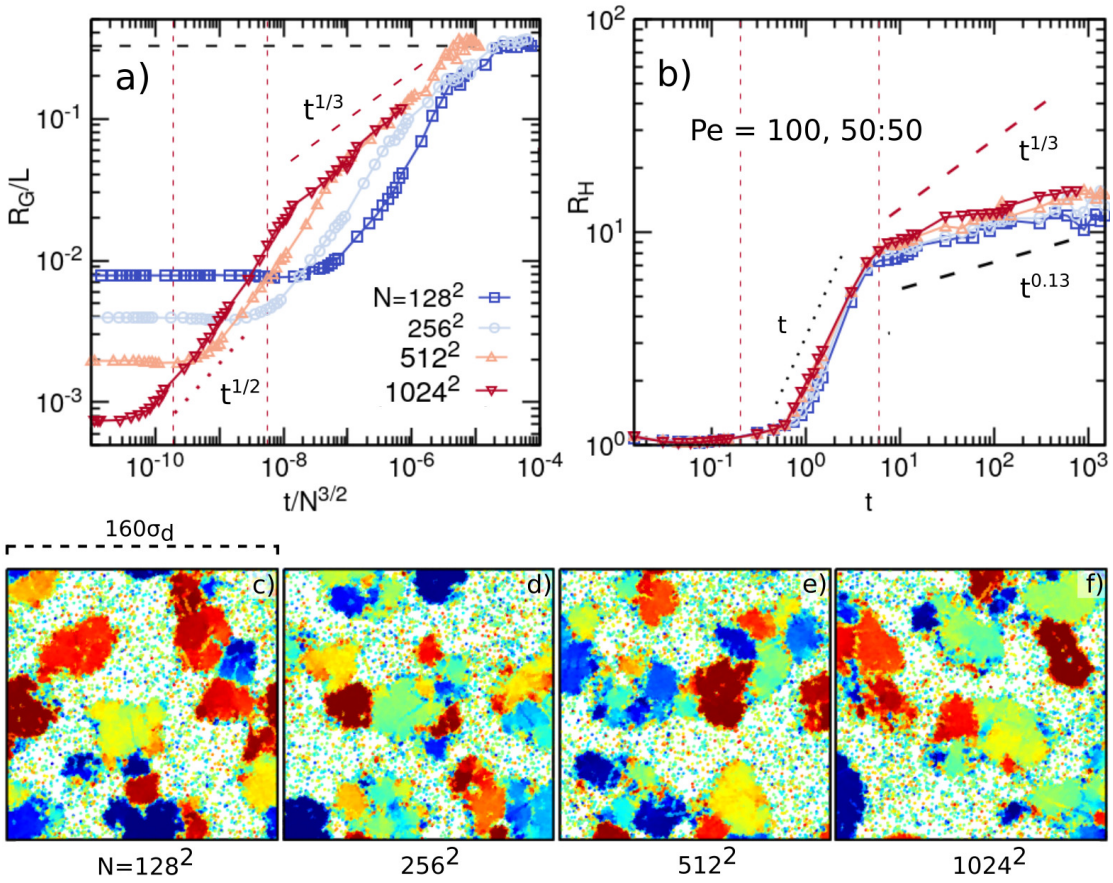

Figure 3.5: **Macro-droplet against hexatic micro-domains.** Growth of the dense phase radius of gyration, R_G, normalized by the system size L (a) and the hexatic length R_H (b) for Pe = 100 and different N on the 50:50-curve. In (a) R_G/L saturates at $\sqrt{5/48}$ (a droplet that occupies half the available surface). In (b) we represent the slow growth $t^{0.13}$, and $t^{1/3}$ for comparison. The vertical dotted lines mark the crossover between the three regimes in the largest system. Below, (c-f), a zoom over a sector of these systems with linear size $160\,\sigma_d$ taken at $t = 15$ (scaling regime) is shown.

Micro phase separation: hexatic ordering

Now that we cleared how the dense phase evolves, we look to the other relevant length scale in the system, not present in equilibrium phase separation: the hexatic length.

From the knowledge of equilibrium phase separation, one may expect that any kind of length scale associated with a relevant order parameter to either grow to reach a macroscopic value $\propto L$ or, on the contrary, relax to a vanishing one. We now show that this does not apply to the hexatic order of ABP in the MIPS regime. Moreover, we demonstrate that several so-far ignored features are different from the ones in equilibrium co-existence.

In order to study the hexatic ordering, we attach a hexatic order parameter to each particle,

$$\psi_{6j} = \frac{1}{N_j} \sum_{k \in \partial_j} e^{i6\theta_{jk}}, \tag{3.6}$$

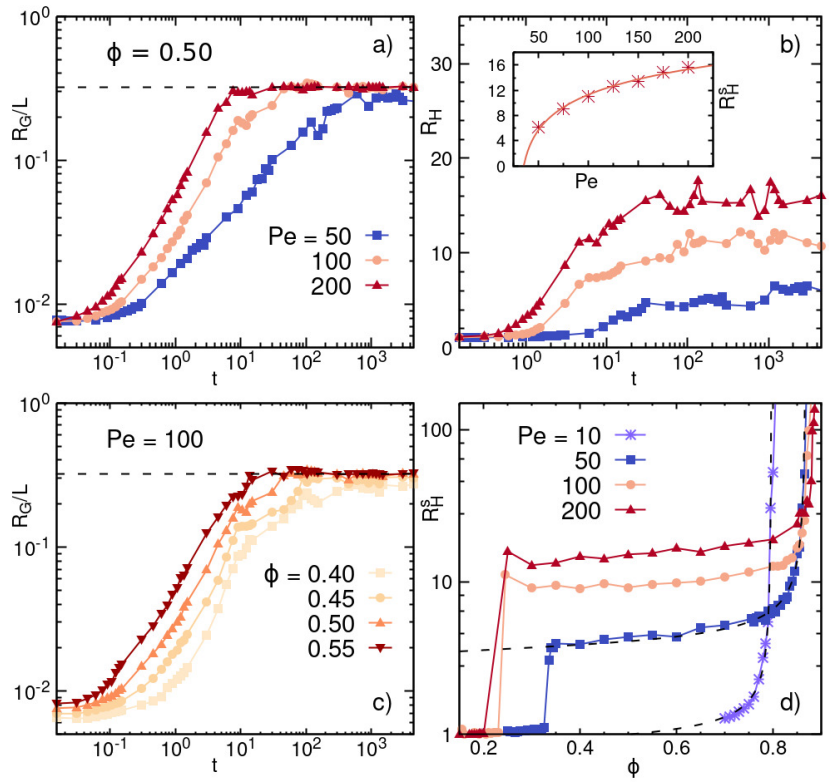

Figure 3.6: **Parameter dependencies of the dense phase and hexatic growing lengths.** $N = 128^2$ at fixed $\phi = 0.5$ and varying Pe (a), (b); at fixed Pe = 100 and varying ϕ (c) and the asymptotic R_H^s for Pe = 50, 100, 200 (in MIPS) and Pe = 10 (before MIPS) as a function of ϕ (d). An exponential growth $a \exp[b\,(\phi^{-1} - \tilde{\phi}^{-1})^{-1/2}]$ is shown in dotted lines (for Pe = 10: $a = 0.778$, $b = 0.214$, and $\tilde{\phi} = 0.797$; for Pe = 50: $a = 3.172$, $b = 0.232$, and $\tilde{\phi} = 0.868$). Inset in (b): dependence of the asymptotic value R_H^s on Pe; the continuous line is $R_H^s \propto \ln[\mathrm{Pe} - a] + b$ with $a = 29.01$ and $b = -1.79$ (vanishing at the transition point).

where θ_{jk} is the angle formed by the segment that connects the center of the jth disk and the one of its kth, out of N_j, nearest neighbours found with a Voronoi construction. The colours in the snapshots in Figs. 3.1 and 3.5 represent different local hexatic order, defined as the projection on their global average, a continuous variable in $[-1, 1]$. The clusters that aggregate do not necessarily share the same ψ_{6j}, and grain boundaries progressively appear in the growing dense phase. Whether they heal or not is the issue that we now address. We identify the hexatic domains according to the argument of ψ_{6j} or by the gradient of its modulus, coarse-grained over a small cell, (expected to vanish in the domain's bulk), and we find equivalent results with the two methods, see Sec. A.3.

The average (over domains) gyration radius, R_H, is exposed in Fig. 3.5(b) for different N, and in Fig. 3.6(b), (d) for different Pe. R_H is quite independent of the system size. In the intermediate regime $R_H \simeq t$. At a sharp crossover concomitant with the entrance in the scaling regime the evolution slows down remarkably to $R_H \simeq t^{0.13}$. This law is confirmed also by the analysis of the corresponding structure factor, that we defined as

$$S_H(\mathbf{k}) = \frac{1}{N} \langle |\psi_6|_{\mathbf{k}}\, |\psi_6|_{-\mathbf{k}} \rangle, \tag{3.7}$$

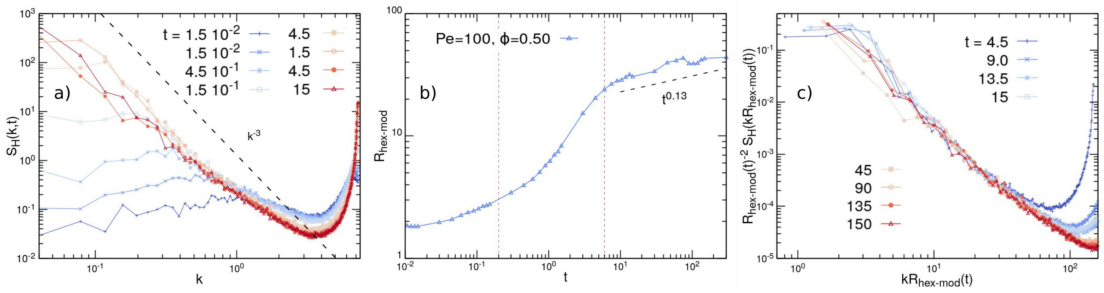

Figure 3.7: (a) Hexatic modulus structure factor, as defined in Eq. (3.7), in a system with Pe $= 100$ and $\phi = 0.500$. (b) Average hexatic size, computed as $\pi/\bar{k}$ from the first moment $\bar{k}$ of $S_H(k,t)$. The dashed black line $\sim t^{0.13}$ is shown next to the data. It is the growth law found from the measurement of the averaged radius of gyration of the hexatic patches presented in the main text. (c) Scaled hexatic structure factor following a scale-free shape.

where $|\psi_6|_{\mathbf{k}}$ is the Fourier transform of the modulus of the local hexatic order parameter. The results, for the spherically averaged quantity, are shown in Fig. 3.7(a) for Pe $= 100$, $\phi = 0.500$ and different times spanning the entire dynamical range, from the disordered initial configuration to stationarity. The inverse of the first moment of S_H, which we call $R_{\mathrm{hex-mod}}(t)$, is shown Fig. 3.7(b). It consistently shows the hexatic coarsening, and it very well agrees with our results on the power-law growth in the scaling regime, obtained from the analysis of the averaged gyration radius of the micro-domains. The decay of S_H from the hexatic peak towards lower wave vectors satisfies Porod's law with $d = 2$, which allows us to formulate the right scaling hypothesis. Figure 3.7(c) demonstrates the scaling of the structure factor, using the typical length-scale $R_{\mathrm{hex-mod}}(t)$. Similar small exponents were found in the growth of order in certain pattern formation processes [CH93] and in the growth of hexatic order in block co-polymer systems [VHA$^+$05].

Later in the evolution, R_H approaches a finite limit, R_H^s, proving the *arrested coarsening* of hexatic order, see Fig. 3.5(b). The snapshots in Fig. 3.5(c)-(f) show that hexatic domains have roughly the same size in systems of different dimensions. The asymptotic R_H^s increases with Pe at fixed ϕ but does not change appreciably with ϕ at fixed Pe, Fig. 3.6(d), meaning that self-propulsion controls the size of the hexatic micro-domains. This is confirmed by the exponential distributions of the individual $\tilde{R}_H$ in Fig. 3.8 with average compatible with the data in the inset in Fig. 3.6(b).

Liquid-Hexatic coexistence in equilibrium

Now, we put our focus on the difference of the polycrystal of hexatic domains which appears in the dense phase of the MIPS with respect to the hexatic phase obtained at Pe = 0. In fact, as stated in Chapter 1, hard disks at equilibrium undergo a first-order phase transition with coexistence between a liquid and hexatic phase. The dense component in MIPS is not, indeed, like the hexatic component in equilibrium co-existence: the map of local hexatic order at Pe = 0 is not of the multicolour kind in Fig. 1 but it has just one reddish denser component, the single hexatic domain, Fig 3.9. This reflects the fact that the hexatic co-existing phase in equilibrium is inherited from a proper hexatic phase with a diverging correlation length. Moreover, our equilibrium or active liquid is also homogeneous from the hexatic order point of view, with a very low R_H. This

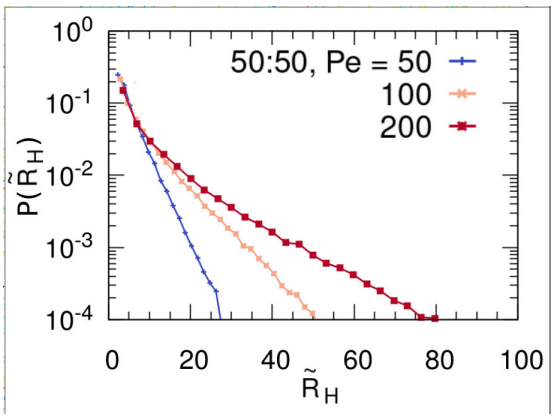

Figure 3.8: Stationary distribution of hexatic domain radii $\tilde{R}_H$ for three Pe and an equal fraction of dense and dilute coexisting phases.

is illustrated by the Pe = 10 data in Fig. 3.6(d), which show $R_H \sim 1$ until very close to the transition where an exponential divergence à la BKT takes over in this case. For the three sets of data points within MIPS, the mosaic length R_H^s is almost constant and much larger than the one of a homogeneous liquid, until an exponential takes over close to the upper border of MIPS. One may wonder how this compares to hexatic ordering in the phase separation of equilibrium fluids of attractive particles. This is an issue that has only recently been addressed, with the observation that attractive interactions generically destabilize hexatic order [HK19, NCP$^+$20a]; therefore, a stationary mosaic structure as the one in Fig. 3.1 is not expected in these systems.

In order to differentiate quantitatively the equilibrium hexatic phase, after constructing a Voronoi tessellation out of configurations of our model at Pe = 0, we computed the ratio between the area covered by the sum of all the Voronoi cells for which the projection of ψ_6 along the mean orientation of the sample is > 0.4. In such a way, we tracked the growth of the fraction of the system occupied by the hexatic phase. The results of this analysis are shown in Fig. 3.9. The snapshots on the right show the map of the projection of the local hexatic order parameter ψ_6 in the direction of its global average for four densities across the coexistence region at Pe = 0. As shown in the left panel and illustrated by the hexatic maps, the hexatic is dominated by the mean orientation (reddish area in the snapshots), and its extent grows across the coexistence region as the density increases. The growth of the hexatic in the coexistence regime is compatible with linear growth: as the density increases, the fraction of the system belonging to the dense hexatic phase increases proportionally, and thus the area covered by the hexatic. Note that this behaviour strongly differs from the MIPS scenario, where the dense phase is made of a mosaic of patches with different orientations (different colors in the hexatic maps, not a single reddish one) whose size remains constant all along the MIPS coexistence region.

In the inset, we display the size dependence of the typical length of the hexatically ordered zone ξ_6 extracted from the decay of the hexatic correlation function $g_6(r) = \langle \psi_6(0)\psi_6^*(r)\rangle / \langle |\psi_6(0)|^2 \rangle$. Its dependence on the system size is close to $\sqrt{N}$ for the three packing fractions shown. Such behaviour is expected as the length scale associated with hexatic order grows with the size of the system and the fraction of it belonging to each phase. However, this contrasts with the behaviour across MIPS where the hexatic

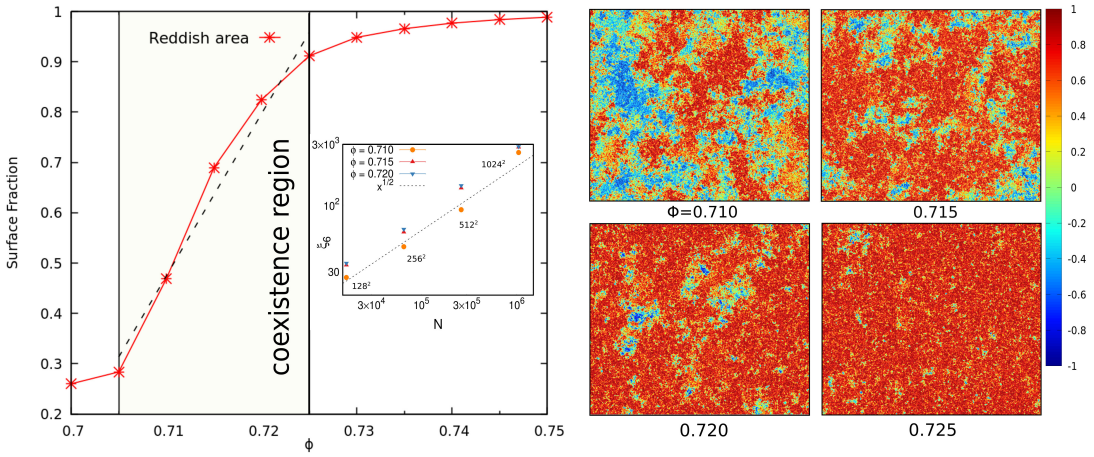

Figure 3.9: Fraction of the total surface of the system occupied by the hexatic phase as a function of the packing fraction across the equilibrium liquid-hexatic transition (left). In the coexistence region, indicated by two vertical lines, the evolution of the area fraction occupied by the hexatic as the density of the system increases, is compatible with a linear growth (shown by the dotted line). In the inset we show the hexatic correlation length ξ_6 as extracted from the spatial decay of orientational correlations in systems of different size N and at different packing fractions indicated in the key. On the right we illustrate the growth of the hexatic area in the coexistence region with four snapshots showing how the reddish area corresponding to the hexatic phase grows at the packing fraction increases.

length scale remains finite and constant independently of the system size.

Vapour Bubbles

Besides the emergence of hexatic micro-domains, MIPS is accompanied by the formation of gas bubbles. Figure 3.10 shows six snapshots in the form of heat maps of the local density, according to the scale in the right vertical bar, running from close-packed (red) to the dilute limit (blue). These snapshots correspond to steady-state configurations of $N = 512^2$ ABPs for the different values of ϕ and Pe indicated in the key. The panels are ordered in such a way that Pe increases from left to right. On the first row, the system phase separates into half dense and half dilute, while on the second row, the packing fraction is just constant, $\phi = 0.75$. In all cases, one clearly notices the phase separation between dense and dilute regions. Several other features can be noted as well. First, for increasing Pe, the density contrast between the two coexisting phases is more pronounced, and thus the phase boundaries (in yellowish) become sharper. Second, in all cases, gas bubbles populate the dense (red) phase. Third, the bubbles have different sizes and their characteristic average size increases with Pe. Fourth, the density of the bubbles inside the dense phase seems close to the one of the surrounding dilute phase.

We now make these statements more quantitative. First, we measure the bubble averaged size, measured, for example, from their radius of gyration, R_B (see Appendix A.4 for details), increases with Pe, Fig. 3.10. Second, we measure the local density distribution of the dilute, dense and bubble phases for different parameter values shown in the key, shown in Fig. 3.11. As expected, the density pdfs split in two modes in the

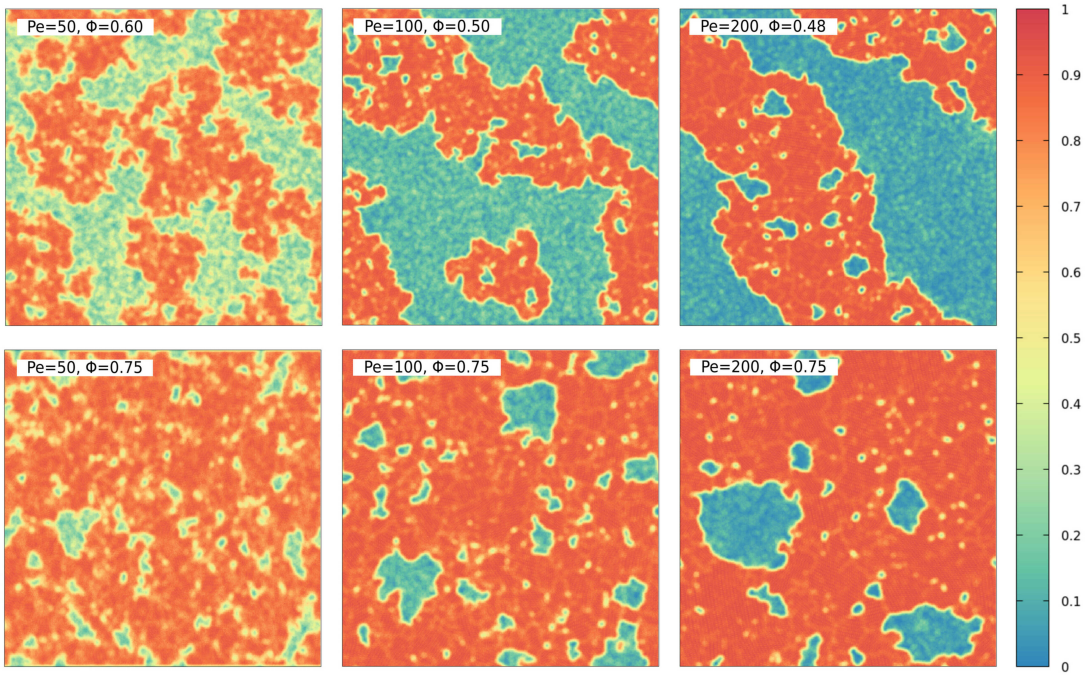

Figure 3.10: Local density map of different steady-state configurations of systems with $N = 512^2$ ABP using the color scale shown in the right bar. The parameters are given as labels within each panel.

MIPS regime, and the location of the low-density peak matches the one of the bubbles' density pdf, thus showing that the dilute phase and the bubbles share the same average density.

The microscopic origin of micro-bubbles in ABP can be tracked down to the presence of topological defects (mis-coordinated particles with more or less than the 6 neighbours) mostly localized at the boundaries of the hexatic micro-domains, see Figure 3.12(b) and [DLC+19]. A fluctuation is thus more likely to generate a bubble at a grain boundary than within a hexatic domain. Some of the bubbles thus generated quickly decay, while others grow and have very long lifetimes ($\sim 10 - 100\,\tau$), of the same order as the reorganization time scale of the hexatic domains.

Just as the hexatic micro-domains, bubbles do not coarsen indefinitely. Figure 3.12(d) shows that R_B is delayed with respect to R_H, but after the transient the two quantities grow parallelly in the log-log representation indicating that they follow a similar trend until eventual saturation to a Pe-dependent value (this is clear looking at the steady-state of the simulations, Fig. 3.10). The steady state-distribution, Fig. 3.12(e), decays algebraically, $P(\tilde{R}_B) \sim \tilde{R}_B^{-2.19}$ for $\phi = 0.75$, independently of Pe, until a Pe-increasing cut-off $\tilde{R}_B^*(\mathrm{Pe})$. Interestingly, the system approaches the same finite R_H^s and R_B^s independently of the initial condition. This fact can be visualized in the movies[4,5], where a disk and a slab drop with uniform hexatic order are used as initial states. In both cases

[4] https://www.dropbox.com/scl/fi/tx8kj58en335n0xss4dtu/Movie2.mp4?rlkey=287uadfsdj00m2bj3zanguwjn&dl=0

[5] https://www.dropbox.com/scl/fi/n197p9dch31baet0uz57l/Movie3.mp4?rlkey=dm9knevhylzznowr9gp2q8o5z&dl=0

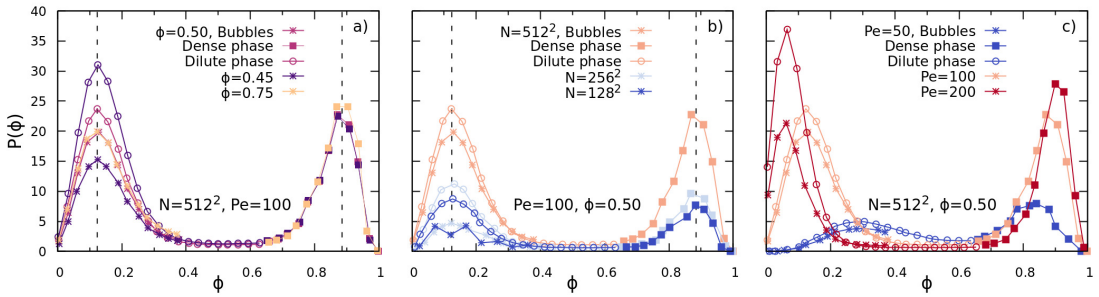

Figure 3.11: Probability distribution function of the local density of the bubbles (star symbols), dense (square symbols) and dilute (open circle symbols) phases for three different simulation parameters N, Pe and ϕ. The dotted vertical lines are a guide to the eye, and locate the peaks' positions. In each panel, the two parameters in the label are fixed, and the values of the other one are represented using different colors. As shown in the first two panels, varying the density (a) or the number of particles (b) does not affect the peaks' position of the distribution, but only their relative weight $P(\phi_{\text{peak}})$. In particular, the density values ϕ_{peak} for the dense phase and the bubbles are the same for each parameter choice. In panel (c) we show that the peaks move apart by increasing Pe, and the gap between the dense and dilute densities increases. For each Pe value, the bubbles' and dilute phase peaks coincide.

the dense component progressively breaks into finite-size domains with different orientations, leaving space for bubbles at their interfaces. Consistently, Fig. 3.12 (c) shows the rise of R_B, and the corresponding drop-off of R_H, which approach asymptotic values that are consistent with the ones obtained after a quench from disordered initial conditions.

The emergence of a finite Pe-dependent length scale associated with the hexatic order must be responsible for the presence of micro-bubbles as suggested by the growth kinetics of R_H and R_B, which evolve at the same very slow rate. Furthermore, the cut-off algebraic distribution of bubble radii, Fig. 3.12(e), is intimately related to the same kind of statistics found for topological defect clusters [DLC$^+$19].

Micro-bubbles have been predicted by a continuum model of MIPS [TNC18], but their existence in particle systems has not been studied yet. Micro-phase separation in the continuum model takes place in a specific parameter regime. However, such parameters (in particular the one quantifying the term leading to the micro-bubbles) cannot be readily translated in terms of the ϕ and Pe of ABP. Here, contrarily to the mean-field calculations in [TNC18], we observe micro-bubbles as long as MIPS takes place, both at moderate and high densities, from Pe = 40 to Pe = 200 (see Figs. 3.1 & 3.12 at $\phi = 0.25$ and 0.75, respectively, and show that their size can be controlled by Pe.

3.2 MIPS Cluster Dynamics

As seen in the previous section, when we let the ABPs evolve at large activities from an initial homogeneous state, they progressively aggregate and, after a transient, enter a scaling regime in which structural measurements scale with a growing length compatible with $R(t) \sim t^{1/3}$ [RHB13d, SMAC14a, CDL$^+$20a], Hence, as equilibrium, the MIPS kinetics was ascribed to Ostwald ripening, in line with universality. We already showed that cluster diffusion is central in the scaling regime of phase separation. In

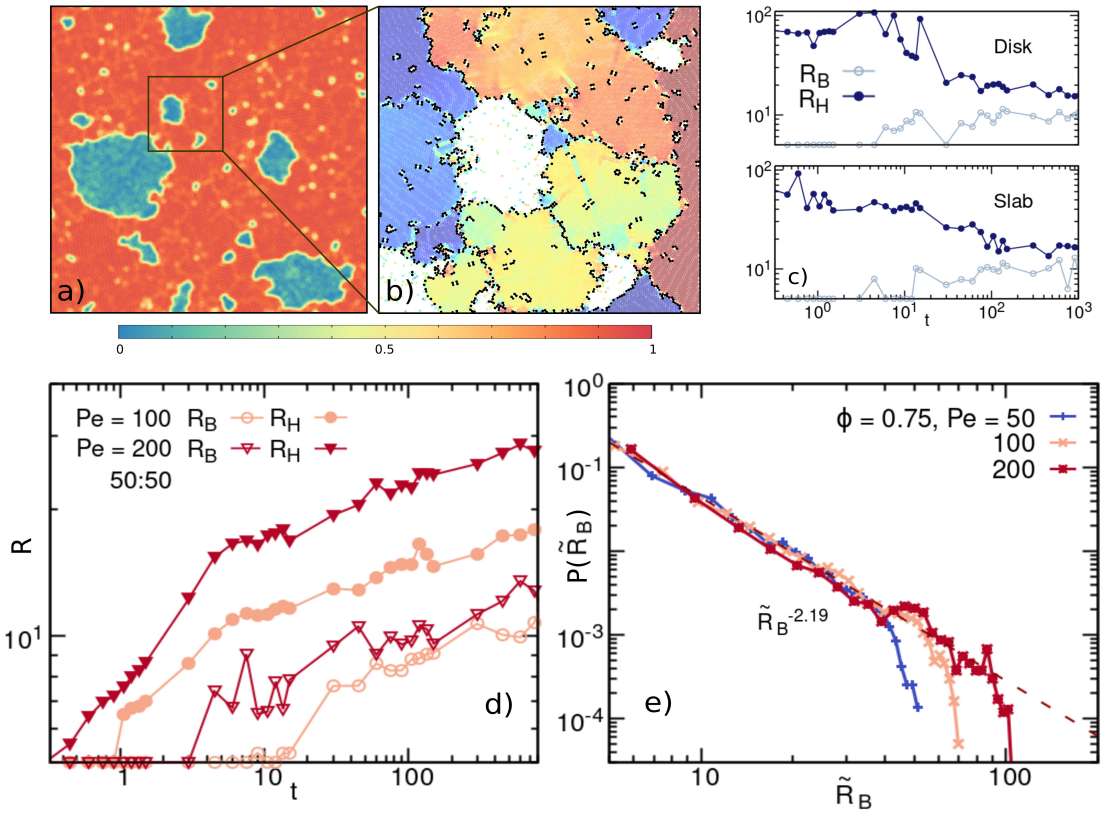

Figure 3.12: **Gas micro-bubbles.** Snapshot at $\phi = 0.75$, Pe = 200 (a). The color scale (below) is associated with the local density. In (b) a zoom over a sector of (a) showing hexatic domains delimited by clusters of defects (represented by black dots), where bubbles (dilute regions) are likely to emerge. (c) Evolution of R_B and R_H from an initial hexatically ordered disk or slab at Pe = 100 and $\phi = 0.5$. (d) Growth of the bubble typical radius R_B (empty symbols) confronted to the one of the hexatic order R_H (filled symbols) for two Pe. (e) Steady-state distribution of bubble radii $\tilde{R}_B$ (parameters given in the key).

the following, we aim to elucidate the role played by cluster motion in the MIPS. With the cluster tracking method that we conceived, explained in detail in Appendix A.5, we show that cluster diffusion is the actual key player for aggregation, leading to the same $1/3$ exponent expected from Oswalt Ripening but with a different mechanism. We show that active clusters break up and recombine and, are pushed by particles at their surface, and are much more mobile than their passive counterparts. This enhanced motility is indeed evidenced by a diffusion coefficient with anomalous mass dependence, $D \sim \mathrm{Pe}^2/\sqrt{M}$. In particular, with a parallel study of passive-attractive particles, we exhibit qualitative and quantitative differences with equilibrium phase separation.

Statistical Proprieties of Active Clusters

Before focusing on the dynamics of clusters in MIPS, we start characterizing their statistics. In particular, we measure the average cluster mass and the clusters' mass distri-

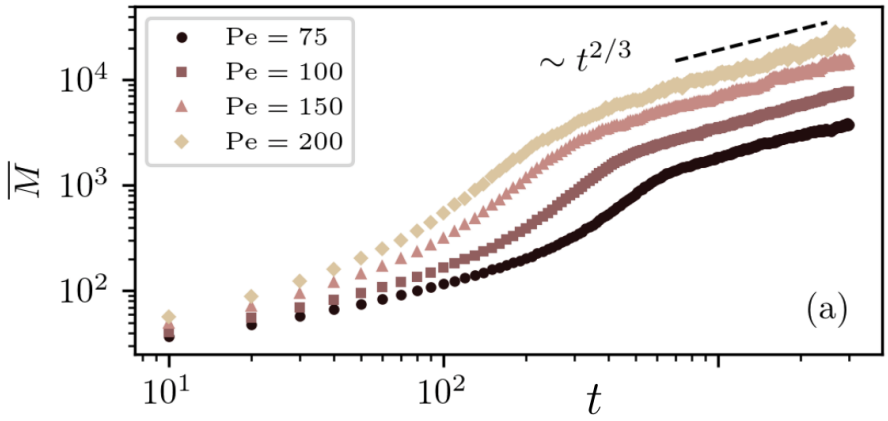

Figure 3.13: **Cluster masses.** (a) Time dependence of their average, $\overline{M}$, for various Pe. In the scaling regime, reached after $t_s \sim \mathrm{Pe}^{-1}$, $\overline{M}(t) \sim t^{2/z}$ with an estimated dynamic exponent $z = 3$.

butions.

Scaling of the averaged cluster mass

The averaged cluster mass (number of particles in the cluster) $\overline{M}$ is shown in Figure 3.13 for several values of Pe. This quantity can be directly related to the average radius of the cluster using the relation $M(t) \propto R(t)^d$, where d is the spatial or, more in general, the fractal dimension. In particular, in $d = 2$, we expect that

$$M(t) \sim R(t)^d \sim t^{2/3}, \tag{3.8}$$

where we used the growth law in the scaling regime, $R(t) \sim t^{1/3}$.

From the shoulder position of $\overline{M}$, we can estimate the time t_s at which the system enters the scaling regime, after which the asymptotic $t^{2/3}$ behaviour is established. This confirms with a very good agreement that the linear size of the clusters increases with an exponent close to $1/3$, independently from the activity. In Fig. 3.14(a) we plot the Pe dependence of t_s extracted in this way. An algebraic fit to the numerical data yields $\mathrm{Pe}^{-0.93}$. We, therefore, assume that the decay is

$$t_s \sim (\mathrm{Pe} - a)^{-1}, \tag{3.9}$$

as this time should diverge at a finite $\mathrm{Pe} > 0$, the limit of the MIPS sector of the phase diagram. The fit of the exponent is shown in Fig. 3.14(a). Concomitantly, the mass at this time, $\overline{M}_s$, also shown in this plot, is fitted by a growing function of Pe as $(\mathrm{Pe}-b)^{0.98}$, and we will assume it simply goes as $\overline{M}_s \sim \mathrm{Pe}$. Next, in Fig. 3.14(b) we perform a scaling of the $\overline{M}$ data using t_s, as previously determined, and the value of $\overline{M}_s$ extracted from the vertical position of the shoulder in Fig. 1 of the main text, $\overline{M}_s = \overline{M}(t_s)$, see Fig. 3.14(a). The scaling is quite satisfactory both in the long-time (scaling) regime in which $\overline{M}$ grows as $t^{2/3}$ (black dashed line in the figure) as well as in the previous regime in which the growth is faster.

The scaling implies that the dependence of the time-dependent averaged mass with Pe is

$$\overline{M} = \mathrm{Pe}\, \overline{f}(t\,\mathrm{Pe}), \tag{3.10}$$

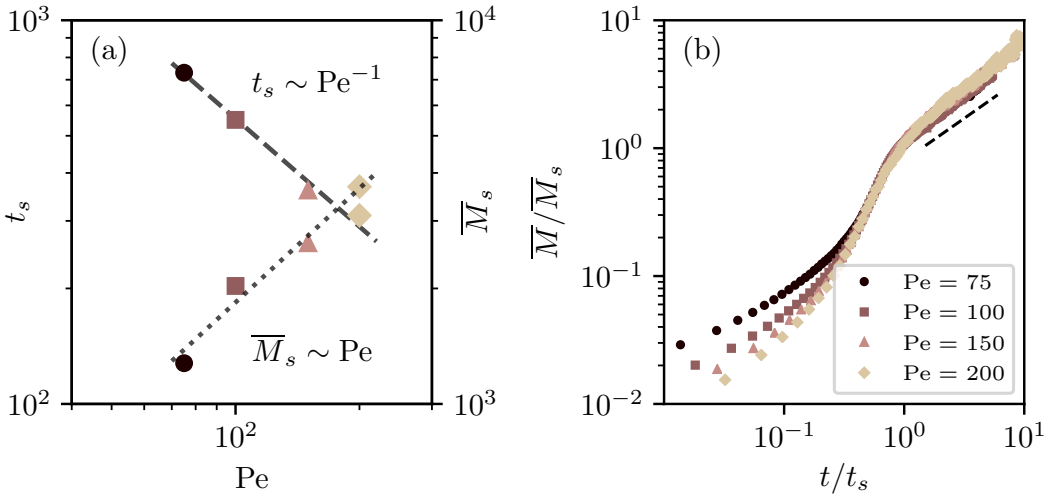

Figure 3.14: **Scaling of the averaged cluster mass.** (a) The time needed to enter the scaling regime, t_s, against Pe, with a fit of the power law decay Pe^{-1}, and the mass at the scaling time t_s with the power law growth proportional to Pe. See the text for the details. (b) Scaling of the averaged mass, using t_s and $\overline{M}_s$: $\overline{M}/\overline{M}_s = f(t/t_s)$ with $f(1) = 1$ and $f(x) \sim x^{2/3}$ for $x > 1$ and before saturation (dashed segment close to the data). Due to the Pe dependence of t_s and $\overline{M}_s$, the time-dependent mass follows $\overline{M} = \mathrm{Pe}\,\overline{f}(t\,\mathrm{Pe})$ with $\overline{f}(1)$ finite and $\overline{f}(t\,\mathrm{Pe}) \sim (t\,\mathrm{Pe})^{2/3}$ for $t > t_s$ which implies $\overline{M}(t > t_s) \sim \mathrm{Pe}^{5/3}$ at fixed t.

with $\overline{f}(1)$ finite and $\overline{f}(t\,\mathrm{Pe}) \sim (t\,\mathrm{Pe})^{2/3}$ for $t > t_s$ which implies

$$\overline{M}(t > t_s) \sim \mathrm{Pe}^{5/3} \tag{3.11}$$

at fixed t. We checked that this Pe dependence complies with the data at long times, with a fit yielding an exponent of 1.67.

An averaged cluster mass $\overline{M}$ growing linearly with Pe was found in the steady state of the Janus particle suspension at intermediate densities studied in [TCBP+12a]. Simulations of various active particle models which also reach steady states often showed the opposite trend [AVP17, PS14].

Mass and radius of gyration distributions

The average cluster mass does not give any information on the different kinds of clusters present in the system (that we will show to be fundamentally two). In order to do that, we use the cluster size and radius distributions instead.

The second analysis on which we focus is the study of the cluster size distribution of the system, represented by the histogram of the cluster of mass $N(M)$, reported in Fig. 3.15(a-b), and the distribution of the gyration radii $N(R_g)$, in Fig. 3.15(c-d).

The mass histogram has a rapid exponential decay at times $t \leq t_s$ over the full range of M. Similar distributions of rather small clusters were measured experimentally in dilute samples [GTD+18]. In the scaling regime, $N(M)$ changes functional form by developing a long plateau for $M \gtrsim 100$, and further exponential decay. This shows that the system is populated by many large clusters of different sizes and different geometry. In particular, in the time regime in which dynamical scaling is verified, $t > t_s$, we

observe small compact clusters of rounded shapes and large fractal clusters coexisting, Fig.3.16. A similar behaviour is observed for the gyration radius distribution. After entering the scaling regime at $t_s \sim 300$, the data flatten and even develop a shallow minimum, for small R_g. The global average $\overline{M}$ and $\overline{R}_g$ at each time is indicated with inclined arrows in (a)-(c), with the colour of the corresponding full curve, and with a vertical dashed blue line in (b) and (d).

The behaviour of $N(R_g)$ and $N(M)$ over time calls for further characterization of their functional forms. We propose that the distribution of the radii of gyration in the tail of the curve (for large R_g) takes the Weibull form

$$N(R_g) \sim R_g^{k-1} e^{-(R_g/R_g^*)^k} . \tag{3.12}$$

with parameter k. Figure 3.15(b) shows $N(R_g)$ at $t = 500$ together with this fit (done for $R_g > 30$). The value of R_g^* extracted from the fit is very close to the averaged value $\overline{R}_g$. The value of k obtained is 1.45, which - as we will characterize accurately later in the Section - corresponds to the fractal dimension of the elongated large clusters of the kind of Fig.3.16(a), $d_f^l = 1.45$, in contrast to the fractal dimension of the round clusters as the one in Fig.3.16(b), $d_f^s = 2$. Note that, for this reason, the data at small R_g are not well fitted by this curve, as they represent mainly small round clusters, which potentially follow a different law. At the same time, $N(R_g)$ is not well suited to see which law is followed for small masses, as the latter are represented by few points. Instead, we show below that the $N(M)$ distribution is better suited for the purpose and allows us to better identify the complete functional form which includes both small and large masses.

In order to obtain a functional form of the mass distribution $N(M)$ that works for both small and large masses, we can start from the functional form of the radii distribution expected for each case, and transform them separately in the relative mass distribution using the relation $M \sim R_g^{d_f}$, with the fractal dimension being either d_f^s or d_f^l depending on the case. For large masses, we can use Eq. (3.12), which correspond to an exponential mass distribution e^{-M/M_l^*}. For small masses, we find that the best function is an exponential e^{-R_g/R_{gs}^*}, which corresponds to a Weibull distribution for the masses. Thus, the total mass distribution is given by a superposition of the two following forms:

$$N(M) \quad \sim \quad c_s \, M^{(1/d_f^s - 1)} \, e^{-(M/M_s^*)^{1/d_f^s}} + c_l \, e^{-(M/M_l^*)} . \tag{3.13}$$

The two constants c_s and c_l and the two masses M_l^* and M_s^* are left as free parameters of the fit. As shown in Fig. 3.15(d), the distribution form is fully consistent with the histogram of the cluster masses. The values of M_s^* and M_l^* returned from the fit are reasonable and the latter is compatible with the full average $\overline{M}$.

Finite-size clusters have been observed in experiments of active Janus colloids in [GTD$^+$18], in a segregated steady state where the dynamics proceed through an aggregation fragmentation process involving only single particles. Clusters are small compact objects of regular shape, while the formation of large aggregates is suppressed in the regime of activity considered in this experiment. Therefore, a second length scale is not present and a single exponential distribution was measured.

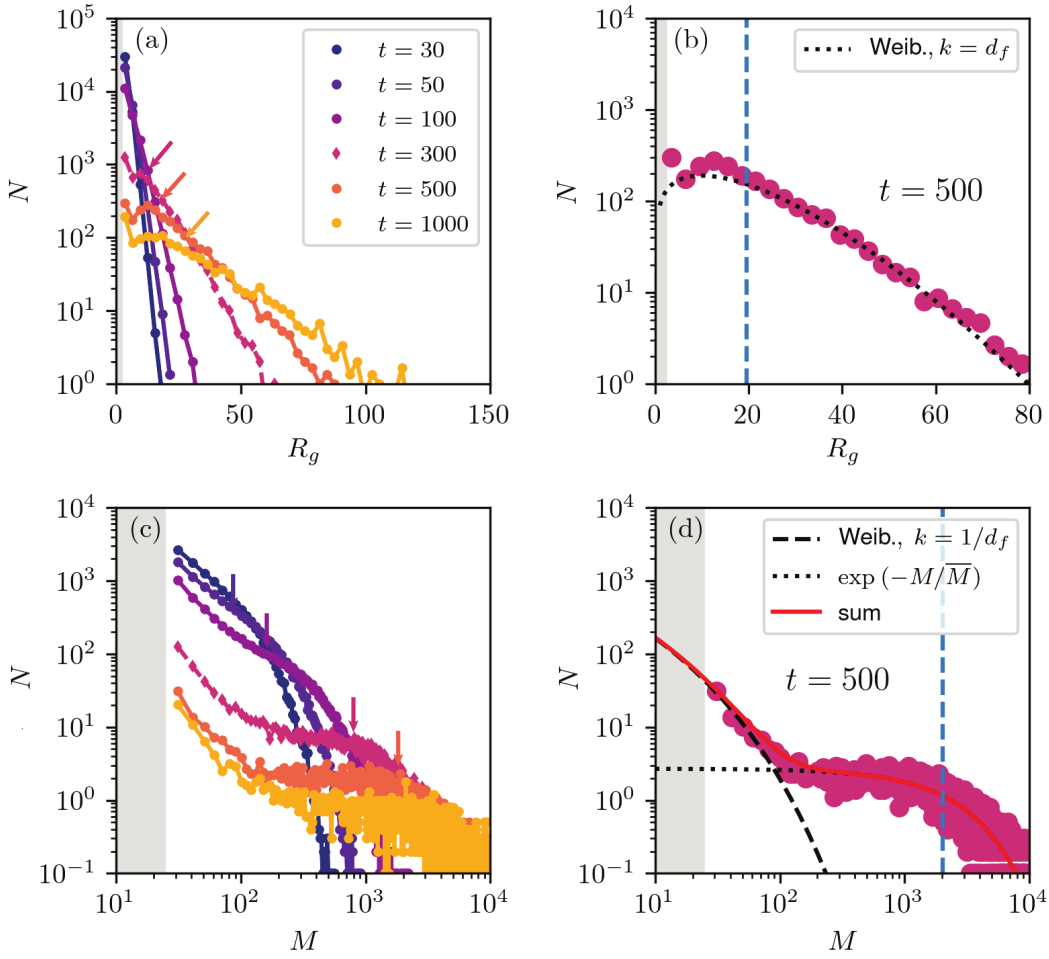

Figure 3.15: TODO: Invert row (ab) with row (cd) **Radius of gyration and mass distributions in an active system** at Pe $= 100$ and $\phi = 0.5$. $t_s \sim 300$ is approximately the beginning of the scaling regime for these parameters. (a) Histogram of the radius of gyration for all clusters at several times within the scaling regime. The arrows indicate the global averages. Here and in the other panels the gray regions are excluded by the cut-off $M > 25$ that we imposed on the size of the clusters taken into account. (b) The data at time $t = 500$ together with a fit to a Weibull form $N(R_g) = R_g^{k-1} e^{-(R_g/R_g^*)^k}$ with $k = 1.45$ which we will interpret as the fractal dimension of large clusters, and $R_g^* \sim 16$, which is very close to the average $\overline{R}_g$ at this time shown with a vertical dashed (blue). (c) Histogram of the cluster masses at the same times as in (a). The arrows indicate the global averages. (d) Fit of the histogram of clusters masses at $t = 500$ with a Weibull distribution with $k = 1/d_f^s = 1/2$, see Eq. (3.13) dashed line describing the regime $M < \overline{M}$, added to a pure exponential (dotted line) describing the regime $M > \overline{M}$. The red curve shows the sum of the two terms, with parameters $c_s = 2377$, $M_s^* = 4.3$, $c_l = 2.7$, and $M_l^* = 2374$ which is very close to $\overline{M} = 2019$. These plots should be compared to the ones in Fig. C.4 where the same distributions for the passive model are studied.

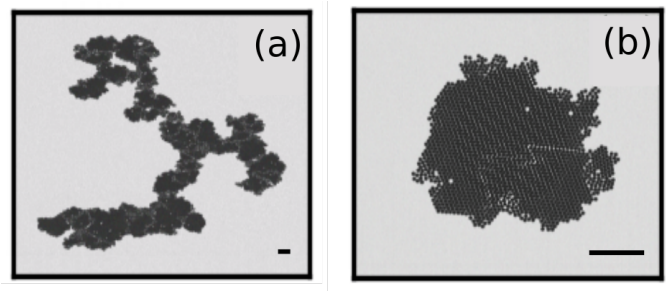

Figure 3.16: (a) A large ($M \approx 2 \times 10^4$) and (b) a small ($M = 1751$) typical cluster plotted with different scales (the two segments of length 25σ)

Cluster Diffusion

Now, we turn our attention to the cluster's motion and dynamics. This will allow us to better grasp the growth mechanism, and identify similarities and differences with the equilibrium (passive) passive systems. We will track the trajectories both "in bulk", meaning that we track clusters in the whole system, while they may interact with each other, and for isolated clusters. Each method has cons and pros that allow us to extract different information.

We start first tracking trajectories in bulk - see Appendix A for a complete description of the algorithm. This method allows us to track the true dynamics of interacting clusters, although it has an intrinsic limitation: we are only able to track clusters until they collide with each other or undergo some other event that changes their shape or size. Therefore, we cannot follow the clusters' evolution for a long time.

Using the clusters' trajectories, we can extrapolate their center of mass (c.o.m.) mean-square displacements, that we average over the $\mathcal{N}(t)$ clusters followed until t:

$$\Delta^2 \equiv \mathcal{N}^{-1} \sum_{\alpha=1}^{\mathcal{N}} \Delta_\alpha^2, \tag{3.14}$$

with $\Delta_\alpha^2 \equiv (\mathbf{r}_\alpha^{\rm cm}(t) - \mathbf{r}_\alpha^{\rm cm}(t_0))^2$, and $\mathbf{r}_\alpha^{\rm cm}(t)$ the instantaneous position of the αth cluster' c.o.m. in the scaling regime, $t_0 > t_s$. The results are plotted in Fig. 3.17(a). The initial slope of Δ^2 indicates super diffusion though not as pronounced as for a single ABP. Later, *enhanced diffusion* sets in, $\Delta^2 \simeq 2dD(t - t_0)$. The diffusion coefficient (insert) satisfies

$$\gamma D = T_{\rm eff} = T(1 + c{\rm Pe}^2), \tag{3.15}$$

the same functional form as for a single ABP, though taking a considerably smaller value ($c = 8.1 \times 10^{-5}$ compared to $1/6$ [FM12a]). This result is compatible with the measurement of the effective temperature of the full dense component [PCGS20a], with a comparable value $T_{\rm eff} \simeq 0.08$ for these parameters. The individual Δ_α^2, though noisy, demonstrates that the trajectories are Brownian when examined at sufficiently long $t - t_0$. The diffusion constants decrease with the clusters' mass and, although quite dispersed, following $D(M) \sim M^{-\alpha}$ with $\alpha = 0.5$ (b). Data for $\phi = 0.35$ are fitted with a similar α.

This exponent is unexpected since for equilibrium clusters one expects $\alpha = 1$, see for example Appendix D. This means that activity is enhancing the diffusivity of the

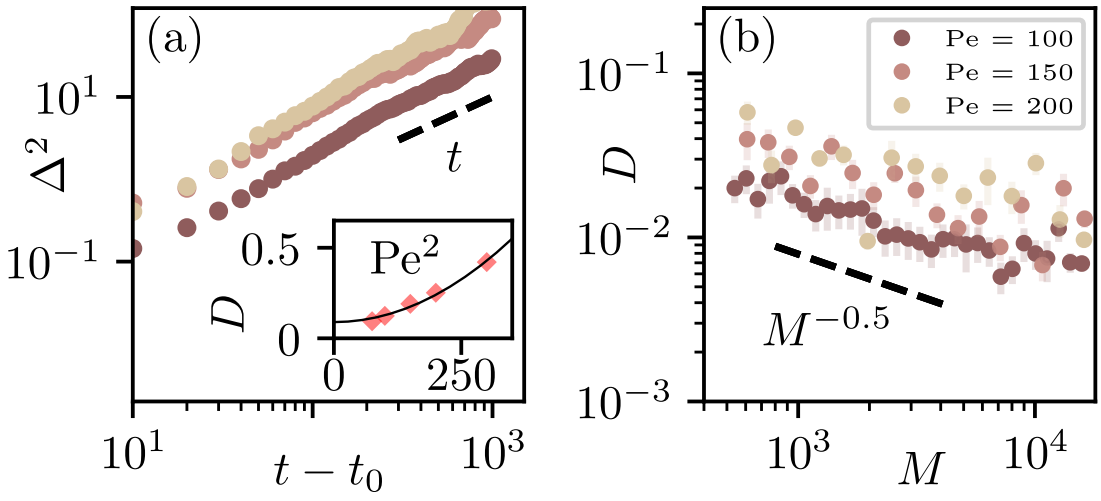

Figure 3.17: **Cluster dynamics in the bulk.** (a) Average over all clusters' c.o.m. mean-square displacements, at three Pe, with $t_0 > t_s$ ($t_0 = 900$, 700 and 500 for $\mathrm{Pe} = 100, 150, 200$, respectively). Inset: Pe dependence of the diffusion constant together with the fit $T/\gamma\ (1 + c\mathrm{Pe}^2)$ with $c = 8.1 \times 10^{-5}$ (i.e. $c\mathrm{Pe}^2 \sim 1$) and T/γ given by the external parameters. (b) Mass dependence of the single clusters' diffusion constant. $\overline{M}(t_0)$ are between 10^3 and 5×10^3 for all Pe.

clusters. We next argue about the origin of the enhanced diffusion and how it affects the clusters' growth.

Isolated cluster dynamics

In order to extract information on the clusters' dynamics, we need to follow them over longer periods. Therefore, we extracted and created an ideal environment where the cluster can be "isolated": we put them in a box with a linear size of the order of the typical inter-cluster distance in the bulk conditions studied above, then we filled space with an active gas mimicking the global conditions of the interacting clusters. The three snapshots in Fig.3.18(a)-(c) illustrate the evolution of one such cluster. The light and rather straight lines are at interfaces between different orientational (hexatic) orders In this way, active clusters are free to evolve indefinitely and we can fully characterize their dynamics and infer the origin of their anomalous diffusion. The cluster changes form, by opening up gas bubbles [TNC18, CDL+20a, SFC+20] and growing protrusions, and displaces by a kind of crawling mechanism. The movie[6] displays the evolution of a similar cluster. Sudden rearrangements yield rather large mass (and shape) variations, see Fig. 3.18(d). The active behaviour is directly confronted with simulations of clusters formed in a passive (attractive) system, which is thus at equilibrium - details and parameters of the passive-attractive system are reported in Appendix C. The passive behaviour is represented by the upper (red) curve which is smoother. The pdf of the instantaneous masses is plotted in Fig. 3.18(e).

Being able to track clusters in isolated conditions, we can now access to measurements that were denied in bulk, due to the extremely limited time window. In particular, we measure i) the forces acting inside the cluster, ii) the statistic of their displace-

[6] https://www.dropbox.com/scl/fi/g9tujqovvyelqarv9kepa/M1.mp4?rlkey=6wj2jqp0cck53bzu6tii8cuo0&dl=0

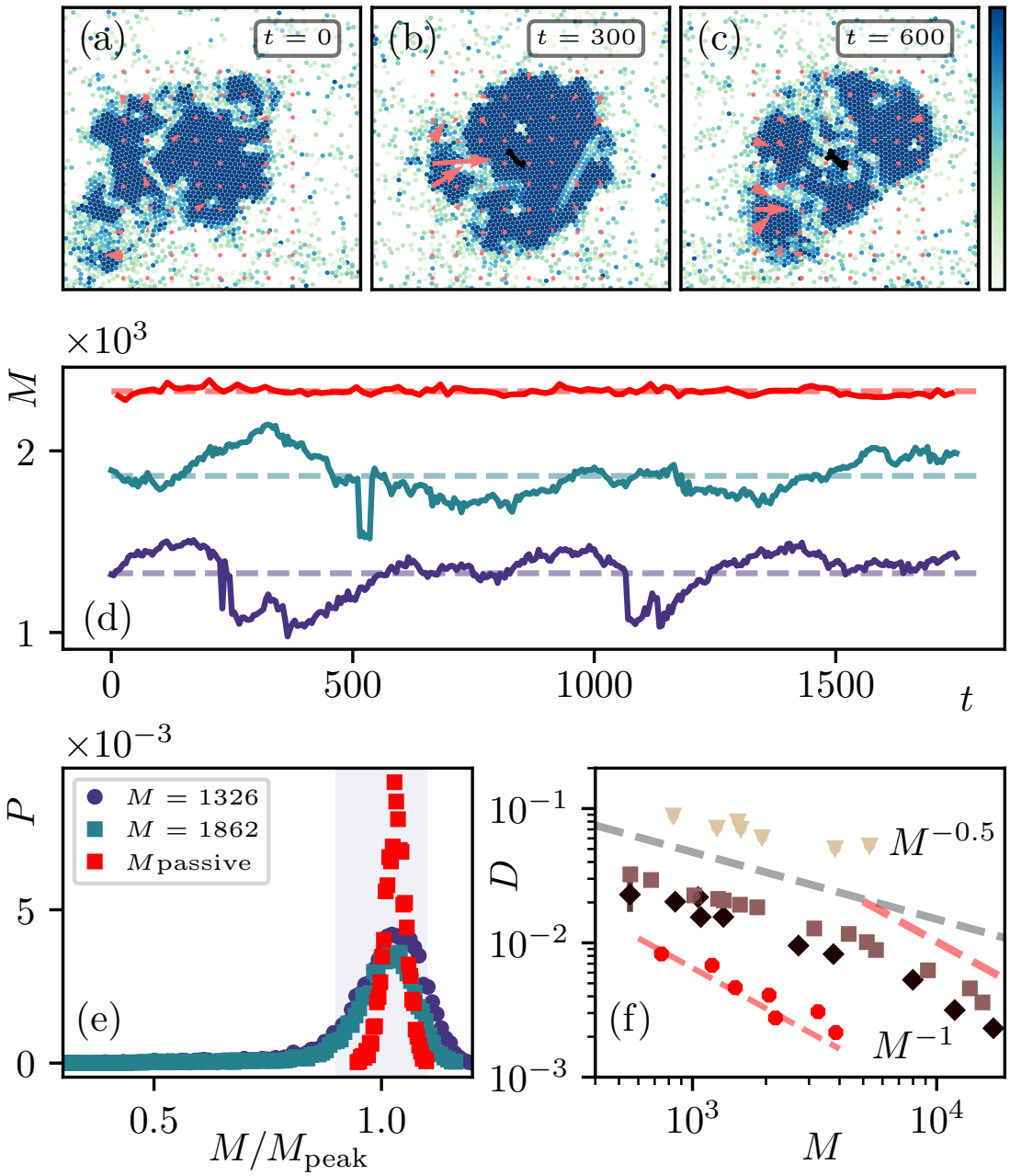

Figure 3.18: **Dynamics of isolated clusters.** (a)-(c) Subsequent snapshots of the same active cluster. The color code represents the modulus of the local hexatic order. The c.o.m. trajectory is shown in black and the local red arrows the active force coarse-grained on a square grid. (d) Mass evolution of two active clusters with different initial masses (lower curves) compared to a typical passive one formed by attractive particles (upper red curve). The horizontal dashed lines are the time averages. (e) Probability distribution of the instantaneous masses. The shaded gray region indicates the clusters used to calculate $D(M)$. (f) Mass dependence of D for ABP clusters (diamonds Pe = 80, squares Pe = 100, triangles Pe = 200) and clusters of passive attractive particles (red bullets, translated upwards by a factor 40). In the ABP case, we identify two algebraic regimes, $D \sim M^{-\alpha}$, with fitted $\alpha \sim 0.5$ (solid line) and $\alpha = 1$ (dashed line), for small and large masses. In the passive case, the slope $\alpha = 1$ is very close to the data. The temperature is $T = 0.05$ (active) and $T = 0.3$ (passive).

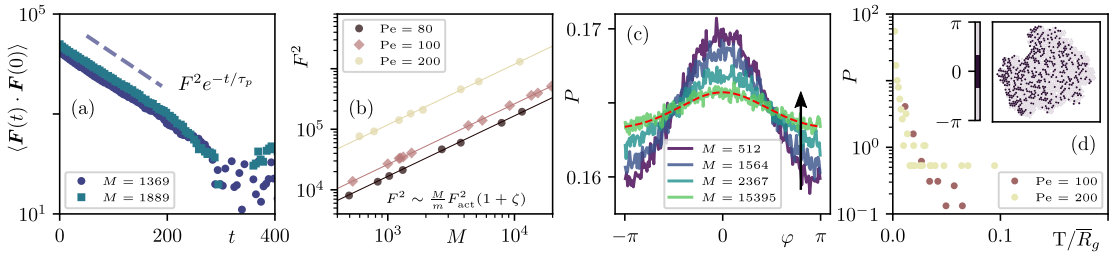

Figure 3.19: TODO: divide in 2x2 figure and enlarge it **Forces on individual clusters extracted from the bulk.** (a) Exponential decay, with characteristic time $\tau_p \approx 60$, of the correlation of the total active force acting on the clusters, Pe = 100. (b) Equal time value as a function of the cluster mass M. These curves confirm the $F^2_{\rm act}$ dependence, a fit yields $\zeta = 0.05$, and extrapolate to $F^2_{\rm act}$ for $M \to m$. (c) Distribution of the angles between the $\mathbf{n}_i$ and $\boldsymbol{F} = F_{\rm act} \sum_{j=1}^{M/m} \mathbf{n}_j$. (d) Distribution of the total torque T normalized by the averaged radius of gyration. Inset: map of the local active force alignment with the direction of motion.

ment, and finally, iii) the diffusion coefficient of isolated clusters (to be compared with the one measured for clusters in bulk).

Forces on single cluster

Each cluster is subject to a net potential force, a net active force, and a total torque. The total potential force vanishes identically due to the action-reaction principle. The total active force, instead, does not. It is the vectorial sum of the individual active forces and equals

$$\boldsymbol{F} = F_{\rm act} \sum_{i=1}^{M/m} \mathbf{n}_i. \tag{3.16}$$

Its temporal correlations are shown in Fig. 3.19(a) for clusters extracted from the bulk, and for all masses studied they decay exponentially, with a characteristic time $\approx \tau_p$, that is of the order of the persistence time of the single active particle. At equal times

$$F^2 \equiv \langle \boldsymbol{F}^2(0) \rangle = F^2_{\rm act} [\sum_{i=1}^{M/m} \langle \mathbf{n}_i^2(0) \rangle + \sum_{i \neq j}^{M/m} \langle \mathbf{n}_i(0) \cdot \mathbf{n}_j(0) \rangle] \tag{3.17}$$

and, assuming that the $\mathbf{n}_i(0)$ have independently identically distributed (*i.i.d.*) random components, $F^2 \equiv \langle \boldsymbol{F}^2(0) \rangle \sim (M/m) F^2_{\rm act}(1+\zeta)$. The measurement on clusters extracted from the bulk is in good agreement with this assumption, with $\zeta \approx 0.05$, see Fig. 3.19(b).

However, the active forces are correlated and the components of the $\mathbf{n}_i(0)$ are not *i.i.d.*. This is proven by the pdf of the angle φ between $\mathbf{n}_i$ and $\boldsymbol{F}$, which is shown in Fig. 3.19(c) as measured in clusters with four different masses extracted from the bulk. These pdfs are not flat, on the contrary, they are well described by the function

$$P(\varphi) = b/(2\pi\sigma^2)^{1/2}\, e^{-(\varphi-\overline{\varphi})^2/\sigma^2} + (1-b)/(2\pi)\ , \tag{3.18}$$

with $b, \sigma, \overline{\varphi}$ fitting parameters. The red dashed red line shows one such fit for the data for the largest cluster mass. The extra weight close to $\varphi = 0$ is more pronounced for the smaller clusters. The particles contributing to the peak are the ones for which the

active forces point along the direction of motion, and hence 'push' the cluster. As the configuration in the inset in Fig. 3.19(d) exemplifies, in this case these particles are situated at the left boundary and their forces have a preference to point right, the direction of motion. Quite typically, the particles with a correlated direction of the active force are situated at the boundaries of the clusters.

Finally, the total torques exerted on the clusters are negligible. The distribution of the ratio between the torque acting on an extracted cluster and its radius of gyration is plotted in Fig. 3.19(d). We see that for the two Pe values show, the distributions fall off to zero quite rapidly. This measurement is consistent with the fact that we do not see the clusters rotate significantly.

Cluster Displacements

Now, we show the probability distribution function of the displacements $\delta r_a^{\rm cm} = r_a^{\rm cm}(t) - r_a^{\rm cm}(t_0)$, with $a = 1, 2$, respectively, the x and y Cartesian components. The displacements are computed by numerical simulation for the c.m. trajectory of isolated clusters in the time interval $\delta t = t - t_0$, where, as usual, t_0 is the initial time of the tracking. In order to improve the statistics, we gather together the two displacement components, and we compute the cumulative probability distribution function. In the figure, we denote simply as $\delta r_a^{\rm cm}$ these gathered Cartesian displacements.

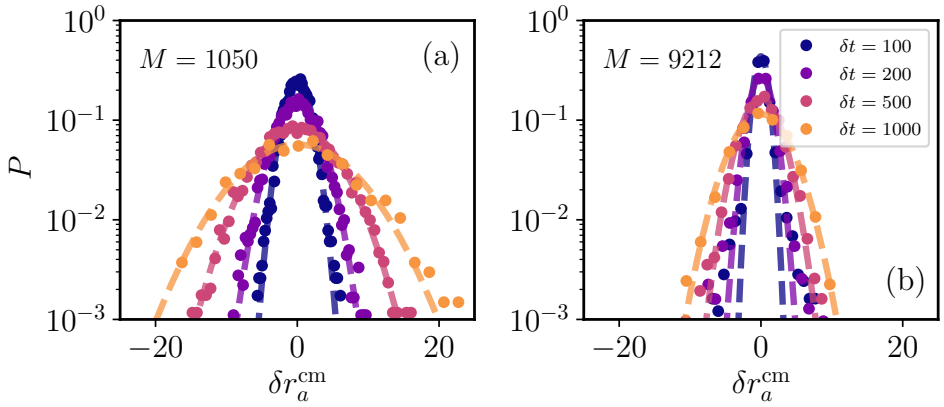

Figure 3.20: **Distribution of displacements** $\delta r_a^{\rm cm}$ along the two Cartesian directions at different tracking times δt (in the key). In one case, the cluster is such that $D \sim M^{-0.5}$ regime (left), and in the other it corresponds to the $D \sim M^{-1.0}$ regime (right). The stationary average masses over all the different evolutions of the same initial condition are reported in top left part of the two panels.

The results for two initial masses and different time delays are shown in Fig. 3.20. Panel (a) displays data for clusters with an averaged mass $M \approx 1050$ that is clusters such that the diffusion coefficient goes as $D \sim M^{-0.5}$. (On average, the cluster's mass increases a little bit until reaching stationary conditions at a new value in the extraction procedure.) Instead, panel (b) presents data for larger clusters, representative of the $D \sim M^{-1}$ regime. All data are satisfactorily fitted with Gaussian distributions, and we did not find any significant difference between the small and large mass cases. (Some outliers for very large masses may not be sufficiently well sampled.)

These measurements confirm that smaller clusters move, in general, more than larger ones, as demonstrated by the broader distribution of displacements in panel (a) than in panel (b), at equal tracking times.

Diffusion coefficient

We now proceed to estimate the diffusion coefficient of isolated clusters. Compared to the bulk case, the measurement on isolate clusters can benefit of better statistics and a larger mass window. The procedure that we use for the estimation of the diffusion coefficient of the isolated cluster in Appendix A.6. Simplistically, D is the average over the instantaneous values in the gray window of Fig. 3.18(e). Figure 3.18(f) represents the resultant diffusion coefficient D *vs.* the cluster mass M. Differently from the bulk data in Fig. 3.17(b), for which we observe a single decay $D \sim M^{-0.5}$, in the isolated cluster system D displays two regimes, described by $D \sim M^{-0.5}$ and M^{-1}. Clusters of passive attractive particles with similar packing fractions exhibit $D \sim M^{-1}$ over the full mass range (red bullets).

The large mass dependence can be estimated with a simple argument. The total active force has exponentially decaying temporal correlations, with characteristic time $\approx \tau_p$ and, at equal times, $\langle \boldsymbol{F}^2(0)\rangle \propto (M/m)F_{\rm act}^2$, see Fig.3.19, for all masses studied. Using these pieces of information in the calculation in Appendix D, which treats the active gas as a white noise bath and the active forces as independent yields $D \propto M^{-1}$.

However, for small clusters, two mechanisms conspire against $D \propto M^{-1}$. One concerns the clusters themselves. Firstly, the pdf of the angle φ between $\mathbf{n}_i$ and $\boldsymbol{F}$ has extra weight around $\varphi = 0$ (more pronounced for smaller clusters), Fig.3.19(c). Indeed, the active forces on boundary particles can be more aligned with the direction of motion, Fig.3.19(d), and make the small clusters more mobile. Secondly, the cluster's motion exhibits sudden events in which pieces detach and glue back after collisions (Fig. 3.18(a)-(c)). Thirdly, it is almost impossible to find large isolated clusters in the scaling regime at a not-too-low packing fraction (their form is much more contorted than in isolation, Fig. 3.13(c) and below). The impact of other clusters, favoured by their mobility, cannot be neglected and this seems to be the main reason why we do not see the crossover to the expected M^{-1} in the bulk. The other mechanism focuses on the active gas around the clusters. The size dependence of the diffusion coefficient of a spherical passive tracer immersed in an active gas is $D \sim M^{-1/2}$, just as in Fig. 3.18(f), with the cross-over increasing with the persistence length of the gas particles [SH22].

Beyond Oswald Ripening scenario

At this point, it is clear that cluster diffusion and collisions play a key role in the aggregation mechanism and the growth of the dense phase in the phase separation process. Now we elucidate this claim and compare it directly with the equilibrium (passive) counterpart.

In equilibrium phase separation, the mechanism of growth of the droplet in the late stage of the process is Ostwald ripening. For active systems, however, the cluster dynamics is different and their enhanced motility increases the collision rate. We thus tailor the tracking algorithm to measure mass variations and distinguish Ostwald ripening from cluster-cluster aggregation as growth mechanisms in the bulk (see Appendix A.5 for details). In Fig. 3.21(a) we show the normalized counting of small mass

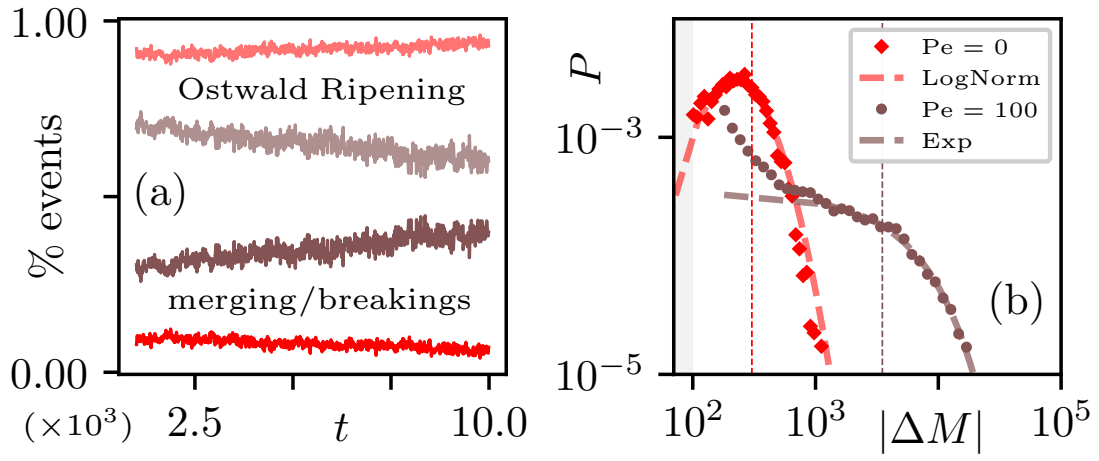

Figure 3.21: **Collisions.** (a) Percentages of events with mass changes $|\Delta M| < 100$ (above), and those with $|\Delta M| \geq 100$ (below) for Pe = 0 (red), 100 (brown). (b) Distributions of absolute mass changes at $t = 10^3 > t_s$ for $\delta t = 10$. The dashed lines are fitted with the functions in the key.

variation events, that we attribute to evaporation/condensation of particles (above), and large mass variation events due to breaking/merging of clusters (below), during the observed timeframe $\delta t = 10$. The threshold is set at the cluster mass variation $|\Delta M| = |M_{t+\delta t} - M_t| = 100$ but similar results are found for other choices nearby. In the passive case (red data) the former percentage is very close to one and slowly grows in time, underscoring that Ostwald ripening is the dominant mechanism at long timescales [FJ16]. Instead, for ABPs, the trend is the opposite, with the percentage of large cluster rearrangements due to aggregation and/or break up becoming more important in the course of time. Further differences are shown by the distributions of $|\Delta M|$ at the beginning of the scaling regime, Fig. 3.21(b). The passive system displays a clear peak, due to the aggregation of clusters with the preferred averaged size, well fitted by a log-normal function. Instead, the form in the active system is rather different and can be attributed to the merging of approximately independent clusters with an exponential size distribution.

Before proceeding, a few words are needed on the variation of mass distributions of clusters undergoing merging and breaking events, that we identify as those with $|\Delta M| \geq 100$. In Fig. 3.22(a) we show the mass distributions $P(M_t)$ and $P(M_{t+\delta t})$ for $t = 10^3$, the starting time of the tracking that we choose to be roughly at the beginning of the scaling regime for the corresponding Pe, and $\delta t = 10 \ll t$. We select a relatively short δt to be able to identify the fate of each cluster correctly. Since the time delay δt is very short compared to t, the two distributions are practically identical $P(M_t) \sim P(M_{t+\delta t})$. They both have a tail that can be well approximated by an exponential decay, as proved in Fig. 3.15 and its discussion. The probability distribution $P_{\Delta M}(\Delta M)$ of the

new random variable $\Delta M = M_{t+\delta t} - M_t$, reads

$$\begin{aligned} P_{\Delta M}(\Delta M) &= \int dM_t \int dM_{t+\delta t}\; P(M_{t+\delta t}, M_t)\, \delta(\Delta M - M_{t+\delta t} + M_t) \\ &\sim \int dM_t \int dM_{t+\delta t}\; P(M_{t+\delta t}) P(M_t)\, \delta(\Delta M - M_{t+\delta t} + M_t) \\ &= \int dM_t\; P(\Delta M + M_t)\, P(M_t) \end{aligned} \tag{3.19}$$

and it is just the convolution of the probability density functions of the masses at the two times, if the variables are independent, the assumption used in the second line. If we further use, for the tails, $P(M_{t+\delta t}) \sim e^{-M_{t+\delta t}/\overline{M}_{t+\delta t}} \sim e^{-M_{t+\delta t}/\overline{M}_t}$ valid for $M_{t+\delta t} > 100$, and similarly for $P(M_t)$, the convolution yields another exponential

$$P_{\Delta M}(\Delta M) \sim e^{-\Delta M/\overline{M}_t}\ . \tag{3.20}$$

In Fig. 3.22(a) and (c) we show the probability distribution functions of the masses M_t and $M_{t+\delta t}$ at $t = 10^3$ and $t = 8 \cdot 10^3$, respectively. In panels (b) and (d) we compare the probability distribution of ΔM sampled directly with the algorithm and the outcome of Eq. (3.19) using the full $P(M_t)$ at the corresponding time t. The agreement is very good on the full decaying tails, and even the small ΔM regime is rather well captured with this approximation.

Cluster Geometry

As anticipated in the analysis of the cluster mass distribution, not all clusters have the same shape and their geometry may influence the growth of the dense component: we now analyze this possibility. Regular (with fractal dimension d_f equal to the dimension of space $d = 2$) and fractal (with $d_f < 2$) clusters co-exist. In Fig. 3.23(a) we plot M^*, the mass normalized by its average $\overline{M}$, against R_g^*, the radius of gyration also normalized by its average $\overline{R}_g$, of individual clusters sampled in the scaling regime $t = 10^3 - 10^5$. The data follow $M^* \sim R_g^{*d_f}$, with $d_f \simeq 2$ for $M^* < 1$, and $d_f \simeq 1.45$ for $M^* > 1$ both in the active and the passive case. The crossover at $M^* \sim R_g^* \sim 1$ is controlled by $\overline{M}$ and $\overline{R}_g$, which depend on time in the form reported in Fig. 3.13(a) and 3.23(b), respectively. For diffusion limited cluster-cluster aggregation $d_f \simeq 1.45$ in $d = 2$ [KBJ83, Mea83], as well as in passive Lennard-Jones systems at very low ϕ [PBD21]. Having identified two kinds of clusters we calculated the average mass and radii separately. In Fig. 3.23(b) we show the growth of the mean R_g for regular (lower curve) and fractal (upper) clusters, as well as the completely averaged $\overline{R}_g$ (middle). All kinds of clusters enter the scaling regime at the same t_s. Fractal (regular) clusters grow slightly faster (slower) than the average within numerical precision. There are roughly 2-3 times more regular than fractal clusters, see the N_C curves on the right scale.

Having found clusters' diffusion and aggregation in the active system, we are tempted to test the Smoluchowski relation $z = d_f\,(1 + \alpha)$, valid for Brownian diffusive binary cluster aggregation under mean-field assumptions, described in Section 2.3. For $M < \overline{M}$ we found $d_f \approx 2$ and $\alpha \approx 0.5$, leading to $z \approx 3$ (see Fig. 3.23 (a) and Fig. 3.18(f)). Instead, for $M > \overline{M}$ while d_f changes to $d_f \approx 1.45$, we still measure $\alpha \approx 0.5$ in the bulk, and this gives $z \approx 2.2$ which is very close to the value fitted in Fig. 3.23(b).

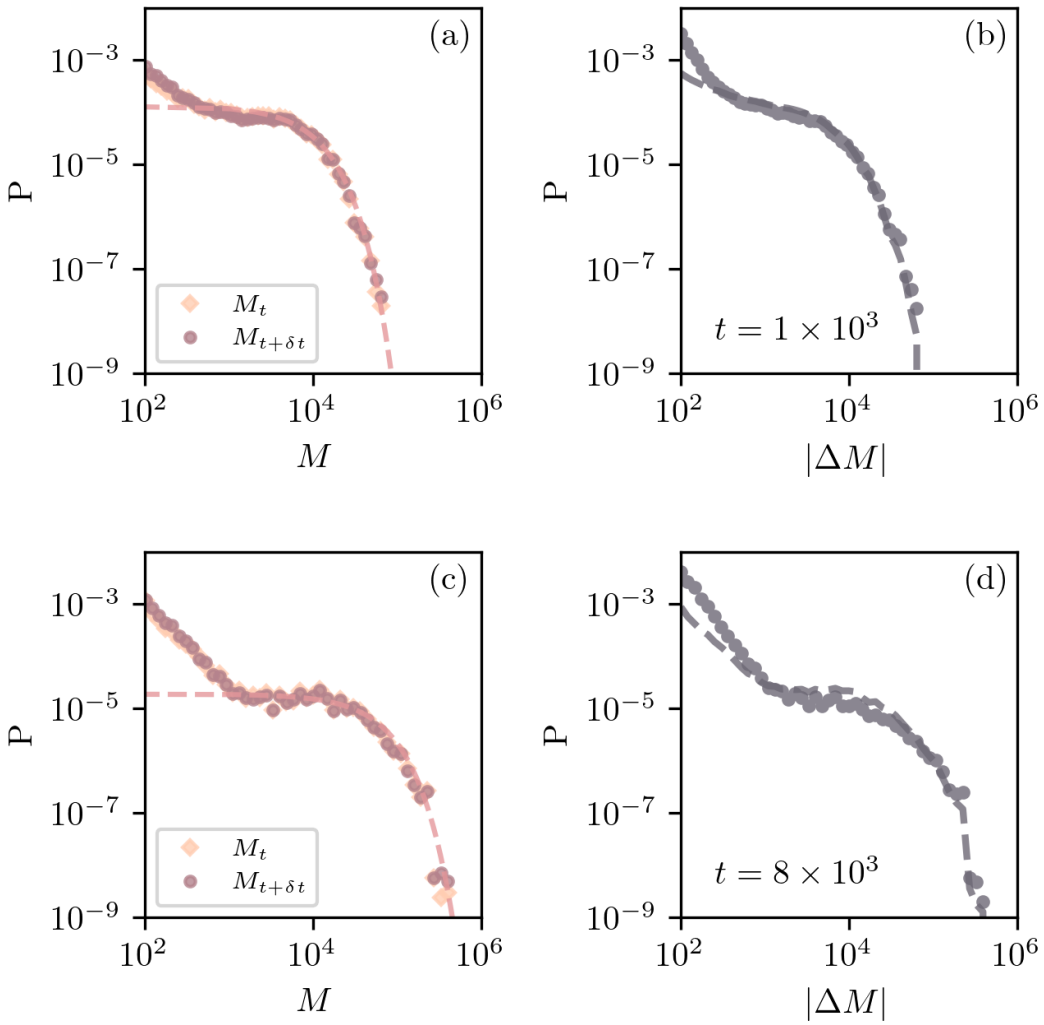

Figure 3.22: **Mass and mass variation distributions at early times.** (a) Distribution of the mass M_t (diamond) and $M_{t+\delta t}$ (circles) for merging/breaking clusters at $t = 10^3$, the dashed line shows the fit with an exponential distribution of the large mass tail. (b) Distribution of mass variations $\Delta M = M_{t+\delta t} - M_t$ at $t = 10^3$ computed from numerical data (circles), and using Eq. (3.20) (dashed line) for the convolution of the numerical probability distributions of M_t and $M_{t+\delta t}$ (see the text for details). (c) and (d) same as in (a) and (b) for $t = 8 \cdot 10^3$ The characteristic mass of the exponential fits of the tails of the distributions of M at different times is $\overline{M}_t \approx 5 \cdot 10^3$ and $\overline{M}_t \approx 2 \cdot 10^4$ at $t = 10^3$ and $t = 8 \cdot 10^3$, respectively. These values are compatible with the mass averages and, within numerical errors, with the exponential tails of the distributions of $|\Delta M|$.

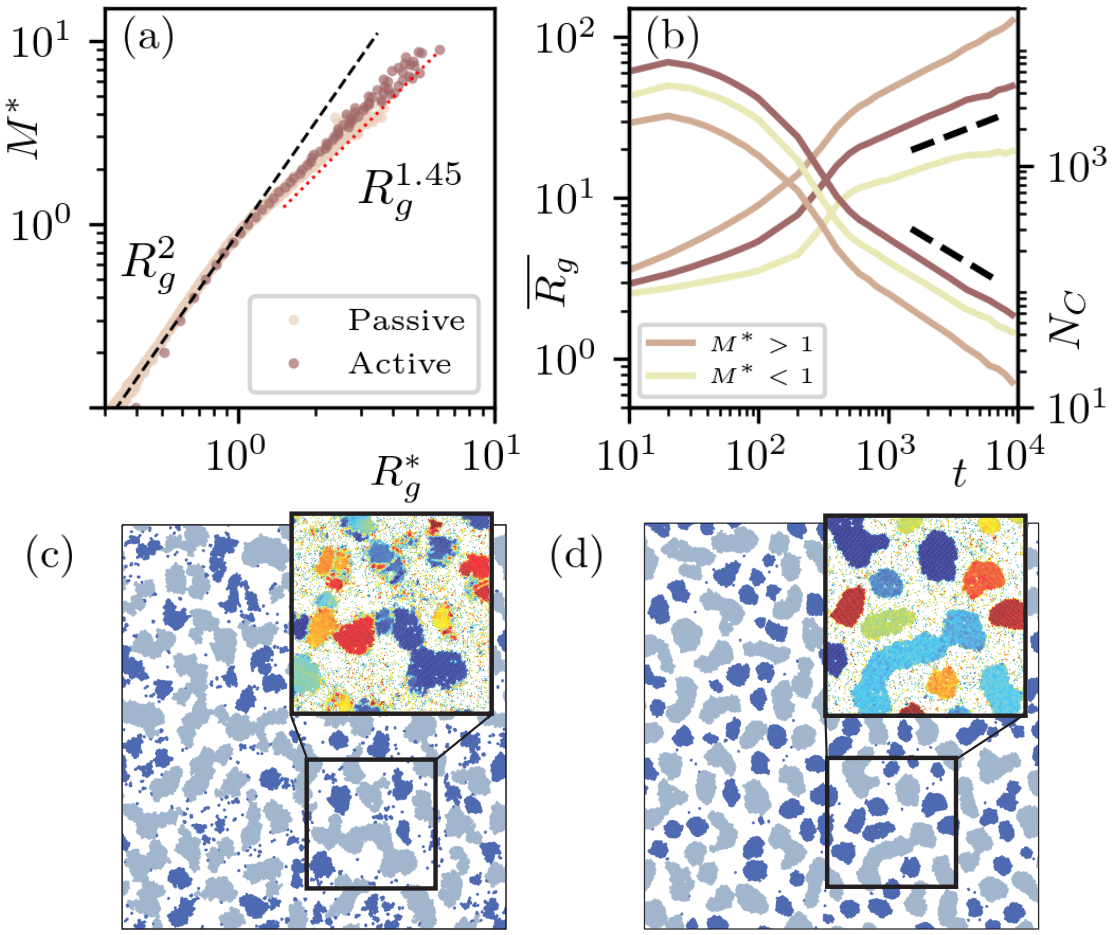

Figure 3.23: **Clusters geometry.** (a) Scatter plot of $M^* = M/\overline{M}$ against $R_g^* = R_g/\overline{R}_g$, for passive and active (Pe = 100) clusters. (b) Left scale: the averaged radius of gyration of regular ($M^* < 1$), fractal ($M^* > 1$) and all clusters. Right scale: the number of clusters. The dashed lines are fits of the total averaged curves, $t^{0.31}$ and $t^{-0.65}$. Separate fits of the fractal and regular $\overline{R}_g$ data yield z, close to 2.2 and 3.85, respectively. A snapshot of (c) the ABP system and (d) the passive system in the scaling regime. Fractal clusters are gray and regular ones are blue. The zooms in the boxes represent the local hexatic order with a color map.

Had we claimed that $\alpha = 1$ and kept $d_f \approx 1.45$ for sufficiently large masses, as measured for the clusters extracted from the bulk, then $z \approx 2.9$, very close to 3. For the equilibrium system, instead, cluster aggregation becomes irrelevant at long times (movie[7] and Fig. 3.21) and there is no reason to use the Smoluchowski relation.

3.3 Conclusions

In these works, we studied the morphology and dynamics of Motility-Induced Phase Separations and the difference with respect to an equilibrium first-order phase separa-

[7] https://www.dropbox.com/scl/fi/248sara4vsjuidkwnck5v/M3.mp4?rlkey=tsp098fuzre2smn4fqaes4fai&dl=0

tion.

First, We monitored MIPS of large systems of ABPs. On top of the dense-dilute phase separation, governed by a $t^{1/3}$ growing length in the scaling regime, $2d$ MIPS involves another ordering mechanism controlled by activity, giving rise to a new finite characteristic length associated with hexatic order. As a result, the dense phase breaks into a mosaic of differently oriented patches.

Second, we focused on the dynamics of active clusters and their role in the growth mechanism of the dense phase. Our analysis evidences several important differences between MIPS and equilibrium phase separation. As appreciated from a visual inspection of the numerical simulations[8,9], and confirmed in Fig. 3.21, passive small clusters evaporate (à la Ostwald ripening) while active ones can break and sometimes recombine (à la Smoluchowski). The interfaces between the different (hexatic) orientations of the colliding ABP clusters do not heal. Consequently, active clusters are patchworks of different hexatic orders (with dynamic bubbles in cavitation), while passive ones are homogeneous. The external surfaces of the active clusters are much rougher than the passive ones, see Fig. 3.23(c)-(d). Due to the enhanced cluster's diffusion constant, $D \sim \mathrm{Pe}^2/M^{1/2}$, growth is faster for active than passive particles. In both cases, there is a co-existence of small regular and large fractal clusters with the crossover at the averaged scales.

We conclude by adding that, although the global growth laws in MIPS and equilibrium phase separation are both $t^{1/3}$, in the MIPS regime studied here, Ostwald ripening combines with aggregation-fragmentation - with the same growing exponent - and the latter becomes more and more important over time.

[8] https://www.dropbox.com/scl/fi/zkfm8zq06vpu90312ygyz/M2.mp4?rlkey=s2wvkpyef6solw5a6ljxl1j46&dl=0

[9] https://www.dropbox.com/scl/fi/248sara4vsjuidkwnck5v/M3.mp4?rlkey=tsp098fuzre2smn4fqaes4fai&dl=0

4

Effects of Inertia and Hydrodynamic Interactions

Having clarified the aggregation and growth process in the intermediate-density / high-activity region - where MIPS arise - of the phase diagram of two-dimensional ABPs, we now focus on the high-density / low-activity region. As mentioned in Sec.1.3, here ABPs present ordering phase transitions which are connected to those encountered for passive hard colloids; at small values of the self-propelling force, a liquid-hexatic critical transition is followed by a hexatic-solid transition, where the solid phase has quasi-long-range (QLR) positional and long-range (LR) orientational order, the hexatic phase has short-range (SR) positional and QLR orientational order, while the liquid phase is homogeneous and has SR positional and orientational order.

These features of the ABP phase diagram have been well established in the context of over-damped motion and without an explicit underlying thermo-hydrodynamic bath; the effects of these factors on the phase behaviour remain to be considered. In this Chapter, we introduce inertia and hydrodynamic interactions in the standard ABP model, obtaining a generalized model that we call Active Hydrodynamic Particle (AHP) model, and characterize how the critical density for the liquid-hexatic transition of active particles is modified, in a low activity regime where MIPS does not occur, by i) the inertial effects due to mass changes, and ii) the presence of hydrodynamics interactions. The Chapter is organized as follows. The first section introduces the Active Hydrodynamic Model. The second section illustrates the results of the study of the liquid-hexatic transition under the effects of inertia and hydrodynamics.

4.1 The AHP Model

We first proceed to describe the Active Hydrodynamic Model and the coupling with the hydrodynamic solvent. In particular, hydrodynamics has been implemented by using the multi-particle collision method (MPC)[1] [MK99, GIKW09], which seamlessly integrates with the dynamics of active Brownian particles [BGL+14]. We focus here

[1]This method is also known in the literature as Stochastic Rotational Dynamics (SRD)

only on 2D systems where the rotational diffusion follows the same equations as for ABP. This allows us to have, for the AHP model, the same friction, temperature and rotational diffusion as the ABP model, providing a way to quantitatively compare them.

Solvent dynamics

The solvent consists of N_s identical point-like particles of mass m_s embedded in a two-dimensional square box of size L. Each particle i is characterized by a position $\mathbf{r}_i$ and velocity $\mathbf{v}_i$, both of which are continuous variables. In this algorithm, the time is discretized in units Δt_s, and the evolution of the system is composed by two steps, propagation and collision, which are applied consecutively for each Δt_s.

In the propagation step, particles are freely streamed according to their velocities as

$$\mathbf{r}_i(t + \Delta t_s) = \mathbf{r}_i(t) + \mathbf{v}_i(t)\Delta t_s. \tag{4.1}$$

In order to perform the collision step, the system is partitioned into cells of a square lattice with mesh size σ_s. Each cell is the scattering area where an MPC occurs, which updates particle velocities according to the rule [MK99, MK00]

$$\mathbf{v}_i(t + \Delta t_s) = \mathbf{u}(t) + \Omega[\mathbf{v}_i(t) - \mathbf{u}(t)], \tag{4.2}$$

where $\mathbf{u} = (\sum_{i=1}^{m} \mathbf{v}_i)/m$ is the mean velocity of the m colliding particles in the cell, also assumed to be the macroscopic velocity of the fluid. Ω is a rotation matrix with angle $\pm\alpha$ ($0 < \alpha < \pi$). The angle α is fixed at the beginning of the simulation while its sign is assigned with equal probability to every cell at each time step. In each cell, all the m relative velocities are rotated with the same angle. Linear momentum and kinetic energy are conserved under this dynamics.

The transport coefficients of this model can be analytically derived. In particular, for our purposes the kinematic viscosity ν_s and the self-diffusion coefficient D_s will be useful. In 2D the viscosity is equal to [KPRY03, ITK04]:

$$\begin{aligned}\nu_s = \frac{\sigma_s^2}{2\Delta t_s}\Big[\left(\frac{\lambda}{\sigma_s}\right)^2 \Big(\frac{n_s}{(n_s - 1 + \exp(-n_s))\sin^2(\alpha)} - 1\Big) \\ + \frac{(n_s - 1 + \exp(-n_s))(1 - \cos(\alpha))}{6n_s}\Big],\end{aligned} \tag{4.3}$$

while the coefficient D_s is [TIK06]:

$$D_s = \frac{\lambda^2}{2\Delta t_s}\Big(\frac{2n_s}{(n_s - 1 + \exp(-n_s))(1 - \cos(\alpha))}\Big), \tag{4.4}$$

where $n_s = N_s\sigma_s^2/L^2$ is the average number of particles per cell and $\lambda = \Delta t_s\sqrt{k_BT/m_s}$ is the mean-free path.

Solvent-colloids coupling

The next step would be to integrate the solvent particles with the colloids, meaning we need to decide how to couple colloids and solvent dynamics. Different strategies are possible and a review for MPC with passive colloids can be found in [GIKW09]; here we adopted the one implemented in the LAMMPS software [BGL+14].

In this implementation colloids are evolved for n timesteps Δt_c, following the equation of motion (1.8) without the force terms $\boldsymbol{\xi}_i$ and $\gamma \dot{\boldsymbol{r}}_i$, which accounted implicitly for the thermal bath in the ABP model, and are substituted here by the MPC bath. Afterwards, solvent particles are propagated for a timestep equal to $\Delta t_s = n\Delta t_c$. Note that both Δt_c and Δt_s are expressed in the same time unit as in the ABP model, see Appendix A for details. Before computing the collision (4.2), the algorithm checks if solvent particles are overlapping with disks having diameter σ_c and mass m_c, that is if the position of point-like solvent particles is inside the area of the disk. In this case, an exchange of momentum occurs, followed by a change in the position of solvent particles to place them out of the colloids, and, finally, the collision step for solvent particles is applied.

The exchange of momentum is decided by the proper colloid–solvent boundary condition (BC) adopted, which can be either no-slip or slip. No-slip BC means that linear and angular momentum are exchanged between colloid and solvent particles [BB94], while for slip BC only linear momentum is transferred as in the case with radial interactions [MK00].

In the no-slip thermal BC, when a solvent particle of velocity $\mathbf{v}$ overlaps with a disk, it is moved back to the disk surface along the shortest vector $\mathbf{r}_d$ and then streamed for a distance $\mathbf{v}'\Delta t_s \varepsilon$, where $\mathbf{v}'$ is the updated velocity and ε is a uniformly distributed random number in the interval $[0, 1]$ [HHIH05]. The new velocity $\mathbf{v}'$ is divided in the normal v_N and tangential v_T velocity components with respect to the particle-colloid distance, and chosen according to the stochastic distributions

$$p_N(v_N) = (m_s v_N / k_B T) \exp\left(-m_s v_N^2 / 2k_B T\right), v_N > 0 \tag{4.5}$$

$$p_T(v_T) = \sqrt{m_s / 2\pi k_B T} \exp\left(-m_s v_T^2 / 2k_B T\right), \tag{4.6}$$

centred around the local velocity $\mathbf{v}_d$ of the colloid surface, where $\mathbf{v}_d = \mathbf{V} + \boldsymbol{\omega} \times (\mathbf{r}_d - \mathbf{R})$, with $\mathbf{R}$ being the position of the colloid centre, $\mathbf{V}$ and $\boldsymbol{\omega}$ the linear and angular velocities of the colloid. Regarding the change in momentum for the colloid after the collision, all the linear and angular momenta variations of the overlapping solvent particles are summed up as $\Delta\mathbf{P} = \sum_s m_s(\mathbf{v} - \mathbf{v}')$ and $\Delta\mathbf{L} = \sum_s m_s(\mathbf{r}_d - \mathbf{R}) \times (\mathbf{v} - \mathbf{v}')$, and the linear and angular velocities of the colloid are updated as: $\mathbf{V}' = \mathbf{V} + \Delta\mathbf{P}/m_c$ and $\boldsymbol{\omega}' = \boldsymbol{\omega} + \Delta\mathbf{L}/I$ where $I = m_c\sigma_c^2/8$ is the moment of inertia of a disk. In the case of a high packing fraction of colloids, it may happen that a single solvent particle can scatter with several disks in the same timestep Δt_s. Ignoring such multiple collisions would cause an attractive depletion-like force between disks [HHIH05]. This effect can be kept under control by allowing a maximum number N_M of multiple collisions. It was found empirically that $N_M \simeq 10$ is the best choice to optimize computational speed and accuracy. In the case of slip thermal BC, the tangential component of the fluid particle velocity is preserved during the scattering with disks; thus no torque is imparted to colloids. The normal component v_N of the solvent particle new velocity $\mathbf{v}'$ is sampled from a Gaussian distribution according to the distribution of Eq. (4.5) which is centered around the disk velocity $\mathbf{V}$ (the angular velocity is irrelevant since collisions are now treated as central) [BGL+14].

The choice between no-slip and slip BC is directly connected to the way the axis of colloids $\mathbf{n}_i$ is evolved. In the first case, the solvent-disk interaction determines directly through torque exchange how colloids diffuse rotationally. In the second case, the rotational diffusion is accounted for independently using the angular equation in (1.8).

Here, we choose the slip thermal BC for two reasons. The first one is that in this way we can choose the value of D_θ independently and match it with the one used in the ABP model. The second reason is that the integration of slip conditions is much faster than no-slip ones since there is no need to consider the integration of disks' angular velocities.

Since we will mostly deal with non-equilibrium simulations, solvent particles must be coupled to a thermostat to maintain a constant temperature. We use the method of locally rescaling fluid particles velocities $\mathbf{v}_i$ relative to the centre of mass velocity $\mathbf{u}$ for each cell by a proper factor that enforces the correct temperature [CCVGW15]. We do not expect that this approach may alter flow profiles since, as later shown, we will adopt a very small cell size σ_s compared to variations in flow patterns and a very large value of n_s, the average number of solvent particles per cell. Note that this implementation ensures only local linear momentum conservation, while angular and total linear momenta are not conserved, as typically ensured in simulations of swimmers [TEQ$^+$18].

4.2 Inertial and hydrodynamic effects on hexatic liquid transition

The first question we explore concerns the role of inertia for the 2D ABP model, and in particular the interplay between inertial and active diffusion timescales, which can be varied independently [NCP$^+$20a, CM21a]. It has been pointed out in [OKG$^+$21] that in three-dimensional active systems, inertia should attenuate the destabilizing effect of activity on the ordered phase. Large inertia has also been shown to strongly affect the kinetic energy of the particles into the highly dense phase of MIPS [PCGS20b], and to highly inhibit phase segregation [L$'$ow20]. However, the role of inertia in the context of dense ABP, and in particular how the particle's mass affects the hexatic phase, has not yet been characterized.

The second question concerns the role of hydrodynamic interactions in the dense phase, using the AHP model we introduced earlier. Regarding the influence of hydrodynamics in MIPS, it is found that in 2D MIPS is suppressed [TWQ$^+$18b, MNGLF14, GWS$^+$20], as hydrodynamics favour reorientation of particles' self-propulsion direction, while in quasi-2D systems MIPS has been observed for low-density fluids[ZS14] and not when the fluid was made incompressible [TEQ$^+$18, GWS$^+$20].

In particular, we will focus on characterizing the presence and location of the liquid-hexatic transition, by varying the system density in a region of the phase diagram at intermediate active forces where MIPS does not occur for over-damped ABP. The latter undergo the transition at $\phi_c = 0.795$ for $Pe = 10$ and at $\phi_c = 0.83$ for $Pe = 20$ [CDGS17c].

The transition can be characterized by measuring the hexatic order parameter, $\psi_6(r_i) = \frac{1}{N_i}\sum_{j=1}^{N_i} e^{i6\theta_{ij}}$, with N_i the number of nearest Voronoi neighbours for particle i, and θ_{ij} the angle formed between the segment connecting particles i and j and the x-axis. From $\psi_6(r_i)$ we can compute the hexatic correlation function, defined as:

$$g_6(r) = \frac{\langle \psi_6(\boldsymbol{r}_i)\psi_6(\boldsymbol{r}_j)\rangle}{\langle \psi_6^2(\boldsymbol{r}_i)\rangle}\,, \tag{4.7}$$

where $r = |\boldsymbol{r}_i - \boldsymbol{r}_j|$. The transition between hexatic and liquid phases can be observed by the change in the functional dependence of $g_6(r)$ from exponential decay for short-

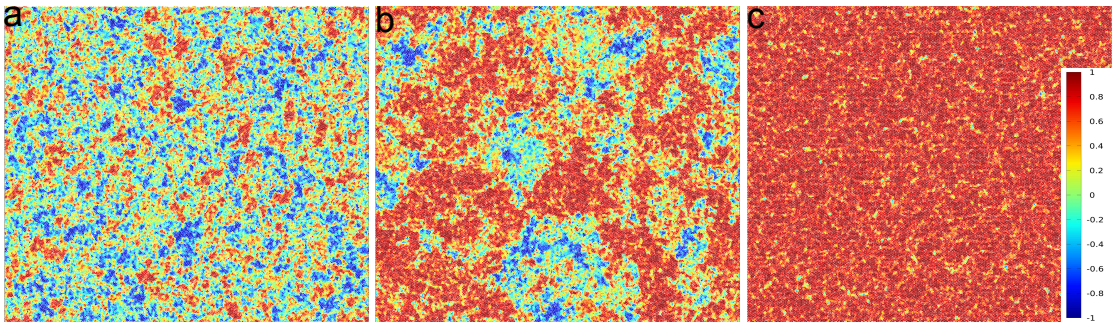

Figure 4.1: **Hexatic order parameter color map in the ABP model. (a)-(c)** Color maps of the projection of the local hexatic order parameter of each particle, $\psi_{6,j}$, onto the direction of the system's global average, $\mathbf{\Psi} = 1/N \sum_j \psi_{6,j}$, at fixed $\mathrm{Pe} = 10$ and $m_c = 44$ for $\phi = 0.710, 0.730, 0.760$ respectively, for a system of size $L = 256\sigma_c$. The values of global hexatic parameter $\psi_6 = \frac{1}{N}|\sum_i^N \psi_{6,i}|$ are $\psi_6 = 0.015, 0.375, 0.85$, respectively (see Fig. 4.6).

range order, $g_6(r) \sim e^{-r/l_c}$, where l_c is the correlation length, to algebraic for quasi-long-range order, $g_6(r) \sim r^{-\beta}$.

Inertial effects

Now, we characterize the evolution of ABP turning off hydrodynamic interactions and thus following the standard model described in Eq.(1.8) at $\mathrm{Pe} = 5, 10, 20$ and compare the results with the ones obtained in Ref. [CDGS17c] and also described in Section 1.3. In particular, while there only the value $m_c = 1$ was considered, here we will study the system with various masses ranging from $m_c = 5$ to 50. The use of large masses will allow a direct comparison with the AHP model (where $m_c = 44$) that will be used in the following.

We will focus on measuring approximately the value of the critical density ϕ_c where the liquid-hexatic transition occurs, computing the hexatic correlation at a fixed Pe within intervals of ϕ ranging from 0.05 to 0.1. Fig.4.1(a)-(c) show typical configurations at $\mathrm{Pe} = 10$, $m_c = 44$ and three different densities. Configurations are colored according to the local hexatic parameter $\psi_{6,j}$, projected onto its average value. In panel (a) ($\phi = 0.71$) we do not observe the appearance of any macroscopic hexatic domain, while in panel c ($\phi = 0.76$) we observe a fully hexatically ordered system. Panel (b), with $\phi = 0.73$, is an intermediate density where macroscopic and orientationally ordered domains emerge, suggesting that this density is close to the transition point. To locate the liquid-hexatic transition point at a fixed activity, we resort to studying the hexatic correlation functions, finding the density at which these functions change from exponential to algebraic decay. Fig.4.2 shows these functions for $m_c = 44$ and $\mathrm{Pe} = 10, 20$. At densities below $\phi = 0.72$ for $\mathrm{Pe} = 10$ and $\phi = 0.74$ for $\mathrm{Pe} = 20$, we find that the correlations have an exponential decay, while for larger values the behaviours that best fit the decay are that of an algebraic function. Thus, we find that at both activities considered the values where the liquid-hexatic transition occurs are lowered with respect to the ones at $m_c = 1$ reported in Ref. [DLC$^+$22b], suggesting that the increase in mass enhances the orientational ordering at fixed activity. In particular, we estimate $\phi_c = 0.730 \pm 0.01$ and 0.760 ± 0.01 for $\mathrm{Pe} = 10, 20$, respectively.

We also checked that this ordering effect occurs while fixing the system density and

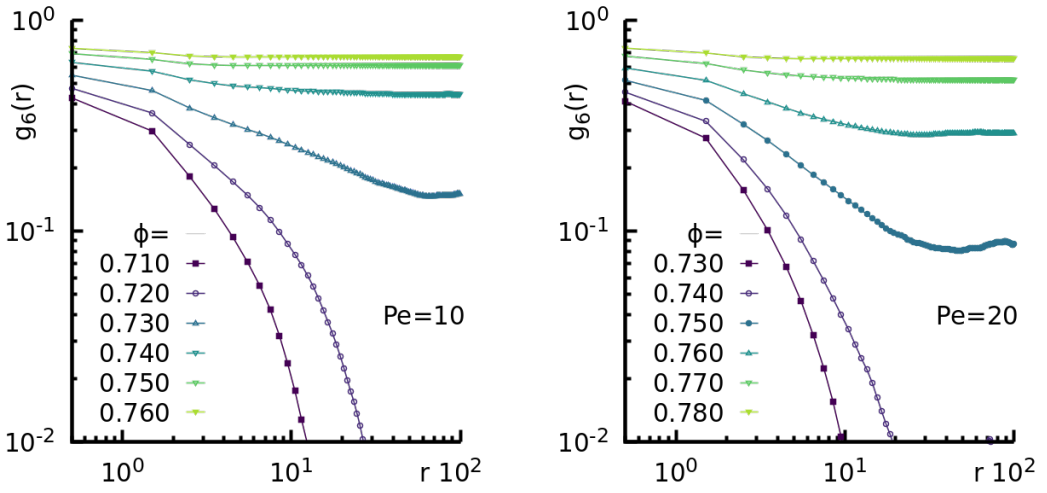

Figure 4.2: **Hexatic order correlation functions for the ABP model.** Hexatic order correlation functions $g_6(r)$ for $m_c = 44$ at $\mathrm{Pe} = 10$ (left) and $\mathrm{Pe} = 20$ (right) for different global packing fractions given in the keys.

activity, and increasing the colloids mass. The correlation functions in Fig. 4.3, left side, at $\mathrm{Pe} = 10$ and $\phi = 0.74$, show that by increasing the mass the system crosses from a liquid state to a hexatic one. We summarize these measurements in the right panel of Fig. 4.3, where we show the location of the critical density for different Pe and different m_c. It is evident that the critical density of the liquid-hexatic transition continuously decreases increasing the value of the mass for the different Pe considered. Interestingly, the data fit with the function $\phi_c(m_c) = a + be^{-m_c/c}$, with coefficients reported in the caption.

To summarize, the results shown here point out that an enlarged mass, and therefore an increase in the inertial time t_I, enhances the orientational ordering of the system. It is important to note that this is a non-equilibrium effect not present in the passive system. Indeed, we checked (not shown) that in the absence of activity, the transition density value is independent of the mass value. as there is only one relevant timescale in this case. We also observed that the asymptotic values for large m_c (coefficient a in the fitting function) are close to the transition density at $\mathrm{Pe} = 0$ [CDGS17c]. When the persistence number is $pn \gtrsim 10^{-2}$ ($m_c \approx 10$), the system behaves closer to the passive case. On the other hand, when $pn \lesssim 10^{-2}$ the active force has a disordering effect in the hexatic ordering.

Hydrodynamics effects

We now turn our attention to the role of hydrodynamics by studying the AHP model. To do so, we employ the hybrid mesoscopic approach presented at the beginning of the Section, where the MPC solvent is coupled with the active colloids to account for hydrodynamic interactions. The parameters of AHP, chosen to fulfil the constraints of the model - see Appendix A.1 for a complete description - fix the colloid mass to $m_c = 44$ and $\gamma = 10$. In this way, the AHP simulation results can be directly compared with the ones of ABP with the same m_c. We will scan values of ϕ between 0.5 and 0.85.

We start by looking at how the ordering properties are affected by hydrodynamics.

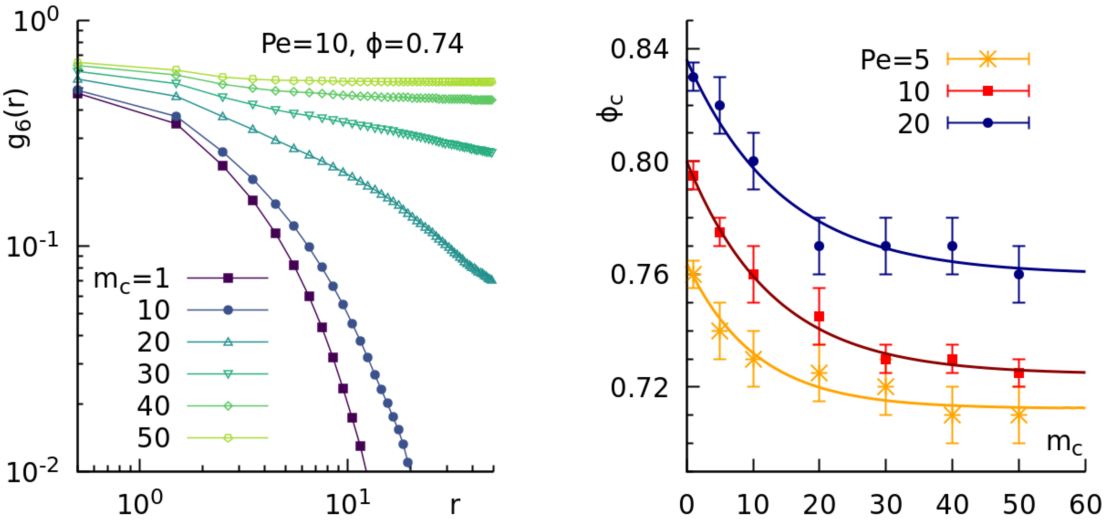

Figure 4.3: **Inertial effects on the Liquid-Hexatic transition**. On the left panel, orientational correlation functions, $g_6(r)$, at fixed $\mathrm{Pe} = 10$ and $\phi = 0.74$ for different values of the mass of the particles given in the keys. On the right panel, the liquid-Hexatic critical density, ϕ_c, at fixed $\mathrm{Pe} = 10$, as a function of the mass of the colloids m_c. The solid line is a fit of the data using the function $\phi_c(m_c) = a + be^{-m_c/c}$, with parameters $a = 0.71$, $b = 0.05$, $c = 10.37$ for $\mathrm{Pe} = 5$; $a = 0.72$, $b = 0.08$, $c = 12.92$ for $\mathrm{Pe} = 10$; and $a = 0.76$, $b = 0.08$, $c = 14.30$ for $\mathrm{Pe} = 20$. The error bars correspond to the gap $\Delta\phi$ between the densities scanned in the simulations for each value of the mass m_c.

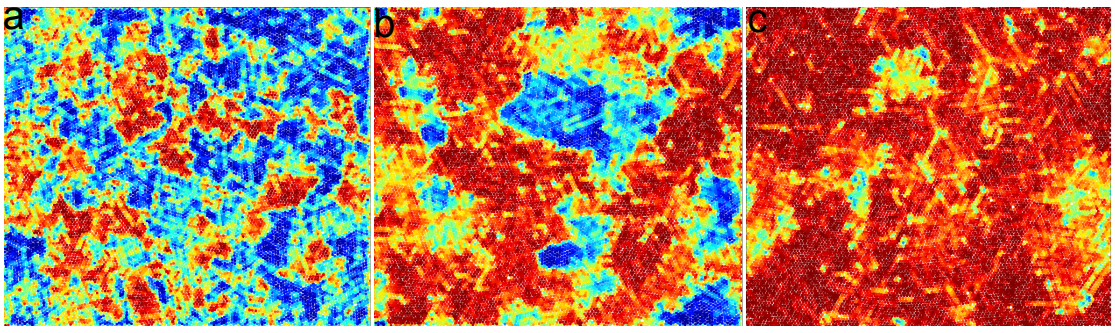

Figure 4.4: **Hexatic order parameter color map in the AHP model (a)-(c)** Color maps of the local hexatic order parameter, $\psi_{6,j}$, projected onto the direction of the system's global average, $\mathbf{\Psi} = 1/N \sum_j \psi_{6,j}$, for $\mathrm{Pe} = 10$ and $m_c = 44$, with $\phi = 0.78, 0.8, 0.81$ from left to right, for a system of size $L = 128\sigma_c$. The color code is the same as the one in Fig. 4.1. The values of global hexatic parameter $\psi_6 = \frac{1}{N}|\sum_i^N \psi_{6,i}|$ are $\psi_6 = 0.07, 0.23, 0.70$, respectively (see Fig. 4.6).

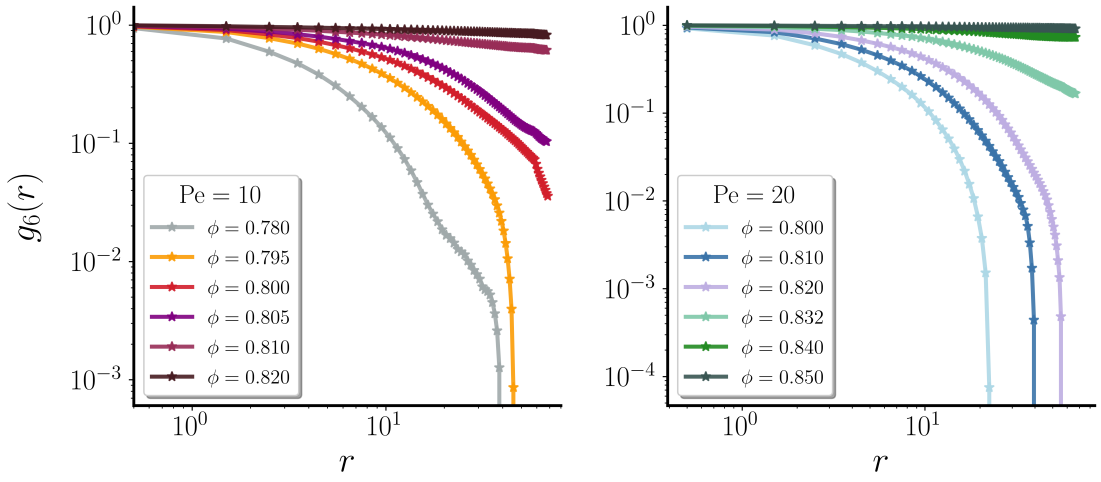

Figure 4.5: **Hexatic order correlation function for the AHP model. (a)-(b)** Hexatic order correlation function $g_6(r)$ at $\mathrm{Pe} = 10$ (d) and $\mathrm{Pe} = 20$ (e) for different global packing fractions given in the keys and $m_c = 44$.

Fig.4.4(a)-(c) show, for three different densities at $\mathrm{Pe} = 10$, the color map of the local hexatic parameter $\psi_{6,j}$ projected onto its average value. In panel (a) ($\phi = 0.78$) we do not observe the appearance of macroscopic hexatic domains, but locally we still observe small orientationally ordered regions. These regions appear to become larger upon increasing the density (panel (b), $\phi = 0.8$), although global ordering is not observed. At $\phi = 0.81$, panel (c), a single fully hexatically ordered system is observed. Thus, also AHP present a transition between liquid and hexatic phases. Fig. 4.5 shows the hexatic correlation functions varying the density for $\mathrm{Pe} = 10, 20$, to be compared with the results presented in Fig. 4.2 for the ABP system. For both values of activity, we find that the hexatic order correlation function shift from an exponential decay to a power-law decay at substantially higher values of packing fraction ϕ. More precisely the transition is located at $\phi_c \approx 0.805 \pm 0.01$ for $Pe = 10$, and $\phi_c \approx 0.840 \pm 0.01$ for $Pe = 20$.

The increase in value of the transition density ϕ_c with respect to the ABP model suggests that the addition of hydrodynamic interactions has a disordering net effect regarding the global orientational order. This is opposite to the effect of inertia, which instead promotes hexatic ordering. Indeed, if we measure the average global hexatic parameter $\psi_6 = \frac{1}{N}|\sum_i^N \psi_{6,i}|$ as a function of the global packing fraction ϕ (Fig. 4.6), we find that the liquid-hexatic transition is significantly shifted. Note that both curves converge to almost the same values for very high densities, suggesting that for densely packed systems hydrodynamic does not disrupt the ordering properties of colloids. We also checked that in the absence of activity, the transition density values that limit the coexistence region of the liquid-hexatic transition of passive colloids [DDS$^+$18] are not affected by the presence of hydrodynamic interactions. However, hydrodynamics produces other relevant effects which will be now discussed.

We now want to better understand the behavior and the role of the fluid velocity field, which for AHP can be locally organized, while the ABP model has no such feature, and relies only on hard-core repulsion. Thus, we will have a deeper look into the velocity field of AHP, and if it can trigger a coherent motion of small clusters of

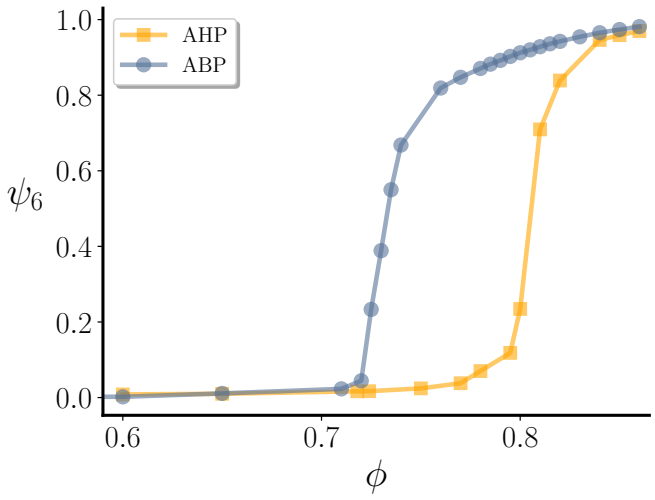

Figure 4.6: **Liquid-Hexatic transition in the ABP and AHP model.** Global hexatic parameter as a function of the global packing fraction for $\mathrm{Pe} = 10$ and $m_c = 44$,. The orange and blue curves correspond to simulations with and without hydrodynamics, respectively, for active colloids with the same mass.

particles.

Fig. 4.7 shows the coarse-grained steady-state velocity fields of the fluid, $\mathbf{v}(\mathbf{r})$ (panels d-f) along with associated snapshots of the configurations colored according to the hexatic parameter (panels a-c), for AHP with $\mathrm{Pe} = 10$ and three different values of packing fraction ϕ. Coarse-grained velocity fields of the fluid are realized by averaging the velocity of fluid particles inside blocks of size $4\sigma_c = 20\sigma_s$ (such large coarse-graining cells are chosen for the sake of visualization; similar profiles can be obtained with smaller cells). The first density, $\phi = 0.60$ (panels (a), (d)), is characterized by the absence of any orientational order. At the same time, however, its corresponding velocity field presents the formation of vortexes along with regions where flow is both not correlated and lower in magnitude. The associated velocity field for the active colloids (not shown) has a matching profile, while the local average direction of the active force is random, and thus not coherent with the velocity field.

Fig.4.7b,e show instead a larger density $\phi = 0.80$. We observe, here, a case close to the hexatic transition point, with locally formed fluctuating hexatic domains with their typical size remaining stationary over time. Along with these clusters, the flow becomes more coherent than at $\phi = 0.60$, with fluid and colloids having again a similar velocity field. Again, we do not observe a local average direction of the active force coherent with the flow field. The same behaviour becomes even more pronounced upon increasing the density ($\phi = 0.860$ panels (c) and (f)), where the system is fully orientationally ordered. In this case, the associated flow field becomes an unidirected self-sustained flow, with particles moving typically on the same direction, and with the global direction of the flow slowly changing over time. Interestingly, this behaviour is similar to travelling bands occurring in Vicsek-like models [TZ12, MGLDGP18], where an additional alignment interaction of active force directions is introduced, which allows particles to move coherently. Velocity correlations between particles have also been found in systems of ABP with different persistence times [CMP20a, CMM$^+$20, MCP21, CM21b], flowing crystals made of spontaneously aligning self-propelled hard

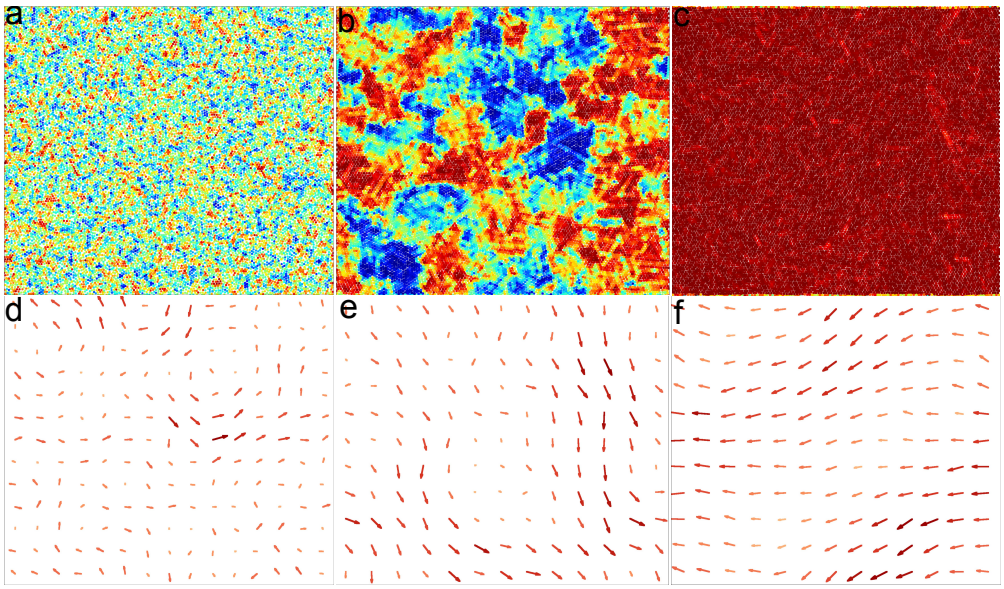

Figure 4.7: **Self-sustained active flow. (a)-(c)** Color maps of the local hexatic order parameter for $\mathrm{Pe} = 10$ and $\phi = 0.60, 0.80, 0.86$, respectively. Panels **(d)-(f)** show the corresponding steady-state fluid velocity field. The color code is the same as the one in Fig. 4.1.

disks [BSD18] and self-sustained spontaneous flows in active gels [CGL$^+$19, NCA$^+$19, GBC$^+$21].

We do not have at the moment a full theoretical understanding of the emergence of coherent motion, which occurs even when there is no orientational ordering. We can only try to interpret the phenomenology in the following way: the self-propulsion force of colloids continuously injects energy into the fluid, setting it into motion. Fluid particles can later self-organize their motion in a coherent form, and drag colloids along their direction of motion, which is not necessarily the same direction of the active force of each particle.

A quantitative measure of this transition to undirected self-sustained flow, as a synergetic effect of self-propulsion and hydrodynamic interactions, can be obtained by measuring the spatial velocity correlation function for the fluid velocity:

$$C_{\mathrm{v}}(\mathbf{r}) = \frac{\langle \mathbf{v}(\mathbf{r})\mathbf{v}(\mathbf{0})\rangle}{\langle \mathbf{v}(\mathbf{0})^2\rangle} \ . \tag{4.8}$$

Fig. 4.8 shows $C_{\mathrm{v}}(\mathbf{r})$ for different values of ϕ, for $Pe = 10$. For low values of ϕ (see e.g. $\phi = 0.600$) the curve shows an exponential decay. This corresponds to the case shown in Fig. 4.7(d), characterized by the presence of isolated vortexes. When we increase the density, we observe that the velocity correlation has a slower decay or a longer correlation length. Above density $\phi \simeq 0.730$, the correlation becomes almost constant. We note that the transition in the velocity correlations between exponential and algebraic decay does not manifest itself at the liquid-hexatic transition, since the latter appears at higher values of ϕ. In the inset of Fig. 4.8 the velocity correlation function for ABP in the hexatic phase ($Pe = 10$ and $\phi = 0.760$) is also shown for comparison. It shortly decays to zero, while for AHP, even in the liquid case (yellow curve), the decay is much slower.

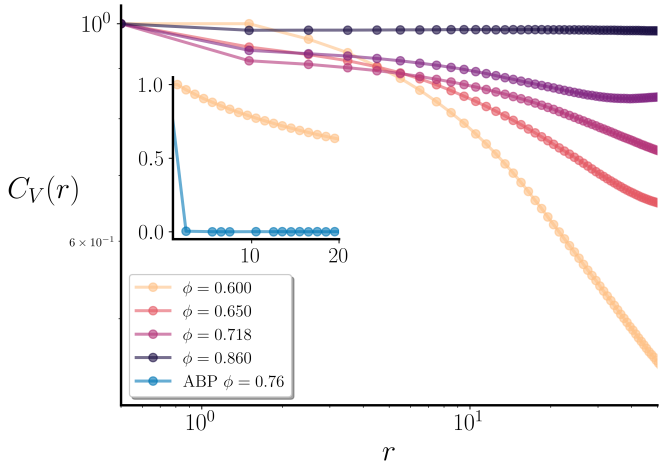

Figure 4.8: **Spatial velocity correlations.** Spatial velocity correlation functions $C_{\mathrm{v}}(r)$, for different values of ϕ, for $\mathrm{Pe} = 10$. In the inset, the velocity correlation function of ABP at $Pe = 10$ and $\phi = 0.760$ is compared with $\phi = 0.60$ for AHP at the same Pe.

As a last check, we switched off/on the hydrodynamics by just removing or adding the solvent particles and adding or removing the Langevin friction and noise terms in the colloids equation of motion (1.8), respectively. This enables us to check if a stationary AHP configuration is naturally able to relax to a stationary conformation of the ABP when hydrodynamics is switched off. We choose $Pe = 10$ and $\phi = 0.795$, a density where the system is hexatically disordered/ordered with/without hydrodynamics. The results are shown in Fig. 4.9. We start with AHP in a fully ordered configuration; after an equilibration time of 10^4 simulation time units, the system forms fluctuating ordered domains which change over time but do not grow (panel (a)). We then turn off hydrodynamics, and the system gradually sets after $t = 10^5$ simulation time units to an almost fully hexatically ordered conformation (panel (b)). The corresponding colloids velocity field is shown in panels (c)-(d). Note that the configuration is still not fully ordered only due to the large time required to relax to the fully ordered state; however, we observe that the global hexatic parameter is steadily growing over time. Switching on hydrodynamics again the system returns to the configuration shown in Fig. 4.9(a).

We have studied with extensive simulations the role of inertia and hydrodynamics in active colloids and showed how they affect the liquid-hexatic transition in an intermediate activity regime in which MIPS does not occur yet ($Pe = 10, 20$). Regarding the role of inertia, we have characterized the ABP by changing their mass, while maintaining the same Pe and D_θ, so that we have a non-trivial interplay between the inertial time and the persistence time $t_p = 1/D_\theta$. We showed that the critical density of the transition is shifted to a lower density upon increasing the colloid mass. This critical density is close to the one found at $Pe = 0$, suggesting that inertia has an orientational ordering effect on the system bringing the system closer to equilibrium behaviour and counteracting the disordering role of self-propulsion.

When hydrodynamic interactions are taken into account, we found instead that the liquid-hexatic transition moves towards higher values of packing fraction ϕ, thus sug-

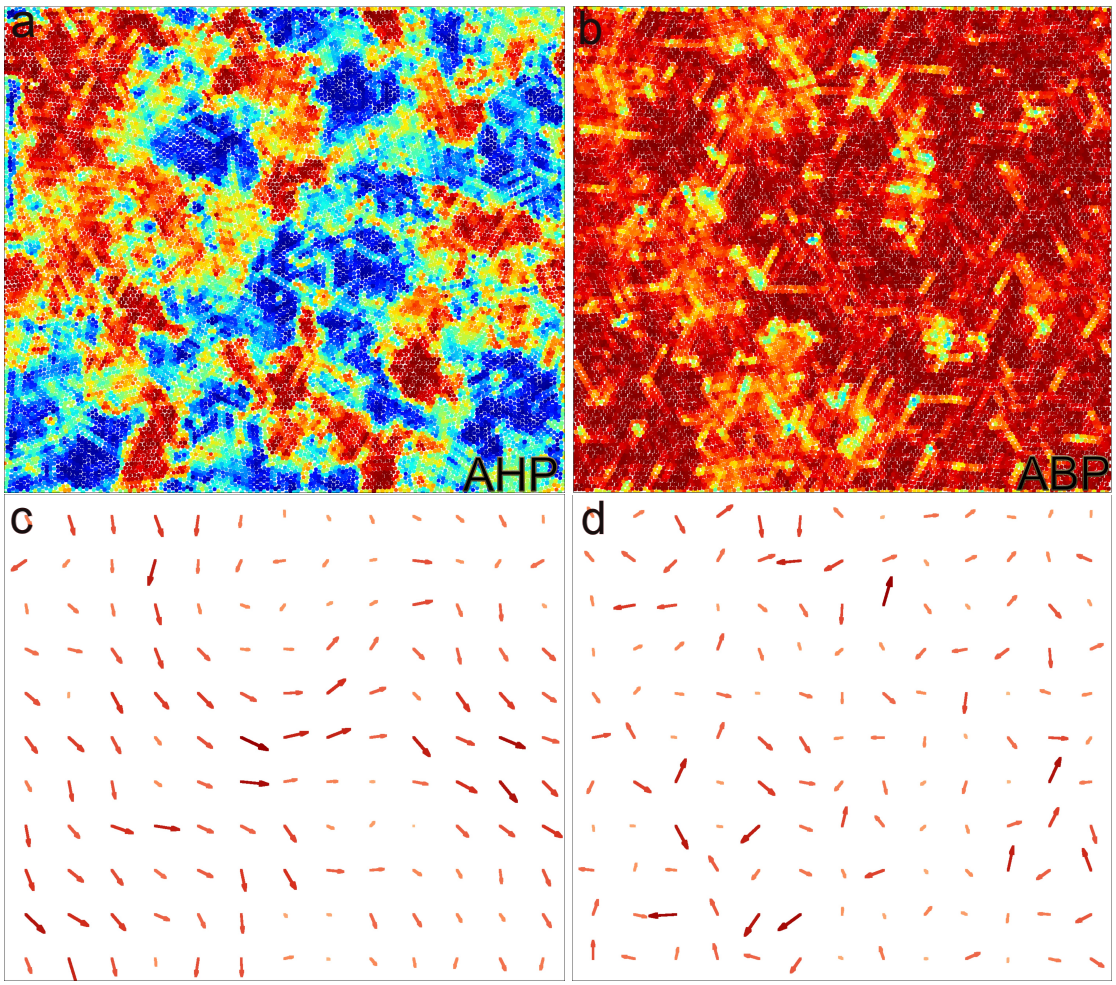

Figure 4.9: **Switch between ABP and AHP model.** (a)-(b) Snapshots of the system at different times $t = 10^4, 10^5$ of the local hexatic order parameter, at $\mathrm{Pe} = 10$ and $\phi = 0.795$, before (panel (a)) and after (panel (b)) switching off hydrodynamics. The corresponding colloid velocity fields are shown in panels (c)-(d).

gesting that hydrodynamics has a net effect of orientationally disordering the system.

We also analyzed the fluid velocity field of AHP, and found at $Pe = 10$ two results: i) the formation below $\phi \approx 0.72$ of small correlated velocity field regions, characterized by the presence of vortices, that are not associated to any local orientational ordering; ii) the arisal above $\phi \approx 0.720$ of a self sustained motion, with the fluid particles moving in one direction. This change in behavior has been characterized by measuring the spatial velocity correlation which was found to change from an exponential to an algebraic decay.

5

Aggregation of Anisotropic Active Particles

In this chapter, we focus on the second topic of the PhD project: the study of anisotropic (elongated) active particles. These particles are relevant to model both biological systems (e.g., bacteria) and artificial realizations of active matter. We investigate the aggregation phenomena and the collective dynamics of these particles, using a simple but effective model: the Active Brownian Dumbbell Model (ABD). We also compare the results with those obtained in Chapter 3 for isotropic active particles.

The chapter is organized as follows. In Section 2.1, we introduce the reference model (in this work) for anisotropic active particles, the active dumbbells, and review some of their main features and properties, as reported in the recent literature. In Section 2.2, we analyze the dynamics of aggregation of active dumbbells in two dimensions and study the properties of the resulting active clusters. In Section 2.3, we extend the analysis to three dimensions and explore the effects of different parameters on the aggregation and dynamics of active dumbbells.

5.1 Anisotropic Active Particles

The behavior of anisotropic active particles is generically richer than that of their isotropic counterparts [MBSG22]. Some specific features of these systems which have been discussed in the recent literature are the following. (i) The pressure calculated from mechanical, virial, and thermodynamic routes do not necessarily coincide. In the mechanical version, torque interaction between the constituents and the confinement may render this *active pressure* a boundary-dependent property [SSW$^+$15b, FKS$^+$18, PCY21]. Moreover, the pressure exerted by an under-damped dumbbell system depends on the damping coefficient [JB16, Joy17]. (ii) Local nematic and even polar ordering can set in. The axial form of the dumbbells allows for the alignment of head-tail dumbbell orientations [SMGO14, PDC$^+$18]. (iii) At sufficiently strong activity dumbbells aggregate and the clusters exhibit coherent and long-lived rotations due to steric interactions which essentially quench the dumbbell's polarisation within the dense droplets. On the

experimental side, colloidal particles with non-convex shapes have been proposed to serve as the building blocks for active colloidal molecules with a dynamical function [LÏ8, MVC18, RCD$^+$].

One of the most simple models used to describe active anisotropic particles is the Active Dumbbell Model (ADB). Each dumbbell is a diatomic molecule, with two identical disks rigidly connected (a dimer). The distance between the two centres of the disks forming each dumbbell is fixed. The dumbbells are thus identified by a tail and a head, which remain the same throughout the system's evolution, and the active force acts along this direction (see [SLSV17] for variations around these choices).

Active Brownian Particles (ABP) placed in two-dimensional spaces and interacting repulsively undergo Motility Induced Phase Separation (MIPS) [CT15b, GMST15b, DLS$^+$18b] when the activity is larger than a critical value. Two-dimensional rigid and repulsive dumbbell systems, instead, phase separate all the way down to zero activity [CDGS17a] when the active force acts along their main axis. Shape and force anisotropy can combine to produce critical densities both lower and higher than those of disks [MBSG22].

Note that dumbbells are not the only way to obtain anisotropic particles; another is for example rods. However, differently from disks and dumbbells, rods can slide past each other and do not undergo MIPS [PDB06a, GPBC10, YMG10, vDRvRD19a, BGHP20].

The Active Dumbbell Model

We consider a two-dimensional system of N dumbbells. As anticipated, each dumbbell is formed by two identical disks (for a total of $2N$), each of one with a diameter σ_d and mass m_d. The distance between the two centres of the disks forming each dumbbell is equal to σ_d. The disks, labelled by $i = 1, \dots, 2N$ with center position $\mathbf{r}_i$, follow the Langevin equation of motion

$$m_\mathrm{d}\ddot{\mathbf{r}}_i = -\gamma_\mathrm{d}\dot{\mathbf{r}}_i - \boldsymbol{\nabla}_i U + \mathbf{f}_\mathrm{act} + \sqrt{2k_BT\gamma_\mathrm{d}}\,\boldsymbol{\eta}_i \,, \tag{5.1}$$

where $\boldsymbol{\nabla}_i = \partial_{\mathbf{r}_i}$, γ_d and T are the friction coefficient and the temperature of the thermal bath, respectively, and k_B is the Boltzmann constant. The last term in the right-hand-side is proportional to $\boldsymbol{\eta}_i$, a time-dependent Gaussian white noise acting on each disk, with vanishing mean, $\langle \eta_{ia}(t)\rangle = 0$, and independent delta correlations, $\langle \eta_{ia}(t_1)\eta_{jb}(t_2)\rangle = \delta_{ij}\delta_{ab}\delta(t_1 - t_2)$, with $a, b = 1, 2$ the label for the two spatial coordinates. Henceforth we will indicate the noise averages with angular brackets $\langle \dots \rangle$. We note that the thermal noise affects the translational and rotational degrees of freedom of the dumbbells.

We use the Mie internal potential energy introduced in Section 1.3. The potential is truncated at its minimum ($r = 2^{1/n}\sigma$) so that it is purely repulsive and with exponent $n = 32$ to be as close as possible to the hard disk limit without losing computational efficiency. For further numerical details, see Appendix A.1.

The term $\mathbf{f}_\mathrm{act}$ in Eq. (5.1) represents the active force. It acts on the tail-to-head direction of each dumbbell and has constant modulus f_act. Differently from ABP models, dumbbells do not need an additional force in order to randomly rotate $\mathbf{f}_\mathrm{act}$ in the two-dimensional space. In fact, the thermal noises acting on the two disks forming each dumbbell are independent, and their combination allows for the dumbbell's effective diffusive rotation.

Also here, we focus on the system's behavior dependence on two control parameters: the surface fraction covered by the beads,

$$\phi = \frac{N\pi\sigma_{\rm d}^2}{2L^2} \ , \tag{5.2}$$

with L the linear size of the square box which contains the molecules, and the Péclet number,

$$\mathrm{Pe} = \frac{2\sigma_{\rm d} f_{\rm act}}{k_B T} \ , \tag{5.3}$$

Note that, differently from ABPs, the definition of Péclet number contains a factor 2 that accounts for the fact the force is applied to each bead of the dummbbell.

Phase diagram

The phase-separated region of the phase diagram was established in [CDGS17a, PDC$^+$18, DLS$^+$19] under similar conditions and reproduced in Fig. 5.1. The dimers' beads that we consider have the same symmetry as disks do and, therefore, their perfect crystalline order is also hexagonal, with closed packing fraction $\phi_{\rm cp} \sim 0.9$, shown with a dashed horizontal line. The phases are represented with different colors and they correspond to the gas/liquid (white), hexatic (blue), and phase-separated regions (grey). The colour code (online) will be the same in all figures. We note that differently from the ABP system, in the dumbbell's one, the co-existence region close to Pe = 0 extends continuously to large Pe. There is no critical ending point for a Motility-Induced Separated Phase (MIPS). The transition at the lower critical line is discontinuous all along the curve.

The active dumbbell liquid.

The stationary dynamics of repulsive dumbbells at not too high densities, so that the samples remain homogeneous, were studied in quite some detail [SGL$^+$14, CGS15]. In these papers, the mean-square displacement, linear response function, and deviation from the equilibrium fluctuation-dissipation theorem were characterized as a function of activity strength, packing fraction, and temperature. The dynamics of passive thermal (in contact with the thermal bath) and athermal (disconnected from it) tracers interacting repulsively with the elements of active dumbbells' dilute baths were analyzed in [SCG16]. The point of this paper was to show for which parameters the dynamics of the tracers represent faithfully the ones of the dumbbells.

The phase separated regimes.

Rigid dumbbells cannot freely (at no energy cost) rotate within a crystallite without affecting its underlying structure. More precisely, in the clusters and even at their surface, the dumbbells get stuck and this facilitates phase separation. Thus, aggregates made of dumbbells behave quite differently from those made of disks, when particle self-propulsion is switched on. In consequence, clusters not only translate but also rotate with, on average, an angular velocity that decays proportionally to their inverse size [SLVC$^+$12a, THVC16, PDC$^+$18] but also depends on their shape.

In the phase separated region of the phase diagram, the dilute phase has no order and behaves as an active liquid or gas. Instead, the dense phase has local orientational order, in the sense that the modulus of the local hexatic order parameter takes a large

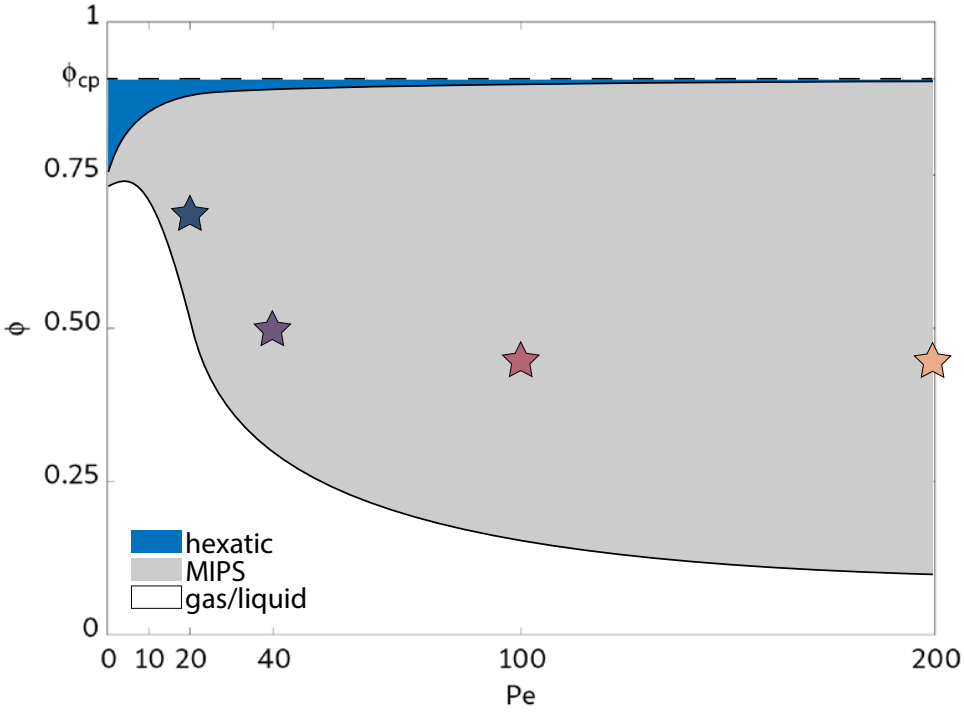

Figure 5.1: The Pe $-$ ϕ **phase diagram** of the dumbbell system [CDGS17a]. The stars locate parameters on the curve of a 50:50 mixture, i.e., in which the surface occupied by the dense phase is half the total one. Most of the results that we present in the rest of the paper are for these parameters.

value [CDGS17a, PDC$^+$18]. The axial form of the molecules allows for the development of polar order, which turns out to change with Pe: no polarization is found at small Pe, the dumbbells within the clusters orient along the radial direction for intermediate Pe, and the clusters show a spiralling structure at large Pe [PDC$^+$18].

Similarly to what was measured for Active Brownian Particle systems within MIPS [PCGS20a], the motion and linear response of the dumbbells confined to clusters or freely displacing in the dilute phase are expected to be very different.

The cluster's motion.

At sufficiently large Pe the clusters not only translate but can also rotate [SMGO14, PDC$^+$18]. Each particle exerts a local torque which is balanced by the drag on the cluster, sustaining rotations. For Pe $\geq$ 50, the spontaneously formed rotating clusters turn around their center of mass with an angular velocity that is proportional to the inverse of their radii.

A careful analysis of this kind of motion was carried out in [PDC$^+$18] were, in particular, the dependence of the enstrophy on Pe was compared to the one of the kinetic energy. While the latter measures the strength of flow in the system, the former measures the presence of vortices in the velocity field. For high values of the activity the probability distribution function of the enstrophy has a multi-peak structure. These peaks progressively disappear for decreasing values of Pe. Below Pe $\sim$ 40 the probability of finding non-vanishing enstrophy is almost zero.

Other aspects.

Other aspects of two dimensional dumbbell models were addressed in the literature. Dilute suspensions of active Brownian dumbbells interacting with competing short attractive and long range repulsive potentials, a potential that mimics the interaction of weakly charged particles in the presence of depletants, for different degrees of particle activity were studied in [THVC16]. The dynamics of flexible active Brownian dumbbells with and without shear flow was addressed in [Win16, CGW20]. Other studies include tests of Green-Kubo relations in a chiral active dumbbell fluid [HKEM20] and the analysis of similarities and differences between active and passive glasses made of dumbbell molecules [MBC$^+$17, NMB$^+$18]. The influence of correlations in the propulsion direction was studied in [SLSV17], where systems of dumbbells joined by an elastic string, with forcing in uncorrelated direction, or correlated direction but not necessarily the axial one, were simulated. In the former case phase separation is pushed to higher values of Pe since part of the propulsion energy is spent in stretching the elastic bond between the disks.

We close this introduction by mentioning that Eq. (5.1) can be straightforwardly generalized in three dimensions. The latter model is well suited for modelling systems often encountered in real-life settings, such as bacteria colonies. We will study the phase diagram of a (rather dilute) active attractive dumbbell system in $3d$ space in Section 5.3.

5.2 Aggregation Kinetics and Cluster Dynamics in two-dimensional Active Dumbbell Systems

Having introduced the Active Dumbbell Model in two dimensions, we focus on studying, with numerical methods, the approach to stationarity of such system quenching it into the MIPS region, such that an initial state tends to phase separate and form clusters [SMGO14, CDGS17a, PDC$^+$18]. Indeed, although quite a lot is known about the dynamics of active dumbbell systems in their steady states, the kinetics of phase separation has been much less considered. Compared to previous studies of growth in Active Brownian Dumbbell (ABD) systems, we use much larger system sizes, which let us to properly control the finite size effects, and we run the simulations over much longer time scales, which allow us to explore in detail the scaling regime. Moreover, we will compare the dynamic behaviour of this system to the one of Active Brownian Particles (ABP) which has been already analysed in Chapter 3.

This section is divided into three main parts. In the first part, we analyse the growth of the dense component and in the second one its internal orientational order. In the third part, we investigate the motion of active clusters and develop a simple mechanical model that rationalizes it.

Growth of dense phase

We start discussing the way in which the dense component increases its size from an initial random configuration. We also study the organization of the internal structure of this dense component. More precisely, we focus on the local hexatic (orientational) order.

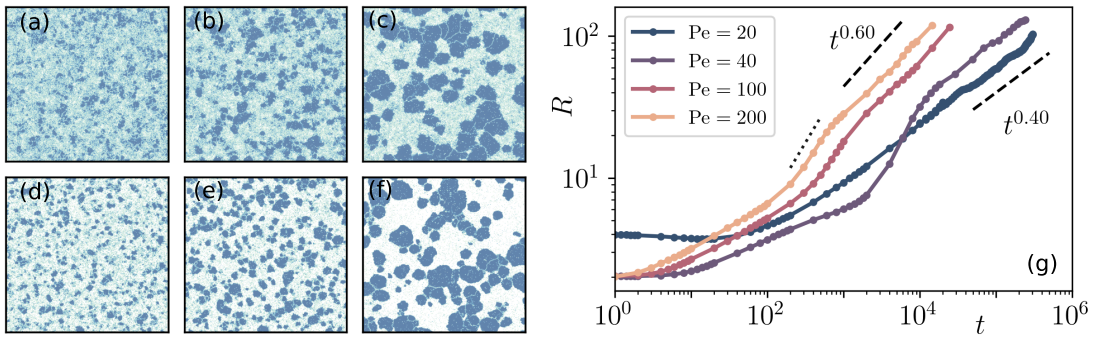

Figure 5.2: **The phase separation process.** (a)-(f) Snapshots of the systems at Pe = 20 (first row) and Pe = 100 (second row), at times such that the average size of the dense component is the same (corresponding to an average density, respectively, $\phi = 0.70$ and 0.50). The instants at which the images were taken fall in different regimes: $t = 2 \times 10^3$ for Pe = 20 (a) and 5×10^2 for Pe = 100 (d) are very short times, 6×10^3 (b) and 10^3 (e) fall in the rapid growth regime, finally 10^5 (c) and 8×10^3 (f) are in the scaling regime. Light/dark blue color regions correspond to low/high local density regions. (g) Grow length as a function of time for parameters corresponding to the stars in Fig. 5.1: Pe = 20, 40, 100, 200 and the global packing fractions $\phi = 0.70,\ 0.50,\ 0.50,\ 0.450$, respectively, averaged over 5 independent runs. The short dotted segment represents the power 1 which is very close to the intermediate algebraic rapid growth. The dashed segments show the power law fits for the two extreme cases, Pe = 20 and Pe = 200, in the scaling regime.

Growing length and dynamical regimes

In Fig. 5.2(a)-(f) we show snapshots of the evolution of a dumbbells system at Pe = 20 and 100 starting from a random conformation, in a phase-diagram region where the dense phase occupies 50% of the surface at steady-state (long times). The time dependence of the typical length of the dense component $R(t)$ is calculated from the inverse first moment

$$R(t) = \frac{\pi \int dk\ S(k,t)}{\int dk\ k\, S(k,t)} \tag{5.4}$$

of the spherically averaged disks centers' structure factor

$$S(\mathbf{k},t) = \frac{1}{2N} \sum_{i}^{2N} \sum_{j}^{2N} e^{i\mathbf{k}\cdot(\mathbf{r}_i(t)-\mathbf{r}_j(t))}\ . \tag{5.5}$$

The radially symmetric $S(k,t)$ is the average over the reciprocal lattice vectors inside a spherical shell of thickness $2\pi/L$. This growing length, $R(t)$, for four Pe - ϕ pairs for which there is a 50:50 surface occupied by the dense and dilute phases in the steady state is plotted in Fig. 5.2(g). We will later discuss in Fig. 5.4 the structure factor for the same Pe - ϕ parameters. We also considered the structure factor of the dumbbells' center of mass finding similar results (not shown).

We are able to distinguish three dynamic regimes in $R(t)$ curves of Fig. 5.2(g) for Pe ≥ 40, corresponding to different growth stages of the dense region. For very short times (first regime) we see multi-nucleation of many small dense droplets, see Fig. 5.2(d). In the second regime there is a rapid growth of the typical length, corresponding to the growth of some droplets by condensation and aggregation, and evaporation of other

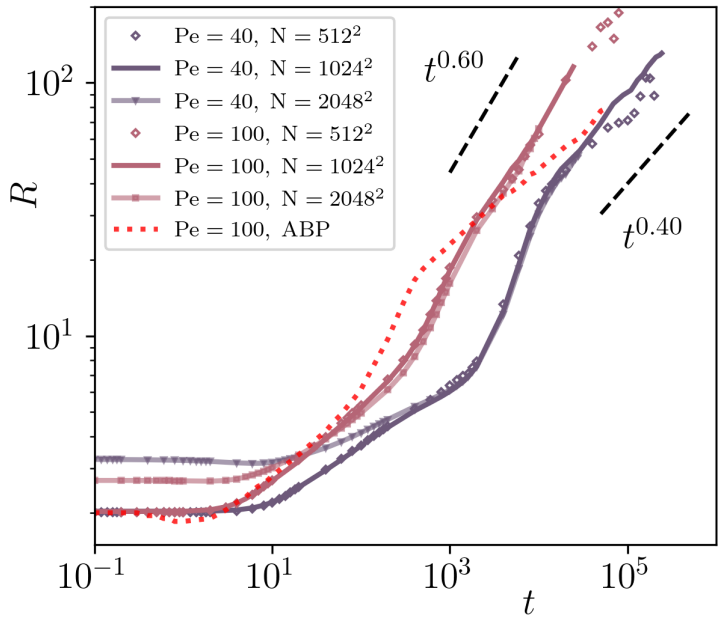

Figure 5.3: **Finite size dependence of the growing length.** Comparison between dumbbells' data for $N = 512^2/2$, $N = 1024^2/2$ and $N = 2048^2/2$ at Pe = 40 (blue solid lines and datapoints below) and Pe = 100 (purple solid lines and datapoints above), and the ABP's growing length at Pe = 100 with $N = 1024^2/2$ (dotted red line). Densities are the same as those considered in Fig. 5.2.

droplets, see Fig. 5.2(e) and movies M1 and M2 [1]. In the third and final regime clusters grow using as main aggregation mechanism translation, collision and merging, eventually forming irregular and elongated structures (Fig. 5.2(f)), which will be discussed later in Sec. 5.2. We will prove in Sec. 5.2 that this is a coarsening scaling regime. For now we will reference to it with such name.

We checked that the curves of $R(t)$ are not affected by significant finite size effects, by considering larger system sizes of $N = 512^2/2, 1024^2/2$ and $2048^2/2$ dumbbells, see Fig. 5.3. Only at $N = 512^2/2$, the data become noisier for the small Pe and deviations from the asymptotic behaviour are visible at long times. At even later times, the size of the dense phase saturates to a value that is proportional to the linear system size as will be clear from the analysis of the averaged gyration radius of the dense clusters, displayed in Fig. 5.6.

For the weakest activity, Pe = 20, the behavior of $R(t)$ is quite different (Fig. 5.2(g)). The typical length enters directly the last algebraic growth, without an intermediate rapid growth. The difference between the behaviour at weak and strong activities can be traced back to the fact that, while the 50:50 curve at high Pe lies at relatively low packing fractions, $\phi \sim 0.5$, at low Pe this curve is at very high global densities, $\phi \sim 0.75$, and, moreover, the ϕ interval over which there is co-existence of dilute and dense phases is very narrow. The dumbbells are already quite packed initially and the density of the gas is also very high at low Pe. The global conditions are therefore quite different from the ones at high Pe. The difference between the high and low Pe behaviors can

[1] Movies of this section can be found at `www.dropbox.com/scl/fo/dhthjnhtpawy1xyr60k72/h?rlkey=3lpqd7e4zskm5hu2nb8ohoa8e&dl=0`

be appreciated from the snapshots in Fig. 5.2(a)-(c). They not only show the different initial conditions (compare Figs. 5.2(a) and (d), with average initial density $\phi = 0.50$ and $\phi = 0.70$, respectively), but also the fact that at late times (Figs. 5.2(c) and (f)) the density of the gas, determined by the lower limit of the phase-separated region of the phase diagram (Fig. 5.1) is much lower at high Pe than at low Pe.

In the last scaling regime, the typical length calculated from Eq. (5.4) grows algebraically,

$$R(t) \sim t^{1/z} \ , \tag{5.6}$$

with a dynamic exponent z that, for our numerical data, increases with decreasing Pe from roughly $z = 1.6$ at Pe = 200, to $z = 2.5$ at Pe = 20. One could expect the dynamic exponent to approach the standard value of conservative phase separation, $z = 3$, at Pe going to zero, but it is very hard to make reliable measurements at still lower Pe since the packing fractions with phase separation are very high ($\phi \gtrsim 0.77$, see Fig. 5.1). In all Pe $\neq 0$ cases that we studied, the growth is faster than for ABPs, see the red dotted curve also plotted in Fig. 5.3, where we found $z \sim 3$ for all Pe in the MIPS region of the phase diagram [CDL$^+$20a].

We recall that the growth of the dense component of the same active dumbbell model was first studied in Ref. [GLS14] . However, in that paper the system sizes considered were much smaller than the ones we consider here, and the separation of time scales (with a late scaling limit) was not established. Growing lengths of the order of the small box sizes used were quickly reached and only the second regime was observed, with a very fast power law growth with exponent $1/z \approx 0.9$. Indeed, this large power is similar to the one that we measure in the intermediate regime of rapid growth, see the dotted segment in Fig. 5.2(g).

Structure factor

We now analyze in more detail how the structure factor evolves in time during growth. The structure factors for two extreme values of Pe, Pe = 20 and Pe = 100, and densities of Fig. 5.2, are displayed in Fig. 5.4(a)-(b) at different times, from $t = 50$ to $t = 5 \times 10^4$. Before commenting the structure factor functions, we need to observe that while for the Pe = 20 case, at $t \sim 50$ the growth length $R(t)$ has already reached its asymptotic algebraic form (the scaling regime), for Pe = 100 the growth length is in the rapidly increasing intermediate regime and crosses over to the asymptotic algebraic one only at $t \gtrsim 10^3$ (Fig. 5.2(g)).

The structure factors in Fig. 5.4(a)-(b) have a very clear peak at a time-independent large wave-length, $k \sim 2\pi/\sigma_{\rm d}$ related to the short-distance crystalline structure of the dense phase. We also have the presence of time-independent secondary peaks at multiple frequency values $2\pi n/\sigma_{\rm d}$, with n integer. These peaks have a lower intensity than the one at $k \sim 2\pi/\sigma_{\rm d}$, and are also characteristic of the crystalline order.

More interesting is the low k peak which does depend on time, and moves towards smaller values as time increases. It is related to the progressive growth of the typical cluster size of the dense component.

The wave vector dependence, in between the first and second characteristic values, is algebraic $S(k,t) \sim k^{-a}$. For segregated systems with sharp and regular interfaces between the phases, the Porod law yields $a = d + 1$. For Pe = 20 we measure $a \sim 2.6$, possibly due to the fact that the high global density makes the interfaces be contami-

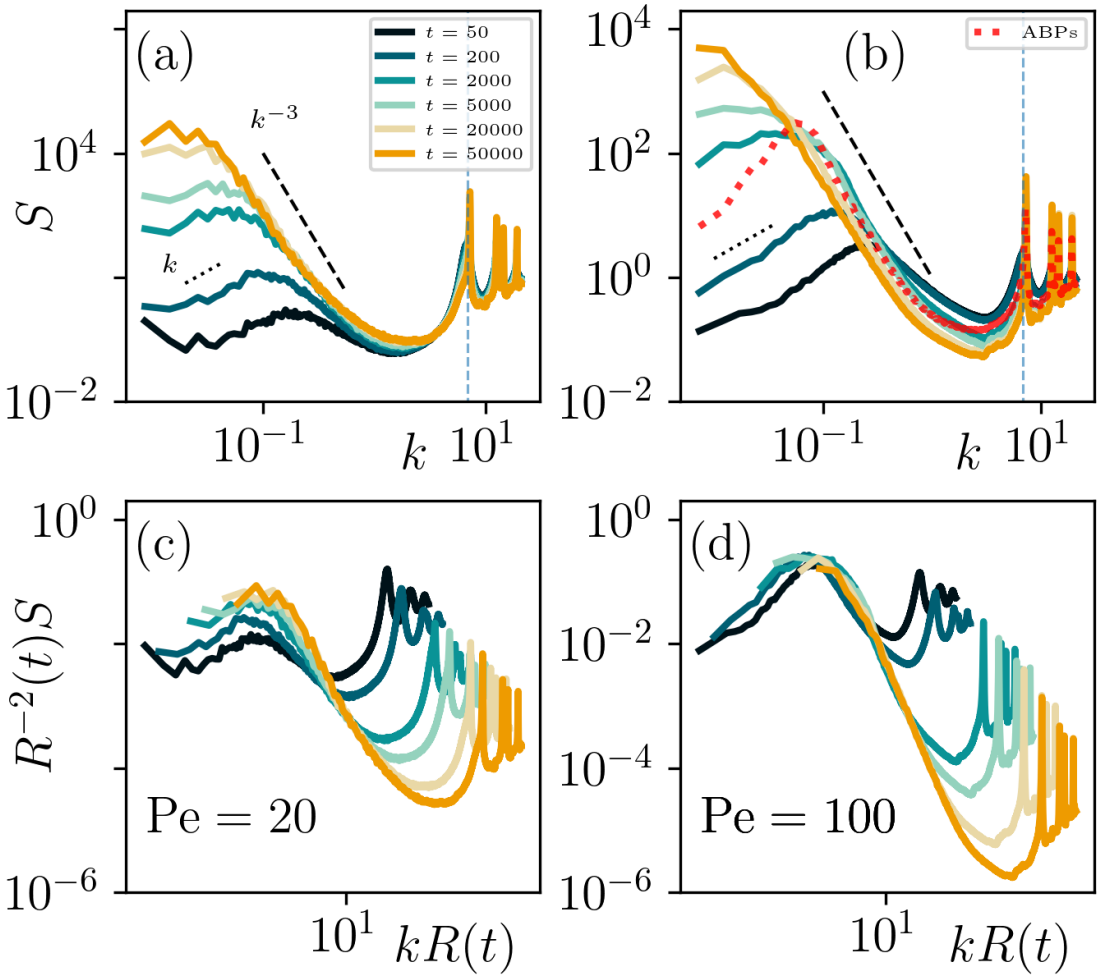

Figure 5.4: **The dynamic structure factor.** In the upper row, the wave vector dependence of the structure factor at different times given in the keys, for Pe = 20 (a) and Pe = 100 (b), with densities $\phi = 0.7$ and $\phi = 0.5$, respectively, which locate the system on the 50:50 line in the phase diagram. In the first two panels, the powers k^{-3} and k are indicated with dashed and dotted black lines, respectively, and the vertical blue dotted line represents the time-independent peak related to the crystal structure of the dense phase. The minimal wave vector due to the finite box is $k_{\min} \sim 0.006$, in the system with $N = 1024^2/2$ used here. The red dotted curve in (b) corresponds to the ABPs data. A fit of the Pe = 20 data would yield a weak deviation from Porod's law, k^{-a}, with $a \sim 2.6$. In the lower row, scaling plots according to Eq. (5.7) with $R(t)$ extracted from the numerical data (no fit assumed).

nated by nearby dumbbells of the gas. For Pe = 100, instead, the power is very close to the expected $a = 3$, see the dashed line in the figure, practically identical to the one measured for ABPs (red dotted curve) [CDL$^+$20a].

At strictly $k = 0$ the structure factor that we define should equal $2N + 1$. However, due to the finite size box, the minimal wave vector that we can access is $2\pi/L$ and, for the spherically averaged $S(k, t)$ a slightly bigger $k_{\min}$ guarantees a smoother result. This is the reason why the curves in Fig. 5.4 start from a larger value of k.

In the scaling regime, on the left of the first low k peak, $k \lesssim 2\pi/R(t)$, it is easy to spot a linear behavior for Pe = 100 of the structure factor as a function of k. For Pe = 20, instead, the structure factor appears flat. This is different from what was measured in ABP systems [CDL$^+$20a], where a k^2 behaviour was found, see the dotted red lines on the left in Fig. 5.4(b). The weak k behavior is related to the way in which the variance of the number of particles within a spherical shell σ_N^2 scales with its radius r. A weaker power would indicate less fluctuations, and we could associate this to the fact that the disks, being attached to another one to form the dumbbell, allow for less fluctuations in the molecular system. It is interesting to notice that a similar linear behaviour in the low-k regime is observed in hyperuniform fluids of active particles [LPN19].

The plots in Fig. 5.4(c)-(d) demonstrate that the data of Fig. 5.4(a)-(b) satisfy the dynamic scaling

$$S(k, t) = R^2(t)\ f(kR(t)) \tag{5.7}$$

in the asymptotic algebraic regime. Hence, this justifies naming "scaling regime" this time sector, with the length $R(t)$ already calculated from Eq. (5.4) (no fit assumed). Using the law in Eq. (5.6) would yield a similarly good scaling. We conclude that the scaling properties of $S(k, t)$ in the dumbbells sample are as good as for the ABP system.

Number and size of clusters

We now analyze more quantitatively the evolution of the number of clusters for sufficiently large Pe $\geq$ 40, and link it to the three dynamic regimes. The algorithm to identify clusters has been explained in Appendix A. Data are presented in Fig. 5.5 for Pe = $40, 100$ and 200 and the same densities as in Fig. 5.2. The vertical light lines delimit the three regimes found from the analysis of the growing length.

In the first rapidly nucleating regime, we observe that the number of clusters N_C grows fast until a maximum is reached. Afterwards, we observe a progressively rapid decay in N_C, corresponding to an intermediate algebraic growth phase where droplets grow through condensation and aggregation. When the scaling regime is reached, the decay achieves an algebraic form with an exponent $2/z$,

$$N_C \sim t^{-2/z}, \tag{5.8}$$

that is roughly consistent with the growth of the typical length $R \sim t^{1/z}$. The global form of these curves is the same as the one for ABPs, see Fig. 2(b) in [DLS$^+$18b].

Having identified the clusters, we can also measure their individual gyration radius as

$$R_G^\alpha(t) = \left[\frac{1}{N_\alpha}\sum_{i\in\alpha}(\mathbf{r}_i(t) - \mathbf{r}_{\rm cm}^\alpha(t))^2\right]^{1/2}, \tag{5.9}$$

with $\mathbf{r}_{\rm cm}^\alpha(t)$ the position of the center of mass of the αth cluster and N_α the number of beads in that cluster, and next average it over all $\alpha = 1, \ldots, N_C$ clusters. This gives

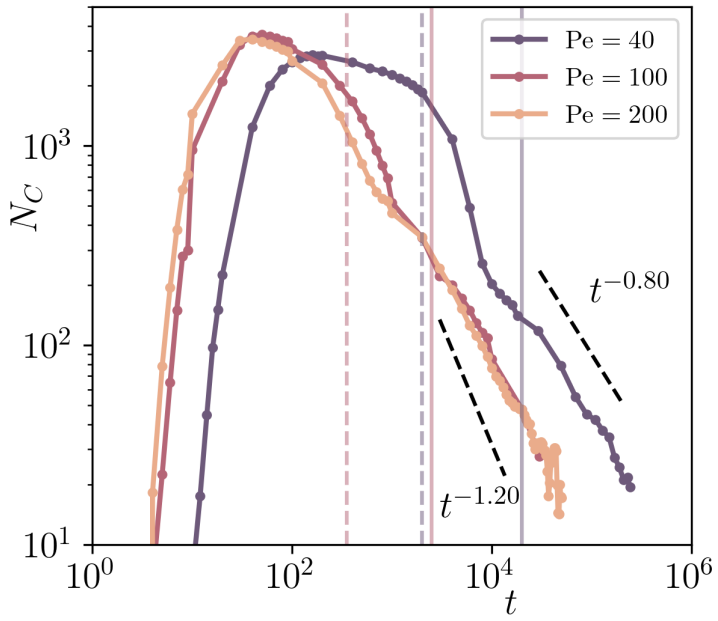

Figure 5.5: **The number of clusters** as a function of time for three Pe and the global densities of Fig. 5.2. The dashed lines are the algebraic decays $t^{-2/z}$, with $z \sim 1.67$ at Pe = 100, 200 and $z \sim 2.5$ for Pe = 40, the values extracted from the analysis of the structure factor. The vertical dashed and continuous lines indicate the transition to the fast-growing and the scaling regime, respectively, of the growing length for the two Pe = 40 and 200 (grey and orange lines) cases.

us another way to estimate the typical growing length of the dense component. We display these measurements in Fig. 5.6 (a), using different system sizes, all at the Pe = 100 and packing fraction of Fig 5.2. The curves, scaled by the system size L, increase monotonically in time, and have roughly the same behaviour as $R(t)$ measured from the structure factor for the same parameters (Figs. 5.3 and 5.6(b), the latter scaled by L). At sufficiently long times R_G, as well as $R(t)$, saturates to a size dependent value (which needs not be the same because of the slightly different definitions). Indeed, in the very long time limit, the dense phase approaches a finite fraction of the total system, that only depends on the ratio between the dense and the dilute phase area and indirectly on Pe and ϕ, and is represented in Fig. 5.6(a) by the horizontal dashed line.

Gas phase

Finally, in Fig. 5.7 we show the surface fraction occupied by the gas or dilute phase, ϕ_g, as a function of time, for the same Pe values and global packing fractions used in the previous plots. The vertical light lines are located at the limits of the three regimes, as found from the analysis of the growing length.

The first regime is characterized by a slow decrease of the density of the gas, due to the nucleation of small droplets, also suggested by the simultaneous increase of the number of clusters (Fig. 5.5) and in the development of a peak in the structure factor (Fig. 5.4). The second regime is characterized by a fast decrease of the gas density. As could be seen from the movies, this regime is characterized by the coalescence of the droplets, that also increase in size absorbing particles from the gaseous phase. The first

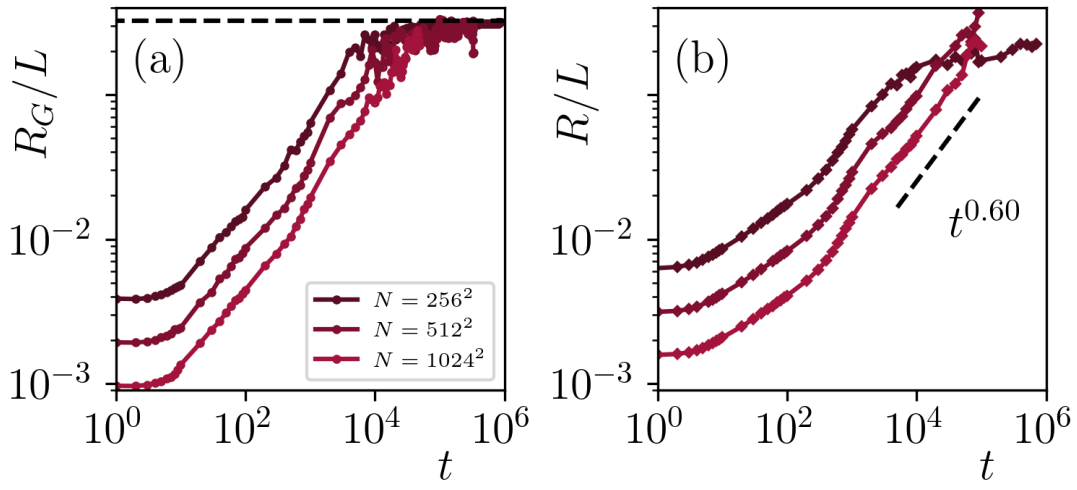

Figure 5.6: **Finite size dependence and saturation of the growing length.** (a) The averaged gyration radius of the clusters, normalized by the linear system size L, for systems with different numbers of dumbbells, all at Pe = 100 and same global density of Fig. 5.2. (b) The growing length of Fig. 5.3 normalized by the system size. The dashed line in (b) represents the growth law $t^{0.6}$, and the horizontal one in (a) is at $R_G/L \approx 0.33$, and indicates the saturation of the size of the dense component with system size.

two regimes have a similar behavior to the one of ABP systems, shown with a dotted red curve.

We note that, on the contrary with ABPs, there is still a decay of gas density in the scaling regime. Saturation is just beginning to manifest in the Pe = 100 case, whereas it has not been attained within the simulation times for Pe = 40.

Orientational order of the dense phase

We now quantify in more detail the internal organization of the dumbbells within the dense clusters during its growth. We focus here on the analysis of the dumbbells disks orientational order, as quantified by the local hexatic order parameter

$$\psi_{6j} = \frac{1}{N_j} \sum_{k \in \partial_j} e^{i6\theta_{jk}} \,, \tag{5.10}$$

with θ_{jk} the angle formed by the segment that connects the center of the jth disk and the one of its kth, out of N_j, nearest neighbors according to a Voronoi construction, and a reference, say horizontal, direction.

Large dense clusters can show a polycrystalline structure, *i.e.* be a mosaic of different hexatically ordered domains. Indeed, the clusters that aggregate do not necessarily share the same average direction of ψ_{6j}, and grain boundaries appear in the growing dense phase. These interfaces may heal and let the orientational order progressively grow or not. In order to identify these domains and measure their average size, R_H, we identify the hexatic domains according to the argument of ψ_{6j} or by the gradient of its modulus, coarse-grained over a small cell. The two methods give consistent results.

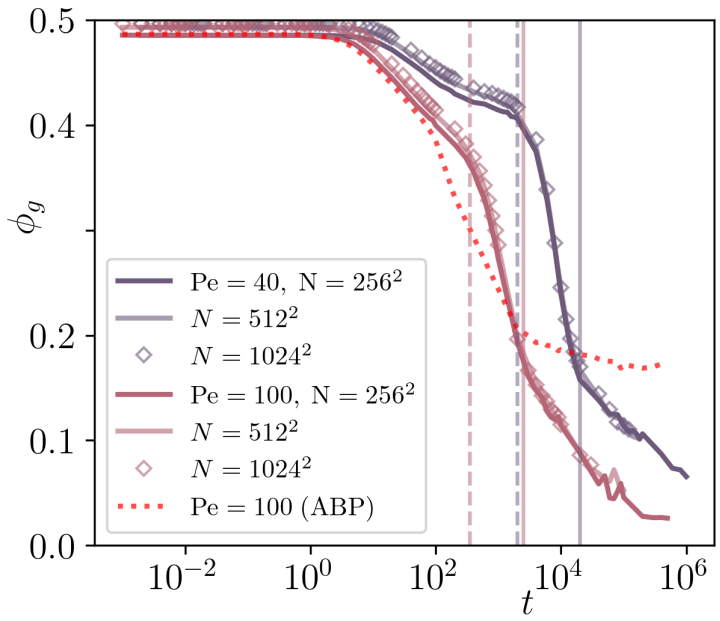

Figure 5.7: **The surface fraction occupied by the gas**. The lower purple curves are for Pe = 100, and the upper blue curves for Pe = 40, in systems with $2N = 256^2$, 512^2 and 1024^2 particles, and same densities as of Fig. 5.2. The dotted red line represents the surface fraction occupied by the gas in the ABPs systems with Pe = 100 and same global density $\phi = 0.5$. The vertical dashed and continuous lines indicate the transition to the fast growing and the scaling regime, respectively, of the growing length for the Pe = 40 and 100 (grey and purple lines) cases.

We discretize the phase of the local hexatic order parameter (5.10) into $n = 6$ bins and we split the system accordingly. We then apply the DBSCAN algorithm to each part of the system separately. We redirect the reader to Appendix A for a detailed explanation of the algorithm.

Hexatic growing length

The analysis of the average of the hexatic length over all dense clusters, which we call R_H, is shown in Fig. 5.8 (a). Concomitantly with the growth of the dense phase, we see that the growth of hexatic order follows the same three dynamical regimes. After the early nucleation stage, the evolution enters the intermediate regime in which $R_H \sim t^{0.8}$ as for ABPs, see the red dotted curve in Fig. 5.8(a). At a smooth crossover the evolution slows down in the scaling regime, but not as dramatically as for ABPs. Here, we find

$$R_H \sim \begin{cases} t^{0.27} & \text{low Pe} \\ t^{0.4} & \text{high Pe} \end{cases} \tag{5.11}$$

while for ABPs in MIPS the exponent was close to 0.13 [CDL$^+$20a]. These features are shown in Fig. 5.8 (a) with dashed lines.

We confirmed (not shown) that in the scaling regime the dynamic behaviour is not affected if we increase the system size.

Dependence on activity Between Pe = 40 and Pe = 100 we observe a clear change in the behaviour of R_H at long times, in the last scaling regime. For weaker activities, R_H

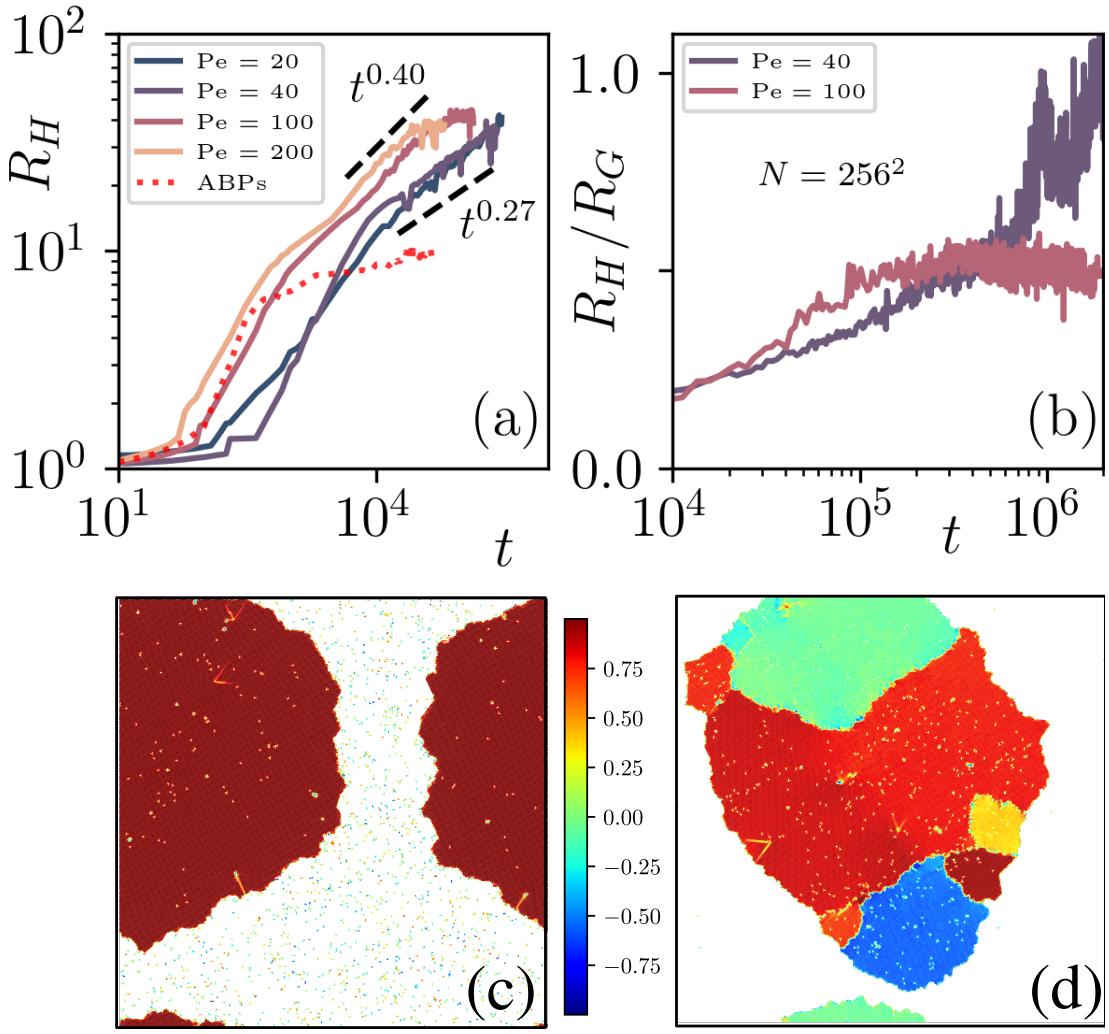

Figure 5.8: **The hexatic order.** (a) The averaged length of the orientationally ordered parts of the dense component, for different Pe and for densities on the 50:50 curve in the phase diagram of Fig. 5.1. The red dotted line shows the data for the ABP system. (b) Comparison between full orientational ordering at low Pe and saturation to a patchwork of different orientational orders at high Pe, averaged over 10 independent runs. In (c) and (d) two examples of the asymptotic configurations at low (Pe $= 40$) and high (Pe $= 100$), respectively.

continues to grow towards the typical size of the dense component, R_G, which thus acquires a uniform orientational order. Instead, for stronger activities R_H approaches a finite limit, R_H^s, that, as we argue below, can be identified with a metastable situation. Figure 5.8 (b) displays these features: while the ratio R_H/R_G tends to one for Pe = 40, it remains blocked at a value close to 0.5 for Pe = 100.

Figures 5.8(c)-(d) illustrate that full orientational order is reached at low Pe, while at high Pe we have saturation into patches of different colors, representing hexatically ordered clusters with the local hexatic parameter pointing in different directions.

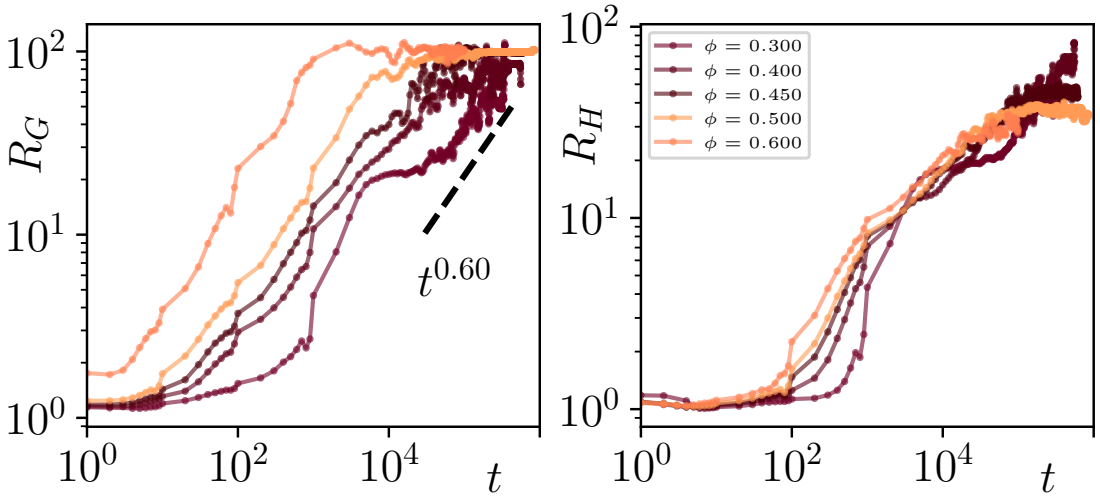

Figure 5.9: **Global density effects** on the growth of the dense phase gyration radius R_G and hexatic radius R_H (left and right panel, respectively). The systems are at Pe = 100 and varying packing fractions reported in the legend. The number of particles is fixed to $2N = 256^2$ and the packing fraction is tuned by changing the size of the simulation box. Note that for this system size the growing regimes are less visible.

Dependence on packing fraction The dependence of the hexatic order on the global packing fraction, at fixed Pe, is analyzed in Fig. 5.9 where R_G and R_H are plotted as a function of time. We reckon that at low ϕ, even for high Pe, the dense phase eventually reaches a unique orientational order, while this is not the case at high ϕ.

The way in which the sub-domains get blocked or the dense phase manages to order orientationally can be appreciated in the movies M3 and M4.

Figure 5.9 gives further support to the fact that the saturation of R_H reached at high Pe is only a metastable feature. Changing the density, R_G tends to a similar asymptotic value, while R_H saturates at larger values decreasing the density. Thus, at lower global densities dumbbells do not get so much stuck and the hexatic domains can further order reaching larger R_H and even the asymptotic R_G value in some cases.

Stability of hexatic domains in the dense phase

In the analysis shown so far, we found that for low Pe the dense phase reaches a full orientational order while at high Pe it does not, and the dense phase is made of patches with different hexatic orders. We now investigate whether these structures are stable or not. Note that all the simulations in this section were done using a system with $2N = 256^2$.

First, we took a long-time configuration at Pe = 40, which has completely ordered to the same hexatic parameter, and we removed the gas. We then restarted the dynamics at a higher value of Pe, for which we were not able to reach a full orientational order when we evolved the system from a random initial condition. The Pe = 40 initial configuration is stable at all Pe, and the dense phase does not break up in differently oriented pieces.

Conversely, we took a blocked configuration at Pe = 100, with its poly-orientational structure, and we suddenly changed Pe, to Pe = 40, the parameter with which we fur-

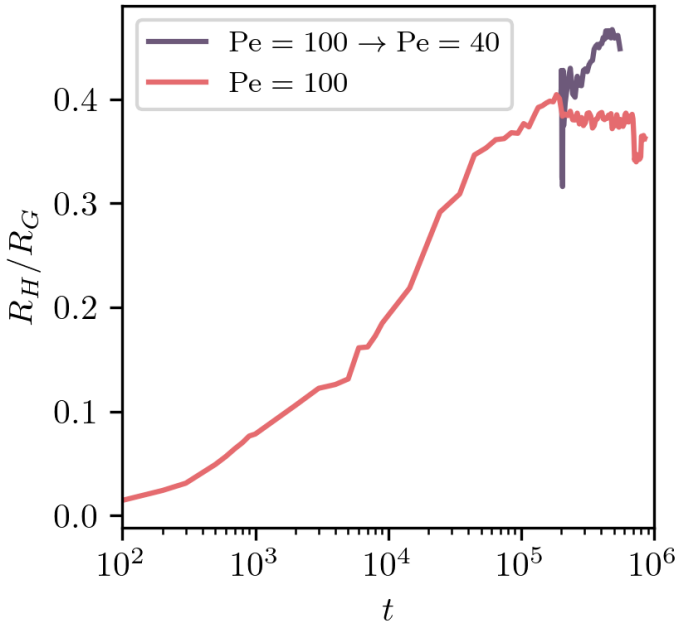

Figure 5.10: **Quench.** A configuration with patches of different hexatic orders at Pe = 100 is instantaneously quenched to Pe = 40 (grey curve), and compared to the same conformation continuing to evolve at Pe = 100 (red curve). The ratio between the averaged hexatic radius and the averaged gyration one increases after the quench, implying clusters acquire an homogeneous orientational order at the lower Pe.

ther evolved the system. Right after the quench we observed an increase in the averaged hexatic radius, Fig. 5.10. The dense phase tends to better order orientationally at the lower Pe.

We also proved that for random initial conditions evolved at even higher Pe, systems with sufficiently low density, manage to order and reach larger averaged hexatic radii, compatible with the averaged radius of gyration itself, see Fig. 5.9.

These tests suggest that the truly stable configurations are the ones with a single orientational order, at all Pe. The patchworks that we find in the evolution of disordered states at high Pe and high densities would then be metastable due to the fact that clusters with different hexatic order that collide get stuck and the simulations are not long enough to erase the interfaces.

Note that the behavior of ABP systems is different from the dumbbells' one. For active disk systems, if one starts the dynamics in the MIPS region of the phase diagram from a completely ordered configuration, the dynamics break the hexatic order and the hexatic length R_H evolves towards the same value obtained using disordered initial conditions [CDL$^+$20a]. This R_H value is smaller than R_G in the asymptotic steady state, with multiple hexatically ordered patches coexisting. For this reason, the authors of [CDL$^+$20a] claimed that there is a truly stable micro-phase separation of different orientational orders in ABP systems.

In the case of the dumbbells, in contrast, for orientationally ordered initial configurations of the dense phase, the cluster does not break over time into smaller patches of different hexatic orders. Conversely, a state with patches of different hexatic orders

should eventually be replaced by a fully orientationally ordered cluster. Moreover, it is important to note that the low Pe behavior found here has no counterpart in the ABP system, since in the latter case the MIPS phase has an ending critical point at a finite Pe.

Clusters geometry and dynamics

We now turn to the analysis of the clusters' geometry and dynamics, using the tracking algorithm developed in Ref. [CCD$^+$23]. We first investigate the cluster's geometry in the bulk. Then we characterize the total active force and torque acting on the clusters. We then identify the typical cluster motion. Adapting the mechanical model derived in [CNS$^+$24] for the motion of 3D dumbbell clusters in dilute conditions, we describe the dynamics of the 2D ones analytically. Of precious help is the extraction of clusters from the bulk of the system and the analysis of their dynamics under isolated conditions.

Geometry

Contrary to ABP clusters, dumbbell ones do not have bubbles within. We do not see large shape fluctuations either. In sum, they are more stable objects and the dynamics does not create holes within them, nor lets pieces easily detach, as one can see happening in ABP clusters [CNS$^+$24].

In Fig. 5.11, we plot the individual cluster mass against its radius of gyration, considering configurations taken in the scaling regime for Pe=100 at the density of Fig. 5.2. Both the mass and radius of gyration are normalized by the average values obtained over all clusters at a given time t considered, $M^* = M/\overline{M}(t)$ and similarly for R_G^*.

Similar to our findings for ABP clusters, the scatter plots reveal two regimes: a small mass - short radius of gyration regime in which the two quantities are related by the compact $M^* \sim {R_G^*}^2$ law, and a large mass - long radius of gyration regime with fractal scaling, $M^* \sim {R_G^*}^{d_\mathrm{f}}$, where $d_\mathrm{f} \sim 1.65 \neq d = 2$.

This behaviour is qualitatively but also quantitatively similar to the one of ABP clusters. The crossover at the average values from compact to fractal was also found for ABPs and, moreover, the fractal dimension of the large dumbbell clusters is very close to the one of large ABP clusters.

Active force and torque

In order to understand and quantify the motion of the clusters, two important quantities to consider are the total active force and the active torque acting on each cluster that we label with $\alpha = 1, \ldots, N_C$. The total instantaneous active force is defined as

$$\mathbf{F}_{\mathrm{act}}^{\alpha} = \sum_{i \in \alpha} \mathbf{f}_{\mathrm{act},i}. \tag{5.12}$$

The total instantaneous active torque is defined as

$$\boldsymbol{T}_{\mathrm{act}}^{\alpha} = \sum_{i \in \alpha} (\mathbf{r}_i - \mathbf{r}_{\mathrm{cm}}^{\alpha}) \times \mathbf{f}_{\mathrm{act},i} \tag{5.13}$$

where $(\mathbf{r}_i - \mathbf{r}_{\mathrm{cm}}^{\alpha})$ is the distance between the ith bead in cluster α and its center of mass.

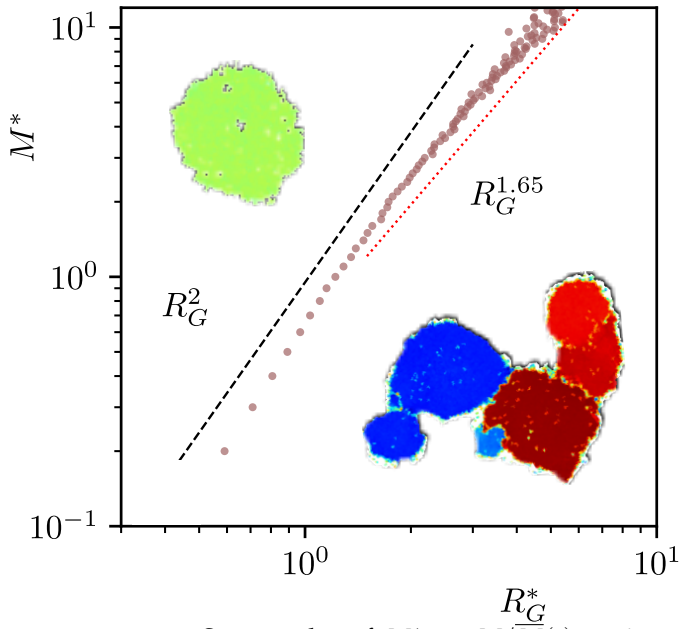

Figure 5.11: **Clusters geometry.** Scatter plot of $M^* = M/\overline{M}(t)$ against $R_G^* = R_G/\overline{R}_G(t)$, considering clusters in configurations taken in the scaling regime ($t = 1000$) for Pe=100 and density of Fig. 5.2. $\overline{M}(t)$ and $\overline{R}_G(t)$ are the average mass and radius of gyration at a given time t considered. The (black) dashed and (red) dotted lines close to the data indicate the estimates of the fractal dimension of the clusters which are smaller, $d_{\rm f} = 2$, and larger, $d_{\rm f} = 1.65$, than the average $\overline{R}_G(t)$ with mass $\overline{M}(t)$. Typical snapshots of compact (top left) and fractal (bottom right) clusters are displayed.

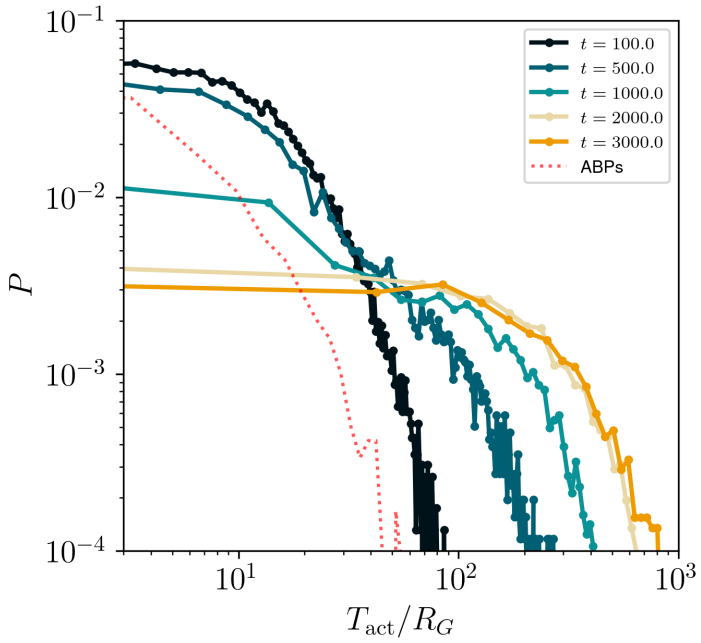

Figure 5.12: **Distribution of the modulus of the torques** exerted on each cluster, normalized by its gyration radius R_G, at Pe = 100 and density of Fig. 5.2, for different instants of the evolution before and during the scaling regime. The red dotted curve represents data for the ABPs system in the scaling regime ($t = 300$).

Both quantities are typically different from zero and have a strong effect on the motion of the clusters, as we will see below. The distributions of the modulus of the torques exerted by the active forces acting on the clusters are shown in Fig. 5.12 for Pe = 100 and several times in the rapid growth and in the scaling regimes. While for ABPs we did not see appreciable active torques [CCD$^+$23], for dumbbells the distributions are wide and have weight on quite large values of $T^{\alpha}_{\rm act}$. We observe that these distributions become wider increasing time.

Motion of clusters in the bulk

The total active force and torque, which do not vanish, act on the clusters and cause a very interesting motion which we now describe.

Clusters trajectories Given a cluster evolving in the whole system (the bulk) with others, its center of mass rotates in an approximately circular trajectory around a center which generally does not coincide with the center of mass of the cluster. The cluster behaves as a solid body, with a further rotation around its center of mass. The angular velocity around the center of the trajectory and around its center of mass are equal, as we demonstrate numerically below when we extract clusters from the bulk. In Fig. 5.13 we display several of center of mass cluster trajectories. The spatial scale is the same in all the panels: $10\sigma_{\rm d} \times 10\sigma_{\rm d}$. Some trajectories appear longer, indicating that the selected cluster has moved for an extended period without encountering another cluster, at which point we halt the tracking. The color scale in the vertical bar on the right represents time, evolving from dark (violet) to light (yellow). The shorter trajectories look like straight segments but in practice they are also circular, with very large radii, and have been interrupted by collisions with other clusters.

Note that ABD clusters behave very differently in comparison to the motility-induced clusters of ABP; the latter in fact do not rotate significantly, but only diffuse [CCD$^+$23].

We observe that clusters with a uniform hexatic order and quite regular shape are those which turn in quite regular spherical trajectories with relatively small radii. Clusters which resulted from merged smaller clusters with opposite directions of rotation and different hexatic orders separated by interfaces, also follow circular trajectories but with very large radii (see e.g. movie M5), and when observed over short time scales the latter seem to behave ballistically. Over longer time scales, as these clusters are typically quite large, they are modified by collisions with other clusters which changes significantly their kinetics (due to the change in the internal dumbbells arrangement, and thus of the total active forces and torques).

Due to clusters collisions and to the exchange of particles between the dense and gas phase, it is difficult to study a trajectory of a single cluster for an extendend period of time. For this reason, in Sec. 5.2 we will extract representative clusters from the bulk and study their isolated dynamics over longer time intervals.

Mean-square displacement In Section 3.2 we used the cluster tracking algorithm to calculate the mean-square displacement of the center of mass of each ABP cluster and we found diffusive behavior with a mass dependent diffusion coefficient. Consequently, the average over them all also resulted in diffusion. In the dumbbell case, instead, clusters have an approximate circular trajectory, and thus cannot diffuse. In-

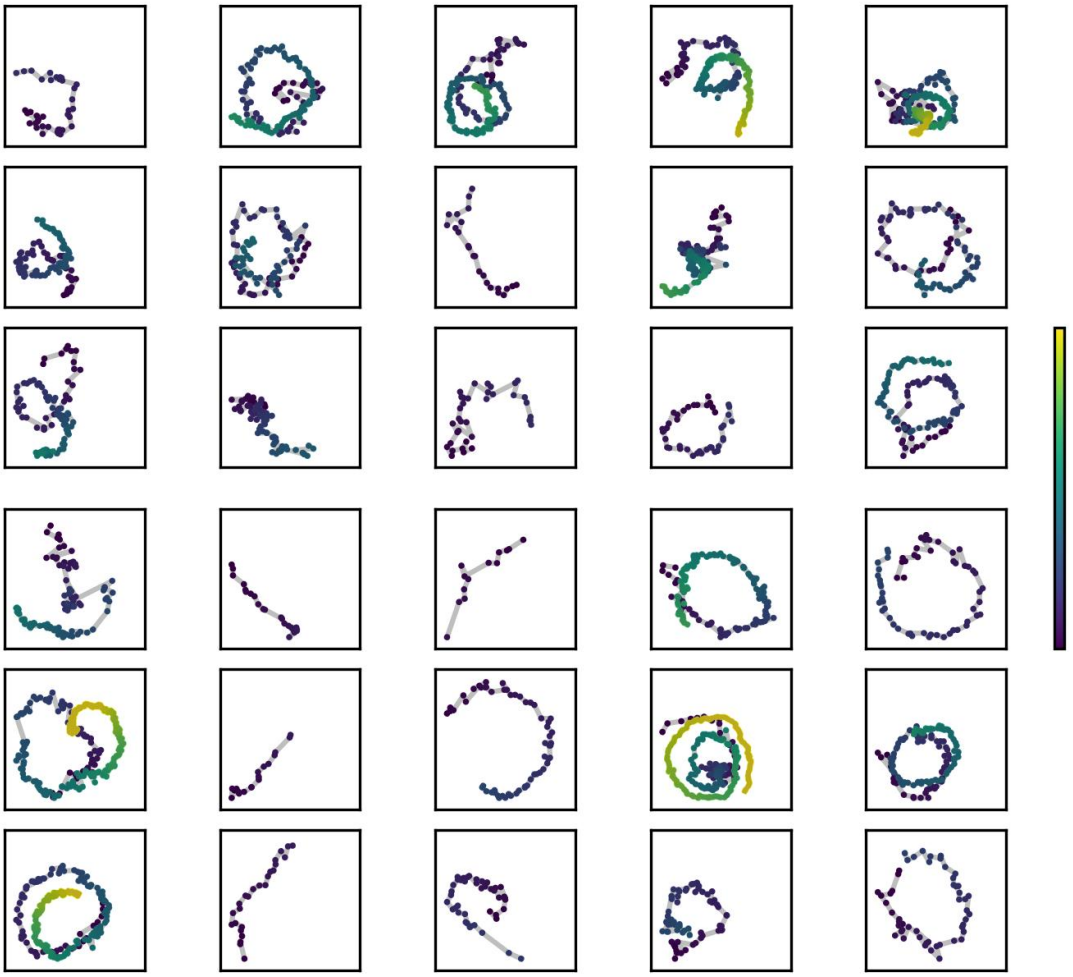

Figure 5.13: **Typical trajectories of the center of mass of some representative clusters** in the interior of a system with Pe $= 100$, $\phi = 0.35$, $T = 0.05$, followed starting from $t_0 = 1000$ in the regime where clusters have formed and through movement are colliding with each other. The box size is $10\sigma \times 10\sigma$ in all cases. The scale in the right vertical bar represents time, increasing from dark (violet), $t = t_0$, to light (yellow), $t = t_0 + 4000$. The trajectories are colored accordingly.

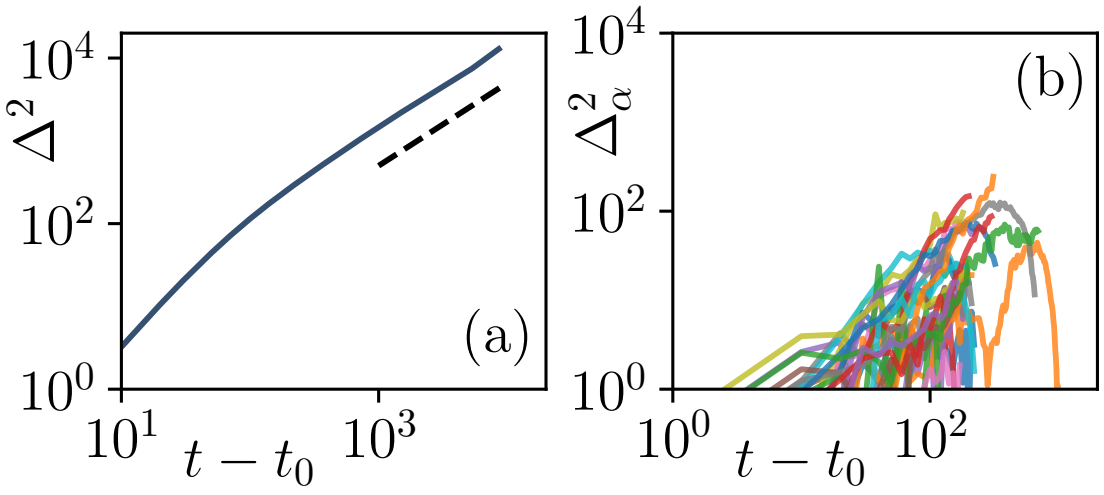

Figure 5.14: **Averaged mean-square displacement** of (a) the individual dumbbells, with $t_0 = 0$, and (b) the center of mass of the clusters, with $t_0 = 1000$ (at the beginning of the scaling regime). The dotted line represent a linear function. The data are for Pe = 100, $\phi = 0.50$ and $T = 0.05$.

deed, computing the individual mean-square displacement of the center of mass of each cluster,

$$\Delta^2_\alpha(t - t_0) = \frac{1}{N_\alpha} \sum_{i=1}^{N_\alpha} |\mathbf{r}_i^\alpha(t) - \mathbf{r}_i^\alpha(t_0)|^2 \,, \tag{5.14}$$

with α labelling the cluster, we see oscillating curves, see selected cases in Fig. 5.14(b).

If one computes the averaged mean-square displacement of *all* dumbbells, instead, starting from the random initial conformation,

$$\Delta^2(t - t_0) = \frac{1}{2N} \sum_{i=1}^{2N} |\mathbf{r}_i(t) - \mathbf{r}_i(t_0)|^2 \,, \tag{5.15}$$

we recover the diffusive behavior, see Fig. 5.14(a). Here, the dumbbells in the gas dominate, see the difference in the vertical scales in Fig. 5.14(a) and (b).These claims are also confirmed by the visual inspection of movies.

Motion of isolated clusters

In this Section we study the motion of clusters, of regular and fractal kind, taken from the bulk in the scaling regime, and evolved in isolated conditions.

Clusters trajectories We extract clusters with different characteristics from the bulk, similarly to what done in [CCD+23]. We place the clusters in a box without gas, and we evolve them at zero temperature and using different values of the active force f_{act}, which do not necessarily coincide with the one in the bulk, and at $T = 0$. Evolving in vacuum, the clusters avoid cluster-cluster collisions and the addition of gas molecules. Under these conditions, their mass remains approximately constant for much longer periods of time. We can therefore follow their dynamics under relatively constant conditions for much longer times than in the bulk.

M	R_G	R	F_{act}	T_{act}
154	4.68	3.64	17.34	125.86
254	6.03	19.14	39.13	87.42
336	6.63	7.54	51.68	355.68
508	8.19	6.57	50.13	590.72

Table 5.1: **Features of some representative clusters.** Here are reported the mass, radius of gyration, radius of the circular trajectory, total active force and torque of four different clusters isolated from the bulk at f_{act}=2.5. All the quantities in the table are very close to being constant, because these clusters were already well stabilized before starting the measurements, and without noise they do not change their internal structure. The center of mass trajectories are shown in Fig. 5.15. As shown in that figure, changing f_{act}, and thus the total active force and torque, does not affect the other quantities.

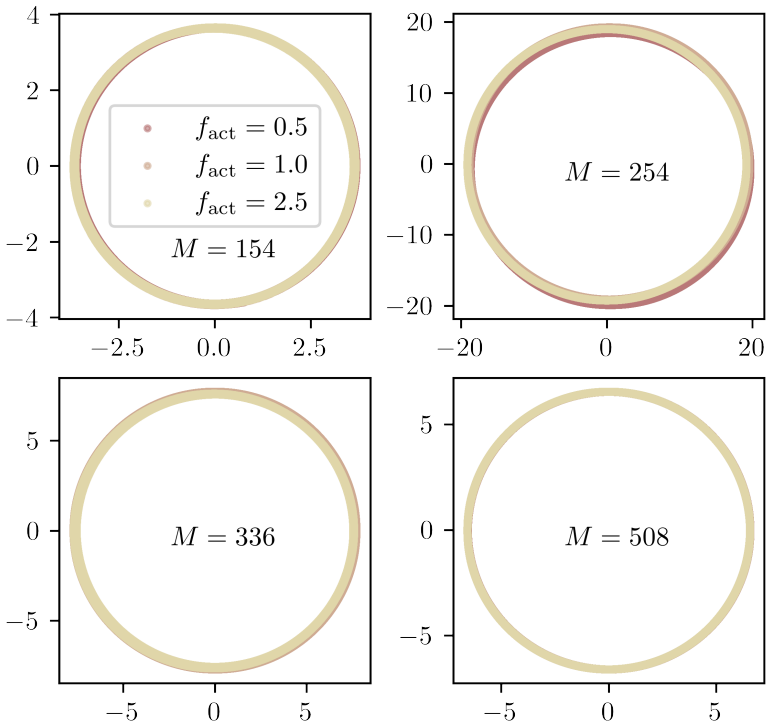

Figure 5.15: **Isolated clusters with uniform hexatic order.** Motion of the center of mass of four clusters with different mass evolved in vacuum and at zero temperature using different active forces, in the key.The spatial scales are not the same in all panels. The trajectories overlap almost perfectly, independently of f_{act}. The values of their mass, radius of gyration, radius of the trajectory are given in Table 5.1.

Figure 5.15 shows the motion of four isolated clusters with different initial masses and a single hexatic order, evolved using active force values given in the keys. Notably, the trajectories are quite independent of the value of f_{act}, and depends only on the geometrical arrangement of the dumbbells inside the clusters. For the clusters in the figure the mass/radius/total active force and total torque relations are given in Table 5.1.

The angular velocity of the center of mass with respect to the center of its circular trajectory and the angular velocity of a bead with respect to the center of mass of the

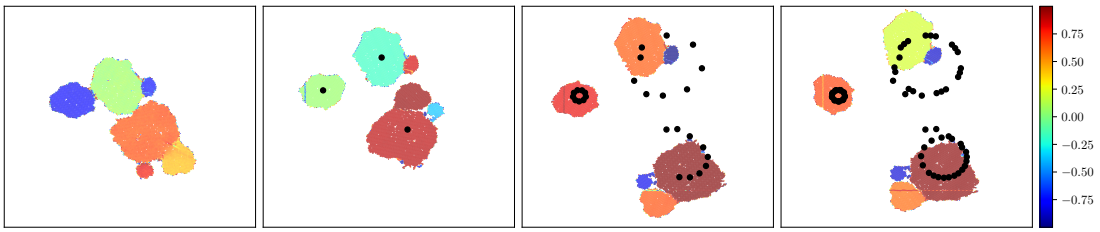

Figure 5.16: **Isolated clusters with multiple hexatic domains.** Four snapshots of the evolution, in isolation, at time $t = 0$, 8000, 16000 and 30000 of a single cluster with heterogeneous orientational order. The single cluster breaks into pieces along the interfaces between the different orientational domains. Each of the new clusters, with homogeneous orientational order, then rotates. The dots traced by their centers of mass are drawn in black.

cluster are equal. This is proven numerically by the trajectory of representative clusters, as the one shown in movie M6.

Very different is the fate of large clusters with several hexatic orders. They are not stable, they break along the internal interfaces and each of the pieces undergoes a noisy circular motion. Their trajectories can be such that they meet again, remain attached for some time, break once more and so on and so forth. The snapshots in Fig. 5.16 and the movie M7 demonstrate these features. This gives support to the fact that stable clusters, although difficult to form, will eventually have uniform orientational order.

Kinetic model of cluster motion Now, we derive the equation of motion for a single cluster in isolation with simple dynamics arguments.

We assume that the cluster is a rigid body, meaning that its shape (the internal arrangement of dumbbells) does not change over time. This is a reasonable approximation for dumbbell clusters that are strongly bound by the active force.

The motion of the center of mass (CoM) of the cluster is described by Newton's second law,

$$M\ddot{\boldsymbol{R}}_{\text{cm}} = \boldsymbol{F}_{\text{act}} + \boldsymbol{F}_{\text{drag}} \,, \tag{5.16}$$

where $2N_c$ is the total number of disks in the cluster, $M = 2N_c m_{\text{d}}$ is its total mass, $\boldsymbol{F}_{\text{act}} = \sum_{i=1}^{2N_c} \mathbf{f}_{\text{act},i}$ is the total active force acting on the cluster, and $\boldsymbol{F}_{\text{drag}} = -(M/m_{\text{d}})\gamma_{\text{d}}\dot{\boldsymbol{R}}_{\text{cm}}$ is the total drag force acting on the cluster. The internal forces arising from the pair potential cancel out in the equation of motion of the CoM.

The forces are drawn in the sketch in Fig. 5.17. The drag force is tangential to the circular trajectory of the CoM. The total active force has a (large) component along this same tangential direction and a (small) component along the radial one.

The equation of motion of the cluster is completed by the equation of motion of the angular momentum,

$$\dot{\boldsymbol{L}} = \boldsymbol{T}_{\text{act}} + \boldsymbol{T}_{\text{drag}} \,, \tag{5.17}$$

where $\boldsymbol{L} = \sum_{i=1}^{2N_c} \boldsymbol{r}_i' \times m_{\text{d}}\dot{\boldsymbol{r}}_i'$ is the total angular momentum, $\boldsymbol{T}_{\text{act}} = \sum_{i=1}^{2N_c} \boldsymbol{r}_i' \times \boldsymbol{f}_{\text{act},i}$ is the total active torque acting on the cluster, $\boldsymbol{T}_{\text{drag}} = \sum_{i=1}^{2N_c} \boldsymbol{r}_i' \times (-\gamma_{\text{d}}\dot{\boldsymbol{r}}_i') = -\gamma_{\text{d}}\boldsymbol{L}/m_{\text{d}}$ is the total drag torque acting on the cluster, and $\boldsymbol{r}_i' = \boldsymbol{r}_i - \boldsymbol{R}_{\text{cm}}$ is the position of the i-th particle with respect to the cluster's CoM.

We now analyze the motion of the cluster. In an overdamped approximation of Eq. (5.17) one can set the time derivative to zero. This yields a relation between the

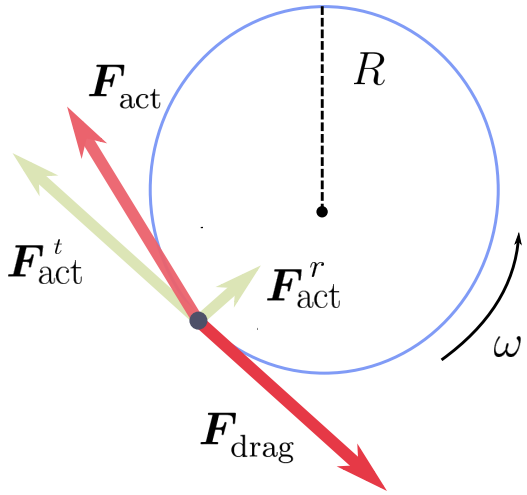

Figure 5.17: **Sketch of the forces** acting on the center of mass of a cluster undergoing circular motion with radius R.

modulus of the total active torque and the one of the angular momentum:

$$L = \frac{m_{\text{d}} T_{\text{act}}}{\gamma_{\text{d}}} \,. \tag{5.18}$$

Instead, the overdamped approximation cannot be applied to Eq. (5.16), since an inertial contribution is needed at all times in order to turn the direction of motion of the cluster, as we observe numerically. We thus decomposed the forces in Eq. (5.16) in radial $\boldsymbol{F}^r$ and tangential $\boldsymbol{F}^t$ components. The former contributes to the change in direction, while the latter to the directed motion only. A good approximation [CNS+24] is to consider the tangential component of the active force almost fully counterbalanced by the drag force $F^t_{\text{act}} \approx \frac{M}{m_{\text{d}}}\gamma_{\text{d}}\dot{R}_{\text{cm}}$, setting in this direction the time derivative to zero in Eq. (5.16). The remaining small mismatch gives rise to a force

$$\boldsymbol{F}^r_{\text{act}} = \boldsymbol{F}_{\text{act}} + \boldsymbol{F}_{\text{drag}} \tag{5.19}$$

equal to the inertial contribution of the motion and directed radially towards the center of the trajectory. In this direction, we have $M\ddot{R}_{\text{cm}} = F^r_{\text{act}}$.

Using the fact that the motion occurs with uniform angular velocity ω, we can substitute $\dot{R}_{\text{cm}} = \omega R$ and $\ddot{R}_{\text{cm}} = \omega^2 R$, where R is the radius of the circle (not to be confused with the growing length of previous sections). Thus,

$$F^t_{\text{act}} = \frac{M}{m_{\text{d}}}\gamma_{\text{d}}\omega R \,, \tag{5.20}$$

$$F^r_{\text{act}} = M\omega^2 R \,. \tag{5.21}$$

From Eq. (5.20), we can express the radius R of the trajectory in terms of the tangential component of the active force and the angular velocity:

$$R = \frac{m_{\text{d}}}{M}\frac{F^t_{\text{act}}}{\gamma_{\text{d}}\omega} \,. \tag{5.22}$$

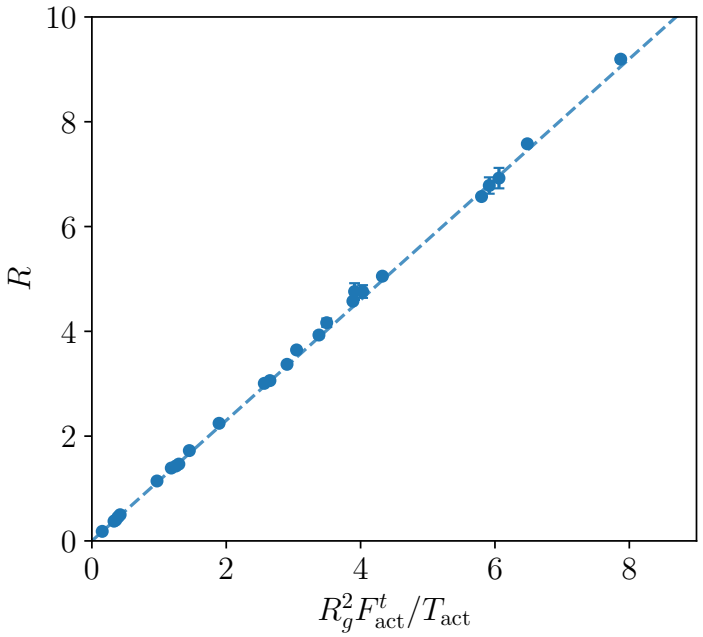

Figure 5.18: **Radius of the trajectory of the cluster.** The radius of the trajectory of the cluster is measured directly from the clusters' trajectories (blue dots) and compared against the linear prevision of Eq. (5.23) (dashed line). The fit yields a slope equal to 1.15.

Finally, expressing the total angular momentum in terms of its moment of intertia, $L = I\omega$, and the latter in terms of the radius of gyration R_G and the mass M as $I = MR_G^2$, using Eq. (5.18) we can obtain an alternative expression for the radius R in terms of the active force and torque:

$$R = R_G^2 \frac{F_{\rm act}^t}{T_{\rm act}} \,. \tag{5.23}$$

Notably, because both $F_{\rm act}^t$ and $T_{\rm act}$ are proportional to $f_{\rm act}$, the model's prediction is that the radius of the trajectory R is independent of $f_{\rm act}$. Indeed, this result has been already verified numerically in Fig. 5.15.

We tested the validity of Eq. (5.23) by independently measuring the radius of the trajectory of the cluster, its radius of gyration, and the total active force and torque acting on it. Some concrete values are listed in Table 5.1. The results are shown in Fig. 5.18 and are in good agreement with the theoretical prediction, with the slope of the linear fit (1.15) slightly larger than the expected value of 1. This discrepancy indicates that probably there are some higher order corrections to Eq. (5.23) that are not accounted for by our model.

In this section, we studied the dynamics of active dumbbell systems, for parameters such that they phase separate into dense and dilute components, focusing on the formation of the dense structures.

Our first goal was to characterize the growth of the dense phase from the study of the structure factor. We used sufficiently large system sizes, with as many as $2048^2/2$ dumbbells, so as to eliminate any finite size effect during growth. For Pe $\gtrsim 40$ we identified three distinct regimes, similar to the ones observed for ABPs, with different

time-dependencies of the growing typical length: short times transient, rapid growth, and a scaling limit with algebraic growth. For Pe $\lesssim 40$ we do not see the intermediate regime, typical of nucleation, and the dynamics seems to enter directly the asymptotic scaling limit. In the scaling regime, the typical length grows algebraically but, contrary to what was found for ABPs [CDL$^+$20a], the exponent increases with Pe (at fixed percentage of dense and dilute regions), reaching the value 0.60 at the highest activity considered. Moreover, the growth is considerably faster than for disks. The values and parameter dependence of this growing length are consistent with the ones derived from the decay of the instantaneous number of clusters and the averaged gyration radius of the clusters.

Next, we analysed the internal structure of the dense regions paying special attention to the orientational order of the disks forming the dumbbells in terms of their hexatic arrangement. In the scaling regime, the length associated to the orientational order grows algebraically and faster than for ABPs. Furthermore, the growth gets faster for larger Pe value, with $R_H(t) \sim t^{0.3}$ at low Pe and $R_H(t) \sim t^{0.4}$ at stronger activities.

An important difference is found at around Pe ~ 40: at weaker activity the clusters manage to reach a uniform orientational order, while at higher activity this is not achieved and a polycrystalline structure is formed and gets blocked. The latter behavior is similar to the one found in the MIPS phase of ABPs. Quenches between two representative Pe values, and the evolution of fully ordered configurations, suggest that for dumbbell systems the truly stable configurations are the ones with full orientational order, though these are not accessible dynamically at the time scales that we can use in the simulations.

A salient feature of the dense ABP clusters is the fact that bubbles pop up at the interfaces between different orientationally ordered patches. No such gas bubbles appear in the ABD clusters, not even when there are patches of different hexatic order. There are no large shape fluctuations either, with no piece detachment nor any other abrupt event. In sum, the ABD clusters are more stable objects than the ABP ones.

Finally, we focused on the dynamics of the clusters, and we performed a tracking analysis as the one in [CCD$^+$23] for ABPs. In order to perform this study, we needed to work at sufficiently high Pe, Pe $\gtrsim 20$, otherwise the phase separated region of the phase diagram is located at too high global packing fraction and there are no isolated clusters under these conditions.

Concerning the geometrical properties of the clusters, small clusters are regular while large ones are fractal, with the crossover determined by the time dependent growing length, as found for ABP clusters. The fractal dimension measured is $d_{\mathrm{f}} \sim 1.65$.

Interestingly enough, the ABD clusters are not diffusive but they rotate as approximate solid bodies. Indeed, the trajectories of the center of mass of clusters is always circular.

Extracting clusters from the bulk and following their dynamics in isolation we further proved that large polycrystalline clusters are not stable and break up in pieces of uniform orientational order which then follow their own circular motion.

We derived a simple dynamical model to describe analytically the motion of the stable 2D clusters. We found very good agreement between the quantitative predictions of the model for the radius of the center of mass circular trajectory of not too large and homogeneous clusters, and the numerical measurements. The concrete prediction

is given in Eq. (5.23) and relates the radius of the trajectory to the radius of gyration of the cluster itself in a non-trivial manner. Importantly, we found that the radius of the trajectory is independent of the Pe value.

To conclude, the results reported here show the richness of behaviour of the dumbbell model, which differ considerably from the ABP model, and the general importance of considering anisotropic particles in general. These differences span the growth properties, the predicted steady-state, and the cluster movement, and arise due to the difference in particles interlocking when forming a dense phase.

5.3 Phase Behaviour and Cluster Dynamics of three-dimensional Active Dumbbell Systems

Among biological systems, bacteria have gained the attention of the physics community as they represent a simple natural realization of self-propelled particles, by virtue of their biological simplicity and limited ability in interacting with both the environment and other units. Therefore, bacterial systems provide an elementary yet relevant example of how the dynamics of active constituents may lead to self-assembly [BJF15, BJS18, MCMFDL22]. Indeed bacteria exhibit noteworthy chemotactic properties which allow them to respond to external stimuli such as variations of temperature, nutrient availability, oxygen concentration, *etc.* to develop different kinds of colonies, ranging from biofilms to fluidic suspensions, often characterized by the emergence of elaborate patterns, even in absence of guidance and only because of the uncoordinated evolution of the separate units [YDVK19].

Inspired by this huge variety of possible states, many models have been advanced to capture the dynamics of bacterial suspensions. However, most research has focused on two-dimensional systems, while much less is known on three-dimensional realizations, relevant for a full characterization of real biological systems, as these are most often subject to full $3D$ dynamics.

In particular, much less is known about the phase behaviour of these same systems in $3D$ [SMAC14a, WWG14, vDRVRD19b, NCP$^+$20b, OKGG21, TW21, VLP23]. Stenhammar *et al.* [SMAC14a] first observed that the MIPS transition is significantly inhibited in $3D$ for active Brownian spheres in the absence of any attractive interactions and shifted towards higher activities, due to reduced persistence in $3D$ space. On the other hand, van Damme *et al.* [vDRVRD19b] pointed out that MIPS is completely suppressed for spherocylinders in $3D$ of aspect ratio 2. The authors argued that MIPS suppression is ultimately due to passive torques originating from anisotropic steric repulsion between the rods. This makes rods quickly reorient upon binary collisions or encounters with a clusters, preventing accumulation and phase separation. These studies suggest that in $3D$ activity alone is not enough to drive the system towards a phase-separated state.

Three-dimensional systems of active spherical particles [MicvacAU$^+$13] and dumbbells [SLVC$^+$12b] in the presence of attractive interactions have been studied numerically to address the experimental realization of bacterial systems in interaction with non-absorbing polymers [MMMA19, SLVC$^+$12b]. In this case, demixing into coexisting phases is tamed by the aggregation strength, leading to the formation of highly dynamical structures as rotating clusters [SLVC$^+$12b]. However, activity tends to suppress aggregation, consistently with experimental observations of suspensions of motile bac-

teria. The non-equilibrium nature of the phase coexistence is also illustrated by the formation of new dynamical states, such as percolating networks caused by the interplay between attraction and motility [PSF15].

However, collective effects in bacterial suspensions are also observed in $3D$. Our goal in this section is to clarify the relevance of motility in the dynamics of three-dimensional suspensions by performing a systematic analysis of the phase behavior of a system of propelled attractive dumbbells. The discrete mesoscopic approach here implemented allows us to retain only the main features of bacterial suspension (local orientation, attractive interactions)

To this end, we simulate a system of N dumbbells immersed in a three-dimensional space. Beads belonging to different dumbbells interact through the Mie short-range potential, with a cutoff equal to $r_c = 1.5\sigma$, which also includes the attractive part. The active dumbbells move in a cubic box with fully periodic boundary conditions. We stress that model parameters are chosen to ensure that the resulting dynamics is fully over-damped. (see Appendix A.1 for numerica details).

The Section is structured as follows. The first part is devoted to the analysis of the phase behavior of the system in a three-dimensional unconfined geometry. We will identify four phases (gel, disordered, phase-separated and percolating network) while varying the Péclet number Pe and the total packing fraction ϕ. The effect of the attraction strength will also be considered. In the second part, we will focus on the description of the motion of a single isolated cluster in the phase-separated phase.

Phase Behaviour

Before entering into the heart of our study, we confirmed that there is no stable MIPS for purely repulsive interactions between the active dumbbells. The condition for purely repulsive dumbbells is achieved by setting the cut-off lengthscale $r_c = \sigma_{MIE}$, so that only the repulsive core in the Mie potential is preserved and shifting the potential by the corresponding energy value $U_{\mathrm{Mie}}(r_c)$.

The relevance of active injection with respect to thermal fluctuations is captured by the Péclet number Moreover, the aggregation capability of the system can be captured by measuring the ratio between the strength of the attractive force and the active force [MicvacAU$^+$13]

$$P_{\mathrm{agg}} = \frac{\epsilon}{f_{\mathrm{act}}\sigma} \, . \tag{5.24}$$

Finally, the global density or packing fraction is quantified by the volume fraction

$$\phi = N \, \frac{\pi\sigma^3}{3V} \, , \tag{5.25}$$

with V the volume of the box where the dumbbells are placed and N the total number of dumbbells, that is, twice the number of spherical beads [2].

We start by presenting the phase diagram obtained by scanning various values of the packing fraction ϕ and the Péclet number Pe. In Fig. 5.19, snapshots are presented

[2] Although in the following we will mostly consider relatively low packing fractions, $\phi \leq 0.3$, it is worth mentioning that the close-packing value $\phi_{\mathrm{cp}} \simeq 0.74$ and the random close packing value $\phi_{\mathrm{rcp}} \simeq 0.64$ for hard spheres in $3D$. Close packing is achieved by the face center cubic and the hexagonal close packing arrangements. In both cases each sphere touches 12 neighboring spheres [RCD$^+$].

for different combinations of these two parameters. We find that the system exhibits a variety of diverse phases. We start by discussing them at a pictorial level and we later give a quantitative characterization by studying the distribution of local densities, the distribution of cluster sizes, and the dynamics.

The structures

We commence our analysis by setting $\mathrm{Pe} = 0$ and examining the structures formed at long times for the global densities $\phi = 0.05, 0.1, 0.2, 0.3$, as shown in the first row of Fig. 5.19. In the passive limit the dumbbells aggregate in a gel phase, in which particles form a rather static percolating network. This behavior, called gelation [Poo02, CDD$^+$04, Zac07, LZC$^+$08, ZLC$^+$08], is due to a rapid cooling of an initially disordered conformation which in conjunction with the dumbbells' anisotropy and the short-range attraction induce the formation of such a metastable state. The stable state would be instead phase-separated – a configuration which, nonetheless, cannot be reached since the thermal energy is insufficient for the dumbbells to rearrange into a single compact cluster.

In the second row of Fig. 5.19 we consider a higher activity $\mathrm{Pe} = 50$, while maintaining the same densities as in the first row. The dumbbells now aggregate to form a single cluster at any density. We will refer to this state as phase-separated. The resulting cluster exhibits both translational and rotational persistent motion, which we will characterize in detail in Sec. 5.3. Remarkably, a relatively small increase in Pe with respect to the passive case, induced the dumbbells to reorganize destroying the gel network and undergoing phase separation, thanks to the activity that acts as an additional source of noise.

When the activity is further increased to $\mathrm{Pe} = 100$ (third row), an interesting effect is observed upon varying the density. Specifically, at densities $\phi = 0.05$ (i) and $\phi = 0.1$ (j), we still find phase separation. However, at higher densities $\phi = 0.2$ (k) and $\phi = 0.3$ (l), the system becomes more disordered, with small clusters that do not grow in size over time. These clusters connect to each other, forming a phase that is similar to the gel observed at vanishing activity but is more dynamic in nature, with the network connections constantly forming and breaking throughout the simulation (see SM Movie 1[3]). This phase will be referred to as percolating phase, following the nomenclature of Ref. [PSF15] where a similar behavior was found for a system of self-propelled Lennard-Jones spheres.

Finally, at $\mathrm{Pe} = 150$ (fourth row), we notice that at low densities the activity causes the system to become fully disordered (Fig. 5.19(m,n). In this case, the activity is strong enough to overcome the aggregation force, leading to the cluster's breakup. Conversely, at higher densities, (o) and (p), we observe again the formation of a percolating network.

Despite the presence of attraction, we have observed four phases occurring in distinct ways. Such findings suggest the existence of a complex phase diagram, which we will now proceed to characterize.

[3]Movies of this section can be found at `https://www.dropbox.com/scl/fo/julh85npfkhv7rw3tke5r/h?rlkey=botjlcrqs9wpxgtiz2czfmtia&dl=0`

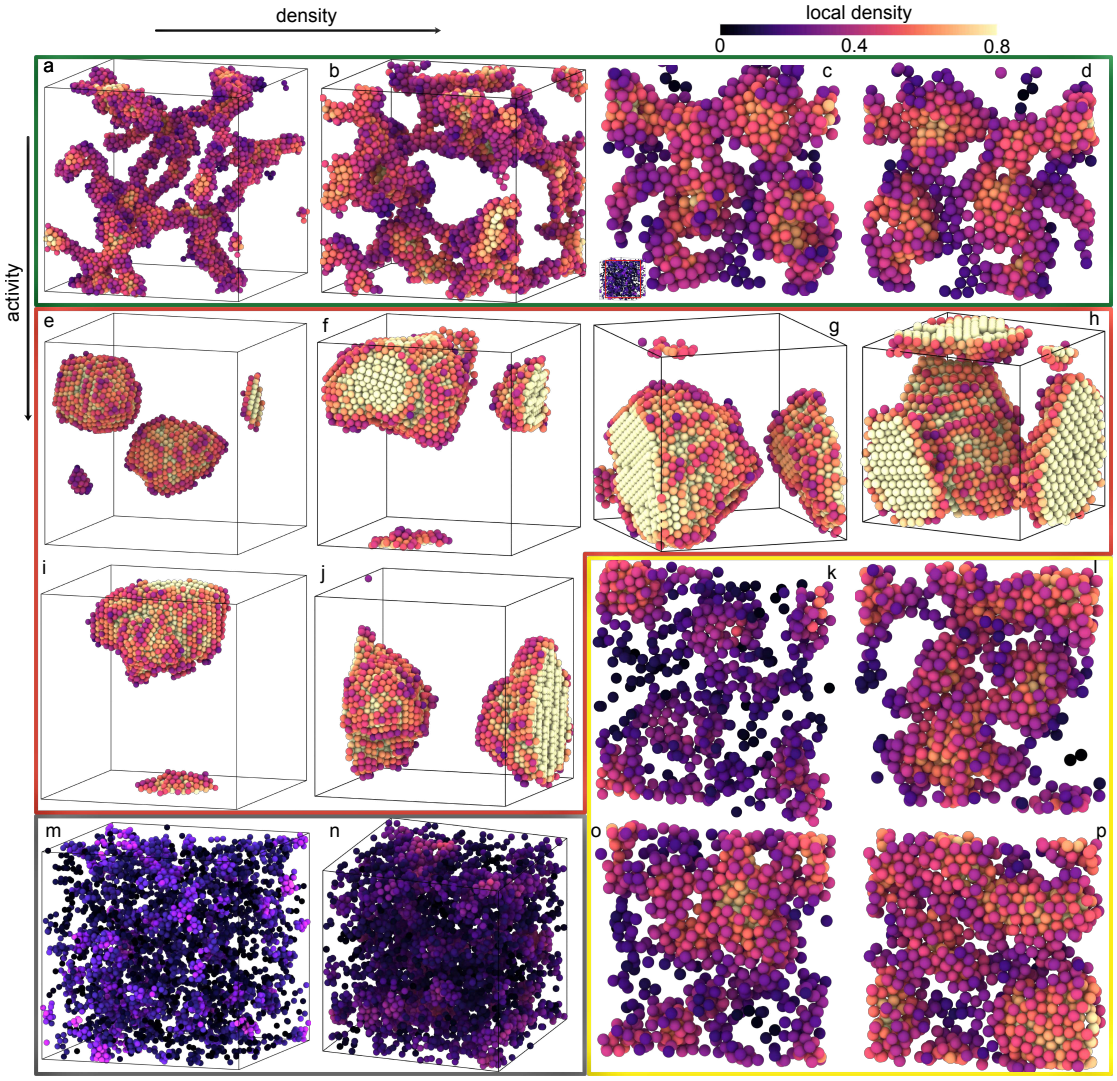

Figure 5.19: **Phase behavior of attractive active dumbbells.** Snapshots of the dumbbells' system for different global densities ϕ and Péclet numbers Pe. The attraction $\epsilon = 0.3$ for all cases presented here. Particles are colored according to the local density. From top to bottom, the rows correspond to Pe $= 0, 50, 100, 150$. From left to right, columns correspond to $\phi = 0.05, 0.1, 0.2, 0.3$. At Pe = 0, panels (a)-(d), the system is in the gel phase. Increasing activity for the same densities, panels (e)-(h) for $\mathrm{Pe} = 50$, or for even higher $\mathrm{Pe} = 100$ and small densities (i)-(j), aggregation is favoured and there is complete phase separation, in the sense described in the main text. At Pe = 150 and low density, panels (m)-(n), the structure breaks down into small pieces. At higher densities, panels (o)-(p), the percolating network subsists. The bar on top of the plot shows the scale for the local density with which the beads are colored, the scale we use to distinguish the phases, see Fig. 5.20 and its discussion, together with the dynamic properties to be presented in Sec. 5.3.

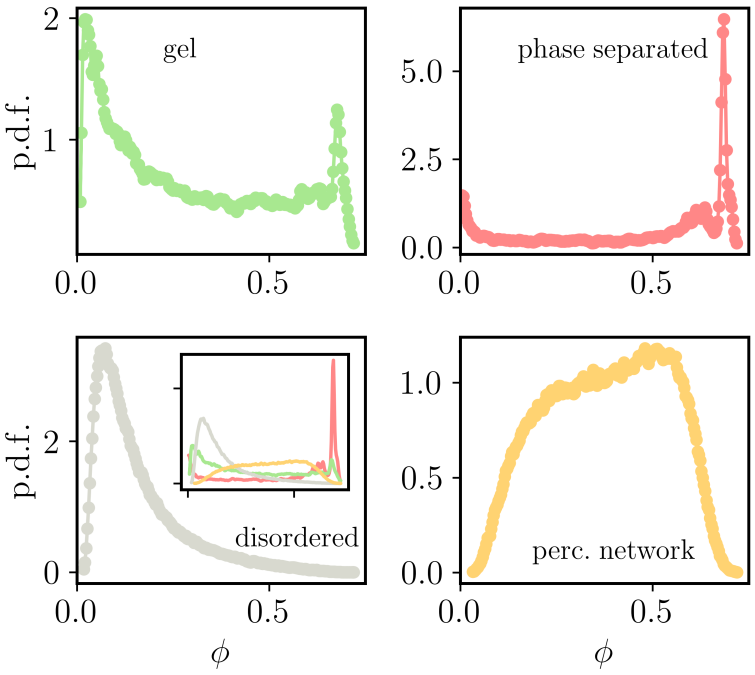

Figure 5.20: **Local Voronoi density.** Distribution of the local packing fraction of Voronoi cells for different global density and Péclet numbers in the four phases: $\phi = 0.10$ and $\mathrm{Pe} = 0$ in the gel, $\phi = 0.10$ and $\mathrm{Pe} = 100$ in the phase-separated state, $\phi = 0.10$ and $\mathrm{Pe} = 200$ in the disordered phase, and $\phi = 0.30$ and $\mathrm{Pe} = 150$ in the percolating network. The high density peak in the gel and phase-separated phase are at the close packing value, shown with a dotted vertical line, while the next one close to it is in between $\phi_{\mathrm{rcp}} \sim 0.64$ and $\phi_{\mathrm{cp}} \sim 0.74$, shown with a dashed vertical line, respectively. Inset: all the distributions plotted together to empathize the relative difference in the peak intensity in the different phases.

The local densities

First of all, we reckon that there are no isolated dumbbells once the steady state is reached. In order to identify the different phases, we developed a method involving the construction of a Voronoi tessellation [OBSC00]. Such a tessellation partitions the simulation box into a set of regions –the Voronoi cells– surrounding each bead such that all points within each cell are closer to the pertaining bead than any other beads. By computing the local packing fraction within each region, ϕ_i, defined as the ratio between a single bead's volume and its Voronoi cell volume, we obtain valuable information about the local packing and structure of the system. In fact, this quantity expresses how much free space the bead has and thus whether it is free, or located in a cluster.

In Fig. 5.20, we present the probability distributions of the local density ϕ_i in the four distinct phases identified in the study (the global density and Pe values are specified in the caption). In each phase the distribution has unique characteristics which can be used as a fingerprint of each phase to classify different configurations.

In the gel phase, the distribution has three well-defined peaks, one at low and two at high density. The low density peak is due to the beads placed on the border of the gel; these beads are located inside very large Voronoi cells and hence return a very low

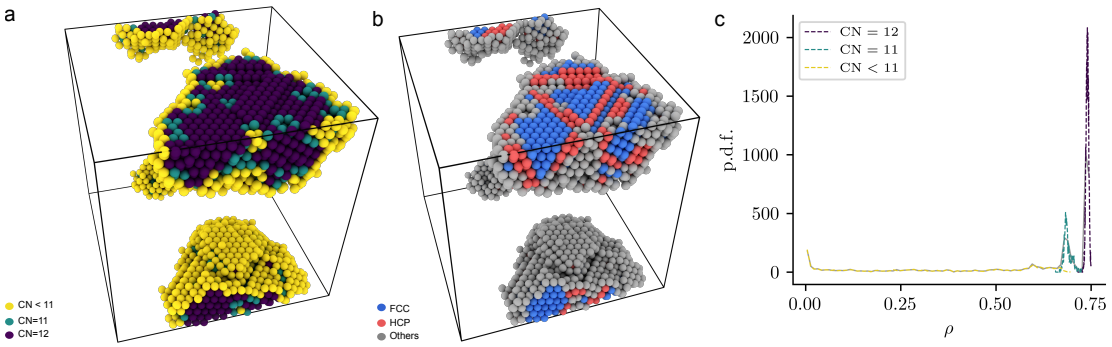

Figure 5.21: **Structural analysis of active clusters.** (a) Snapshot of the system for Pe $= 50$ and $\phi = 0.10$ (phase-separated phase), with particles colored accordingly to the number of neighbouring particles inside a cutoff distance of 1.5σ. (b) Snapshot of the same configurations with particles colored accordingly to the common neighbor analysis [FJ94]. Particles with FCC order are in blue, those with HCP order in red, while particles with no crystalline order are in grey. (c) Distribution of the local packing fraction of Voronoi cells for a configuration in the phase-separated state. The dotted colored lines represent the contribution to the distribution of the beads having a selected Coordination Number (CN), reported in the legend.

ϕ_i. Instead, the high density peaks are due to beads inside the dense regions of the gel. One is centered around the close packing value $\phi_{\rm cp} \sim 0.74$, while the other is at a value in between the random close packing $\phi_{\rm rcp} \sim 0.64$ and $\phi_{\rm cp} \sim 0.74$. We note that for these parameters the low density peak carries more weight than each of the two high density ones. This feature also holds for other values of the parameters corresponding to a gel network.

In the phase-separated systems, the low density peak also corresponds to spheres which are on the single cluster surface. At high local densities, there is a double peak structure with one of the peaks sitting on the close packing density and the other one at a slightly lower value, very similar to what we found in the gel. There is, though, an important difference with the gel data, which resides on the height of these peaks: in the phase-separated phase a much larger portion of particles have the large densities of these two peaks.

To elucidate the origin of the two peaks in the local density distributions of the gel and phase-separated phase, we analyze the relative frequency of beads with different coordination numbers. The coordination number of a bead is defined as the number of its nearest neighbours in the Voronoi sense, that is, two beads are considered to be nearest neighbours if they share a common face of the tesselation, and their centers are located within a distance of $1.5\,\sigma$, Fig. 5.21(a). The data in Fig. 5.21 demonstrate that beads with coordination number 12 contribute to the peak at the close packing value. More precisely, these beads belong to either a face-centered cubic (fcc) or a hexagonal close-packed (hcp) local crystalline structure in the interior of the cluster. As shown in Fig. 5.21 (b), the two structures coexist and both have local density $\phi \simeq \phi_{\rm cp}$, consistently with the location of the purple peak in Fig. 5.21 (c). The secondary peak is associated with beads that have a coordination number equal to 11, and are topological defects that locally disrupt the regular lattice and lower the local packing fraction. The crystalline structure in the bulk of the cluster resembles very closely the high-density ground state of a system of passive dumbbells, which is a so-called *aperiodic crystal*, with all beads arranged on a close-packed ordered structure and disordered bonds be-

tween beads [MD08]. The only difference here is that we see a mix of fcc and hcp structures. This arrangement is very common in close-packed spheres, and the interfacial planes are called stacking faults. We note that our configurations are not ground state and the system is active, so it is reasonable to expect other close-packed structures to be stable. Particles with a lower coordination number contribute to the rest of the distribution and, in particular, to the lower density peak which, as mentioned above, is due to the beads on the surface of the cluster, thus with a smaller number of neighbors compared to the core ones, see Fig. 5.21(a).

In order to distinguish between the gel and phase-separated phases, it is necessary to check the system's motility: in the gel, dumbbells are almost frozen and cannot diffuse, conversely in the phase-separated case diffusion is observed, see Fig. 5.24. More detailed characterizations of the motility of the full system, and of the single clusters of the phase-separated phase, are given in Sec. 5.3 and Sec. 5.3, respectively.

In the disordered phase, the beads are more homogeneously distributed, resulting in an equally partitioned space and the development of only a single peak at small density, around $\phi_i \sim 0.1$. The percolating network has a significantly different ϕ_i distribution. It is broad, with the appearance of all intermediate densities, with almost equal probability. As noted in the fourth row of Fig. 5.19, the system smoothly transitions between the disordered and the percolating phases.

A comparison between the local packing fraction distributions in the four phases can be appreciated in the inset of the lower left panel in Fig. 5.20. In the former, the distributions of the four panels are plotted together. In the latter, the evolution of the distribution with Pe, at fixed $\phi = 0.1$ and $\epsilon = 0.3$ is shown. The variation of Pe takes the system from the gel, across the phase separated and finally to the percolating network phase. We see no signature of discontinuity in the height of the two peaks at high local packing fraction when crossing the transition lines. z

The cluster size distribution

In order to identify the global density ϕ at which the percolating network appears, one can proceed as in the usual analysis of percolation [SA17] and gel [LZC$^+$08, Zac07, ZLC$^+$08] transitions. A common observable to detect a percolating structure is the cluster size distribution, displayed in Fig. 5.22 for $\mathrm{Pe} = 150$ and two packing fractions, $\phi = 0.1, 0.2$. After clustering each conformation using DBSCAN (here modified to account for the fact that in three-dimension the number of first neighbors in a face-centered configuration is 12), we compute the distribution of cluster sizes. Near the density where clusters start to connect to form a percolating network, the cluster size distribution takes a power-law form with an exponential cutoff [SA17] ($\phi = 0.1$ in Fig. 5.22). Notably, the Fisher exponent τ in the algebraic law $N_c^{-\tau}$ matches the one of standard random percolation for a three-dimensional system, $\tau \sim 2.18$, associated to a fractal dimension $d_f \sim 2.53$ by a hyperscaling relation , shown for comparison in Fig 5.22(a,b). Increasing density, percolation starts to occur and the system becomes interconnected, with a large cluster and a few small ones. In this case, the cluster size distribution appears to have a peak at a cluster size of the order of the number of beads in the system ($\phi = 0.2$ in Fig. 5.22).

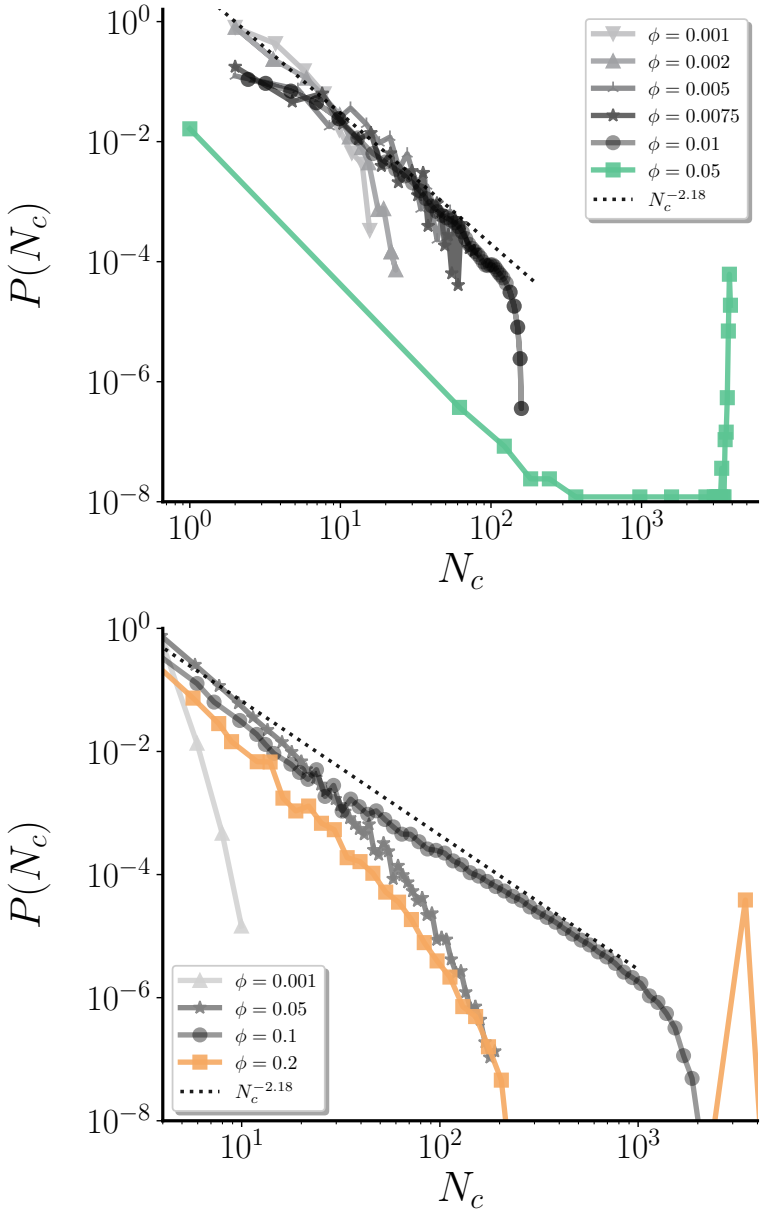

Figure 5.22: **Cluster size distribution in the gel, disordered and percolating network cases.** (a) Probability distribution of cluster sizes N_c at Pe $= 5$, for two values of the global packing fraction $\phi = 0.01$ (grey curve corresponding to the disordered phase) and $\phi = 0.05$ (green curve corresponding to the gel phase). Panel (b) shows the cluster size distribution for $Pe = 150$, and $\phi = 0.1$ (black curve corresponding to the disordered phase) and $\phi = 0.2$ (yellow curve for the percolating network phase). The dotted line corresponds to an algebraic decay $N_c^{-\tau}$ with Fisher exponent $\tau = 2.18$. The cluster size distribution was obtained by counting the number of coarse-grained clusters identified with the DBSCAN algorithm [EKSX96a, DLC+22a, CDL+20b, NCD+22]. For panel (a) 10 different simulations where performed, and for each of them 10^3 configurations where used for sampling. Panel (b) has been obtained using a single run and 5×10^3 configurations, exploiting the shuffling induced by activity.

The phase diagram

The aforementioned observations allowed us to identify at each Pe and ϕ the corresponding phase, and build a complete phase diagram, which is displayed in Fig. 5.23 for the particular case $\epsilon = 0.3$. The analysis of the dynamics which will be presented in Sec. 5.3 will further support this classification.

Let us fix ϕ and discuss the various transitions found upon increasing Pe in Fig. 5.23. At $\phi = 10^{-3}$ (very dilute system), and for all Pe, the system appears to be always disordered. Upon considering $\phi = 0.05$, we observe a small region where the system is in a gel phase, followed by the appearance at $\mathrm{Pe} \sim 10$, or $P_{\mathrm{agg}}^{-1} \sim 1$, of phase separation [4]. This is due to the activity acting as an additional noise, which enables particles to rearrange and d to not get stuck in a metastable conformation. At $\mathrm{Pe} = 150$, or $P_{\mathrm{agg}}^{-1} \sim 12$, activity is high enough so that the phase-separated configurations start to break, and the disordered phase takes over. At a higher packing fraction, *e.g.* $\phi = 0.15$, we also observe a transition between gel and phase-separation, now at a slightly higher Pe or P_{agg}^{-1}. We attribute this increase with respect to what was found for lower ϕ to the fact that at higher densities the gel becomes thicker, and thus more difficult to break. At $\mathrm{Pe} \sim 120$, or $P_{\mathrm{agg}}^{-1} \sim 10$, we observe a transition between a phase-separated phase and a percolating network. Again, activity is strong enough to break the single dense phase, but the density is high enough so that the small clusters are interconnected, forming the network. At still higher ϕ, the behavior remains the same as for $\phi = 0.15$, with the Pe threshold between gel and phase separation slightly increasing with density, and the one between phase separation and percolating network weakly decreasing.

It goes beyond the scope for this article to study in detail the phase behavior at high global densities. Having said so, we observe that for higher global packing fractions the gel phase tends to squeeze the phase-separated regime. We also notice that the percolating network phase squeezes the phase-separated regime for increasing ϕ. In all in all, the extent of the phase-separated (red triangles) region of the phase diagram gets reduced for larger ϕ.

We can now explore the effects of the beads attraction strength ϵ. These can be visualized in a new phase diagram, on the $(\phi, 1/\epsilon)$ plane, built at fixed $k_B T$ and Pe and shown in Fig. 5.23(b). We note that the topology of this phase diagram is very similar to the one in Fig. 2 of Ref. [Zac07] derived for a passive system.

For both $\epsilon = 0.2$ and $\epsilon = 0.4$ we find the four phases described in Fig. 5.20, and a subdivision similar to that in Fig. 5.23 of the regions pertaining to each phase. However, the critical Pe between these phases are shifted. In more detail, for $\epsilon = 0.2$ the transition between gel and phase-separated at low ϕ and the one between phase-separated and percolating network at sufficiently high densities take place at smaller Pe than for $\epsilon = 0.3$. This can be attributed to the fact that both activity and temperature have a higher role in degrading the clustered system as the ratio Pe/ϵ is increased. At the extreme case $\epsilon = 0$ (not shown) we do not see ordering nor structure in the system, at any given Pe or ϕ considered. The phase diagram here presents only a disordered phase. This confirms that attraction plays an essential role in the formation of the aggregates. Conversely, for $\epsilon = 0.4$, there is more than in Fig. 5.23, and it takes a stronger activity to break the clusters. Both gel and phase-separated phases extend towards slightly higher

[4] We stress that the numerical values for the dimensionless numbers that we give here are approximated.

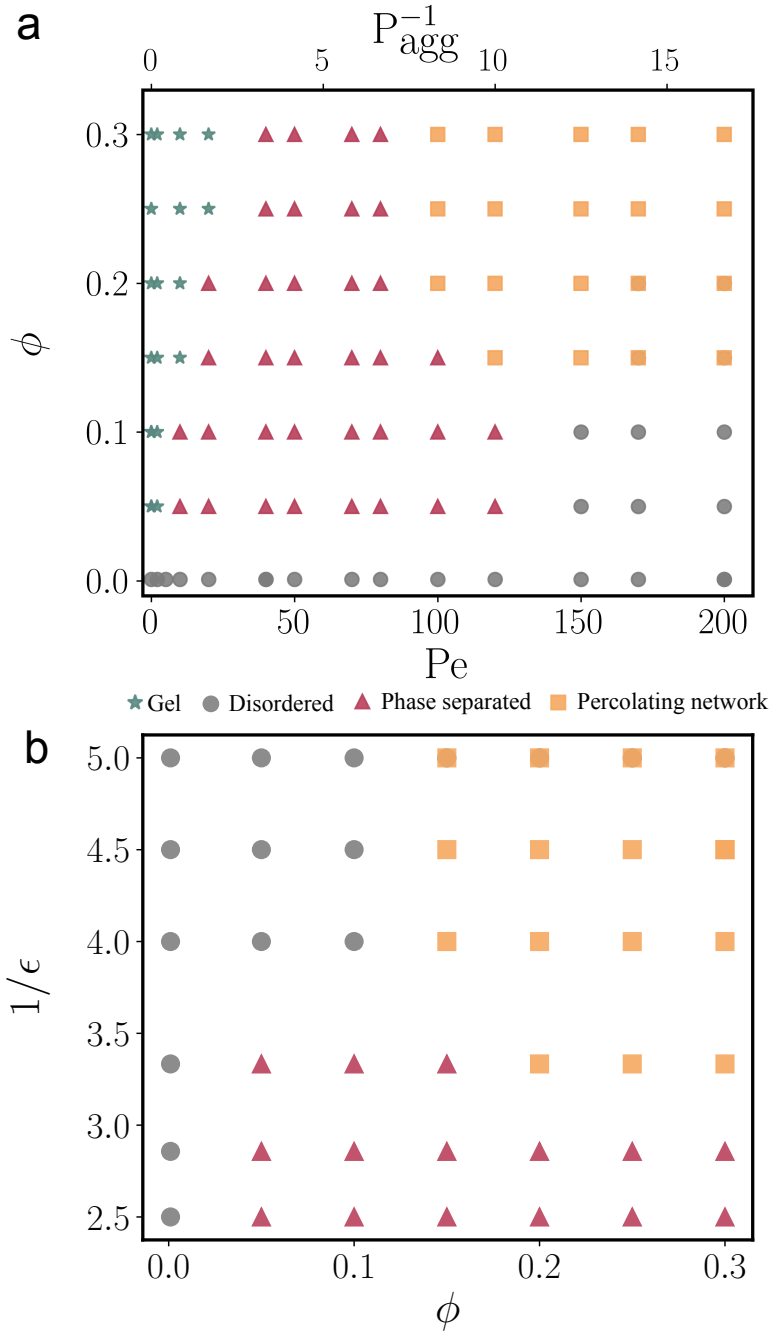

Figure 5.23: **Bulk phase behaviour.** (a) Phase diagram in the Pe-ϕ plane, at fixed $\epsilon = 0.3$. (b) Phase diagram in the $\phi - 1/\epsilon$ plane for Pe $= 100$.

values of Pe at the same packing fraction.

Dumbbells dynamics

We now complement the analysis of the structural properties that led us to the phase diagram in Fig. 5.23 with a characterization of the dynamics. In particular, we measure the global dumbbells' mean square displacement (MSD) in each of the four phases, and the motion of the single clusters formed via phase separation when a non-vanishing active force is applied.

The total mean square displacement (MSD) is the result of the sum of the MSDs of the $2N$ colloids composing the N dumbbells. It is defined as

$$\Delta^2(t, t_0) = \frac{1}{2N} \sum_{l=1}^{2N} \langle (\boldsymbol{r}_l(t) - \boldsymbol{r}_l(t_0))^2 \rangle \ , \tag{5.26}$$

where $\boldsymbol{r}_l$ are the positions of the centers of the spheres. Fig. 5.24 shows Δ^2 for four combinations of parameters ϕ and Pe representative of the four phases we described beforehand. In these plots, we do not explicitly subtract the global motion of the center of mass of the system; however, we checked that the resultant behaviour is not affected by it.

In the gel phase, the MSD is sub-diffusive (green curve in Fig. 5.24(a)). This can be understood in terms of particles being confined within the gel, resulting in limited movement. In contrast, the disordered phase and percolating network (grey and yellow curves in Fig. 5.24(a)) show diffusive motion after a brief ballistic regime.

When considering the phase-separated system (red curve in Fig. 5.24(b)), there is, instead, a ballistic behaviour at long time-scales, characterised by a quadratic behavior $\Delta^2 \sim t^2$, associated to the motion of a single aggregate, as we do not see any particles in the dilute phase. This indicates that the cluster exhibits persistent motion over time, and suggests to analyze its dynamics in more detail.

Single cluster motion

We now characterize the ballistic motion of a single cluster in the phase separated regime. We use a kinematic and dynamical approach to decipher the interplay between frictional dissipation and active forcing which leads to the persistent motion of the active cluster.

Figure 5.25(a) shows a typical trajectory of the center of mass (CoM) of a single cluster (red curve). This trajectory was obtained by extracting one typical cluster from the system and placing it in a box with no gas dumbbells around (in the figure the cluster has been resized to make the trajectory visible). More details of the motion can be appreciated in the video SM Movie 2. The cluster moves along a trajectory resembling a helix. Indeed, its motion can be seen as the composition of a linear motion at constant velocity along the direction defined by the axis of the helix (dashed grey straight line), and an additional rotation around this axis. Notice that $\gamma = 1$ the radius of the helix is of the order of the beads size; therefore, rotational motion around the persistence axis does not significantly contribute to the MSD, as it will be rationalized in the following. Under weaker damping coefficients the oscillatory motion around the propulsion axis has a larger amplitude. We focus here on the behavior under relatively

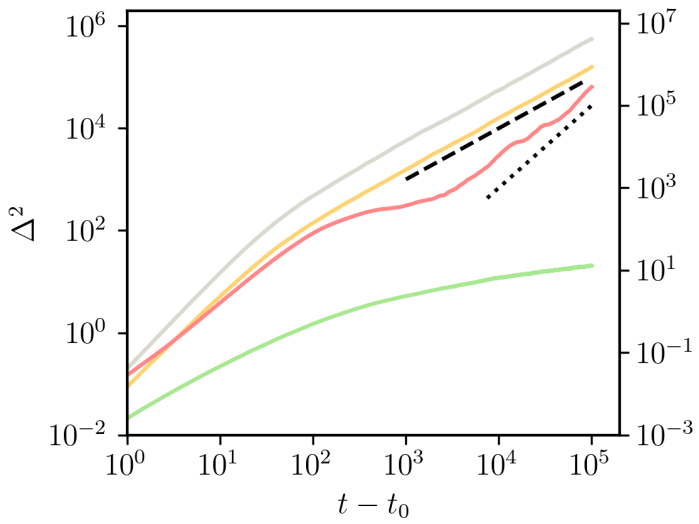

Figure 5.24: **Mean-square displacement** (MSD) in the different phases. Left scale: MSD in the gel (green, Pe = 0 and $\phi = 0.1$), disordered phase (gray, Pe $= 200$ and $\phi = 0.1$) and percolating network (yellow, Pe $= 150$ and $\phi = 0.3$). The percolating network and disordered phases exhibit diffusive behavior at late time delays, as evidenced by the linear fit (dashed line), while the dynamics of the gel is much slower and may also tend to freeze. Right scale: MSD in the phase-separated case (red curve) with Pe = 50 and $\phi = 0.1$. The dotted line represents a quadratic law, suggesting that the motion of the dumbbell clusters is, on average, ballistic in this case.

large γ for which the dynamics is overdamped. Importantly, once the cluster is formed, the beads do not change their arrangement, so that the cluster effectively behaves as a rigid body.

We introduce a new reference frame, with its center placed on a fixed point within the cluster and moving along the axis of the helix with the same persistence velocity of the cluster itself. The axes of this new coordinate system are defined by the unit vectors $\hat{\boldsymbol{\imath}}$, $\hat{\boldsymbol{\jmath}}$, $\hat{\boldsymbol{k}}$ and are chosen in such a way that $\hat{\boldsymbol{k}}$ is the direction of the helical axis and $\hat{\boldsymbol{\imath}}$, $\hat{\boldsymbol{\jmath}}$ are mutually perpendicular so that the triad forms an orthonormal basis for the three-dimensional space. This is shown in Fig. 5.25(a). We stress that such a reference frame is inertial, as it only translates (and does not rotate) with respect to the laboratory frame with constant velocity.

In order to rationalize the dynamics of the cluster, we plot in Fig. 5.25(b) the CoM trajectory during a single helical period on the $\hat{\boldsymbol{k}}, \hat{\boldsymbol{\imath}}$ plane (dashed black line), along with the motion of a generic bead in the cluster (solid blue curve). Two movies in the SM give a three-dimensional view of these motions. By comparing the two, one finds that their motion is periodic with the same period. However, while the CoM trajectory has a sinusoidal profile (with a rather small amplitude), consistently with a circular motion on the $\hat{\boldsymbol{\imath}}, \hat{\boldsymbol{\jmath}}$ plane normal to the helix axis, the bead's motion describes an epicycloid. This is the fingerprint of the composite dynamics of the beads which rotate around the CoM while the latter rotates around the helix axis. Such dynamics is reminiscent of that of the Moon orbiting the Earth and, in turn, rotating on itself with the same period. Analogously, the cluster rotates around the helix axis showing always the same face (see SM Movie 3).

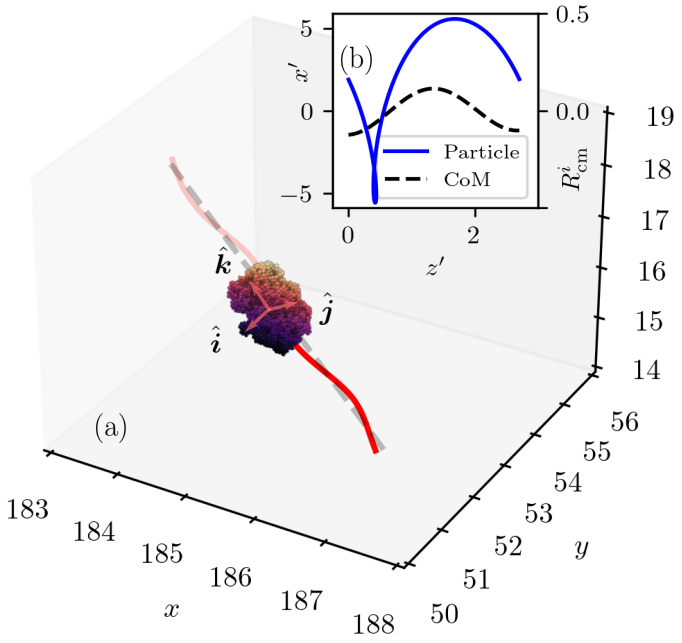

Figure 5.25: **Approximately helical trajectory of a typical cluster.** (a) In red the trajectory of the center of mass of a cluster with $N_c = 3728$ beads, with no surrounding gas, formed by aggregation at $f_{\rm act} = 1$ and evolving at $T = 0$. The size of the cluster has been reduced by a factor of 2.5 to ease the visualization of the trajectory. The scales of the Cartesian axes are measured in units of the bead's diameter σ. The aggregate is, approximately, an ellipsoid of revolution, or spheroid. The approximate lengths of the semi-axes of the associated inertia tensor are $(10.11, 9.71, 13.34)$. The principal eigenvector is roughly parallel to $\hat{\boldsymbol{k}}$ – the direction along which the net force momentum is null – while the remaining eigenvalues associated to the other two eigenvectors are roughly degenerate, taking values $(17.7, 16.2, 37.5)$. In dashed gray the axis of the helix. The $\hat{\boldsymbol{i}}$, $\hat{\boldsymbol{j}}$, $\hat{\boldsymbol{k}}$ Cartesian and inertial coordinate system, superimposed to the cluster, moves along the helical axis with constant velocity. The unit vectors do not change their orientation with respect to the laboratory reference frame, with $\hat{\boldsymbol{k}}$ oriented in the direction of the helical axis and $\hat{\boldsymbol{i}}$, $\hat{\boldsymbol{j}}$ and perpendicular to it. (b) One period of the trajectories of the center of mass (dashed line, right scale), and of one bead in the cluster (blue line, left scale), on the $\hat{\boldsymbol{k}}$, $\hat{\boldsymbol{i}}$ plane. Two movies in the SM highlight these two trajectories in the full three-dimensional space.

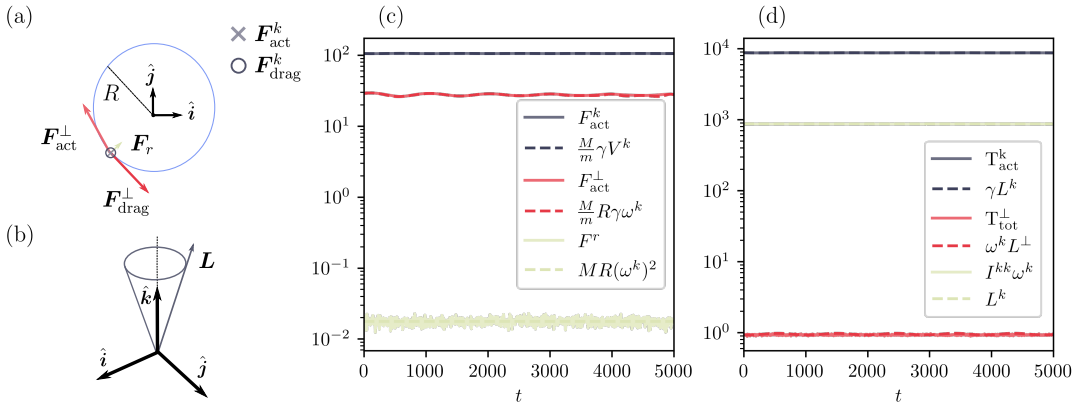

Figure 5.26: **Schematic representation of the forces on the cluster and its helical and processional motion.** (a) Top view, showing the components of $\boldsymbol{F}_{\rm act}$ and $\boldsymbol{F}_{\rm drag}$ on the normal plane, as well as the radial force $\boldsymbol{F}_r$. (b) Side view, showing the processional motion of the angular momentum $\boldsymbol{L}$ around the axis $\hat{\boldsymbol{k}}$. Unit vectors $\hat{\boldsymbol{i}}$, $\hat{\boldsymbol{j}}$ in panels (a) and (b) represent orthogonal basis vectors defining the plane normal to $\hat{\boldsymbol{k}}$. (c) Time evolution of the k and modulus of the perpendicular component of the active force $\boldsymbol{F}_{\rm act}$, and F^r, compared to the theoretical predictions (dashed lines) from the equations described in the text. (d) Time evolution of the active torque $\boldsymbol{\mathcal{T}}_{\rm act}$ and angular momentum $\boldsymbol{L}$, also compared to the theoretical predictions (dashed lines).

We stress that the motion displayed by the cluster in Fig. 5.25 is not a particular case; it is consistently observed for any typical cluster in the phase-separated region of the phase diagram. We have checked that the analysis that we develop below describes the motion of such clusters with number of beads ranging from 100 to 4000. Other clusters with more complex forms and dynamics can also exist (as the result, for example, of the aggregation of two colliding ones) but we do not discuss them here.

To go beyond the kinematic description of the cluster's motion, we now solve its dynamics building on the assumption that the cluster is, for all practical effects, a rigid body. Therefore, the motion can be described by separating positional and rotational degrees of freedom.

The CoM motion is governed by the effects of the total active force and friction. Newton's equation for the CoM position $\boldsymbol{R}_{\rm cm}$ reads

$$M\ddot{\boldsymbol{R}}_{\rm cm} = \boldsymbol{F}_{\rm drag} + \boldsymbol{F}_{\rm act}\ , \tag{5.27}$$

with $M = mN_c$ the total mass of the cluster, N_c the number of particles in the cluster, $\boldsymbol{R}_{\rm cm} = N_c^{-1}\sum_{l=1}^{N_c}\boldsymbol{r}_l$ the position of the CoM, $\boldsymbol{F}_{\rm act} = \sum_{l=1}^{N_c}\boldsymbol{f}_{{\rm act}l}$ the total active force, and $\boldsymbol{F}_{\rm drag} = -(M/m)\gamma\dot{\boldsymbol{R}}_{\rm cm}$ the total drag acting on the center of mass. We stress that internal forces, arising from the Mie potential and bond constraints, do not contribute to the dynamics of the center of mass.

The equations describing the rotational dynamics are given by

$$\dot{\boldsymbol{L}} = \boldsymbol{T}_{\rm drag} + \boldsymbol{T}_{\rm act}\ . \tag{5.28}$$

Here $\boldsymbol{L} = \sum_{l=1}^{N_c}\boldsymbol{r}'_l \times \dot{\boldsymbol{r}}'_l$ is the angular momentum of the cluster computed choosing the CoM as pole, with $\boldsymbol{r}'_l = \boldsymbol{r}_l - \boldsymbol{R}_{\rm cm}$ the position of the $l-$th bead with respect to the CoM. The right-hand-side is the total force momentum, decomposed in a contribution from

the active force $\boldsymbol{T}_{\rm act} = \sum_{l=1}^{N_c} \boldsymbol{r}'_l \times \boldsymbol{f}_{{\rm act}l}$ and another one from the drag force $\boldsymbol{T}_{\rm drag} = -\gamma \boldsymbol{L}$. Once more, torques originating from internal forces do not contribute to the overall rotational dynamics.

Before proceeding, we stress that a peculiarity of this system is that the active force $\boldsymbol{F}_{\rm act}$ and torque $\boldsymbol{T}_{\rm act}$ are solidal to the body itself, so that they undergo the same rotational and translational motion as the rigid body, as beads do not reposition during the trajectory.

With the equations of motion at hand, we are now ready to derive an expression relating forces and momenta with kinematic quantities. First, we observe that the CoM acceleration is null along the $\hat{\boldsymbol{k}}$ direction, therefore the k-th component of the active force is counterbalanced by the drag:

$$F^k_{\rm act} = \frac{M}{m}\gamma V^k \,, \tag{5.29}$$

where $\boldsymbol{V} = \dot{\boldsymbol{R}}_{\rm cm}$, so that, by construction, V^k is the persistence velocity of the cluster along the helix axis, measured in the laboratory reference frame.

Conversely, in the perpendicular plane defined by the unit vectors $\hat{\boldsymbol{i}}, \hat{\boldsymbol{j}}$, the CoM velocity rotates with constant angular velocity $\boldsymbol{\omega} = \omega^k \hat{\boldsymbol{k}}$, see Fig. 5.26(a). As the dynamics of the cluster is also in the overdamped regime, the active force is approximately counterbalanced by the frictional force so that to $\boldsymbol{F}^{\perp}_{\rm act} \approx M\gamma \boldsymbol{V}^{\perp}/m$, with the mismatch $\boldsymbol{F}^r = \boldsymbol{F}^{\perp}_{\rm drag} + \boldsymbol{F}^{\perp}_{\rm act}$ between the active and the frictional force directed radially with respect to the circle in the normal plane. This radial contribution acts as a centripetal force pulling the cluster towards the axis of the helix. It is indeed the combination of the balancing of the forces along the tangent to the cluster trajectory and the centripetal unbalanced radial component that gives rise to the helical motion. Moreover, since the circular motion occurs with uniform velocity $V^{\perp} = \omega^k R$, with R the radius of the circle, the forces can be expressed in terms of the rotational velocity, as follows:

$$F^{\perp}_{\rm act} = \frac{M}{m} R\gamma\omega^k \,, \tag{5.30}$$

$$F^r = MR(\omega^k)^2 \,. \tag{5.31}$$

(Note that in Eq. (5.30) we have dropped the inertial contribution, consistently with the observation that ω^k does not change in time.)

We now test whether the formulæ (5.29)-(5.31) are in agreement with the simulation data. In Fig. 5.26(c), we show the forces considered (continuous lines) as functions of time, and we compare them to the corresponding quantities appearing on the right-hand-sides of Eqs. (5.29)-(5.31) (dashed lines). We find good agreement in all cases. In particular, we notice that the $\hat{\boldsymbol{k}}$ direction roughly coincides with that defined by the principal eigenvector of the inertia tensor $\boldsymbol{I}$ while, instead, the radial force F^r is significantly smaller than the other ones. Moreover, the forces are hierarchically organized, with $F^k_{\rm act} \sim 100$, $F^{\perp}_{\rm act} \sim 20$, and $F_{\rm r} \sim 10^{-2}$, in units of $f_{\rm act}$.

We now proceed with the analysis of the rotational dynamics by assuming that the angular momentum component L^k in the $\hat{\boldsymbol{k}}$ direction remains constant over time – or equivalently drag and active force momenta compensate along $\hat{\boldsymbol{k}}$, i.e. $\gamma L^k = T^k_{\rm act}$. The normal component in the normal plane are constant in modulus, and rotate with angular velocity $\boldsymbol{\omega}$ around the helix axis under the action of the total force momentum

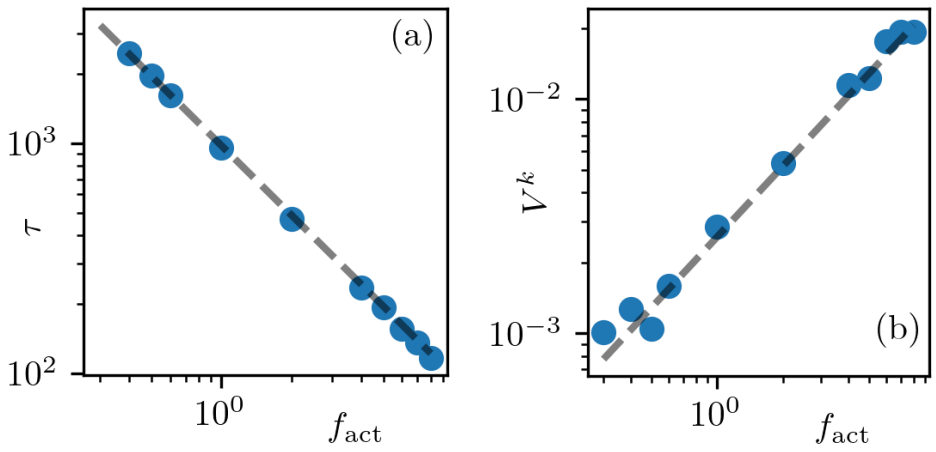

Figure 5.27: **Motion of a cluster** with mass $M = 3728$ at temperature $T = 0$. (a) Rotation period τ as a function of the active force $f_{\rm act}$ on a single bead. The slashed straight line represents the theoretical prediction $\tau \propto f_{\rm act}^{-1}$ in Eq. (5.34), with $\kappa = 48.71$ and $R = 0.204$ measured independently. (b) Linear velocity of the CoM, V^k, as a function of the single bead active force $f_{\rm act}$. The dashed line is the theoretical prediction inverting Eq. (5.29), $V^k = m\ell/(M\gamma)f_{\rm act}$, using $\ell = F^k_{\rm act}/f_{\rm act} \approx 96.34$ (measured independently) and $\gamma = 10$.

$\boldsymbol{T}_{\rm tot} = \boldsymbol{T}_{\rm drag} + \boldsymbol{T}_{\rm act}$. Under these assumptions, it is straightforward to rewrite the time derivative in Eq. (5.28) so that

$$\boldsymbol{\omega} \times \boldsymbol{L} = \boldsymbol{T}_{\rm tot} \ . \tag{5.32}$$

This expression suggests that $\boldsymbol{L}$ performs a precessional motion around the helical axis under the action of transversal force momenta, see also Fig. 5.26(a). Moreover, one can also relate the angular momentum along $\hat{\boldsymbol{k}}$ with the kk component of the inertia tensor so that

$$L^k = I^{kk}\omega^k \ , \tag{5.33}$$

being I^{kk} the helical axis component of the inertia tensor $\boldsymbol{I}$ of the cluster.

These equations are tested against simulations in Fig. 5.26(d), and we find again good agreement. This confirms that the angular momentum performs a precession around the $\hat{\boldsymbol{k}}$ axis with precession angular velocity equal to that of the cluster, confirming *a posteriori* our initial assumption.

As further tests, we checked the dependence of the period on the magnitude of the active force $f_{\rm act}$ derived from Eq. (5.30),

$$\tau = \frac{2\pi M\gamma R}{\kappa m}\frac{1}{f_{\rm act}} \ , \tag{5.34}$$

where $F^{\perp}_{\rm act} = \kappa f_{\rm act}$ with κ a proportionality coefficient measured from simulation data that turns out to be independent of the active force $f_{\rm act}$. To this purpose, we considered the same cluster and we varied $f_{\rm act}$. The results of this analysis show that the period and the active force are indeed inversely proportional, see Fig. 5.27(a), with the proportionality coefficient κ depending on the structural properties of each individual cluster considered, and being consistent with the parameter dependencies in Eq. (5.30) At the same time, we find that the radius R remains constant while we vary $f_{\rm act}$ (not shown).

In fact, inverting Eq. (5.30), one finds that $R = F_{\rm act}^{\perp} m/(M\gamma\omega^k)$, with both $F_{\rm act}^{\perp}$ and ω^k proportional to $f_{\rm act}$, leaving no dependence on the active force.

Finally, we put Eq. (5.29) to the numerical test. We show in Fig. 5.27(b) that V^k is proportional to $f_{\rm act}$ with a proportionality constant which agrees with the parameter dependence of the prefactor in Eq. (5.29).

We stress that the description of the cluster's dynamics is based on the assumption that the rotational velocity $\boldsymbol{\omega}$ is oriented parallel to the helical axis, with negligible transversal components. The latter could lead in principle to more complex effects – such as nutation for instance – which, nevertheless, were not observed in simulations. This also resonates with the fact that in absence of net torques, a rigid body with two degenerate eigenvalues in its inertia tensor would rotate by keeping constant the component of the angular momentum parallel to the non-degenerate eigenvector [Gol59]. Interestingly enough, in our case the particle aggregates indeed exhibit elongated shapes with the principle eigenvector roughly parallel to $\hat{\boldsymbol{k}}$ and the two dimensions being roughly similar, see the values given in the caption of Fig. 5.25. Nevertheless, the motion of the cluster considered here is in general significantly more complicated as, in this case, the net force and torque are not null, leading to a more complex dynamics, with the radial force sustaining the rotational dynamics of the CoM of the cluster, ultimately leading to the intriguing helical motion described above.

To conclude, we investigated the nature of the phase behavior and the dynamics of an active dumbbell system with attractive interactions in three dimensions. We characterized the phase diagram in the (Pe, $\phi \leq 0.3$) plane at fixed $\epsilon = 0.3$ and we elucidated the effect of the strength of the attraction ϵ by studying the stationary state reached at Pe = 100 and parameters in the ($\phi \leq 0.3$, $1/\epsilon \leq 5$) plane. In this way we showed that four cases are realized: a disordered state, a percolating network, phase separation and an active gel. We believe that this phase diagram will serve as a reference for further works on elongated self-propelled particles in $3D$, and also more realistic models that may include hydrodynamic interactions, which are known to play a highly non trivial role in competition with particles' anisotropy and self-propulsion [TWQ$^+$18a, NCD$^+$22].

Next, we focused on characterising the motion of a typical dense cluster in the phase-separated phase. First, we found that these clusters typically take a spheroid form, and for $f_{\rm act} < 10$ displace with constant velocity in a direction which is very close to its main axis of symmetry while performing a rotational motion of very small radius in the transverse plane. All in all, the motion is very close to helical. With some simple arguments, explained in Sec. 5.3, we then related the linear and angular velocities to the strength of the active force acting on the single molecules finding very good agreement with the numerical measurements. The dynamics of formation of these clusters, a full characterization of their morphology and statistics, and many other details are very interesting but fall beyond the scope of this work.

6

Chiral Active Particles

In this chapter, we introduce the third (and last) topic of the PhD project: non-equilibrium systems interacting *via* transverse forces. This class of systems break parity and time-reversal symmetries, defying our fundamental description of soft materials.

We focus in particular on a specific class, the chiral active fluids. These are fluids composed of magnetic spinners driven by an external rotating field. We use such systems as a guide for developing a non-equilibrium "chiral" extension of the well-known Lennard-Jones fluid model in two dimensions, that we study with extensive numerical simulations.

The chapter is organized as follows. In the first section, we describe the Chiral Lennard-Jones fluid and the model we used in our numerical simulations. In the second section, we investigate the phase behaviour of the chiral fluid and adapt the equilibrium thermodynamics tools to analyze it. In the last section, we study the emergence of the edge currents and use them to validate the microscopic measurement of the rotational transport coefficient of the system.

6.1 The Chiral Lennard-Jones Fluid

Salient examples of chiral fluids include suspensions of magnetic colloids driven by an external rotating field [Sne16, SBM$^+$19, MCLH$^+$21, JB22, BBUG$^+$22], and chiral grains put into motion by an inner motor or a vibrated plate [SEP18, WRDD18, YRCZ20, LCSS$^+$22, VRLCRR22]. In spinning colloids, the transverse pairwise forces result from the advection of the flow field generated by their rotation [LJJP03, MCLH$^+$21].

As spinning colloids carry a permanent magnetic moment, they feel a dipolar attractive interaction that make them self-assemble into clusters that eventually coarsen, and the resulting drops sustain steady edge currents at their surface [SBM$^+$19, MCLH$^+$21]. The dynamic properties of such chiral liquid interface have been described within hydrodynamic models, allowing to measure odd transport coefficients that capture the breakdown of parity symmetry in the constitutive equations [BSAV17, SBM$^+$19], akin to odd viscosity in quantum Hall systems [ASZ95, Avr98]. The possibility to control edge states in soft matter has boosted the interest on these systems, both from experiments and theory [FSV23].

Despite recent progress, there is still much to understand about the nature of phase transitions in chiral particle systems, as well as the minimal ingredients needed to sustain such edge currents and their impact on the large-scale behaviour. To address such question, we study a chiral extension of the Lennard-Jones model in two dimensions (2D) [BHA81, RHB90, SF91, LC20], with pairwise, non-conservative, transverse forces. Although dipolar interactions are responsible for the clustering of magnetic colloids [JSK12, JSK13, Sne16, MCLH$^+$21], here we mimic the effect considering attractive and excluded volume interactions. Moreover, extending a well-known paradigmatic reference model allows us to identify the impact of self-spinning on general grounds.

We consider $N = 512^2$ disks located at $\boldsymbol{r}_i$ moving in a $V = L_x \times L_y$ box with periodic boundary conditions (PBC) and obeying the Langevin equation

$$m\ddot{\boldsymbol{r}}_i + \Gamma\dot{\boldsymbol{r}}_i = \sum_{j(\neq i)} [\boldsymbol{f}_{ij} - \boldsymbol{\nabla}_i U(r_{ij})] + \sqrt{2\Gamma k_B T}\boldsymbol{\nu}_i, \tag{6.1}$$

where $\boldsymbol{r}_{ij} = \boldsymbol{r}_i - \boldsymbol{r}_j$, m is the mass of the particles, Γ the damping coefficient, T the temperature and $\boldsymbol{\nu}_i$ a Gaussian white noise with zero mean and unit variance. The disks interact via the Lennard-Jones potential $U(r) = \epsilon\left[(\sigma_d/r)^{12} - (\sigma_d/r)^6\right] + \epsilon$, truncated at $r_c = 5\sigma_d$. Inspired by colloidal spinners [MCLH$^+$21], the disks experience a transverse force $\boldsymbol{f}_{ij} = -\Gamma\boldsymbol{u}_{ij}$ where $\boldsymbol{u}_{ij} = \Omega\sigma_d^3\hat{z} \times \boldsymbol{r}_{ij}/r_{ij}^3$ would be the (far field) flow at $\boldsymbol{r}_j$ generated by a spinning particle at $\boldsymbol{r}_i$ (we use the same cut off r_c). We quantify chirality, and thus the departure from equilibrium, by the non-dimensional parameter $\Omega = \Gamma\Omega\tau^2/m$. Note that we explicit the inertial term $m\ddot{\boldsymbol{r}}$ in Eq. (6.1), although we choose the parameters (see Appendix A for details) in order to be in an overdamped regime and thus the latter can be neglected.

As opposed to mesoscopic descriptions, our particle-based model allows us to investigate how transverse forces affect the phase behaviour of a prototypical soft matter system, exhibiting a liquid-gas phase separation and a fluid-solid transition, and compare the results with experimental findings. Using extensive numerical simulations we establish its phase behaviour, identifying a coexistence region between a dilute gas and a *chiral liquid* (G+CL), followed by a (homogeneous) chiral liquid (CL) and finally a *chiral solid* phase (S). Despite being out-of-equilibrium, we show that phase separation in this system can be well characterized using equilibrium concepts. The resulting chiral liquid shows steady edge currents at its interface, akin to the ones observed in colloidal spinner suspensions. From the analysis of such currents, one can estimate the rotational viscosity, which can also be computed in bulk from the microscopic stress tensor. We compared the two measurements finding a good agreement.

6.2 Phase Behaviour

The Phase Diagram

Having defined the model, we can investigate its phase behaviour. We let the system relax from initial configurations where particles are arranged in a hexagonal lattice (with the spacing fixed by ϕ). Fig. 6.1(a) shows the resulting phase diagram in the (ϕ, Ω) plane at a fixed $k_BT = 0.47$. In the $\Omega \to 0$ limit the transverse force vanishes and we recover the equilibrium 2D Lennard-Jones phase diagram [LC20], that comprises a fluid and a solid phase, together with a liquid-gas and fluid-solid coexistence region.

This differs significantly from other particle models such as in [HFS+21, PL23], since, like colloidal spinners, our particles experience attractive forces, in the presence of fluctuations and dissipation. Our model thus allows for an exploration of the role played by chirality in the (thermal) phase transitions exhibited by an otherwise classical equilibrium system. Indeed, as the density is increased from the homogeneous gas, our system phase separates, a phenomenon inherited from the equilibrium liquid-gas demixing, triggered by attractive interactions, and observed for all the values of Ω explored. We identify a coexistence region (brown area in Fig. 6.1 (a)) in which dense liquid droplets form and coarsen in a gas background (see Fig. 6.1 (b) and the movie[1]). The coexisting densities are not significantly altered by Ω. Beyond, a chiral liquid phase exists for all the Ω values explored, characterized by collective flows and short-range hexatic order, see Fig. 6.1(c). As the density increases the hexatic correlation length grows and eventually diverges, signalling the presence of a chiral solid phase, see Fig. 6.1(c)[2]. The liquid-solid transition shifts towards higher ϕ with Ω. showing that it destabilizes hexatic order. The phase diagram of the model at a lower temperature, $k_BT = 0.35$, is reported in Fig. 6.2. We observe that the coexistence region between the chiral liquid and gas phase expands as the temperature decreases, up to reaching $\phi = 0$ for the lower branch and overlapping the solid transition for the higher density branch at small Ω.

The regions in the phase diagrams are obtained by visual inspection of the simulations and measuring different quantities according to the region of the phase diagram investigated, which we will deal with extensively in the rest of this section. In particular, the coexistence region is obtained through i) the analysis of the local density distribution and the pressure, see Fig. 6.4 and Fig. 6.5(a), respectively. The solid phase boundary is located through the decay of the global hexatic order parameter modulus, see Fig. 6.7(a).

The Structure Factor

Before tackling in depth the analysis of the phase behaviour, we investigate the positional order of the particles in the dense phase and the phase separation kinetics after a quench into the coexistence region. We calculate the structure factor $S(q,t) = N^{-1}\sum_{ij} e^{i\boldsymbol{q}(\boldsymbol{r}_i(t)-\boldsymbol{r}_j(t))}$. The results are reported in Fig 6.3. In Fig. 6.3(a)-(c), we plot the spherically averaged structure factor as a function of time for a fixed chirality $\Omega = 1.0$ at fixed density $\phi = 0.40$ and temperature $k_BT = 0.35$, 0.47, respectively. We find that the peak at low q shifts to smaller values as time progresses, indicating that the domains of the dense phase increase in size, and the system undergoes coarsening. In Fig. Fig. 6.3(b)-(d), we show the structure factor at a fixed time $t = 7 \cdot 10^5$, which is deep inside the long-time scaling regime (the latter starts around $t \sim 10^2$ for all the values of Ω considered), as a function of Ω, again at density $\phi = 0.40$ and temperature $k_BT = 0.35$ and 0.47. The secondary peak corresponding to the crystalline order, located at $q \approx 2\pi/\sigma_d$, becomes broader and lower as Ω grows, suggesting that Ω reduces the local positional order. We observe that for $q \to 0$, $S(q) \sim q$ followed by a second regime $S(q) \sim q^{-d-1}$ at larger wavenumbers, where $d = 2$ is the dimensionality

[1] https://www.dropbox.com/scl/fi/ok9qxouc1qraqu3uooyfh/coarsening_n_262144_t_0.47_om_10.0_rho_0.2.mp4?rlkey=exqc2oomw3kelkbv37af3i2f8&dl=0

[2] Note that we do not wish to make the difference here between a hexatic and solid phase in terms of the nature of orientational and positional correlation functions.

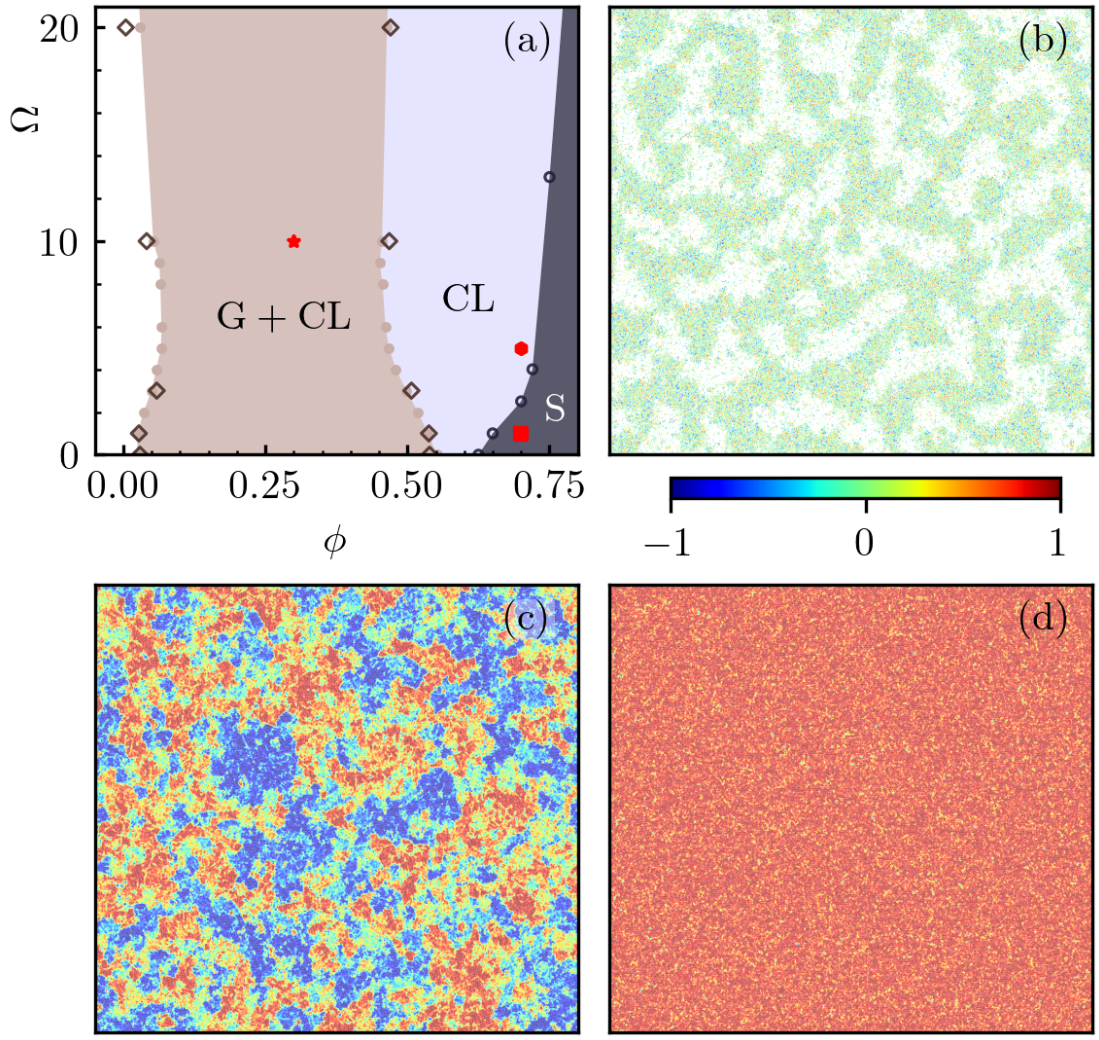

Figure 6.1: (a) Phase diagram at $T = 0.47$ comprising a gas (white), chiral liquid (blue) and solid (grey) phases, and a coexistence region (brown). Filled symbols are obtained from density distributions while the empty ones are from the pressure. Black circles come from the analysis of the hexatic order parameter. (b)-(d) Snapshots of the system corresponding to $(\phi, \Omega) = (0.3, 10)$ (b), $(0.7, 5)$ (c) and $(0.7, 1)$ (d). Particles are colored according to the projection of the local hexatic order $\psi_6(r_i)$ on the global mean orientation.

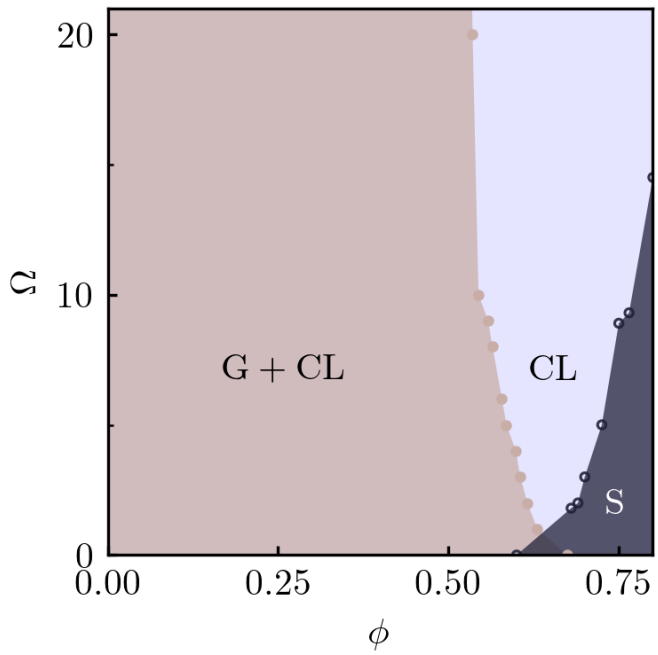

Figure 6.2: The phase diagram of the model at $k_BT = 0.35$, showing the coexistence region between the chiral liquid and gas phases (brown shaded area), the chiral liquid phase (blue shaded area), and the solid phase (dark shaded area). The brown dots indicate the points where the peak of the local density was measured, and the black circles indicate the ones obtained from the behaviour of the global hexatic order parameter $|\Psi_6|$.

of the system, consistently with the predictions of Porod's law for systems with sharp interfaces between coexisting phases [CDL$^+$20c].

Local density distributions

The coexistence of chiral liquid and gas phases is accompanied by the appearance of two peaks in the probability distribution function (PDF) of the local density $\phi(\boldsymbol{r})$ in the system, corresponding to the densities of the coexisting phases. The local density was obtained by dividing the simulation box into cells of linear size $5\,\sigma_d$ and counting the number of particles in each cell (although we checked that the results did not significantly depend on the chosen size of the cells). Figure 6.4 shows the PDF of the local density for different values of Ω at the temperatures $k_BT = 0.35$ and $k_BT = 0.47$ and global density $\phi = 0.30$. The PDF has indeed a bimodal shape. We identified the coexistence densities $\phi_{G/CL}$ by locating the positions of the peaks in the PDF. We observed that the two peaks' location does not change varying the overall global density in the coexistence region (not shown). We found that the density of the gas phase ϕ_G slightly increases with Ω, while the chiral liquid one ϕ_{CL} decreases slightly. This is consistent with the phase diagram shown in Fig. 1 of the main text and Fig. 6.2.

Thermodynamic Analysis

Bringing thermodynamic tools to this new context, we first estimate the coexistence boundary (or binodals) from the density-dependence of the mechanical pressure $P =$

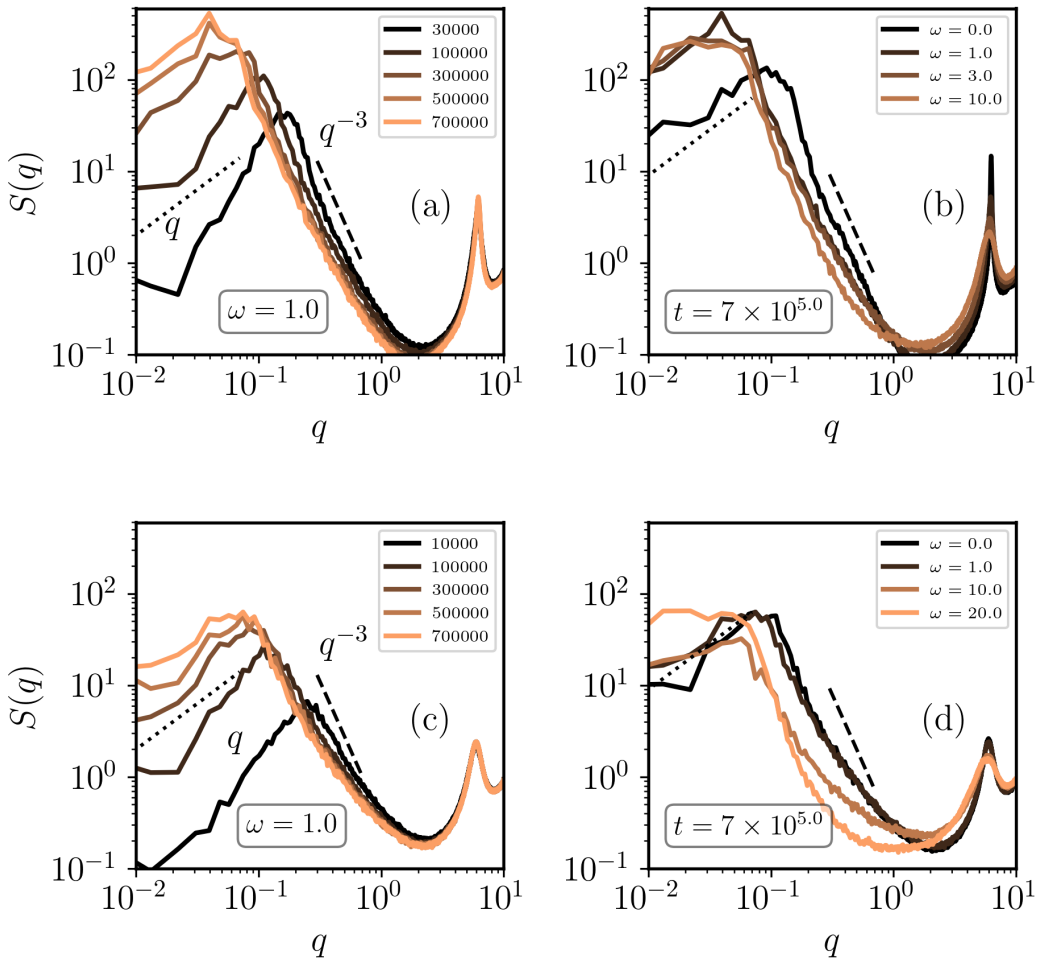

Figure 6.3: The structure factor $S(q,t)$ of the system, showing the coarsening process and the effect of Ω on the positional order, at temperature (a-b) $k_BT = 0.35$ and (c-d) $k_BT = 0.47$, and fixed density $\phi = 0.40$. (a-c) The structure factor at different times for $\Omega = 1.0$. (b-d) The structure factor at a fixed time for different values of Ω. The expected theoretical scaling for $q \to 0$ and for the tail of the distributions in the scaling regime is reported with a dotted and dashed line, respectively.

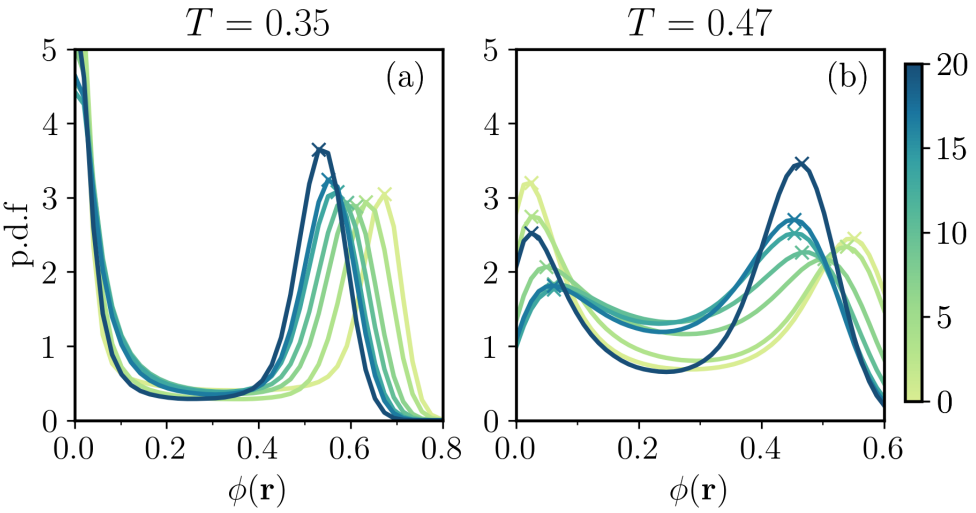

Figure 6.4: The probability distribution function (PDF) of the local density $\phi(\boldsymbol{r})$ for different values of Ω at two temperatures, (a) $k_BT = 0.35$ and (b) $k_BT = 0.47$. The positions of the peaks are found with a local maximum searching algorithm and are shown with crosses. The color map indicates the corresponding value of Ω of each curve.

$-\mathrm{Tr}(\sigma)/2$, given by the trace of the Irving-Kirkwood stress tensor [IK50]:

$$\sigma^{ab} = -\frac{1}{V}\sum_i m v_i^a v_i^b - \frac{1}{2V}\sum_{i,j\neq i} r_{ij}^a F_{ij}^b, \tag{6.2}$$

where $\boldsymbol{F}_{ij} = \boldsymbol{f}_{ij} - \boldsymbol{\nabla}_i U(r_{ij})$ and $a = x, y$ a cartesian component. As $\boldsymbol{f}_{ij}$ is transverse, it does not bring any explicit contribution to the pressure (but it does implicitly via the statistics of collisions) and $P(\phi)$ defines an *equation of state*, shown in Fig. 6.5(a) for different values of Ω. By construction, one recovers the ideal gas law in the dilute limit, where the pairwise interaction among particles vanishes. Then, the pressure shows a double-loop structure characteristic of phase coexistence. In equilibrium, these Mayer-Wood loops are an interface effect in finite size systems, as phase separation brings a free energy excess $\Delta\mathcal{F} = \gamma\ell$, where γ is the interface tension and ℓ the length of the interface. At moderate ϕ, a liquid drop becomes asymptotically circular, while at higher densities, the liquid drop closes onto itself via PBC, resulting in a slab with two flat interfaces, see Fig.6.5 (c,d). As described in Section 2.3, the binodals can be obtained through the Maxwell, or equal-area, construction. Although such construction cannot be readily applied for $\Omega \neq 0$, we use it by extension (as done to identify the coexistence region in systems of active particles [SSW$^+$15b, LCP17b, CDGS17b, DLS$^+$18c, SSC$^+$18a]). The coexistence pressures we obtain for $\Omega = 0$ and 20 are shown in Fig. 6.5 (a). As shown in Fig 6.1(a), we find a very good agreement between the location of the binodals obtained from the equal-area construction and the analysis of the density distribution of Fig. 6.4.

Interestingly, the area of the Mayer-Wood loops increases with Ω. Pushing the thermodynamic mindset further, this would mean that the free energy excess due to the interface is larger in the chiral system. As we are out-of-equilibrium, we can't compute the interface tension from the free energy excess but should rely on a purely statistical mechanical definition [KB49, Eva79]. It can be defined as the difference between the

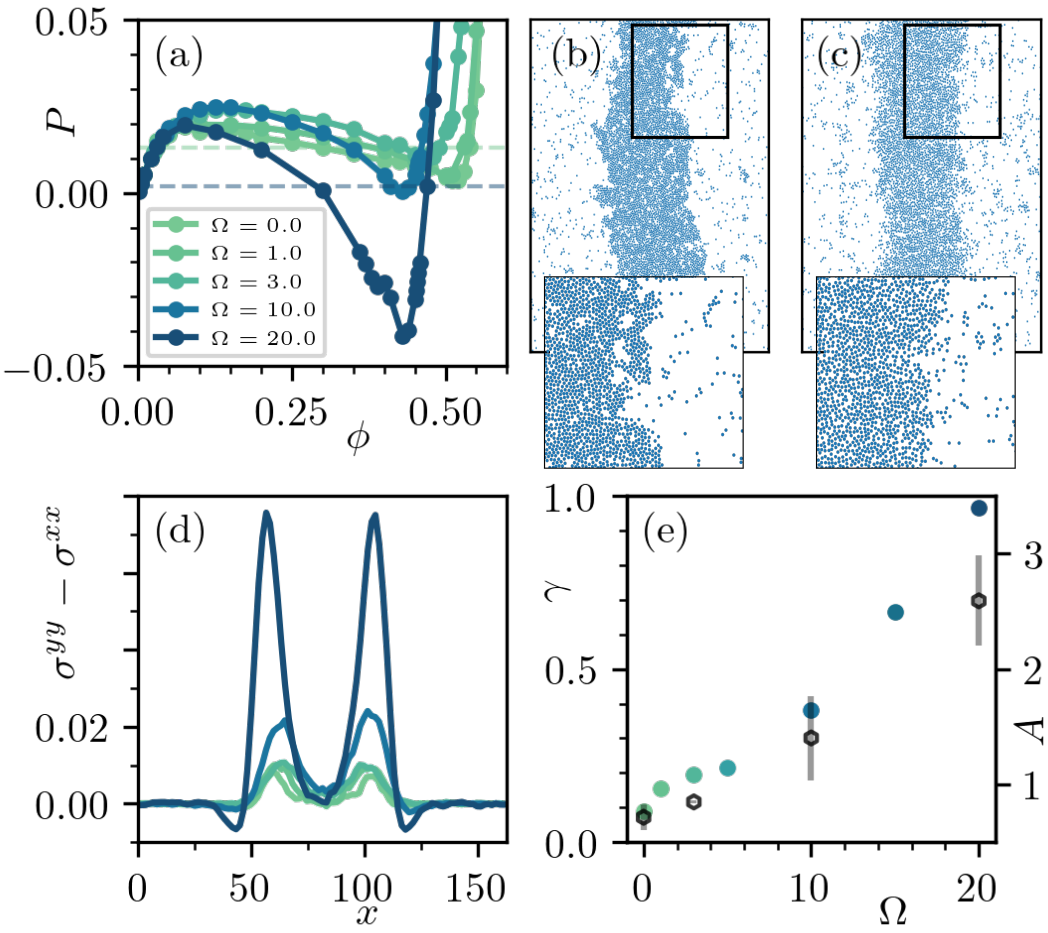

Figure 6.5: (a) Equation of state for different values of Ω at $k_BT = 0.47$. The dotted lines correspond to the equal-area construction applied to $\Omega = 0, 20$ curves. (b-c) Slab configurations at (b) $\Omega = 0$ and (c) $\Omega = 20$ with a detailed view. (d) Corresponding profiles of the difference $\sigma^{xx} - \sigma^{yy}$ and resulting (e) surface tension γ (left y-scale), and area A of the pressure loop ($\times 10^3$) (right y-scale).

normal σ^{xx} and transverse σ^{yy} pressure across a flat interface

$$\gamma = -\frac{1}{2}\int_0^{L_x} dx\,[\sigma^{xx}(x) - \sigma^{yy}(x)]\,. \tag{6.3}$$

To compute γ we prepare the system under conditions for which the interfaces are flat (on average, along y), removing the Laplace pressure contribution. Such slab configurations Fig. 6.5 (b, c) show that the chiral liquid interface is smoother than the equilibrium one. This visually confirms the interpretation that, upon self-spinning, the interface tension increases. To quantify this claim,

We computed the profiles of the tangential stress component σ^{yy}, the normal one σ^{xx} and their difference $(\sigma^{yy} - \sigma^{xx})$ in a slab configuration, oriented with the interface along the y-axis. We calculated a coarse-grained version of the stress tensor over square cells of linear size $2.5\,\sigma_d$, and averaged it along the interface direction (y), obtaining a one-dimensional profile $\sigma^{ab}(x)$. Fig. 6.5(d) displays the difference between

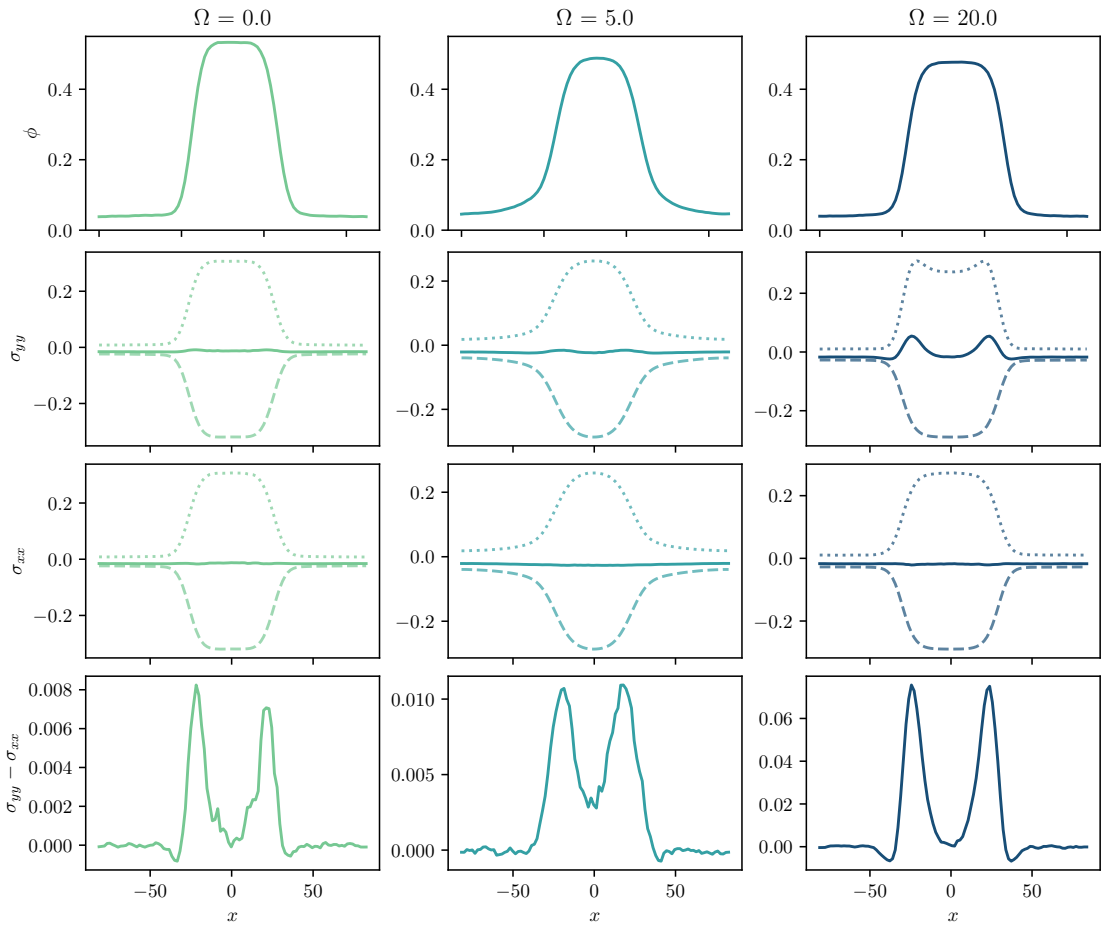

Figure 6.6: Profiles of the normal stress component σ^{xx} (first row), the tangential stress component σ^{yy} (second row), and their difference $\sigma^{yy} - \sigma^{xx}$ (third row) across a slab for $\Omega = 0$, 5 and 20 (respectively, first, second and third column)

.

the two across the slab, showing a similar behaviour as in equilibrium Lennard-Jones [TA99, MPD$^+$05] and active particles systems [BSLS15, PPFD17, HKdLHS19, LKM$^+$21]. As expected, the normal and tangential pressure (reported in Fig. 6.6 for selected $\Omega = 0$, 5 and 20) are identical and constant in the bulk phases. The normal pressure remains constant across the interface, while the tangential one exhibits a moderate drop followed by a fast increase across the interface, signalling that it is first smaller than larger than the normal pressure as we cross the interface from the gas. Such behaviour, present in equilibrium (we find $\gamma = 0.088$ at $T = 0.47$, compatible with previous measurements [SVLVB87, EGRX22]), becomes more pronounced as Ω increases. The explanation relies on the establishment of edge currents (that we will discuss in the next section), that enhance particle collisions at the interface in the tangential direction. As reported in Fig. 6.5(e), the excess tangential pressure results in a growth of γ with Ω, that roughly follows the same trend as the area of the pressure loops, supporting the thermodynamic description of phase coexistence developed so far.

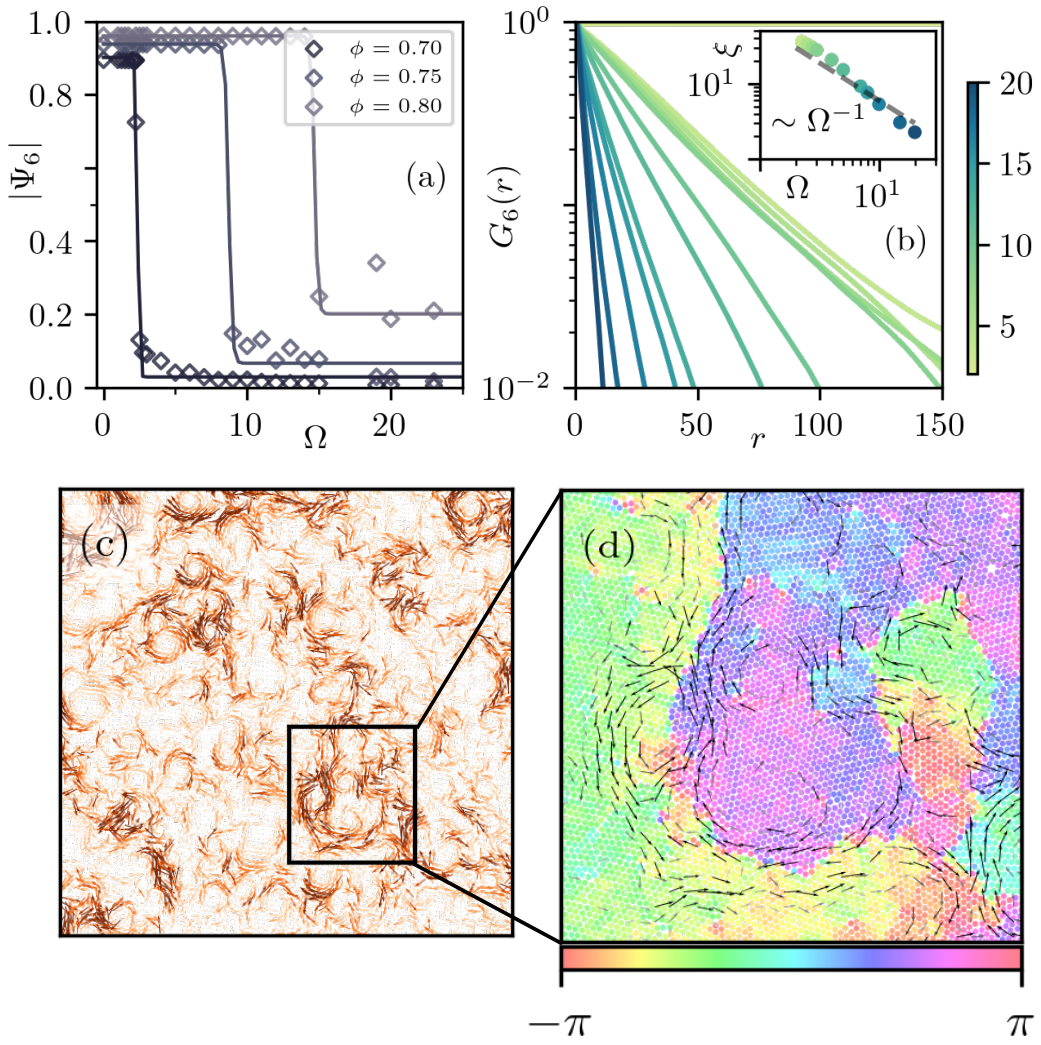

Figure 6.7: (a) Global hexatic order $|\Psi_6|$ as a function of Ω at fixed $k_BT = 0.35$, for three different densities. The solid line is a hyperbolic tangent fit. (b) Exponential decay of $G_6(r)$ for systems at $\phi = 0.70$ and different values of Ω, shown in the colormap. Inset: corresponding correlation lengths ξ. (c) Displacement field $\delta\boldsymbol{r}$ in a chiral liquid configuration ($k_BT = 0.35$, $\phi = 0.70$, $\Omega = 3.0$), (darker arrows indicate larger displacements). (d) Detailed view showing the local bond orientation $\mathrm{Arg}(\psi_6)$ together with particle displacements.

Melting and Flow

In equilibrium, the system is solid for densities higher than a threshold ϕ_s (≈ 0.6 at $k_BT = 0.35$ and ≈ 0.62 at $k_BT = 0.47$) (Fig. 6.1 (d)). By turning on Ω, we introduce extra stresses that can eventually melt the solid, breaking its long-range orientational order and resulting in a chiral liquid state composed of rotating hexatic patches, see Fig. 6.7 (c,d) and in the movie[3]. To quantify it, we use the hexatic order parameter $\psi_6(\boldsymbol{r}_j) = n_j^{-1} \sum_{k \in \partial_j} e^{i6\theta_{jk}}$, where θ_{jk} is the angle formed by the segment connecting

[3] https://www.dropbox.com/scl/fi/w75g8878tlxelzxqxt47z/solidmelting_n_262144_t_0.35_om_3.0_rho_0.7.mp4?rlkey=ctro4c65sem2coox87qab01zw&dl=0

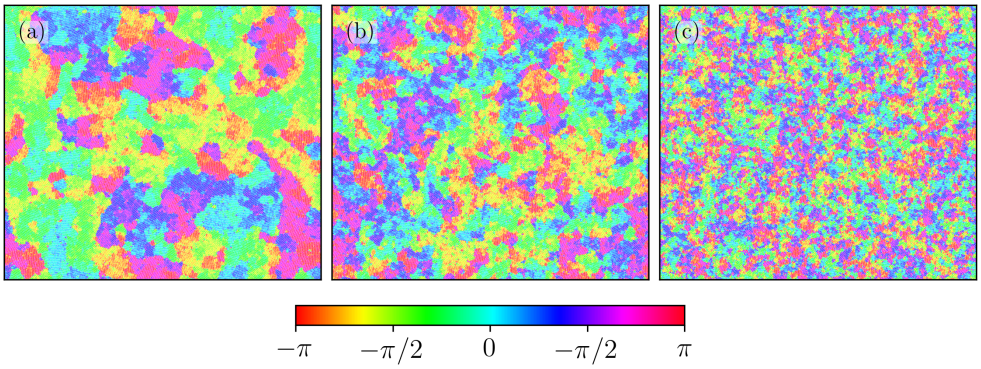

Figure 6.8: Colormap of the hexatic local bond order parameter Arg(ψ_6) (as defined in the text) for configurations at fixed $\phi = 0.70$ and different Ω: (a) $\Omega = 3.0$, (b) $\Omega = 5.0$ and (c) $\Omega = 10.0$, respectively.

the center of the jth disk with a nearest neighbor (out of n_j) and the x-axis. As shown in Fig. 6.7 (a), the global hexatic order parameter $|\Psi_6| = \sum_{i=1}^{N} |\psi_{6i}| / N$ exhibits sharp drop at a critical value Ω_c, that shifts to higher values with ϕ. We determine Ω_c with a hyperbolic tangent fit and report its values in the phase diagram Fig 6.1(a) and Fig. 6.2 as delimiting a solid from a chiral liquid phase. We compute the correlation function $G_6(r) = \langle \psi_6(r)\psi_6(0) \rangle$ to quantify the typical size of the hexatic domains observed [NCD$^+$22, CDL$^+$20c]. As shown in Fig. 6.7(b), G_6 decays exponentially, defining a characteristic length scale ξ that scales as $\sim \Omega^{-1}$. Such decay of a typical length associated with a spatial pattern induced by chirality has also been found in chiral active matter models [LL17, SSLP22], planar rotors [RL21] and experiments of chiral colloids [MCLH$^+$21, BBUG$^+$22]. Selected snapshots at $\Omega = 3$, 5 and 10 are reported in Fig. 6.8, supporting the result that the typical length of hexatic domains become smaller upon increasing Ω.

The dynamics of the dense chiral liquid is highly heterogeneous, as particles close to the hexatic domain walls are mobile while the ones within remain roughly frozen. The snapshot, Fig. 6.7(c), together with its detailed view, Fig. 6.7(d), showing both the displacement field and the local orientation of the hexatic domains, Arg($\psi_{6,i}$), show that particle flow is localized around the boundaries of the domains, while inside each patch particles are frozen. These domains are a consequence of the transverse interaction, as in equilibrium one would get global hexatic order in this regime, and are responsible for the fluidization of the system. The domains can slide over each other, resulting in a 'swirling motion' akin to what is observed in experiments [BBUG$^+$22].

6.3 Edge Currents

Velocity Profile of a Chiral Droplet

In the hydrodynamic description (see Appendix E), chirality introduces a *rotational viscosity* η_R that can be estimated from the analysis of the edge currents [SBM$^+$19, PL23]. Indeed, hydrodynamic models predict a localized flow at the surface of a chiral liquid drop of radius R, which is linked to the rotational viscosity. Rewriting the momentum equation of a chiral liquid described in Appendix E in cylindrical coordinates, assum-

ing an azimuthal flow $\boldsymbol{v} = v(r)\hat{\theta}$, one obtains for the radial component of the pressure $\partial_r p(r) = 0$, and for the azimuthal one:

$$r^2\partial_r^2 v + r\partial_r v - \left(1 + \frac{1}{\delta^2}r^2\right) v = 0, \tag{6.4}$$

with δ a characteristic penetration length $\delta = \sqrt{(\eta_0 + \eta_R)/\mu}$, where η_0 and η_R are the shear and rotational viscosity, respectively, and μ the friction coefficient.

Eq. (6.4) is satisfied by $v(r) = AI_1(r/\delta)$, where I_1 is the modified Bessel function of the first kind and A a constant. Using the boundary condition $\sigma\hat{\boldsymbol{r}} = -\gamma/R\hat{\boldsymbol{r}}$, with γ the surface tension, one can fix the constant A and the value of the pressure p obtaining the relations

$$p = \frac{\gamma}{R} + \eta_0\frac{u(R)}{R} + p_0, \tag{6.5}$$

$$v(r) = \frac{\eta_R I_1(r/\delta)}{\eta_0 I_2(R/\delta) + \eta_R I_0(R/\delta)} 2\Omega\delta, \tag{6.6}$$

valid for $r \leq R$. Using (6.6), the edge velocity $v_e = v(R)$, i.e. the tangent velocity of particles v_t right at the chiral drop interface, can be expressed in terms of η_R:

$$v_e \approx 2\Omega\delta\frac{\eta_R}{\eta_0 + \eta_R}. \tag{6.7}$$

Therefore, using the definition of δ, one can estimate the rotational viscosity from the analysis of the particles' velocity profile within a chiral drop, as

$$\eta_R = \frac{\Gamma\delta v_e}{2\Omega}. \tag{6.8}$$

Note that we have used here the damping coefficient Γ of Eq. (6.1) as the friction coefficient; we will justify this assumption later in the text.

We now proceed to measure the velocity profile and extract the parameters δ and v_e needed for obtain η_R in Eq. (6.8). We let a spherical drop relax to its steady state at a fixed Ω. As shown in Fig. 6.9(a,b) and movie[4], the visual inspection of simulations confirms that a localized current of particles establishes, for any Ω, at the liquid-gas interface. We then measure the velocity field $\boldsymbol{v}(t) = \delta\boldsymbol{r}(t)/\delta t$ from particle displacements $\delta\boldsymbol{r}(t) = \boldsymbol{r}(t + \delta t) - \boldsymbol{r}(t)$ over a time interval $\delta t = 10^3\ \tau$[5]; this is to reduce the effect of the noise related to the thermal bath.

We then coarse-grain the tangential component of the velocity over circular sectors, and spherically averaged it, obtaining a one-dimensional profile $v_t(r)$ that depends only on the distance from the center of mass of the droplet. Fig. 6.9(c) shows these profiles: $v_t(r)$ is almost zero across the bulk of the droplet, and increases exponentially towards the edge. We then fit our data with Eq. (6.6) and find that, in agreement with hydrodynamics and experiments [SBM$^+$19], δ appears to be independent of Ω while v_e grows linearly, see Fig. 6.9(d). Combining δ and v_e in Eq. (6.8) we extract a rotational viscosity $\eta_R \approx 1.32$, reported in Fig. 6.9(d).

[4] https://www.dropbox.com/scl/fi/xw6u5499vja8djw99p3jz/movie_droplet_n_16384_t_0.35_om_5.0_rho_0.2.mp4?rlkey=nll44vyryb4581pagwclwepxz&dl=0

[5] We checked indeed that the time interval δt for computing the displacement field was larger than the typical relaxation times of the particles inside the droplet

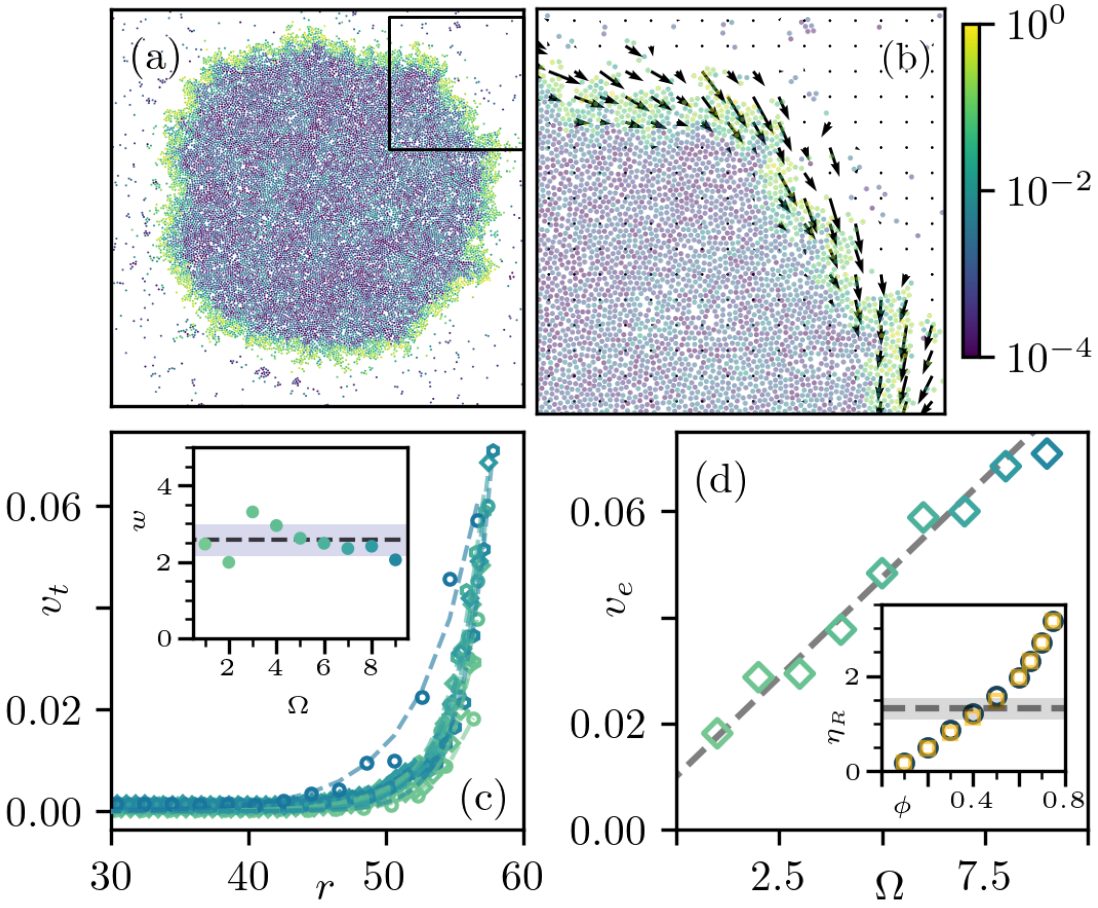

Figure 6.9: (a) A chiral drop at $T = 0.35$ and $\Omega = 5.0$. The global density of the system is $\phi = 0.2$ with $N = 16384$ particles. Particles are colored according to their velocity (normalized by the fastest particle in log scale). (b) Detailed view of the configuration showing the velocity field. (c) Tangential velocity as a function of the distance from the droplet center for $\Omega = 1...9$. The exponential fits (discontinuous lines) allow the extraction of the values of δ shown in the inset, with the dotted line representing the average value $\delta = 2.57 \pm 0.42$. (d) Dependence of the edge velocity v_e with Ω, showing a linear growth. Inset: $\eta_R(\phi)$, from the computation of σ^{xy} for $\Omega = 3.0$ (yellow) and $\Omega = 10.0$ (blue) together with the estimation from the edge currents $\eta_R = 1.32 \pm 0.22$ (dotted line).

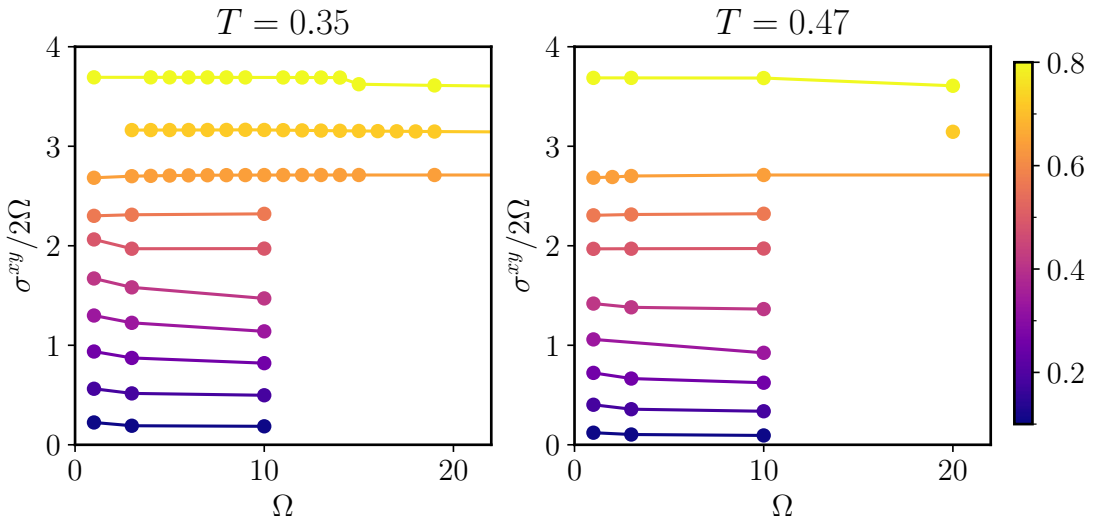

Figure 6.10: Rotational viscosity $\eta_R = \sigma^{xy}/(2\Omega)$ for (a) $k_BT = 0.35$ and (b) $k_BT = 0.47$, at different values of Ω, and colored according to the system's density ϕ (reported in the colorbar).

.

Rotational viscosity from the microscopic stress tensor

One can also put the hydrodynamic description aside and provide a measurement of η_R from the microscopic dynamics, provided by the expression of the stress tensor in Eq. 6.2. Indeed, from the hydrodynamical description (see Appendix E), one obtains in absence of a global vorticity and of shear stress that

$$\eta_R = \frac{\sigma^{xy}}{2\Omega}. \tag{6.9}$$

Note that here we are identifying the hydrodynamical stress with the Irwing-Kirkwood microscopic expression. This identification is strictly valid at equilibrium, and there are no guarantees that the same holds in this system. The only justification for doing so is the *a posteriori* good agreement with the expression of the rotational viscosity obtained in this way with the one of Eq. (6.8).

The rotational viscosity obtained through Eq. (6.9), as a function of on Ω and ϕ and temperatures $k_BT = 0.35$ and $k_BT = 0.47$, is reported in Fig. 6.10. We find that the stress tensor is largely independent of temperature and of Ω, and mostly depends on the density of the system. In particular, in Fig. 6.9(d) is reported the dependence with ϕ for $\Omega = 3,\ 10$. They show that η_R grows with ϕ but has little dependence on Ω. For $\phi = 0.6$ - slightly above the density of the dense drop in this case - the value of η_R extracted in the homogeneous chiral fluid from the microscopic stress tensor, $\eta_R \approx 1.9$, is reasonably close the one estimated from the edge currents in the coexistence regime.

The microscopic expression of η_R, Eq. (6.9), is most useful, as it provides a systematic route to compute it in the absence of distinct interfaces [SBM$^+$19] such, for example, in the homogeneous chiral liquid phase. The demonstration that it gives comparable results to the hydrodynamical one represents a central result of our work.

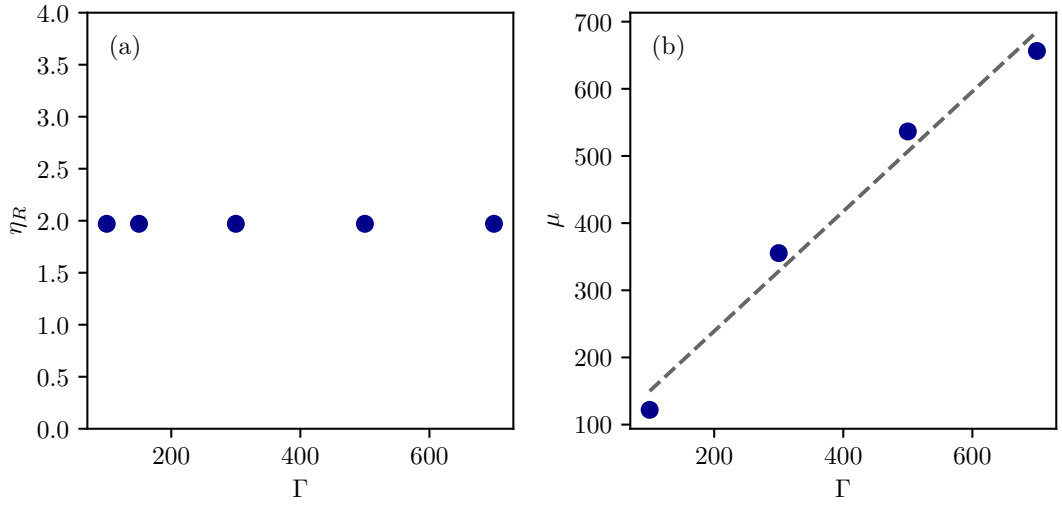

Figure 6.11: (a) Rotational viscosity η_R as a function of damping coefficient Γ in an homogeneous system at $\Omega = 3.0$, $\phi = 0.60$ and $k_BT = 0.35$. (b) Friction coefficient μ as a function of the damping coefficient Γ. The dotted line is a linear fit $\mu = a\Gamma + b$, with $a = 0.89 \pm 0.09$ and $b = 60.69 \pm 41.16$.

Estimation of the friction coefficient

Now we demonstrate by a numerical experiment the relation $\Gamma = \mu$ we used in Eq. (6.8). To this end, we perform simulations with different values of the damping coefficient of the model Γ in (homogeneous) systems with $\Omega = 3.0$ and $\phi = 0.60$ at $k_BT = 0.35$. From the simulations, we compute the rotational viscosity from the stress tensor as $\eta_R = \sigma^{xy}/2\Omega$. We find it to be independent of Γ, as shown in Fig. 6.11(a).

Next, we simulate a chiral fluid drop, similar to the one shown in Fig. 6.9, with fixed $\Omega = 3.0$ at $k_BT = 0.35$ and varying Γ. We measure the edge velocity as a function of the damping coefficient $v_e(\Gamma)$. By inverting the first expression for η_R, we then obtain the relation

$$\mu(\Gamma) = \frac{2\Omega\eta_R}{\delta v_e}, \tag{6.10}$$

which we show in Fig. 6.11(b), obtained using the values of η_R measured from the homogeneous system and $v_e(\Gamma)$ measured from the fluid drop. Finally, We fit the data with a linear function, $\eta_R = a\Gamma + b$, which yields $a \sim 1$ and, therefore, $\mu \approx \Gamma$.

In summary, introducing transverse forces to an otherwise standard Lennard-Jones system, is enough to generate edge currents and, at large densities, a mosaic of rotating domains with a characteristic length, as observed in experiments [SBM+19, MCLH+21, BBUG+22]. The breakdown of parity symmetry leads to a rotational viscosity, a transport coefficient that can be measured from the microscopic stress tensor, providing results compatible with the predictions of hydrodynamic models. This gives hope for the development of systematic derivations of Irving-Kirwood kind of formulas relating the transport coefficients appearing in the constitutive equations of chiral systems and the microscopic particle variables [FS16]. The impact of chirality on the liquid-gas transition can be well rationalized using the thermodynamics of phase coexistence: chirality

increases the liquid-gas interface tension, giving rise to larger Mayer-Wood loops in the equations of state, that allows locating the binodals, applying the equal-area construction. Overall, our work provides a simple framework to investigate how chirality affects the liquid and solid phases of matter from a statistical mechanics viewpoint.

Conclusions

In this thesis, we have studied the aggregation and the dynamics of active particle systems, utilizing numerical simulations and minimal models that capture the essential physics of the active systems considered. We focused on three principal topics (i) investigate the differences between a passive (equilibrium) phase separation and the active counterpart, the Motility-Induced Phase Separation; (ii) the role played in the aggregation process by the shape of the constituents and by the dimensionality of the system; (iii) the effects in the phase separation process of introducing transverse interactions among colloids. Our main findings can be summarized as follows.

- **MIPS morphology and kinetics** We have shown that the morphology of the dense phase of MIPS in two-dimensional ABPs is more complex than an equilibrium one: on top of the dense-dilute phase separation, governed by a $t^{1/3}$ growing length in the scaling regime, $2d$ MIPS exhibits a microscopic phase separation of domains with different lattice orientations and cavitation bubbles, whose size can be controlled by the activity.

  We have also uncovered the role of Active Clusters in the phase separation process and in the growing mechanism of the dense phase. Passive small clusters evaporate (à la Ostwald ripening) while active ones can break and sometimes recombine, and grow through cluster-cluster collisions, although the global growth laws in MIPS and equilibrium phase separation are both $\sim t^{1/3}$.

- **Effects of inertia and hydrodynamics** We have studied with extensive simulations the role of inertia and hydrodynamics in active colloids and showed how they affect the liquid-hexatic transition in an intermediate activity regime in which MIPS does not occur. We discovered that inertia has an orientational ordering effect on the system, counteracting the disordering role of self-propulsion. On the other hand, we found that hydrodynamics has the opposite effect, orientationally disordering the system.

- **Aggregation of anisotropic active particles** We have explored the role of the particle shape in the MIPS aggregation process, using a minimal model of elongated particles, the active dumbbells. We have shown that the morphology of the MIPS differs from the standard ABPs model, as the grow law exponent depends on the activity and dense phase forms clusters with uniform orientational order. In three dimensions, we have shown that MIPS is suppressed and that active dumbbells exhibit a rich phase behavior, depending on the activity and the attractive interaction. Both in $2d$ and $3d$, we developed a dynamic model to explain the active dumbbell clusters' motion.

- **Chiral Active Particles** We have studied a chiral extension of the Lennard-Jones model in two dimensions, with pairwise, non-conservative, transverse forces. We have derived the non-equilibrium extension of the Lennard-Jones phase diagram, finding that chirality affects both the coexistence and the liquid and solid phases of matter, reducing the local positional order and inducing edge currents at the interface of the dense droplets. We have also validated the measurements of the edge currents using a hydrodynamic theory, and estimated the rotational viscosity of the chiral fluid.

While this work sheds light on the these aspects of active systems, significant questions remain unanswered. A comprehensive understanding of active systems and their full technological potential necessitates further exploration. We hope this study serves as a springboard for future research, inviting in particular for a confrontation through experimental systems.

A

Numerical Methods

In this Appendix, we explain the numerical techniques that we used to identify the dense phase, or droplet, the hexatic domains and the gas bubbles.

A.1 Parameters and integration of the numerical simulations

Numerical integration

We used a Velocity Verlet algorithm in the NVT ensemble, where the number of particles N, the simulation box V and the temperature T are fixed. The algorithm solves Newton's equations of motion with the addition of two force terms, friction and noise, which mimic a Langevin-type thermostat [Tuc09].

Before integration, we express all units in non-dimensional units. We use the mass m, length σ and energy ϵ as a basis for the other units and then set $m = \sigma_d = \epsilon = 1$. In Section 3.1, we set the time unit to $\tau = 1/D_\theta$, meanwhile, in the other Sections we set the time unit to $\sqrt{m\sigma_d^2/\epsilon}$.

The algorithm integrates at time t the position $\boldsymbol{r}_i$ and the velocity $\boldsymbol{v}_i$ of each particle in the simulation:

$$\boldsymbol{r}_i(t+\delta t) = \boldsymbol{r}_i(t) + \dot{\boldsymbol{v}}_i(t)\delta t + \frac{\boldsymbol{F}_i(t)}{2m_i}\delta t^2 \tag{A.1}$$

$$\boldsymbol{r}_i(t) = \boldsymbol{r}_i(t+\delta t) - \dot{\boldsymbol{v}}_i(t+\delta t)\delta t + \frac{\boldsymbol{F}_i(t+\delta t)}{2m_i}\delta t^2 \tag{A.2}$$

where δt is the chosen timestep. Combining the two equations, one obtains

$$\boldsymbol{v}_i(t+\delta t) = \boldsymbol{v}_i(t) + \frac{\boldsymbol{F}_i(t+\delta t) + \boldsymbol{F}_i(t)}{2m_i}\delta t. \tag{A.3}$$

Eqs.(A.3) and A.2 give the updates to the position and velocity of the particles at the next timestep $t + \delta t$ according to this scheme:

1. Computing $\boldsymbol{r}_i(t+\delta t)$ using Eq.(A.2);

2. Computing forces from the interaction potential using the new particles' positions;

3. Computing $\boldsymbol{v}_i(t+\delta t)$ using Eq.(A.3)).

In order to mimic the bath at temperature T, the integration is supplemented with a thermostat, which guarantees the temperature remains constant throughout the simulation. In general, this operation is obtained through a fictitious drag force, which modifies the velocity of the particles, in a way that the latter obeys the equipartition theorem. The new equations of motion therefore read

$$m_i \ddot{\boldsymbol{r}}_i = \boldsymbol{F}_i - \gamma(t) m_i \boldsymbol{v}_i, \tag{A.4}$$

where γ is computed as

$$\dot{\gamma} = \frac{1}{Q}\left[\sum_i^N m_i \frac{\boldsymbol{v}_i^2}{2} - N k_B T - \frac{1}{2} k_B T\right], \tag{A.5}$$

where Q is a parameter. A modified approach is required for thermostatting Langevin equation [SS78]. Here, the fictitious force term reads

$$\boldsymbol{F}_i^{\text{tot}} = \boldsymbol{F}_i - m\gamma(t)\boldsymbol{v}_i(t) + \sqrt{\frac{2 m_i \gamma k_B T}{\delta t}}\boldsymbol{\zeta}_i(t). \tag{A.6}$$

To integrate the equation of motion, we used the open-source software Large-scale Atomic/Molecular Massively Parallel Simulator (LAMMPS) [TAB+22], which enables us to perform a simulation in parallel using multiple CPUs. On average, a typical simulation lasting $\approx 10^4\ \tau$ was run on 96 processors for a total of 72 hours on each CPU. In the main text, we do not write the time units explicitly.

In the case of dumbbells, both its beads are constrained at fixed distance via the SHAKE algorithm, which adjusts the positions of the beads by applying an additional force so that to fix the bond length at the next iteration step. The required force vector at each iteration is found by solving a system of linear equations [RCB77]. The integration timestep used was $\delta t = 0.005$ whose assured numerical stability for the parameter range we used.

Parameters

Here we report the parameters we use in the numerical simulations described throughout the Thesis.

Simulations of Section 3.1

We fixed $\gamma = 10$ and $k_B T = 0.05$, which ensures the dynamics are in the overdamped regime. The time unit is defined as $\tau = 1/D_\theta$. We put $m = \sigma_d = \epsilon = 1$, providing the units of mass, length and energy, respectively. The translational and rotational diffusion constants D_t and D_θ are coupled in this model. Specifically, $D_\theta = 3D_t$, with $D_t = k_B T/\gamma = 0.005$. We note that one cannot take the limit $T \to 0$ independently for D_t and D_θ. At zero temperature, thus, both the translational and rotational diffusion coefficients go to zero.

Simulations of Section 3.2

We fixed $\gamma = 10$ and $k_BT = 0.05$. Time is expressed in units of $\tau = \sqrt{m\sigma_d^2/\epsilon}$. We put $m = \sigma_d = \epsilon = 1$, providing the units of mass, length and energy. $D_\theta = 3D_t$, with $D_t = k_BT/\gamma = 0.005$.

Simulations of Chapter 4

We fixed $\gamma = 10$ and $k_BT = 0.05$. The time unit is defined as $\tau = 1/D_\theta$. We put $m = \sigma_d = \epsilon = 1$, providing the units of mass, length and energy, respectively. All the simulations are performed at constant temperature $k_BT = 0.05$. $D_\theta = 3D_t$, with $D_t = k_BT/\gamma = 0.005$.

In the case of the MPC fluid, an additional set of simulation parameters has to be set – n_s, m_s, σ_s, α, Δt_s – which will be expressed in terms of the colloids units – $\tilde{m}$, $\tilde{\sigma}$, ϵ. To decide the MPC parameter values, a set of criteria, listed below, has to be satisfied.

The first criterion is that the solvent has to behave as a fluid (we remember that MPC particles satisfy an ideal gas equation of state); for such purpose, we need to have a Schmidt number $Sc \simeq 10^2 - 10^3$, typical of liquids [RMWG04]. The Schmidt number represents the ratio between the rate of momentum diffusion and the rate of mass transfer, and for large values of Sc the dynamics resemble the one of a liquid [RMWG05]. Sc is defined as $Sc = \nu_s/D_s$. Values $Sc \sim O(10)$ can be obtained by requiring small values of λ and large rotation angle [RMWG05]. Note that the choice $\lambda < \sigma_s$ is known to break the Galilean invariance [BP01], although this problem is cured by implementing the random shift procedure [BP01] which is here implemented. By using the expressions of ν_s and D_s in the limit of $\lambda/\sigma_s \ll 1$, we find that the Schmidt number depends only on the mean-free path and takes the simple form [RMWG04]:

$$Sc \simeq \frac{1}{12(\lambda/\sigma_s)^2}\,, \tag{A.7}$$

where the dependence on n_s and α has been omitted since the dominant contribution is with λ.

The second criterion is that we want to have the same value of the friction γ as in ABP simulations, where γ has the same role as in the Langevin equation. For the MPC dynamics, this formula is:

$$\gamma = C_{2D}\pi\nu_s\rho_s(\sigma_c/2), \tag{A.8}$$

where $\rho_s = n_s m_s/\sigma_s^2$ is the solvent density. The coefficient C_{2D} depends on dimensionality [LGV06] and the MPC model considered[TWQ$^+$18b]. We performed simulations measuring the velocity of a colloid dragged by a constant force along a direction in 2D and we fitted a value of $C_{2D} = 1.84 \pm 0.1$, using six different values of forces and averaging over ten realizations. It is evident that also the choice of γ depends directly only on λ when all the other parameters are fixed.

The last criterion that we need to follow is to have a very low compressibility in the presence of the active force, for the fluid to remain homogeneous during the time evolution. This criterion was discussed in [PL06, TWQ$^+$18b]. The correct parameters to look at are the Mach number and the Pumping number. The Mach number Ma is given by the ratio between the average fluid velocity $\mathrm{v_s}$ due to the external forces (in

our case due to activity) and the sound velocity $\mathrm{vsound} = \sqrt{2\mathrm{k_B T/m_s}}$ inside the fluid:

$$Ma = \frac{\mathrm{v_s}}{\mathrm{v}_{sound}}. \tag{A.9}$$

Its value depends directly on flow velocity. In order to reduce the compressibility effects of the MPC fluid it should be $Ma < 0.2$ [LG02, GHPM15]. The Pumping number Pu, instead, is the ratio between the active stationary colloid velocity F_{act}/γ and the fluid self-diffusion:

$$Pu = \frac{\sigma_c F_{act}}{6\gamma D_s}, \tag{A.10}$$

and should be less than 1 [TWQ$^+$18b] for the fluid-particle diffusion to be faster than activity-induced advection, thus avoiding strong density inhomogeneities in the fluid.

Following these criteria, we chose the cell size to be $\sigma_s = 0.2\sigma_c$. This guarantees that there is a sufficiently large number of cells covering a colloid [HHIH05]. We fix $\alpha = \pi/2$, $m_s = 0.15$ and $n_s = 15$ for the fluid. Typically the colloids and solvent mass density should match for the colloids to be buoyant, so we set $m_c = 44.15$ such that $n_s m_s/\sigma_s^2 = 4m_c/(\pi\sigma_c^2)$. This choice provides a good compromise between avoiding compressibility effects[TEQ$^+$18], which for example arises if we choose lower n_s, and computational cost, which arises with higher values of n_s. We use as $\Delta t_c = 10^{-4}$ and $\Delta t_s = 410\Delta t_c$. The temperature T for the solvent and the other parameters relative to the active force and rotational diffusion remain the same as the one used for ABP. These parameters lead to the required values of $\gamma = 10.04$ ($\nu_s = 0.061$ and $\rho_s = 56.24$), $Sc = 99.48$, $Ma = 0.1$ and $Pu = 0.9$ for the highest $Pe = 20$ value considered. We note that the Reynolds number is given by

$$Re = u_0\sigma_c/\nu_s = F_{act}\sigma_c/\gamma\nu_s = 6PuD_s/\nu_s = 6Pu/Sc, \tag{A.11}$$

which is always much less than one for our choice of parameters. Thus we are in the low Reynolds number regime.

Simulations of Section 5.2

We fixed $\gamma = 10$ and $k_BT = 0.05$, which ensures the dynamics are in the overdamped regime. We use $m = \sigma_d = \epsilon = 1$, providing the units of mass, length and energy, respectively.

Simulations of Section 5.3

We fixed $\gamma = 10$ and $k_BT = 0.05$, which ensures the dynamics are in the overdamped regime. We use $m = \sigma_d$, but ϵ can vary. These provide the units of mass, length and energy, respectively.

Simulations of Chapter 6

We fixed $\gamma = 100$, which ensures a overdamped dynamics. As reported in the Section, we use two temperatures: $k_BT = 0.47$ and $k_BT = 0.35$. Time is expressed in units of $\tau = \sqrt{m\sigma_d^2/\epsilon}$ and $m = \sigma_d = \epsilon = 1$, providing the units of mass, length and energy, respectively. Chirality is defined by the non-dimensional parameter $\Omega = \Gamma\omega\tau^2/m$.

A.2 Cluster identification algorithm

Here we describe the algorithm used to identify clusters in the bulk simulations. In order to do that, we apply the standard DBSCAN algorithm to the positions of the disks [EKSX96b]. DBSCAN is a clustering algorithm, which distributes points into clusters according to the local point density. We shortly outline hereafter the fundamental rules of the algorithm, in order to justify our choice of parameters.

- Given that two points are neighbors if their distance is less than a given extent ε, a point is a "core point" if it has at least $n_{\min}$ neighbors;
- any two core points connected through a path in the neighbors network belong to the same cluster, together with their neighbors;
- points which are not cores and are not reachable from a core do not belong to any cluster.

We used $\varepsilon = 1.5\,\sigma_d$ and $n_{\min} = 6$ for a successful identification of the clusters (relying on previous results at different Pe values [DLS$^+$18a]). Since particles in the dense phase are locally arranged on a hexagonal lattice with local surface fraction ranging from $\phi_{\rm loc} \sim 0.800$ at Pe $= 50$ to $\phi_{\rm loc} \sim 0.900$ at Pe $= 200$, a circle of radius $\varepsilon = 1.5\,\sigma_d$ encloses the first shell of neighbors.

An example of the performance of this algorithm is shown in Fig. A.1. In (a) we show a configuration using the representation in which we show each particle with a color associated to its hexatic order $\psi_{6,i}$. As in [DLS$^+$18a], red indicates maximal projection on the averaged orientation of the full sample in the ψ_6 space, and blue the maximal projection in the opposite direction, with a usual color scale in between these two extremes. One clearly observes in Fig. A.1(a) phase separation between very dilute regions and rather dense ones composed of patches with different orientational order. In panel (b) we show the outcome of the use of DBSCAN to identify the clusters (each cluster is shown with a different color). The size of the clusters is then calculated from their radius of gyration,

$$r_G^i = \sqrt{s_i^{-1} \sum_{j=1}^{s_i} (\boldsymbol{r}_j - \boldsymbol{r}_{\rm cm}^i)^2} \tag{A.12}$$

where s_i is the number of particles in cluster i, $\boldsymbol{r}_j$ the positions of particles belonging to the cluster, and $\boldsymbol{r}_{\rm cm}^i$ its center of mass. A black circle, centered at the center of mass and with radius r_G^i, is drawn on each cluster. We then monitor the average radius of gyration $R_G(t)$ obtained after averaging over all the clusters: $R_G(t) = N_C^{-1} \sum_i r_G^i$, N_C being the total number of clusters in the system.

Although the algorithm is quite reliable on the clusters' identification, it is however not able to distinguish between macroscopic clusters leading the coarsening and very small aggregates, the latter being not stable since they continuously arise and evaporate within a timescale of a few simulation time-steps. In order to avoid their impact on the system averages, we discard, as a "rule of thumb", all the clusters containing less than 5% particles with respect to the largest one.

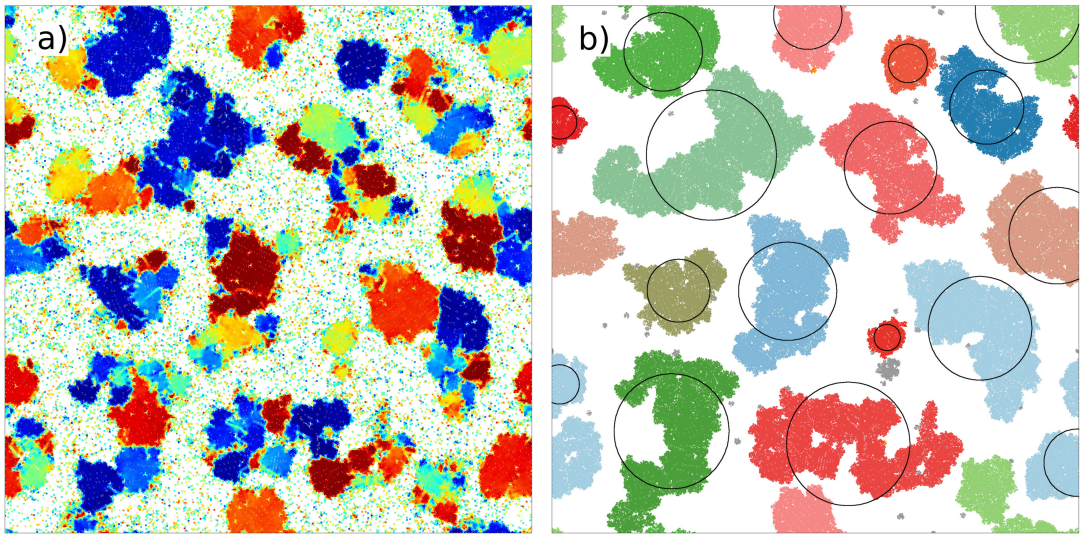

Figure A.1: (a) A configuration drawn using colors that represent the local orientational order. (b) Identification of the dense drops in (a) using DBSCAN (see text for the details). The same color is used for particles belonging to the same cluster, while isolated particles are not printed. Grey is used for small clusters, which have been discarded from the average. Black circles are centered at the center of mass of each cluster and have a radius equal to the radius of gyration of the same cluster.

A.3 Hexatic Domains identification

Large dense clusters do not always have hexatic order to the scale of their whole size [DLS$^+$18a] but, instead, they are arranged in a "polycrystal" or "mosaic" of hexatically ordered domains. We describe below two methods used to measure the average size of these domains, which yield consistent results. We either use a *clustering by argument* approach or a *clustering by gradient* one, to first identify hexatic domains, and then measure their size. Both methods are applied to the particles in the dense phase only, which are previously selected by the application of DBSCAN, as described in Sec. A.2.

1. *Clustering by argument.*

   Within this approach we discretize the range $[0:2\pi]$ of the argument of $\psi_{6,i}$ into n bins and we split the system accordingly. We then apply the DBSCAN algorithm to each part of the system separately and we discard, according to the rule of thumb introduced in Sec. A.2, the clusters with less than 5% particles of the largest one. The two steps are shown in Fig. A.2. We verified that the results depend only weakly on n within the range $n = 4, \ldots, 10$, as shown in Fig. A.4(a). We used $n = 6$ for all the measures presented in this work.

2. *Clustering by gradient.*

   As an alternative approach to separate hexatic domains, we developed a criterion based on the spatial gradient of the argument of the local hexatic parameter. We first coarse-grain the local hexatic order parameter on a square grid of spacing $d = 5\sigma_d$, being such coarse-graining length smaller than the typical size on any hexatic domain. Then we calculate the gradient of the coarse-grained $\mathrm{Arg}(\psi_6^{i,j})$.

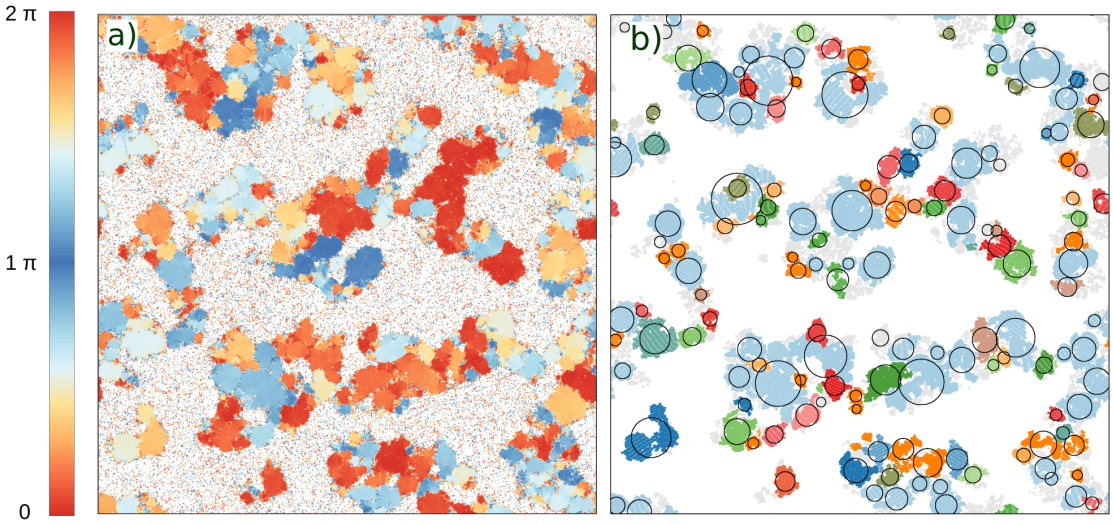

Figure A.2: Identification of hexatic domains using the argument of the local hexatic order parameter ψ_{6_i}. (a) Color map of $\mathrm{Arg}(\psi_{6,j})$. (b) Same system, split according to the binning of the hexatic orientation. Black circles are centered at the center of mass of each hexatic domain and have a radius equal to their radius of gyration.

We then associate to each grid point a '0' or '1' if $|\nabla \mathrm{Arg}(\psi_6^{i,j})|$ is larger or smaller than a certain threshold, which here we fixed to $\mathrm{th}_{grad} = 0.2$ (in units of $1/\sigma_d$), which is approximately the 10% of the typical range of the gradient modulus. Grid points labeled with a '1' are considered to belong to an hexatic domain. We then apply a DBSCAN algorithm to the grid points with $|\nabla \mathrm{Arg}(\psi_6^{i,j})| < \mathrm{th}_{grad}$ in order to identify the hexatic domains. Compared to the previous DBSCAN algorithm, in this case we select only the first eight neighbors for each grid point, and $n_{\min} = 4$. The radius of gyration is evaluated from the positions of the grid points. Such approach is graphically summarized in Fig. A.3.

In Fig. A.4(b) we compare the two methods described above to identify hexatic domains. We plot the averaged radius of gyration of the hexatic domains found with each technique and we show that the results are consistent. In the main text we present results found with the clustering by argument method only, with $n = 6$.

A.4 Bubbles Identification

Here we describe the algorithm used to identify the vapour bubbles inside dense cluseters. We first coarse-grain the system's local surface fraction over the length $d = 5\,\sigma_d$. Specifically, we divide the system area into a grid of square cells of linear size d, we set to 1 all the cells with average surface fraction ϕ_i below a threshold $\mathrm{th}_\phi = 0.65$, and to 0 the ones for which $\phi_i > \mathrm{th}_\phi$. The value of th_ϕ has been chosen to trace the dense droplets contour into the grid as accurately as possible. Bubbles are then identified by means of the lattice-DBSCAN described above, as illustrated in Fig. A.5. The coarse-graining length d we used is large enough to cut off all the small bubbles of size of the order of σ_d. The latter arise from extended defects inside the dense phase (particularly across the boundaries between different hexatic domains), and are not relevant to the large-

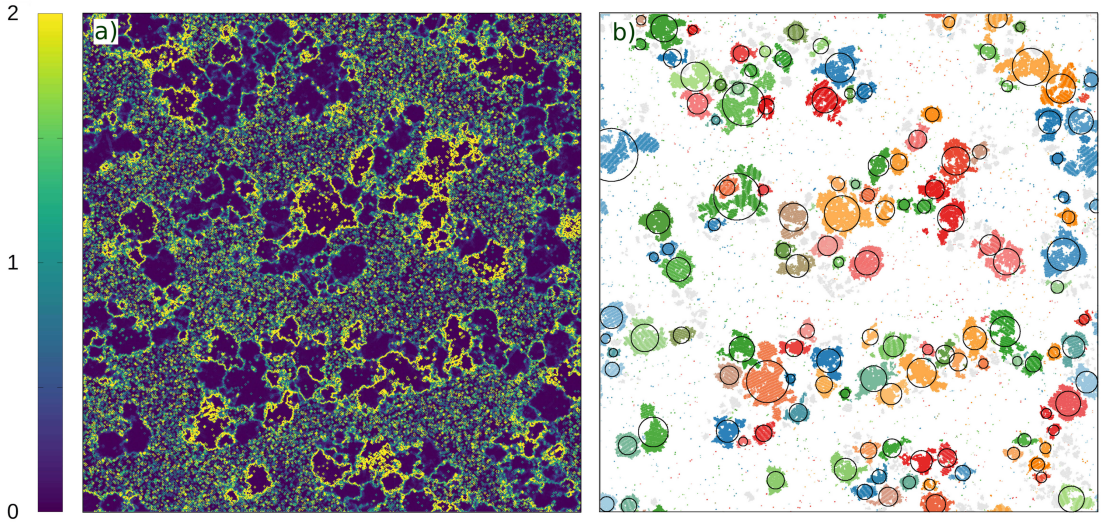

Figure A.3: Identification of hexatic domains using the spatial gradient of $\mathrm{Arg}(\psi_6)$. (a) Gradient field computed over a square grid of side σ_d. (b) Hexatic domains, as identified from the lattice DBSCAN applied to regions in (a) where $|\nabla(\mathrm{Arg}(\psi_6))| < 0.2$.

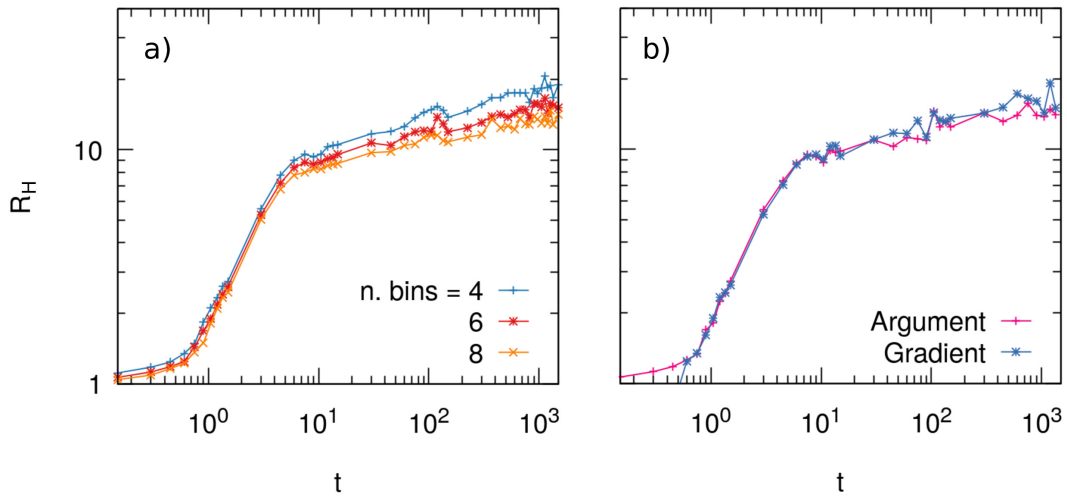

Figure A.4: The average size of clusters with the same hexatic order as a function of time. (a) Clustering by argument method: comparison between results obtained from a single simulation, using different number of bins for the discretization of the argument. (b) Comparison of results obtained using the clustering by argument (with $n = 6$) and clustering by gradient methods.

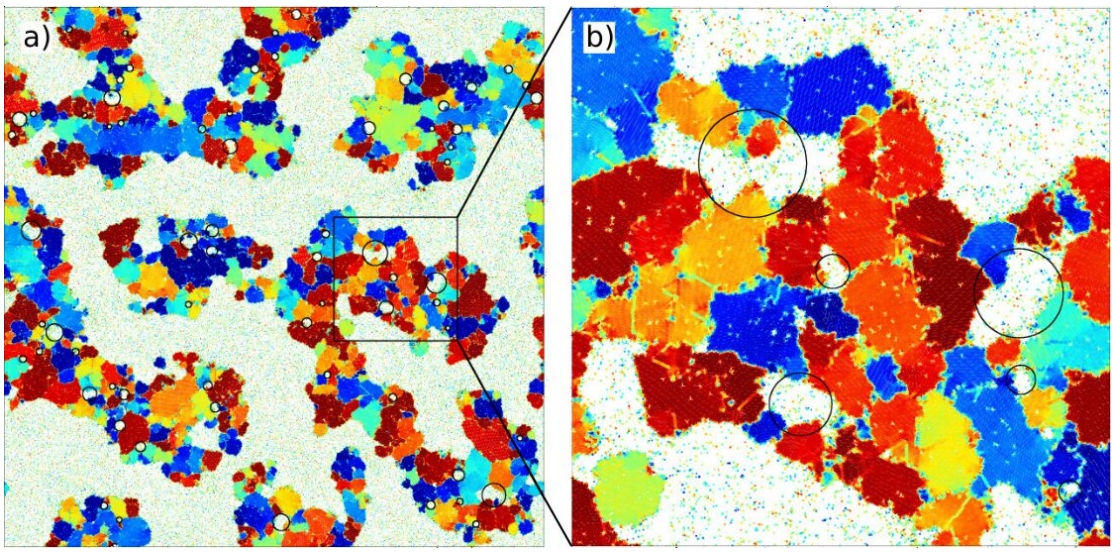

Figure A.5: (a) Hexatic map of a system with $N = 1024^2$ particles, Pe $= 200$ and $\phi = 0.480$. Black circles are centered at the center of mass of each bubble, and have radius equal to their radius of gyration. (b) Zoom over the black squared area in panel (a).

scale phenomenon we aim to address. Finally, we also discard all the bubbles which span the whole system along either the x or the y axis, constituting the gaseous phase of the segregated system.

A.5 Cluster Tracking algorithm

We describe hereafter the numerical algorithm implemented to track the center of mass of each cluster during the phase separating process, and follow their individual motion, in the bulk or extracted from it, during the simulations.

At each time t, we use the DBSCAN clustering algorithm to separate the particles in $N_C(t)$ compact clusters, referred with labels $\mathcal{C}_\alpha$, $\alpha = 1, \dots, N_C$. The parameters for DBSCAN are the radius of search around a particle, equal to $R = 1.5\,\sigma$, σ being very close to the particle's diameter $d = 0.98\sigma$, and the minimum number of neighbours to assign particles to the same cluster $\epsilon = 6$. We checked that the clusters found by the algorithm are well enough preserved for small variations of these parameters. Each cluster $\mathcal{C}_\alpha$ is composed by $N_\alpha = M_\alpha/m$ particles, and in turn, each particle can be labelled with the cluster $\mathcal{C}_\alpha$ it belongs to. This subdivision is then used to compute all the per-cluster quantities presented in this work.

In order to study the evolution of each cluster over time, we need an algorithm that identifies the same cluster at two successive times t and $t + \delta t$, with a fixed $\delta t = 10$ as time separation between two consecutive configurations of the system. During such time window δt the cluster may have lost or gained some particles, it might have disaggregated or even fused with other clusters. The tracking is achieved by considering the position of the cluster's center of mass at t, and search at time $t + \delta t$ all clusters found by DBSCAN within a radius $R = 5\sigma$ from the initial center of mass position. Out of all these clusters, we select the one with the largest subset of particles in common with the initial one at time t, and with a number of particles $N_\beta(t + \delta t)$ in between 0.9 and

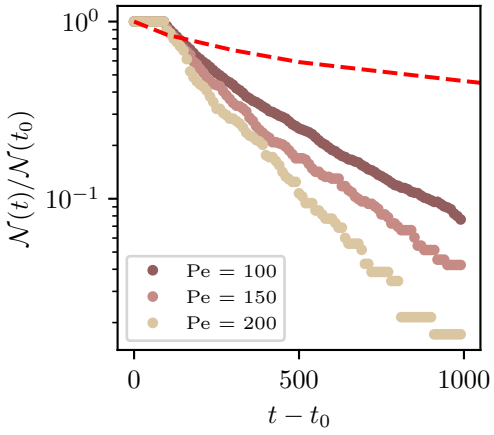

Figure A.6: **Evolution of the total number of clusters**, $\mathcal{N}(t)$, followed by the tracking algorithm at time t, as described in the text, normalized by the total number of clusters identified at the initial time of the tracking, $\mathcal{N}(t_0)$. The dashed red line is $N_C(t)/N_C(t_0)$ for Pe = 100, where $N_C(t)$ is the instantaneous number of clusters, independently of their history.

1.1 times the original number of particles $N_\alpha(t)$. If there is no cluster satisfying these two conditions, the tracking of the selected cluster stops. Consequently, the number of tracked clusters diminishes with time.

As explained above, we lose clusters along the evolution, and the number of successfully tracked clusters decreases in time. We report in Fig. A.6 the number of clusters $\mathcal{N}(t)$ still tracked by the algorithm during the evolution of large systems, when clusters coalesce and grow, divided by the number of clusters found at the initial time t_0, $\mathcal{N}(t_0) = N_C(t_0)$. This fraction decreases with an approximately exponential law, and its characteristic time gives an estimation of the typical time required for the clusters to collide or disgregate. We note that $\mathcal{N}(t)$ is slightly different from the instantaneous number of clusters identified by DBSCAN independently of their history, $N_C(t)$, which is plotted with a red dashed line in Fig. A.6 and is also reported in the main text in Fig. 5(b).

After performing the tracking of each cluster over time, we are able to follow the trajectories of their centers of mass, $\mathbf{r}^\alpha_{\rm cm}(t)$, and from them compute the mean square displacement and other observables. The individual trajectories $\mathbf{r}^\alpha_{\rm cm}(t)$, and hence the displacements $(\mathbf{r}^\alpha_{\rm cm}(t) - \mathbf{r}^\alpha_{\rm cm}(t_0))^2$, last until the tracking is able to follow the selected cluster. The mean-square displacement is computed as an average over all these trajectories and at each time t the normalization is given by the corresponding $\mathcal{N}(t)$, which decreases with t.

In order to study in more depth the mechanism with which the clusters grow, and get a grip on the collision events between clusters, we also use a modification of the previous algorithm. We compare two configurations at two successive times t and $t + \delta t$, and we establish i) a correspondence between clusters, and ii) the type of event the clusters have been involved in, based on the computation of the overlap between them. More precisely, the normalized overlap between cluster i at time t and cluster j at time $t + \delta t$ is defined as

$$o_{ij} = \frac{n_{ij}}{\sqrt{M_i M_j}}, \tag{A.13}$$

where n_{ij} is the number of particles belonging to both clusters and M_i and M_j are the masses of the two clusters. The overlap is computed for all $i = 1, ..., \bar{N}_C(t)$ and $j = 1, ..., \bar{N}_C(t + \delta t)$, with $\bar{N}_C$ the number of clusters of mass $M > 100$. We have identified this mass threshold as the one that separates stable long-living clusters from instantaneous aggregations of particles.

As we find a non-zero overlap $o_{ij} > 0$, we check the mass variation ΔM_{ij} between the cluster i at time t and the cluster j at time $t + \delta t$.

- If $|\Delta M_{ij}| < 100$, then only evaporation or condensation of particles have occurred. The cluster labelled i at time t has not undergone any collisions, and it is the same cluster, labelled j, at time $t + \delta t$. All these N_p events are recorded as events due to Ostwald ripening. In the case one of these events is recorded, any other overlap involving cluster i or j is disregarded.

- All the other N_{coll} occurrences of $o_{ij} > 0$ and $|\Delta M_{ij}| > 100$ are recorded as collisions between clusters or breakups of clusters in pieces.

A.6 Measurement of the Cluster Diffusion Coefficient

We describe in this Section the method that we employed to estimate the diffusion coefficient of the clusters, from the trajectories of their centers of mass.

Compared to single particles, clusters undergo larger mass fluctuations over their evolution, which can result in jumps in the clusters' displacements. For this reason, as already mentioned in Section 3.2, we follow clusters only if their mass fluctuation after the time evolution $t + \delta t$ is within 10% of the mass at the time t.

After obtaining a set of trajectories $\mathbf{r}^{\alpha}_{\text{cm}}$ for the center of mass of each cluster α, with average mass M_α (over the trajectory), we extract an estimate of the diffusion coefficient via the formula:

$$D_\alpha = \frac{1}{2Nd} \sum_{k=0}^{N} \frac{(\mathbf{r}^{\alpha}_{\text{cm}}(t_k) - \mathbf{r}^{\alpha}_{\text{cm}}(t_0))^2}{(t_k - t_0)} \ , \tag{A.14}$$

where t_i are the discretized times, with the initial time of the cluster's trajectory being $t = t_0$, and the sum extended up to the last time $t = t_N$. In this way, we obtain a set of D_α with associated mass M_α. We can then bin appropriately the range of masses, and for each bin compute the average value of the diffusion coefficient, obtaining the diffusion coefficient of the clusters D as a function of the mass M. For clusters tracked in the whole system (Fig. 3.17 of the main text), the average values of D are computed by a logarithmic binning of the respective masses, while for isolated clusters, we average over several independent realizations of the same initial condition.

Figure A.7, left panel, shows the scatter plot (circles) of D_α as a function of M_α for extracted clusters (see main text). The crosses represent the average values of D obtained after binning. The dashed lines correspond to fits of $D(M)$ for $M < 5000$, via $D(M) \sim M^{-1/2}$ (red curve), and for $M > 5000$ via $D(M) \sim M^{-1}$ (black). Figure A.7, right panel, shows the probability distribution of D for some averaged masses given in the key.

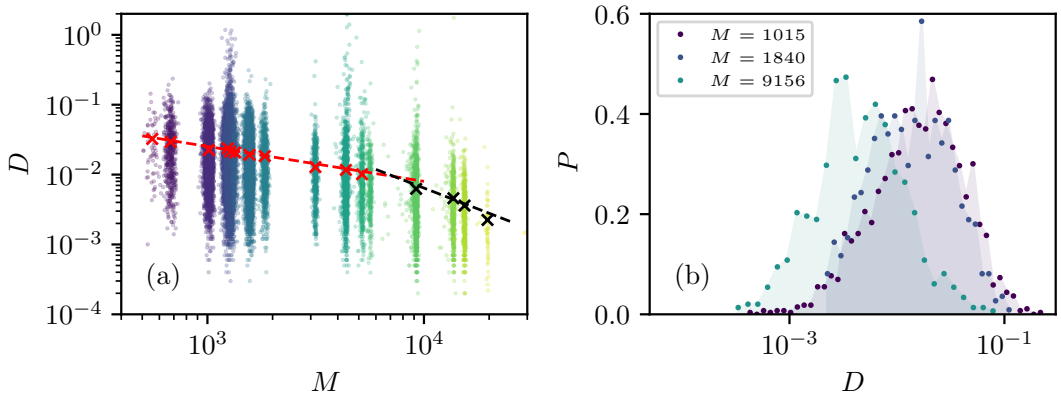

Figure A.7: **Clusters' diffusion coefficient.** Analysis of the diffusion coefficient of the centers of mass of the clusters extracted from the bulk. (a) Scatter plot of the individual diffusion coefficient and the associated average mass over the trajectory. (b) Distribution of the diffusion coefficients of a cluster started with the same initial condition and evolved independently in different runs that give rise to the histograms. The parameters are the same as in other figures, Pe = 100 and $\phi = 0.5$.

B

Gradient expansion for a kinetic coarse-grained model of ABPs

Let us consider a two-dimensional system of N Active Brownian Particles (ABPs), with a rotational diffusion coefficient D_r. In the long time limit, $t \ll 1/D_r$, we can write a coarse-grained master equation for the probability distribution of the particles $f(\boldsymbol{r}, \boldsymbol{u}, t)$

$$\partial_t f(\boldsymbol{r}, \boldsymbol{u}, t) = -\boldsymbol{\nabla}_{\boldsymbol{r}} \cdot [v\boldsymbol{u} f(\boldsymbol{r}, \boldsymbol{u}, t)] - \frac{f(\boldsymbol{r}, \boldsymbol{u}, t)}{\tau} + \frac{1}{2\pi\tau} \int_{|\boldsymbol{u}|=1} d\boldsymbol{u}' f(\boldsymbol{r}, \boldsymbol{u}, t). \tag{B.1}$$

where $\boldsymbol{r}$ is the particle's position and $\boldsymbol{r}$ the orientation. The first term represents the convective flux due to the activity of the particles, the second and the third terms represent the positive and negative balance of particles related to the reorientation of the particles (due to the axis rotation).

We can expand the density distribution in order to solve Eq.(B.1):

$$f = f^{(0)} + f^{(1)} + f^{(2)} + \mathcal{O}(f^{(3)}), \tag{B.2}$$

Inserting the gradient expansion in Eq. (B.1), we obtain a set of equations for each perturbative order. At the lowest order, we get:

$$f^{(0)}(\boldsymbol{r}, t) = \frac{1}{2\pi} \int_{|\boldsymbol{u}|=1} d\boldsymbol{u}' f(\boldsymbol{r}, \boldsymbol{u}', t) = \frac{\rho(\boldsymbol{r}, t)}{2\pi}, \tag{B.3}$$

where $\rho(\boldsymbol{r}, t)$ represent the local density. In the first and second perturbative order one has:

$$\partial_t f^{(0)} + \boldsymbol{\nabla}_{\boldsymbol{r}}(v\boldsymbol{u} f^{(0)}) = -\frac{f^{(1)}}{\tau}, \tag{B.4}$$

$$\partial_t f^{(1)} + \boldsymbol{\nabla}_{\boldsymbol{r}}(v\boldsymbol{u} f^{(1)}) = -\frac{f^{(2)}}{\tau}. \tag{B.5}$$

Summing up Eqs. (B.4) and (B.5), one gets

$$\partial_t \rho + \int_{|\boldsymbol{u}|=1} \prod_\alpha du'_\alpha \, \partial_\beta \left(v u'_\beta f^{(0)} \right) + \int_{|\boldsymbol{u}|=1} \prod_\alpha \, du'_\alpha \partial_\beta \left(v u_\beta f^{(1)} \right) = 0, \tag{B.6}$$

where Greek indexes indicate the different Cartesian components. Using now Eq. (B.3) we obtain

$$\begin{aligned}&\partial_t\rho + \frac{1}{2\pi}\int_{|\boldsymbol{u}|=1}\prod_\alpha du'_\alpha\ \partial_\beta\left(vu'_\beta\rho\right)\\&-\frac{\tau}{2\pi}\int_{|\boldsymbol{u}|=1}\prod_\alpha du'_\alpha\ \partial_t\partial_\beta\left(vu'_\beta\rho\right) - \frac{\tau}{2\pi}\int_{|\boldsymbol{u}|=1}\prod_\alpha du'_\alpha\ \partial_\gamma\left[vu'_\gamma\partial_\beta\left(vu'_\beta\rho\right)\right] = 0\end{aligned} \tag{B.7}$$

The two first terms are equal to zero since they are asymmetric in u_α. Moreover, the last integral can be solved using the formula (with $d = 2$)

$$\int_{|\boldsymbol{u}|=1}\prod_\alpha du'_\alpha\ u'_\gamma u'_\beta = \int_0^{2\pi} d\theta u'_\gamma u'_\beta = \pi\delta_{\gamma\beta}. \tag{B.8}$$

Inserting this solution in B.7 one finally obtains

$$\partial_t\rho = \frac{\tau}{2}\boldsymbol{\nabla}\cdot\left[v\boldsymbol{\nabla}(v\rho)\right]. \tag{B.9}$$

This is called *self-trapping* equation and rationalizes the Motlility-Induced Phase Separation (MIPS) mechanism, for which active particles aggregate in the spatial region where they go slowly.

C

The Passive-Attractive system

In order to better understand the similarities and differences between active and passive phase separation we simulated a system of passive particles ($\mathrm{Pe} = 0$) interacting via the same Mie potential $U(r) = 4\varepsilon[(\sigma/r)^{64} - (\sigma/r)^{32}] + \varepsilon$ though with no truncation at $r = \sigma$ (used in the body of the paper to make it purely repulsive); we set instead the truncation at $r = 2.5\sigma$, in order to include the attractive part of the potential. With its tail, at long distances the particles feel an attractive interaction. We chose the density ($\phi = 0.50$) and temperature ($T = 0.30$), such that the passive attractive system has a liquid-gas co-existence similar to the MIPS phenomenology of the ABPs.

Figure C.1 summarizes the main features of the phase separation in the attractive case. Panels (a) and (b) display the cluster averaged radius of gyration $\overline{R}_g$ and mass $\overline{M}$ as functions of time, together with two dashed lines that indicate the fitted powers in the last reachable regime. For the sake of comparison, in (c) we plot the growing length as extracted from the scaling properties of the structure factor. In both cases we see that the system enters the scaling regime at $t_s \sim 5 \times 10^3$, considerably later than in the active model. From the cluster analysis we read $\overline{R}_g \sim t^{1/z}$ with $z \sim 4$, which is still far from the expected $z = 3$. A similar $z \sim 4$ exponent was measured in [CSSC04] in a numerical simulation of depletion driven colloidal phase separation. The study of the structure factor yields an exponent z closer to $z = 3$ but still not quite it. We note that the system could still be exploring a transient regime, before the asymptotic scaling one. Nevertheless, the times needed to reach the latter are out of our computational reach for the relatively high densities that we use here in order to compare to the active case. We note that even in the ferromagnetic Ising model with conserved Kawasaki (local spin exchange) dynamics, a problem with coarsening dynamics surely characterized by a growing length $R \sim t^{1/3}$, this asymptotic regime is very difficult to reach [TCP18]. The molecular dynamic simulation of particle systems present even further complications [WSII14].

The scatter plot in (d), $M^* = M/\overline{M}$ against $R_g^* = R_g/\overline{R}_g$ in log-log scale, is well described by a bi-fractal form, with the exponents $d_f = 2$ and $d_f \sim 1.25$. We note, however, that the extent of points over which we can apply a fit to the second fractal regime is shorter than in the active case and the spread of data is a bit larger. Though this exponent is smaller than the 1.45 found for ABP clusters, we cannot assure that it will be

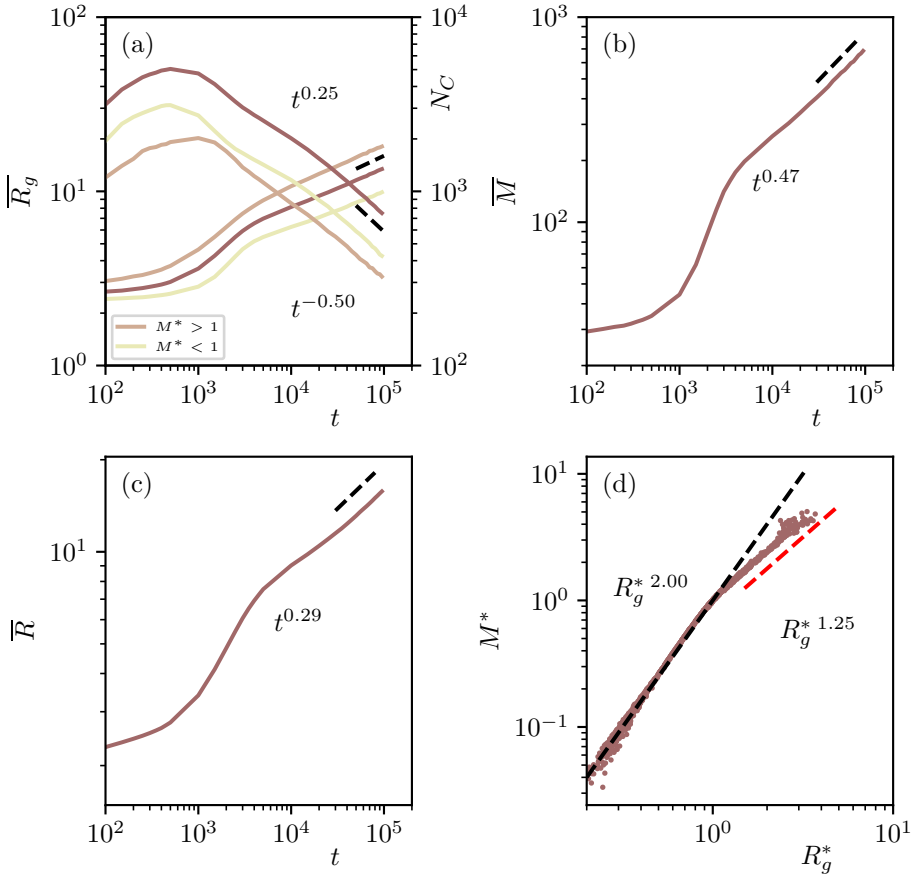

Figure C.1: **Dynamic behaviour of the attractive passive model.** Time dependence of the averaged cluster radius of gyration in the left scale and the number of clusters in the right scale (a), the averaged clusters mass (b), the growing length estimated from the scaling properties of the structure factor (c), and the scatter plot of $M^* = M/\overline{M}$ against $R_g^* = R_g/\overline{R}_g$ (d). See the text for a description of the plots.

the truly asymptotic one. Therefore, as in the ABP case, we see small regular clusters with fractal dimension equal to the dimension of space and a crossover, at the averaged scale $(\overline{R}_g, \overline{M})$, to fractal clusters with a smaller fractal dimension. This could be confirmed directly by a visual inspection of the configuration, with an example reported in Fig. C.2(a).

A fractal exponent $d_f = 1.45$ was measured in [PBD21] in the cluster analysis of a passive Lennard-Jones system, and in one of the several active models treated in [AVP17], in its steady state. In these references, no separation of scales was exhibited, and no bi-fractal structure was shown to exist.

Clusters formed in the passive system have a similar but much more regular shape than the ones formed by MIPS, which are shown in Fig. C.2(b). They are much slower, notably the time needed to enter the scaling regime is around 50 times longer for these parameters, and this is confirmed by the analysis of the diffusion coefficient in the main text (cfr. Fig. 3.18). In particular, their movement is mainly due to fluctuations on the surface of the cluster, from individual particles leaving/joining the clusters, rather than the active force pushing/breaking the cluster.

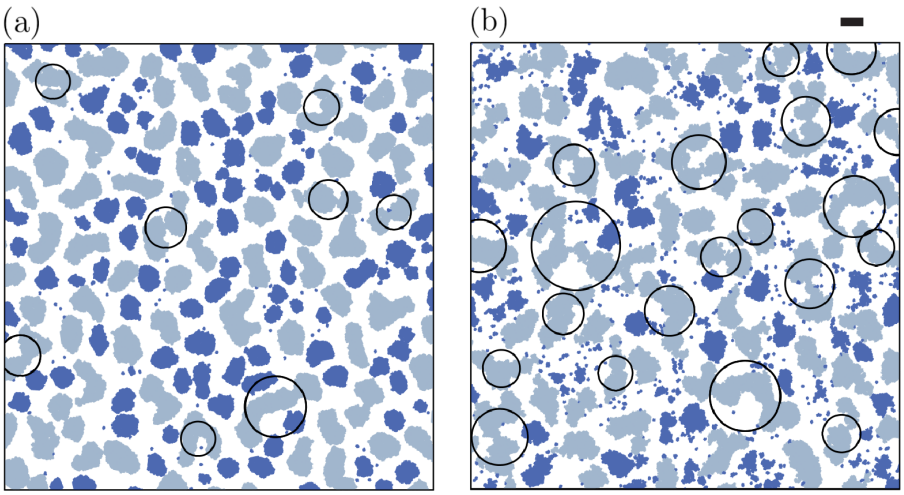

Figure C.2: **Comparison between the configurations of the passive attractive model and the active one.** Snapshots taken from simulations of (a) the passive attractive system described in this section ($\phi = 0.5$ and $T = 0.3$) and (b) the ABPs system described in the main text, with $\phi = 0.5$, $T = 0.05$ and $\mathrm{Pe} = 100$. Both configurations have the same averaged cluster mass $\overline{M}$. The average size of the clusters is shown with a line on top of the right panel. Fractal clusters are colored in gray ($d_f \approx 1.25$) and regular ones in blue ($d_f = 2$). Circles with center at the c.m. and radius equal to the gyration radius of some of the biggest clusters are also shown, to underscore how fractal clusters are far from having a compact shape. The movies M2 and M3 display the evolution of these systems.

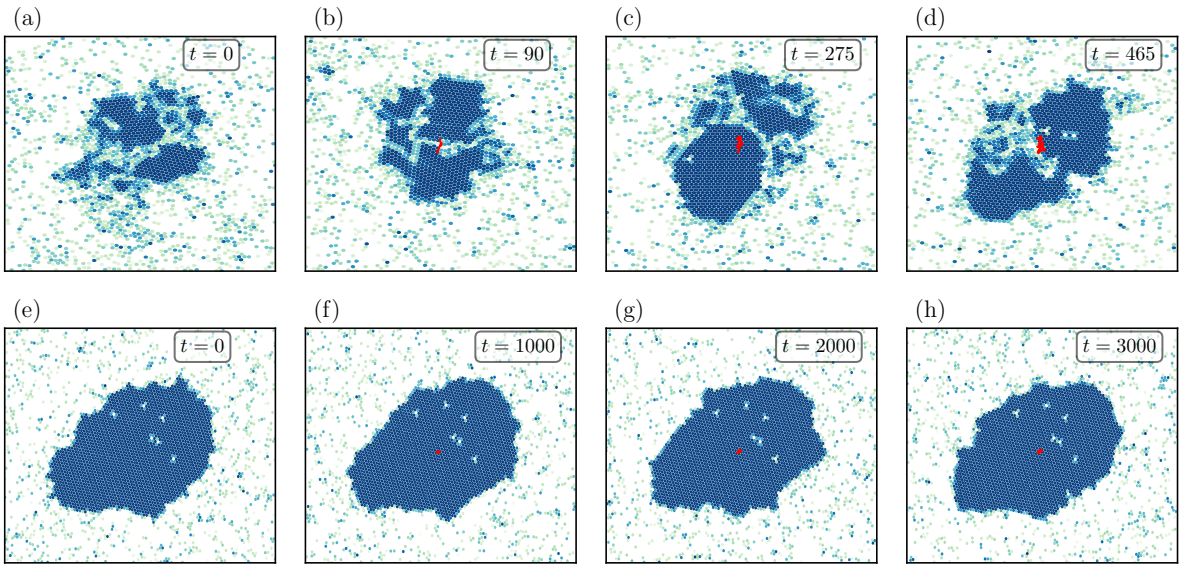

Figure C.3: **Comparison between the motion of active and passive isolated clusters.** Snapshots of (a)-(d) display an isolated cluster of ABPs with $\mathrm{Pe} = 100$, and (e)-(h) an isolated cluster of passive ($\mathrm{Pe} = 0$) attractive particles at the different times indicated in the figures. The trajectory of the center of mass of the clusters is represented by a red line. Note the different time scale at which the different snapshots were taken in both cases, clearly showing that the active cluster moves at much smaller time scales than the passive one (which in the time scale shown barely moves at all). A comparison between the histories of the two clusters is also exposed by the movie M4.

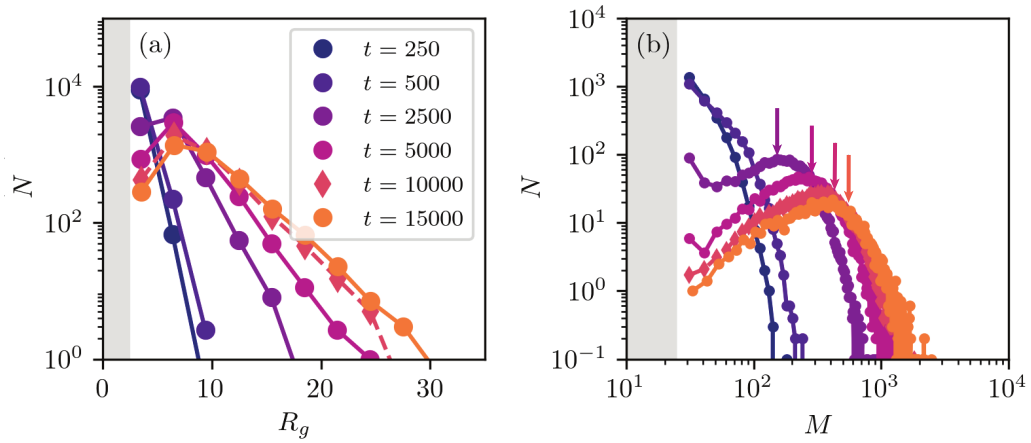

Figure C.4: **The distribution of cluster sizes in the passive attractive model**, at different times given in the key. The gray regions are excluded by the cut-off $M > 25$ imposed on the size of the clusters. The data points plotted in violet scale are for very short times, well before the scaling regime, $t \ll t_s$. The data points in red-dark orange are for times in the intermediate regime of rapid increase of $\overline{R}_g$. Finally, the two last sets of data (orange) are in the scaling regime, $t > t_s$. The vertical arrows in (b) indicate the averaged values.

A direct comparison of the motion of the clusters in the ABP systems and the passive one is reported in Fig. C.3 where we confront the evolution of clusters taken out of the full system, and set in contact with a gas that mimics their conditions in the bulk. In particular, in Fig. C.3(a)-(d), the time evolution of a single ABPs cluster is shown for $\mathrm{Pe} = 100$. One can see that the evolution is characterized by dramatic fluctuations in shape and mass. In general, due to the non-attractive nature of the clustering, breaking events are frequent. In panels (e)-(h), a cluster of attractive particles ($\mathrm{Pe} = 0$) of comparable size and mass, is shown. In this case, the structure of the cluster remains the same along the time evolution and, in general, the cluster is stable, there are no grain boundaries inside and dramatic breaking is extremely rare. The movies M3 and M4 illustrate these issues very clearly.

Figure C.4 displays the probability distribution of cluster sizes in the passive attractive model. These curves are very different from the ones we measured in the active system, shown above (see Fig. 3.15). In particular, in the scaling regime, after a very fast exponential decay of the weight of small clusters, the distribution has a clear minimum followed by a maximum at two well-defined sizes. For even larger clusters, the decay is close to exponential again. The non-monotonic form of $N(R_g)$ excludes a double exponential as a possible description of it.

The corresponding histograms of the cluster masses are displayed in the right panel of the same figure. One can verify that they also show differences with the active cluster mass distributions plotted in Fig. 3.15. The arrows indicate the average values $\overline{M}$. While here one clearly distinguishes the minimum-maximum structure, in the active model this is replaced by a plateau in the same double log representation.

An interesting question now comes to mind: how do these distributions compare to the ones of the same quantities in the active model? In Fig. C.5(a) we plot the number of radii of gyration in the two systems at the same time while in Fig. C.5(b) we plot the same numbers at times such that the averaged $\overline{R}_g$ are the same, and is indicated by the

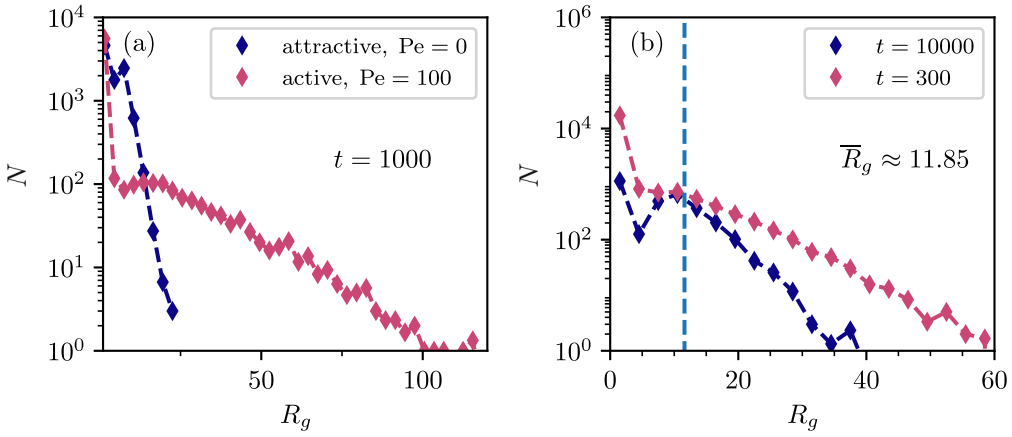

Figure C.5: **The distribution of cluster radii of gyration in the active and passive models.** In (a) data are taken at the same time t, while in (b) they were gathered at different times such that $\overline{R}_g$ is the same. The color of the data points is given by the active or passive character of the system and is the same in the two panels. The vertical dashed line in (b) indicates the averaged $\overline{R}_g$ which is the same in the two systems.

vertical dashed line. In both figures the tail of the active case is longer and higher than in the passive case, proving that the active system has more fractal clusters.

Finally, while in the active case we see that large clusters are formed by smaller patches with different orientational order, in the passive case the dense clusters have a uniform orientational order. These facts can be observed in Fig. C.6 where we plot the same configurations of Fig. C.2 using different colors for different orientational orders, as quantified by the local hexatic order parameter,

$$\psi_i = \frac{1}{nn_i} \sum_{j \in \partial_i} e^{6\mathrm{i}\theta_{ij}} \tag{C.1}$$

where the sum runs over the nn_i first neighbors of the ith particle defined via a Voronoi tesselation, and θ_{ij} is the angle formed by the segment that connects the center of the ith disk with one of its jth nearest neighbor and the horizontal axis.

Video M4 illustrates what is going on in phase separation of the passive attractive system. On the one hand, some small clusters evaporate and single particles from the gas get attracted to larger ones, according to the Ostwald ripening mechanism. On the other hand, there is some cluster aggregation. However, differently to what happens in the active case, here the clusters collide, detach and rotate a little bit until they join in such a way that the whole new cluster gets a global homogeneous hexatic order. Some examples of these processes are seen in the video. The larger clusters thus formed are elongated and therefore have a rather small fractal dimension. Over time, if not hit by another cluster, they will progressively get more round-shaped.

We finally stress that in the passive system the time tracking of clusters, as described in Appendix A, lasts much longer than in the active one. This is because the passive clusters are much more stable than the active ones and there are fewer collisions in the former than in the latter case. This statement can be made quantitative by studying the distribution of end-times t_e. The end-times are the times at which tracking stops, according to the criteria explained in Sec. A2. It is quite clear from Fig. C.7 that in the passive model, the distribution has a much slower decay.

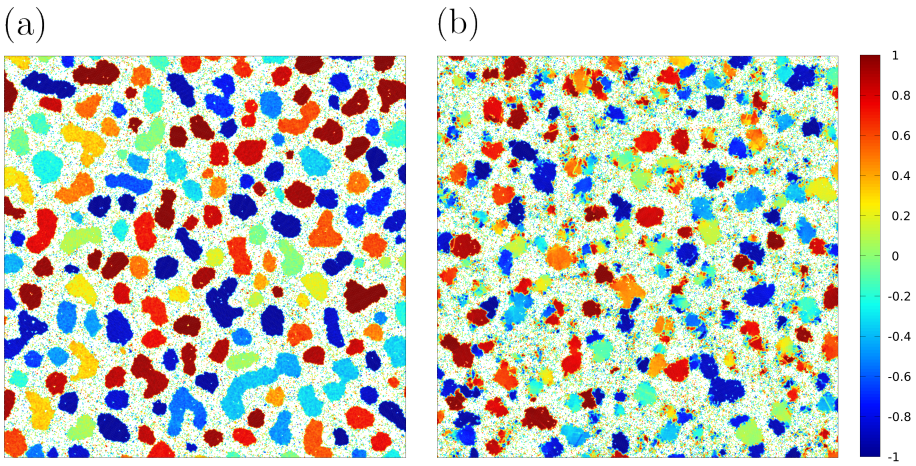

Figure C.6: **Local hexatic order.** Same configurations as in Fig. C.2, but with particles colored according to the value of the projection of the local hexatic order parameter over the global average, see [DLS+18a] for details. In the attractive passive case, clusters are formed by single hexatic domains, while in the active case, large clusters exhibit a micro-separation in smaller hexatic patches [CDL+20a].

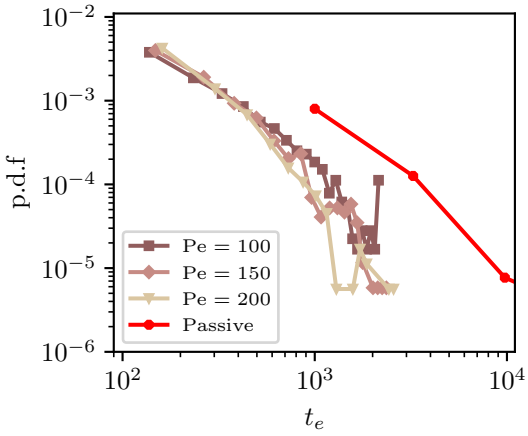

Figure C.7: **Distribution of tracking end-times** t_e for the active and passive models.

We summarize here the outcome of the comparison between active and passive clusters.

- Clusters of passive attractive particles move more slowly than the active ones: the diffusion constant decays faster with M and its absolute value is around 40 times smaller for the parameters that we focus on (Fig. 3 of the main text).

- The large clusters of active particles have patches with different hexatic order within (micro phase separation under way) while the ones of passive particles are uniform in the computational time scales.

- The distributions of gyration radii and masses are different in active and passive systems.

- In the passive attractive case we see mostly evaporation of small clusters and single particle attachment to larger clusters (Ostwald ripening). There is, though, some collision of rounded clusters that gives rise to very elongated clusters with rather low d_f.
- In the active model we see more merging of clusters and less evaporation. In a sense the ordering process is closer to a Smoluchowski diffusion-aggregation one.
- The clusters interfaces are much rougher in the active than in the passive case, where they look pretty smooth.
- In both systems there is co-existence of regular and fractal clusters. For times such that the averaged cluster sizes are the same, the regular ones are more numerous than the fractal (by a factor 3, approximately).

D

Theoretical model of a single cluster

In this Section we study the simplest possible model for a cluster. We ignore the interaction between the cluster and its environment (gas or other clusters) and we keep the number of particles in the cluster fixed. Furthermore, for the sake of simplicity, we consider that the cluster is made of individual Active Ornstein-Uhlenbeck Particles (AOUPs) ruled by the evolution equation

$$m\dot{\boldsymbol{v}} = -\gamma \boldsymbol{v} + \boldsymbol{u}_{\rm act} + \boldsymbol{\xi} \ , \tag{D.1}$$

where $\boldsymbol{\xi}$ is a Gaussian white noise with zero mean and $a, b = 1, d = 2$ component correlations

$$\langle \xi_a(t)\xi_b(t')\rangle = 2\gamma k_B T \delta_{ab}\delta(t-t') \ . \tag{D.2}$$

$\boldsymbol{u}_{\rm act}$ is the active force, modelled as a colored Gaussian noise, described by the equation

$$\dot{\boldsymbol{u}}_{\rm act} = -\frac{1}{\tau_p}\boldsymbol{u}_{\rm act} + \boldsymbol{\eta}, \tag{D.3}$$

with τ_p the persistence time and the components η_a correlated as

$$\langle \eta_a(t)\eta_b(t')\rangle = \frac{F_{\rm act}^2}{\tau_p}\,\delta_{ab}\,\delta(t-t') \ . \tag{D.4}$$

In order to facilitate checks of the expressions we find, we recall that naming m, L and t the units of mass, length and time, the other parameter units are such that $[m\dot{v}] = [m]\,L/t^2 = [\gamma]L/t \implies [m/\gamma] = t$. Also, $mL/t^2 = [u_{\rm act}] = [\xi]$ and $[u_{\rm act}]/t = [\eta]$. From the noise correlations $[\xi^2] = [\gamma k_B T]/t$, which implies $m^2L^2/t^4 = [\gamma k_B T]/t$. With these units, we find $[k_BT] = mL^2/t^2$, which is consistent. We also have $[\eta] = [F_{\rm act}]/t$. Therefore, $[u_{\rm act}] = [F_{\rm act}]$, as it should.

Let us consider a cluster with mass M formed by M/m such AOUPs. Summing up Eq. (D.1) over the particles $i = 1, \dots, M/m$ in the cluster C, and introducing the quantities

$$\boldsymbol{r}_{\rm cm} = \frac{1}{M}\sum_{i\in C} m\boldsymbol{r}_i \ , \qquad\qquad \boldsymbol{v}_{\rm cm} = \frac{1}{M}\sum_{i\in C} m\boldsymbol{v}_i \ , \tag{D.5}$$

the equation of motion of the center of mass becomes

$$\dot{\boldsymbol{v}}_{\rm cm} = -\frac{\gamma}{m}\,\boldsymbol{v}_{\rm cm} + \frac{1}{M}\,\boldsymbol{U} + \frac{1}{M}\,\boldsymbol{\Xi}\,, \tag{D.6}$$

where $\boldsymbol{U} = \sum_{i\in C}\boldsymbol{u}_{{\rm act}\,i}$ and $\boldsymbol{\Xi} = \sum_{i\in C}\boldsymbol{\xi}_i$. The solution is

$$\boldsymbol{v}_{\rm cm}(t) = \boldsymbol{v}_{\rm cm}(0)\;e^{-\gamma t/m} + \frac{1}{M}\int_0^t dt_1\;e^{-(t-t_1)\gamma/m}\,\boldsymbol{U}(t_1) + \frac{1}{M}\int_0^t dt_1\;e^{-(t-t_1)\gamma/m}\,\Xi(t_1)\;. \tag{D.7}$$

We already see from this expression that the relaxation time of the center of mass velocity, the inertial time, is the same as the one of a single particle, m/γ. The short time decay of $\langle \boldsymbol{v}^2(t)\rangle$ in Fig. D.1 confirms that this is also the inertial time in the simulation of the ABP clusters extracted from the bulk.

We want to compare properties of this model to their equivalent in the simulations of the ABP clusters. In the latter, we measure the total active force correlation

$$\langle \boldsymbol{F}(t)\cdot\boldsymbol{F}(t')\rangle = 2F^2\,e^{-|t-t'|/\mathcal{T}_p}\;, \tag{D.8}$$

see Fig. 3.19(a). The total active force correlation in the ABP clusters decays exponentially with a correlation time $\mathcal{T}_p$, which turns out to be, numerically, of the order of the individual τ_p itself, see Fig. 4(a) in the main text.

The force-force correlation can be expressed in terms of single force correlations as

$$F^2 \equiv \langle \mathbf{F}^2_{\rm act}(0)\rangle = F^2_{\rm act}\;\left[\sum_{i=1}^{M/m}\langle \mathbf{n}_i^2(0)\rangle + \sum_{i\neq j}^{M/m}\langle \mathbf{n}_i(0)\cdot\mathbf{n}_j(0)\rangle\right]\;. \tag{D.9}$$

If one assumes that each particle in the cluster is independent of the others, and that the $\mathbf{n}_i$ assume random directions,

$$F^2 \sim \frac{M}{m}\,F^2_{\rm act}\,(1+\zeta)\;. \tag{D.10}$$

The M/m dependence represents the data quite accurately, Fig. 3.19(b), with ζ a number of order one which, actually, takes a quite small value $\zeta\sim 0.05$. However, we also know that this would be an over simplification, given that we observe special alignment of the forces on the boundaries of the clusters, from time to time, see the inset in Fig. 3.19(d). This form gives an idea of the parameter dependence of F^2 which we will adopt in this Section.

Going back to the simple model, the individual noises are truly independent variables and the correlation of the total noise term reads

$$\langle \boldsymbol{\Xi}(t)\cdot\boldsymbol{\Xi}(t')\rangle = \sum_{i\in C}\sum_{j\in C}\sum_{a=1}^{d}\langle \xi_a^i(t)\xi_a^j(t')\rangle = \sum_{ij}\delta_{ij}\;2dk_BT\gamma\,\delta(t-t') = \frac{M}{m}\,4k_BT\gamma\,\delta(t-t')\;. \tag{D.11}$$

Using the results for the active force and noise correlations, the two-time velocity correlation becomes

$$\begin{aligned}&\langle \boldsymbol{v}_{\rm cm}(t)\cdot\boldsymbol{v}_{\rm cm}(t')\rangle = \\ &\boldsymbol{v}^2_{\rm cm}(0)\;e^{-\gamma/m(t+t')} + \frac{2F^2}{M^2}\,\frac{1}{(\gamma/m)^2-1/\mathcal{T}_p^2}\left[\frac{m}{\gamma\mathcal{T}_p}\left(e^{-\gamma/m(t+t')} - e^{-\gamma/m|t-t'|}\right)\right.\\ &\left.+\left(e^{-\gamma/m(t+t')}+e^{-|t-t'|/\mathcal{T}_p}-e^{-t/\mathcal{T}_p-t'\gamma/m}-e^{-t'/\mathcal{T}_p-t\gamma/m}\right)\right] + \frac{2k_BT}{M}\left(e^{-\gamma/m(t-t')}-e^{-\gamma/m(t+t')}\right)\;.\end{aligned} \tag{D.12}$$

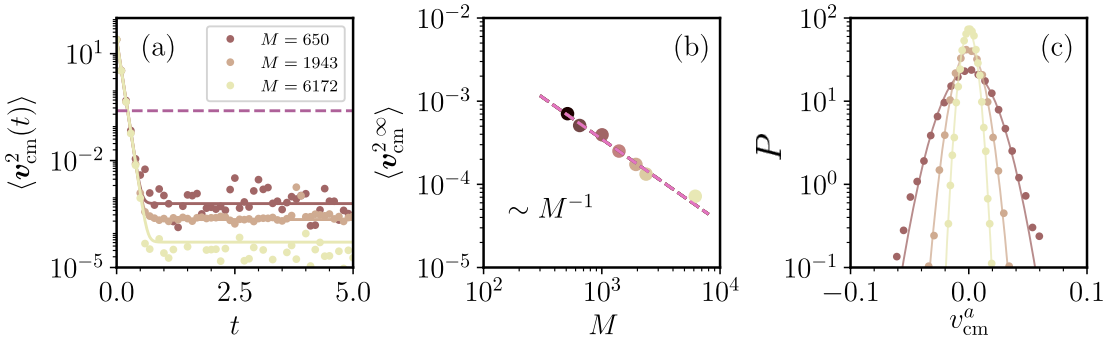

Figure D.1: **Comparison between the simple model and the simulations of ABP clusters extracted from the bulk.** (a) Squared center of mass velocity of the cluster, with an initial velocity term $v_{\rm cm}(0) = 5$. Both the first ballistic regime with the single particle characteristic time m/γ and the plateau proportional to $F^2_{\rm act}/M^2$ at large times are present. The horizontal dashed line represents the typical velocity of the single active particles for the same parameters $(F_{\rm act}/\gamma)^2$. (b) The asymptotic value $\lim_{t\to\infty}\langle \boldsymbol{v}^2_{\rm cm}(t)\rangle$ as a function of the cluster mass, together with the law M^{-1}. (c) Distribution of the center of mass velocities $v^a_{\rm cm}$ along the two Cartesian directions at a fixed tracking time for different clusters' masses. The solid lines are fits with Gaussian distributions. Their width is related to the clusters kinetic temperature.

At equal times

$$\langle \boldsymbol{v}^2_{\rm cm}(t)\rangle = \boldsymbol{v}^2_{\rm cm}(0)\, e^{-2\gamma/m\,t} + \frac{2F^2}{M^2}\,\frac{1}{(\gamma/m)^2 - 1/\mathcal{T}_p^2}\left[-\frac{m}{\gamma\mathcal{T}_p}\left(1 - e^{-2\gamma/m\,t}\right) + \left(1 + e^{-2\gamma/m\,t} - 2e^{-t(1/\mathcal{T}_p+\gamma/m)}\right)\right] + \frac{2k_BT}{M}\left(1 - e^{-2\gamma/m\,t}\right)\,. \tag{D.13}$$

Consistently, one finds $\langle \boldsymbol{v}^2_{\rm cm}(0)\rangle = \boldsymbol{v}^2_{\rm cm}(0)$. In the long time limit, $t \gg m/\gamma$,

$$\langle \boldsymbol{v}^2_{\rm cm}(t)\rangle \xrightarrow[t\gg m/\gamma]{} \frac{2F^2}{\gamma^2}\,\frac{m^2}{M^2}\,\frac{\gamma\mathcal{T}_p}{\gamma\mathcal{T}_p + m} + \frac{2k_BT}{M}\,. \tag{D.14}$$

If we now use the parameter dependencies of F^2 and $\mathcal{T}_p$ estimated numerically from the simulations of the ABP model,

$$\langle \boldsymbol{v}^2_{\rm cm}(t)\rangle \xrightarrow[t\gg m/\gamma]{} 2\,(1+\zeta)\frac{F^2_{\rm act}}{\gamma^2}\,\frac{m}{M}\,\frac{\tau_p}{\tau_p + m/\gamma} + \frac{2k_BT}{M}\,. \tag{D.15}$$

In practice $\tau_p \gg m/\gamma$ and the last factor in the first term is very close to one. Moreover, ζ turns out to be much smaller than one. Thus,

$$\langle \boldsymbol{v}^{2\,\infty}_{\rm cm}\rangle \equiv \lim_{t\gg m/\gamma}\langle \boldsymbol{v}^2_{\rm cm}(t)\rangle \sim \frac{2F^2_{\rm act}}{\gamma^2}\,\frac{m}{M} + \frac{2k_BT}{M}\,. \tag{D.16}$$

From this analysis we conclude that the equal time center of mass velocity correlation decays over a short timescale related to the inertia of the single active particles and, at longer times, it reaches a plateau which is inversely proportional to the cluster mass. This behavior is confronted to simulations of single clusters extracted from the

bulk in Fig. D.1. In panel (a) we plot the full $\langle \boldsymbol{v}_{\rm cm}^2(t)\rangle$ for three cluster masses, all of them in the range in which the measured diffusion coefficient decays as $M^{-1/2}$. The solid lines represent the full analytic expression in Eq. (D.14). In panel (b) we plot the asymptotic value $\lim_{t\to\infty}\langle \boldsymbol{v}^2(t)\rangle$ as a function of the cluster mass including more mass values, together with the law M^{-1}. The predictions of the model for this instantaneous measurement are clearly confirmed. In panel (c) we show the probability density function of the x and y components of the velocity of the center of mass of the clusters, which we gathered together and simply denoted as $v_{\rm cm}^a$, for different values of the clusters' masses. The distributions are well-fitted by zero-mean Gaussians with a variance that decreases with the mass.

We also reckon that one can use this analysis and simulations to estimate the persistence length of the clusters and, more importantly, its dependence on the cluster's mass. From $\ell_p \sim v_{\rm cm}^{\infty}\tau_p$, we obtain $\ell_p \sim M^{-1/2}$ for clusters. This is consistent with the fact that we do not see a ballistic regime in the mean-square displacement of the clusters since, indeed, it is too short to be observed.

Within the same model, the cluster diffusion coefficient at long times $t' \gg m/\gamma$, and for $\tau_p \gg m/\gamma$, is

$$D = \frac{m^2}{M^2}\frac{F^2}{\gamma^2}\mathcal{T}_p + \frac{k_BT}{\gamma}\frac{m}{M} = \left[(1+\zeta)\,\frac{F_{\rm act}^2}{\gamma^2}\tau_p + \frac{k_BT}{\gamma}\right]\frac{m}{M} = \left[(1+\zeta)\,\frac{F_{\rm act}^2}{\gamma^2}\frac{m}{M}\,\tau_p + \frac{k_BT}{M}\frac{m}{\gamma}\right]. \tag{D.17}$$

As a consistency check we verify that the units are right. The ones of the last term are clearly correct. The ones of the first term $[D] = [F_{\rm act}^2]/[\gamma^2]\ [\tau_p] = [u_{\rm act}^2]/[\gamma^2]\ t = (mL/t^2)^2/(m/t)^2\ t = L^2/t$ are also correct. In the limit $m = M$, $\zeta = 0$, one recovers the familiar result for AOUPs and, in the $F_{\rm act} = 0$ case. The more correlated the active forces (higher ζ) the larger the diffusion coefficient.

We note that this simple model predicts a M^{-1} dependence of the diffusion coefficient. This is not what we observe for the clusters in the bulk, nor for the extracted clusters of not too large mass. The M^{-1} dependence is, asymptotically, what is measured for the sufficiently large extracted ones, see Figs. 2 and 3 in the main text. Therefore, the simple model does not capture the parameter dependence of quantities related to delayed measurements like, for example, the diffusion coefficient. We ascribe this mismatch to two reasons. On the one hand, the masses of the active clusters are not fixed and suffer from rather large fluctuations during their evolution. This is due to exchanges with the surrounding gas and clusters and also break-up events. The latter are exhibited, for example, in Fig. 3 of the main text and movie M4. On the other hand, the gas made of active particles themselves is not just the same as an equilibrium one at an effective temperature. This was recently studied in [SH22] where the motion of a passive tracer immersed in an active dilute bath was analyzed in detail and similar crossover from $D \sim R^{-1}$ to $D \sim R^{-2}$ with R the radius of the tracer was found both numerically and with analytic argument. The crossover length is controlled by the persistence length of the active particles in the gas and it then approaches zero in the passive limit.

E

Hydrodynamic Equations of a Chiral Fluid

We follow the derivation of the hydrodynamic equations of motion for a chiral fluid done in [SBM$^+$19], which is based on the work of [TYR$^+$05, Avr98, ASZ95, BSAV17].

The hydrodynamic variables are the mass density of spinners $\rho(\boldsymbol{r}, t)$, the momentum density of spinners $\rho(\boldsymbol{r}, t)u_i(\boldsymbol{r}, t)$, and the angular momentum density of spinners $I_0\Omega(\boldsymbol{r}, t)$, where I_0 is the spinner moment of inertia density. From the conservation of mass, momentum, and angular momentum, we have the continuity equations which describe the hydrodynamic evolution of the system. The conservation of mass is given by

$$(\partial_t + \boldsymbol{u} \cdot \boldsymbol{\nabla} + \nabla \cdot \boldsymbol{u})\rho = 0. \tag{E.1}$$

Assuming that the system is incompressible, we have $\nabla \cdot \boldsymbol{u} = 0$.

The conservation of momentum is given by

$$\rho(\partial_t + \boldsymbol{u} \cdot \boldsymbol{\nabla})u_i = -\partial_i p + \eta\nabla^2 u_i + \nabla_D \partial_i(\boldsymbol{\nabla} \cdot \boldsymbol{u}) + \eta_R \epsilon_{ij}\partial_j(2\Omega - \omega) - \Gamma_{ij}u_j + \eta_0\nabla^2\epsilon_{ij}u_j, \tag{E.2}$$

where η_{ij} is the Leva-Civita symbol, p is the pressure, $\omega = \hat{\boldsymbol{z}} \cdot (\boldsymbol{\nabla} \times \boldsymbol{u}) = \epsilon_{ij}\partial_i u_j$ is the vorticity, η is the shear viscosity, η_D is the dilatation viscosity, η_R is the rotational viscosity, η_0 is a pseudo-scalar called the odd viscosity (or Hall viscosity), and $\Gamma_{ij}u_j$ is the friction force with the substrate.

The conservation of angular momentum is given by

$$I_0(\partial_t \boldsymbol{u} \cdot \boldsymbol{\nabla} + \boldsymbol{\nabla} \cdot \boldsymbol{u})\Omega = -\Gamma^\Omega\Omega - 2\eta_R(2\Omega - \omega) + D_\theta\nabla^2\Omega + \tau, \tag{E.3}$$

where Γ^Ω is the rotational friction coefficient, D_θ is the angular momentum diffusion constant, and τ is the torque density of the spinners.

In experiments, it is found that the LHS terms of the momentum and angular momentum equations are much smaller than the RHS terms. We therefore can neglect the material derivative in these two equations. Assuming constant density $\rho = \rho_0$ and constant spinning frequency $\Omega = \Omega_0$, we have that the momentum equation becomes

$$\eta\nabla^2 u_i - \partial\tilde{p}_i + \eta_R\epsilon_{ij}\partial_j(2\Omega - \omega) - \Gamma_u u_i = 0. \tag{E.4}$$

where $\tilde{p} = p + \eta_0\omega$ is the modified pressure with the Hall viscosity contribution. The angular momentum equation becomes

$$\frac{1}{2}\Gamma^{\Omega}\Omega + \eta_R(2\Omega - \omega) = \frac{\tau}{2}. \tag{E.5}$$

The bulk flow is only determined by the momentum equation, which can be rewritten as

$$\delta^2\nabla^2\boldsymbol{u} - \boldsymbol{\nabla}\overline{p} - \boldsymbol{u} = 0, \tag{E.6}$$

where $\delta = \sqrt{(\eta + \eta_R)/\Gamma_u}$ is the hydrodynamic length scale and $\overline{p} = \tilde{p}/\Gamma_u$. Taking the curl and using the divergence-free condition, we have

$$\delta^2\nabla^2\omega - \omega = 0. \tag{E.7}$$

To consider the free-surface flow instead, we denote D as the chiral fluid domain in the plane, and ∂D as its boundary with the normal vector $\hat{\boldsymbol{n}}$. If we consider the boundary velocity of ∂D as $\boldsymbol{v} = \boldsymbol{u}|_{\partial D}$, then the stress balance equation is given by

$$\boldsymbol{\sigma}\cdot\hat{\boldsymbol{n}} = \gamma\kappa\hat{\boldsymbol{n}}, \tag{E.8}$$

where γ is the surface tension and κ is the curvature of the surface. The stress tensor is given by

$$\begin{aligned}\sigma_{ij} &= -p\delta_{ij} + (\eta_D - \eta)\delta_{ij}\partial_k u_k + 2\eta\frac{1}{2}(\partial_i u_j + \partial_j u_i) + \eta_R\epsilon_{ij}(2\Omega - \omega) + \eta_0(\partial_i\epsilon_{jk}u_k + \epsilon_{ik}\partial_k u_j)\\ &= -(p - \eta_0\omega)\delta_{ij} + \eta_R\epsilon_{ij}(2\Omega - \omega) + \eta(\partial_i u_j + \partial_j u_i) + -\eta_0 O_{ij},\end{aligned} \tag{E.9}$$

where we used the incompressibility condition and defined

$$O_{ij} = \begin{bmatrix} -2\partial_y u_x & +2\partial_x u_x \\ -2\partial_y u_y & +2\partial_x u_y \end{bmatrix}. \tag{E.10}$$

Bibliography

[ASZ95] JE Avron, Ruedi Seiler, and Petr G Zograf. Viscosity of quantum hall fluids. *Physical review letters*, 75(4):697, 1995.

[AVP17] Francisco Alarcón, Chantal Valeriani, and Ignacio Pagonabarraga. Morphology of clusters of attractive dry and wet self-propelled spherical particle suspensions. *Soft matter*, 13(4):814–826, 2017.

[Avr98] JE Avron. Odd viscosity. *Journal of statistical physics*, 92:543–557, 1998.

[BB94] L. Bocquet and J. Barrat. Hydrodynamic boundary conditions, correlation functions, and kubo relations for confined fluids. *Phys. Rev. E*, 49:3079–3092, Apr 1994.

[BBH+08] Sepideh Bazazi, Jerome Buhl, Joseph J Hale, Michael L Anstey, Gregory A Sword, Stephen J Simpson, and Iain D Couzin. Collective motion and cannibalism in locust migratory bands. *Current Biology*, 18(10):735–739, 2008.

[BBUG+22] Ephraim S Bililign, Florencio Balboa Usabiaga, Yehuda A Ganan, Alexis Poncet, Vishal Soni, Sofia Magkiriadou, Michael J Shelley, Denis Bartolo, and William TM Irvine. Motile dislocations knead odd crystals into whorls. *Nature Physics*, 18(2):212–218, 2022.

[BCC+08] Michele Ballerini, Nicola Cabibbo, Raphael Candelier, Andrea Cavagna, Evaristo Cisbani, Irene Giardina, Vivien Lecomte, Alberto Orlandi, Giorgio Parisi, Andrea Procaccini, et al. Interaction ruling animal collective behavior depends on topological rather than metric distance: Evidence from a field study. *Proceedings of the national academy of sciences*, 105(4):1232–1237, 2008.

[BCH09] GA Buxton, N Clarke, and PJ Hussey. Actin dynamics and the elasticity of cytoskeletal networks. *Express polymer letters.*, 3(9):579–587, 2009.

[BGHP20] M. Bär, R. Grossmann, S. Heidenreich, and F. Peruani. Self-propelled rods: Insights and perspectives for active matter. *Annu. Rev. Cond. Matt. Phys.*, 11:441, 2020.

[BGL+14] D.S. Bolintineanu, G.S. Grest, J.B. Lechman, F. Pierce, S.J. Plimpton, and P.R. Schunk. Particle dynamics modeling methods for colloid suspensions. *Computational Particle Mechanics*, 1(3):321–356, 2014.

[BHA81] JA Barker, D Henderson, and Farid F Abraham. Phase diagram of the two-dimensional lennard-jones system; evidence for first-order transitions. *Physica A: Statistical Mechanics and its Applications*, 106(1-2):226–238, 1981.

[BJF15] V. Bratanov, F. Jenko, and E. Frey. New class of turbulence in active fluids. *Proc. Nat. Acad. Sci.*, 112:15048, 2015.

[BJS18] S. Bi, F. Jin, and V. Sourjik. Inverted signaling by bacterial chemotaxis receptors. *Nature Comm.*, 9:2927, 2018.

[BK11] Etienne P. Bernard and Werner Krauth. Two-step melting in two dimensions: First-order liquid-hexatic transition. *Phys. Rev. Lett.*, 107:155704, Oct 2011.

[Bla71] J. R. Blake. A spherical envelope approach to ciliary propulsion. *Journ. Fluid Mech.*, 46:199, 1971.

[BLS13] Julian Bialké, Hartmut Löwen, and Thomas Speck. Microscopic theory for the phase separation of self-propelled repulsive disks. *EPL*, 103(3):30008, 2013.

[BMRS18] Urna Basu, Satya N Majumdar, Alberto Rosso, and Grégory Schehr. Active brownian motion in two dimensions. *Physical Review E*, 98(6):062121, 2018.

[BP01] O.M. Braun and M. Peyrard. Friction in a solid lubricant film. *Phys. Rev. E*, 63:046110, Mar 2001.

[Bra02] Alan J Bray. Theory of phase-ordering kinetics. *Adv. in Phys.*, 51(2):481–587, 2002.

[BS76] Kurt Binder and Dietrich Stauffer. Statistical theory of nucleation, condensation and coagulation. *Advances in Physics*, 25(4):343–396, 1976.

[BSAV17] Debarghya Banerjee, Anton Souslov, Alexander G Abanov, and Vincenzo Vitelli. Odd viscosity in chiral active fluids. *Nature communications*, 8(1):1573, 2017.

[BSC+06] Jerome Buhl, David JT Sumpter, Iain D Couzin, Joe J Hale, Emma Despland, Edgar R Miller, and Steve J Simpson. From disorder to order in marching locusts. *Science*, 312(5778):1402–1406, 2006.

[BSD18] G. Briand, M. Schindler, and O. Dauchot. Spontaneously flowing crystal of self-propelled particles. *Phys. Rev. Lett.*, 120:208001, May 2018.

[BSL12] Julian Bialké, Thomas Speck, and Hartmut Löwen. Crystallization in a dense suspension of self-propelled particles. *Phys. Rev. Lett.*, 108(16):168301, 2012.

[BSLS15] Julian Bialké, Jonathan T. Siebert, Hartmut Löwen, and Thomas Speck. Negative interfacial tension in phase-separated active brownian particles. *Physical Review Letters*, 115:098301, Aug 2015.

[Cat19] Michael E Cates. Active field theories. *arXiv preprint arXiv:1904.01330*, 2019.

[CCD+23] C. Caporusso, L. F. Cugliandolo, P. Digregorio, G. Gonnella, D. Levis, and A. Suma. Dynamics of motility-induced clusters: coarsening beyond Ostwald ripening. *Phys. Rev. Lett.*, 131:068201, 2023.

[CCVGW15] H. Chien-Cheng, A. Varghese, G. Gompper, and R.G. Winkler. Thermostat for nonequilibrium multiparticle-collision-dynamics simulations. *Phys. Rev. E*, 91:013310, Jan 2015.

[CDB+12] Xiao Chen, Xu Dong, Avraham Be'er, Harry L Swinney, and HP Zhang. Scale-invariant correlations in dynamic bacterial clusters. *Physical review letters*, 108(14):148101, 2012.

[CDD+04] A. Coniglio, L. De Arcangelis, E. Del Gado, A. Fierro, and N. Sator. Percolation, gelation and dynamical behaviour in colloids. *J. Phys.: Condens. Matter*, 16:S4831, 2004.

[CDGS17a] Leticia F Cugliandolo, Pasquale Digregorio, Giuseppe Gonnella, and Antonio Suma. Phase coexistence in two-dimensional passive and active dumbbell systems. *Physical review letters*, 119(26):268002, 2017.

[CDGS17b] Leticia F Cugliandolo, Pasquale Digregorio, Giuseppe Gonnella, and Antonio Suma. Phase coexistence in two-dimensional passive and active dumbbell systems. *Physical review letters*, 119(26):268002, 2017.

[CDGS17c] L.F. Cugliandolo, P. Digregorio, G. Gonnella, and A. Suma. Phase coexistence in two-dimensional passive and active dumbbell systems. *Phys. Rev. Lett.*, 119:268002, Dec 2017.

[CDL+20a] C. B. Caporusso, L. Digregorio, D. Levis, L. F. Cugliandolo, and G. Gonnella. Motility-induced microphase and macrophase separation in a two-dimensional active brownian particle system. *Phys. Rev. Lett.*, 125:178004, 2020.

[CDL+20b] C. B. Caporusso, P. Digregorio, D. Levis, L. F. Cugliandolo, and G. Gonnella. Motility-induced microphase and macrophase separation in a two-dimensional active Brownian particle system. *Phys. Rev. Lett.*, 125:178004, 2020.

[CDL+20c] Claudio B Caporusso, Pasquale Digregorio, Demian Levis, Leticia F Cugliandolo, and Giuseppe Gonnella. Motility-induced microphase and macrophase separation in a two-dimensional active brownian particle system. *Physical Review Letters*, 125(17):178004, 2020.

[CGG+08] Hugues Chaté, Francesco Ginelli, Guillaume Grégoire, Fernando Peruani, and Franck Raynaud. Modeling collective motion: variations on the vicsek model. *The European Physical Journal B*, 64:451–456, 2008.

[CGL+19] L.N. Carenza, G. Gonnella, A. Lamura, G. Negro, and A. Tiribocchi. Lattice boltzmann methods and active fluids. *Eur. Phys. J. E*, 42(6):81, 2019.

[CGS15] L. F. Cugliandolo, G. Gonnella, and A. Suma. Rotational and translational diffusion in an interacting active dumbbell system. *Phys. Rev. E*, 91:062124, 2015.

[CGW20] J. Clopés, G. Gompper, and R. G. Winkler. Hydrodynamic interactions in squirmer dumbbells: active stress-induced alignment and locomotion. *Soft Matter*, 16:10676, 2020.

[CH93] M. C. Cross and P. C. Hohenberg. Pattern formation outside of equilibrium. *Rev. Mod. Phys.*, 65:851, 1993.

[CM21a] L. Caprini and U.M.B. Marconi. Inertial self-propelled particles. *The Journal of Chemical Physics*, 154(2):024902, 2021.

[CM21b] L. Caprini and U.M.B. Marconi. Spatial velocity correlations in inertial systems of active brownian particles. *Soft Matter*, 17:4109–4121, 2021.

[CMM+20] L. Caprini, U.M.B. Marconi, C. Maggi, M. Paoluzzi, and A. Puglisi. Hidden velocity ordering in dense suspensions of self-propelled disks. *Phys. Rev. Research*, 2:023321, Jun 2020.

[CMP20a] L. Caprini, U.M.B. Marconi, and A. Puglisi. Spontaneous velocity alignment in motility-induced phase separation. *Phys. Rev. Lett.*, 124:078001, Feb 2020.

[CMP20b] Lorenzo Caprini, U Marini Bettolo Marconi, and Andrea Puglisi. Spontaneous velocity alignment in motility-induced phase separation. *Phys. Rev. Lett.*, 124(7):078001, 2020.

[CNS+24] C. B. Caporusso, G. Negro, A. Suma, P. Digregorio, L. N. Carenza, G. Gonnella, and L. F. Cugliandolo. Phase behaviour and dynamics of three-dimensional active dumbbell systems. *Soft Matter*, 20:923, 2024.

[CSSC04] Juan J. Cerdà, Tomás Sintes, C. M. Sorensen, and A. Chakrabarti. Structure factor scaling in colloidal phase separation. *Phys. Rev. E*, 70:051405, Nov 2004.

[CT13] ME Cates and J Tailleur. When are active brownian particles and run-and-tumble particles equivalent? consequences for motility-induced phase separation. *EPL*, 101(2):20010, 2013.

[CT15a] M E Cates and J Tailleur. Motility-induced phase separation. *Annu. Rev. Cond. Matt. Phys.*, 6(1):219, 2015.

[CT15b] M E Cates and J Tailleur. Motility-induced phase separation. *Annu. Rev. Cond. Matt. Phys.*, 6(1):219, 2015.

[CT15c] M.E. Cates and J. Tailleur. Motility-induced phase separation. *Annual Review of Condensed Matter Physics*, 6(1):219–244, 2015.

[DCC+04a] C. Dombrowski, L. Cisneros, S. Chatkaew, R.E. Goldstein, and J.O. Kessler. Self-concentration and large-scale coherence in bacterial dynamics. *Phys. Rev. Lett.*, 93:098103, 2004.

[DCC+04b] Christopher Dombrowski, Luis Cisneros, Sunita Chatkaew, Raymond E Goldstein, and John O Kessler. Self-concentration and large-scale coherence in bacterial dynamics. *Phys. Rev. Lett.*, 93(9):098103, 2004.

[DDS+18] P. Digregorio, D., A. Suma, L.F. Cugliandolo, G. Gonnella, and I. Pagonabarraga. Full phase diagram of active brownian disks: From melting to motility-induced phase separation. *Phys. Rev. Lett.*, 121:098003, Aug 2018.

[DL09] B. Dünweg and A.J.C. Ladd. *Lattice Boltzmann Simulations of Soft Matter Systems*, pages 89–166. Springer Berlin Heidelberg, 2009.

[DLC+19] Pasquale Digregorio, Demian Levis, Leticia F Cugliandolo, Giuseppe Gonnella, and Ignacio Pagonabarraga. Clustering of topological defects in two-dimensional melting of active and passive disks. arXiv:1911.06366, 2019.

[DLC+22a] P. Digregorio, D. Levis, L. F. Cugliandolo, G. Gonnella, and I. Pagonabarraga. Unified analysis of topological defects in 2d systems of active and passive disks. *Soft Matter*, 18:566–591, 2022.

[DLC+22b] P. Digregorio, D. Levis, L.F. Cugliandolo, G. Gonnella, and I. Pagonabarraga. Unified analysis of topological defects in 2d systems of active and passive disks. *Soft Matter*, 18:566–591, 2022.

[DLS+18a] Pasquale Digregorio, Demian Levis, Antonio Suma, Leticia F Cugliandolo, Giuseppe Gonnella, and Ignacio Pagonabarraga. Full phase diagram of active brownian disks: From melting to motility-induced phase separation. *Phys. Rev. Lett.*, 121(9):098003, 2018.

[DLS+18b] Pasquale Digregorio, Demian Levis, Antonio Suma, Leticia F. Cugliandolo, Giuseppe Gonnella, and Ignacio Pagonabarraga. Full phase diagram of active brownian disks: From melting to motility-induced phase separation. *Phys. Rev. Lett.*, 121:098003, 2018.

[DLS+18c] Pasquale Digregorio, Demian Levis, Antonio Suma, Leticia F Cugliandolo, Giuseppe Gonnella, and Ignacio Pagonabarraga. Full phase diagram of active brownian disks: From melting to motility-induced phase separation. *Physical review letters*, 121(9):098003, 2018.

[DLS+19] P. Digregorio, D. Levis, A. Suma, L. F. Cugliandolo, G. Gonnella, and I. Pagonabarraga. 2d melting and motility induced phase separation in active brownian hard disks and dumbbells. *J. Phys. Conf. Series*, 1163:012073, 2019.

[Dom00] Cyril Domb. *Phase transitions and critical phenomena*. Elsevier, 2000.

[EGRX22] Mohammed Elismaili, David Gonzalez-Rodriguez, and Hong Xu. Gas-liquid interface of a lennard-jones binary mixture controlled by differential activity: phase transition and interfacial stability. *The European Physical Journal E*, 45(10):86, 2022.

[EKSX96a] M. Ester, H.-P. Kriegel, J. Sander, and X. Xu. A density-based algorithm for discovering clusters in large spatial databases with noise. page 226, 1996.

[EKSX96b] M. Ester, H.-P. Kriegel, J. Sander, and X. Xu. A density-based algorithm for discovering clusters in large spatial databases with noise. In *Proceedings of the Second International Conference on Knowledge Discovery and Data Mining*. 1996.

[Eva79] Robert Evans. The nature of the liquid-vapour interface and other topics in the statistical mechanics of non-uniform, classical fluids. *Advances in physics*, 28(2):143–200, 1979.

[EW95] Pep Espanol and Patrick Warren. Statistical mechanics of dissipative particle dynamics. *Europhysics letters*, 30(4):191, 1995.

[FJ94] D. Faken and H. Jónsson. Systematic analysis of local atomic structure combined with 3d computer graphics. *Computational Materials Science*, 2:279, 1994.

[FJ16] C. J. Fullerton and R. Jack. *J. Chem. Phys.*, 145:244505, 2016.

[FKS+18] Y. Fily, Y. Kafri, A. P. Solon, J. Tailleur, and A. Turner. Mechanical pressure and momentum conservation in dry active matter. *J. Phys. A: Math. Theor.*, 51:044003, 2018.

[FM12a] Y. Fily and M. C. Marchetti. Athermal phase separation of self-propelled particles with no alignment. *Phys. Rev. Lett.*, 108:235702, 2012.

[FM12b] Y. Fily and M.C. Marchetti. Athermal phase separation of self-propelled particles with no alignment. *Phys. Rev. Lett.*, 108:235702, Jun 2012.

[FMMT12] F.D. Farrell, M.C. Marchetti, D. Marenduzzo, and J. Tailleur. Pattern formation in self-propelled particles with density-dependent motility. *Phys. Rev. Lett.*, 108:248101, 2012.

[FS16] Antoine Fruleux and Ken Sekimoto. Mesoscopic formulas of linear and angular momentum fluxes. *Physical Review E*, 94(1):013004, 2016.

[FSV23] Michel Fruchart, Colin Scheibner, and Vincenzo Vitelli. Odd viscosity and odd elasticity. *Annual Review of Condensed Matter Physics*, 14:471–510, 2023.

[Fur89] Hiroshi Furukawa. Numerical study of multitime scaling in a solid system undergoing phase separation. *Physical Review B*, 40(4):2341, 1989.

[GBC+21] M. G. Giordano, F. Bonelli, L. N. Carenza, G. Gonnella, and G. Negro. Activity-induced isotropic-polar transition in active liquid crystals. *EPL*, 133(5):58004, 2021.

[GHPM15] E. Guyon, J.P. Hulin, L. Petit, and C.D. Mitescu. *Physical Hydrodynamics*. Oxford University Press, 2015.

[GIKW09] G. Gompper, T. Ihle, D.M. Kroll, and R.G. Winkler. *Multi-Particle Collision Dynamics: A Particle-Based Mesoscale Simulation Approach to the Hydrodynamics of Complex Fluids*, pages 1–87. Springer Berlin Heidelberg, Berlin, Heidelberg, 2009.

[GLS14] Giuseppe Gonnella, Antonio Lamura, and Antonio Suma. Phase segregation in a system of active dumbbells. *Int. J. Mod. Phys. C*, 25(12):1441004, 2014.

[GMST15a] G. Gonnella, D. Marenduzzo, A. Suma, and A. Tiribocchi. Motility-induced phase separation and coarsening in active matter. *C. R. Phys.*, 16:316, 2015.

[GMST15b] G. Gonnella, D. Marenduzzo, A. Suma, and A. Tiribocchi. Motility-induced phase separation and coarsening in active matter. *Comptes Rendus Acad. Sc.*, 16:316, 2015.

[Gol59] H. Goldstein. *Classical Mechanics*. Addison-Wesley, 1959.

[GPBC10] F. Ginelli, F. Peruani, M. Bär, and H. Chaté. Large-scale collective properties of self-propelled rods. *Phys. Rev. Lett.*, 104:184502, 2010.

[GTD+18] F. Ginot, I. Theurkauff, Detcheverry, C. Ybert, and C. Cottin-Bizonne. Aggregation-fragmentation and individual dynamics of active clusters. *Nat. Comm.*, 9:696, 2018.

[GWS+20] G. Gompper, R.G. Winkler, T. Speck, A. Solon, C. Nardini, F. Peruani, H. Löwen, R. Golestanian, U.B. Kaupp, L. Alvarez, T. Kiørboe, E. Lauga, W.C.K. Poon, A. DeSimone, S. Muiños-Landin, A. Fischer, N.A. Söker, F. Cichos, R. Kapral, P. Gaspard, M. Ripoll, F. Sagues, A. Doostmohammadi, J.M. Yeomans, I.S. Aranson, C. Bechinger, H. Stark, C.K. Hemelrijk, F.J. Nedelec, T. Sarkar, T. Aryaksama, M. Lacroix, G. Duclos, V. Yashunsky, P. Silberzan, M. Arroyo, and S. Kale. The 2020 motile active matter roadmap. *Journal of Physics: Condensed Matter*, 32(19):193001, feb 2020.

[HFS+21] Ming Han, Michel Fruchart, Colin Scheibner, Suriyanarayanan Vaikuntanathan, Juan J De Pablo, and Vincenzo Vitelli. Fluctuating hydrodynamics of chiral active fluids. *Nature Physics*, 17(11):1260–1269, 2021.

[HH77] P.C. Hohenberg and B.I. Halperin. Theory of dynamic critical phenomena. *Rev. Mod. Phys.*, 49:435, 1977.

[HHIH05] M. Hecht, J. Harting, T. Ihle, and H.J. Herrmann. Simulation of clay-like colloids. *Phys. Rev. E*, 72:011408, Jul 2005.

[HK19] Amir Hajibabaei and Kwang S Kim. First-order and continuous melting transitions in two-dimensional lennard-jones systems and repulsive disks. *Phys. Rev. E*, 99(2):022145, 2019.

[HKdLHS19] Sophie Hermann, Philip Krinninger, Daniel de Las Heras, and Matthias Schmidt. Phase coexistence of active brownian particles. *Physical Review E*, 100(5):052604, 2019.

[HKEM20] C. Hargus, K. Klymko, J. M. Epstein, and K. K. Mandadapu. *J. Chem. Phys.*, 152:201102, 2020.

[HM13] Jean-Pierre Hansen and Ian Ranald McDonald. *Theory of simple liquids: with applications to soft matter*. Academic press, 2013.

[HYGW15] Jinglei Hu, Mingcheng Yang, Gerhard Gompper, and Roland G Winkler. Modelling the mechanics and hydrodynamics of swimming e. coli. *Soft matter*, 11(40):7867–7876, 2015.

[IK50] JH Irving and John G Kirkwood. The statistical mechanical theory of transport processes. iv. the equations of hydrodynamics. *The Journal of chemical physics*, 18(6):817–829, 1950.

[ITK04] T. Ihle, E. Tüzel, and D.M. Kroll. Resummed green-kubo relations for a fluctuating fluid-particle model. *Phys. Rev. E*, 70:035701, Sep 2004.

[JB16] M. Joyeux and E. Bertin. Pressure of a gas of underdamped active dumbbells. *Phys. Rev. E*, 93:032605, 2016.

[JB22] Kedar Joshi and Sibani Lisa Biswal. Extension of kelvin's equation to dipolar colloids. *Proceedings of the National Academy of Sciences*, 119(12):e2117971119, 2022.

[Jon02] Richard AL Jones. *Soft condensed matter*, volume 6. Oxford University Press, 2002.

[Joy17] M. Joyeux. Recovery of mechanical pressure in a gas of underdamped active dumbbells with brownian noise. *Phys. Rev. E*, 95:052603, 2017.

[JSK12] Sebastian Jäger, Heiko Schmidle, and Sabine HL Klapp. Nonequilibrium condensation and coarsening of field-driven dipolar colloids. *Physical Review E*, 86(1):011402, 2012.

[JSK13] Sebastian Jaeger, Holger Stark, and Sabine HL Klapp. Dynamics of cluster formation in driven magnetic colloids dispersed on a monolayer. *Journal of Physics: Condensed Matter*, 25(19):195104, 2013.

[KB49] John G Kirkwood and Frank P Buff. The statistical mechanical theory of surface tension. *The Journal of Chemical Physics*, 17(3):338–343, 1949.

[KBJ83] M. Kolb, R. Botet, and R. Jullien. Scaling of kinetically growing clusters. *Phys. Rev. Lett.*, 51:1123, 1983.

[KK15] Sebastian C Kapfer and Werner Krauth. Two-Dimensional Melting: From Liquid-Hexatic Coexistence to Continuous Transitions. *Phys. Rev. Lett.*, 114:035702, 2015.

[KKK18] J U Klamser, S C Kapfer, and W Krauth. Thermodynamic phases in two-dimensional active matter. *Nat. Comm.*, 9:5045, 2018.

[KPRY03] N. Kikuchi, C.M. Pooley, J.F. Ryder, and J.M. Yeomans. Transport coefficients of a mesoscopic fluid dynamics model. *The Journal of Chemical Physics*, 119(12):6388–6395, 2003.

[Kre09] RV Krems. Advances in chemical physics, volume 140, 2009.

[KSK18] J.U. Klamser, S.C.Kapfer, and W. Krauth. Thermodynamic phases in two-dimensional active matter. *Nat Commun*, 9, 2018.

[LÏ8] H. Löwen. Active colloidal molecules. *EPL*, 121:58001, 2018.

[LC20] Yan-Wei Li and Massimo Pica Ciamarra. Phase behavior of lennard-jones particles in two dimensions. *Physical Review E*, 102:062101, Dec 2020.

[LCP17a] D Levis, J Codina, and I Pagonabarraga. Active Brownian Equation of State: Metastability and Phase Coexistence. *Soft Matter*, 13:8113–8119, 2017.

[LCP17b] Demian Levis, Joan Codina, and Ignacio Pagonabarraga. Active brownian equation of state: metastability and phase coexistence. *Soft Matter*, 13(44):8113–8119, 2017.

[LCSS+22] Miguel A López-Castaño, Alejandro Márquez Seco, Alicia Márquez Seco, Álvaro Rodríguez-Rivas, and Francisco Vega Reyes. Chirality transitions in a system of active flat spinners. *Physical Review Research*, 4(3):033230, 2022.

[Ley03] F. Leyvraz. Scaling theory and exactly solved models in the kinetics of irreversible aggregation. *Phys. Rep.*, 383:95, 2003.

[LFWG18] Ming Luo, Youzeng Feng, Tingwei Wang, and Jianguo Guan. Micro-/nanorobots at work in active drug delivery. *Advanced Functional Materials*, 28(25):1706100, 2018.

[LG02] A. Lamura and G. Gompper. Numerical study of the flow around a cylinder using multi-particle collision dynamics. *Eur. Phys. J. E*, 9(5):477–485, 2002.

[LGIK01] Antonio Lamura, Gerhard Gompper, Thomas Ihle, and DM Kroll. Multi-particle collision dynamics: Flow around a circular and a square cylinder. *Europhysics Letters*, 56(3):319, 2001.

[LGV06] B. Liu, J. Goree, and O.S. Vaulina. Test of the stokes-einstein relation in a two-dimensional yukawa liquid. *Phys. Rev. Lett.*, 96:015005, Jan 2006.

[Lig52] M. J. Lighthill. On the squirming motion of nearly spherical deformable bodies through liquids at very small reynolds numbers. *Communications on Pure and Applied Mathematics*, 46:109, 1952.

[LJJP03] Peter Lenz, Jean-François Joanny, Frank Jülicher, and Jacques Prost. Membranes with rotating motors. *Physical review letters*, 91(10):108104, 2003.

[LKM+21] Nicholas Lauersdorf, Thomas Kolb, Moslem Moradi, Ehssan Nazockdast, and Daphne Klotsa. Phase behavior and surface tension of soft active brownian particles. *Soft Matter*, 17(26):6337–6351, 2021.

[LL17] Benno Liebchen and Demian Levis. Collective behavior of chiral active matter: Pattern formation and enhanced flocking. *Physical review letters*, 119(5):058002, 2017.

[L′ow20] H. L′owen. Inertial effects of self-propelled particles: From active brownian to active langevin motion. *The Journal of Chemical Physics*, 152(4):040901, 2020.

[LP10] I Llopis and I Pagonabarraga. Hydrodynamic interactions in squirmer motion: Swimming with a neighbour and close to a wall. *Journal of Non-Newtonian Fluid Mechanics*, 165(17-18):946–952, 2010.

[LPN19] Qun-Li Lei, Massimo Pica Ciamarra, and Ran Ni. Nonequilibrium strongly hyperuniform fluids of circle active particles with large local density fluctuations. *Science Adv.*, 5(1):eaau7423, 2019.

[LS61] Ilya M Lifshitz and Vitaly V Slyozov. The kinetics of precipitation from supersaturated solid solutions. *Journal of physics and chemistry of solids*, 19(1-2):35–50, 1961.

[LZC+08] P. J. Lu, E. Zaccarelli, F. Ciulla, A. B. Schofield, F. Sciortino, and D. A. Weitz. Gelation of particles with short-range attraction. *Nature*, 453:499, 2008.

[MBC+17] R. Mandal, P. J. Bhuyan, P. Chaudhuri, M. Rao, and C. Dasgupta. Glassy swirls of active dumbbells. *Phys. Rev. E*, 96:042605, 2017.

[MBSG22] S. E. Moran, I. R. Bruss, P. W. A. Schönhöfer, and S. C. Glotzer. Particle anisotropy tunes emergent behavior in active colloidal systems. *Soft Matter*, 18:1044, 2022.

[MCLH+21] Helena Massana-Cid, Demian Levis, Raúl Josué Hernández Hernández, Ignacio Pagonabarraga, and Pietro Tierno. Arrested phase separation in chiral fluids of colloidal spinners. *Physical Review Research*, 3(4):L042021, 2021.

[MCMFDL22] H. Massana-Cid, C. Maggi, G. Frangipane, and R. Di Leonardo. Rectification and confinement of photokinetic bacteria in an optical feedback loop. *Nature Comm.*, 13:2740, 2022.

[MCP21] U.M.B. Marconi, L. Caprini, and A. Puglisi. Hydrodynamics of simple active liquids: the emergence of velocity correlations. *New Journal of Physics*, 23(10):103024, oct 2021.

[MD08] M. Marechal and M. Dijkstra. Stability of orientationally disordered crystal structures of colloidal hard dumbbells. *Phys. Rev. E*, 77:061405, 2008.

[Mea83] P. Meakin. Formation of fractal clusters and networks by irreversible diffusion-limited aggregation. *Phys. Rev. Lett.*, 51:1119, 1983.

[MFAB+17] DA Matoz-Fernandez, Elisabeth Agoritsas, Jean-Louis Barrat, Eric Bertin, and Kirsten Martens. Nonlinear rheology in a model biological tissue. *Physical review letters*, 118(15):158105, 2017.

[MGLDGP18] A. Martín-Gómez, D. Levis, A. Díaz-Guilera, and I. Pagonabarraga. Collective motion of active brownian particles with polar alignment. *Soft Matter*, 14:2610–2618, 2018.

[MicvacAU+13] B. M. Mognetti, A. Šarić, S. Angioletti-Uberti, A. Cacciuto, C. Valeriani, and D. Frenkel. Living clusters and crystals from low-density suspensions of active colloids. *Phys. Rev. Lett.*, 111:245702, 2013.

[Mie03] Gustav Mie. Zur kinetischen theorie der einatomigen körper. *Annalen der Physik*, 316(8):657–697, 1903.

[MJR+13a] M C Marchetti, J-F Joanny, S Ramaswamy, T B Liverpool, J Prost, M Rao, and R A Simha. Hydrodynamics of soft active matter. *Rev. Mod. Phys.*, 85(3):1143, 2013.

[MJR+13b] M. C. Marchetti, J. F. Joanny, S. Ramaswamy, T. B. Liverpool, J. Prost, M. Rao, and R. A. Simha. Hydrodynamics of soft active matter. *Rev. Mod. Phys.*, 85:1143, 2013.

[MK99] A. Malevanets and R. Kapral. Mesoscopic model for solvent dynamics. *The Journal of Chemical Physics*, 110(17):8605–8613, 1999.

[MK00] A. Malevanets and R. Kapral. Solute molecular dynamics in a mesoscale solvent. *The Journal of Chemical Physics*, 112(16):7260–7269, 2000.

[MLL19] Suvendu Mandal, Benno Liebchen, and Hartmut Löwen. Motility-induced temperature difference in coexisting phases. *Phys. Rev. Lett.*, 123(22):228001, 2019.

[MMMA19] G. Melaugh, D. Marenduzzo, A. Morozov, and R. J. Allen. A simulation study of aggregation mediated by production of cohesive molecules. *Soft Matter*, 15:9120, 2019.

[MNGLF14] R. Matas-Navarro, R. Golestanian, T.B. Liverpool, and S.M. Fielding. Hydrodynamic suppression of phase separation in active suspensions. *Phys. Rev. E*, 90:032304, Sep 2014.

[MPD+05] Andrés Mejía, Josep C Pàmies, Daniel Duque, Hugo Segura, and Lourdes F Vega. Phase and interface behaviors in type-i and type-v lennard-jones mixtures: Theory and simulations. *The Journal of chemical physics*, 123(3):034505, 2005.

[MRS+06] Nicholas C Makris, Purnima Ratilal, Deanelle T Symonds, Srinivasan Jagannathan, Sunwoong Lee, and Redwood W Nero. Fish population and behavior revealed by instantaneous continental shelf-scale imaging. *Science*, 311(5761):660–663, 2006.

[MVC18] S. A. Mallory, C. Valeriani, and A. Cacciuto. An active approach to colloidal self-assembly. *Annu. Rev. Phys. Chem.*, 69:59, 2018.

[MZ88] G.R McNamara and G. Zanetti. Use of the boltzmann equation to simulate lattice-gas automata. *Phys. Rev. Lett.*, 61:2332, 1988.

[NCA+19] G. Negro, L.N. Carenza, A.Lamura, A. Tiribocchi, and G. Gonnella. Rheology of active polar emulsions: from linear to unidirectional and inviscid flow, and intermittent viscosity. *Soft Matter*, 15:8251–8265, 2019.

[NCD+22] Giuseppe Negro, C Basilio Caporusso, Pasquale Digregorio, Giuseppe Gonnella, Antonio Lamura, and Antonio Suma. Hydrodynamic effects on the liquid-hexatic transition of active colloids. *The European Physical Journal E*, 45(9):75, 2022.

[NCP+20a] P. Nie, J. Chattoraj, A. Piscitelli, P. Doyle, R. Ni, and M.P. Ciamarra. Stability phase diagram of active brownian particles. *Phys. Rev. Research*, 2:023010, Apr 2020.

[NCP+20b] P. Nie, J. Chattoraj, A. Piscitelli, P. Doyle, R. Ni, and M. Pica Ciamarra. Stability phase diagram of active Brownian particles. *Phys. Rev. Research*, 2:023010, 2020.

[NF07] Francois Nedelec and Dietrich Foethke. Collective langevin dynamics of flexible cytoskeletal fibers. *New Journal of Physics*, 9(11):427, 2007.

[NMB+18] S. K. Nandi, R. Mandal, P. J. Bhuyan, C. Dasgupta, M. Rao, and N. S. Gov. A random first-order transition theory for an active glass. *Proc. Natl. Acad. Sci. U.S.A*, 115:7688, 2018.

[NS01] F. Nédélec and T. Surrey. Dynamics of microtubule aster formation by motor complexes. *Comptes Rendus Acad. Sci*, 2:841, 2001.

[NSK03] F. Nédélec, T. Surrey, and E. Karsenti. Self-organisation and forces in the microtubule cytoskeleton. *Curr. Opin. Cell Biol.*, 15:118, 2003.

[NSML97] F. Nédélec, T. Surrey, A.C. Maggs, and S. Leibler. Self-organization of microtubules and motors. *Nature*, 389:305, 1997.

[OBSC00] A. Okabe, B. Boots, K. Sugihara, and S. N. Chiu. *Spatial Tessellations – Concepts and Applications of Voronoi Diagrams (2nd ed.)*. John Wiley, 2000.

[OKG+21] A.K. Omar, K. Klymko, T. GrandPre, P.L. Geissler, and J.F. Brady. Tuning nonequilibrium phase transitions with inertia. *arXiv:2108.10278*, 2021.

[OKGG21] A. K. Omar, K. Klymko, T. GrandPre, and P. L. Geissler. Phase diagram of active Brownian spheres: Crystallization and the metastability of motility-induced phase separation. *Phys. Rev. Lett.*, 126:188002, 2021.

[PBD21] S. Paul, A. Bera, and S. K. Das. How do clusters in phase-separating active matter systems grow? a study for vicsek activity in systems undergoing vapor–solid transition. *Soft Matter*, 17:645, 2021.

[PCGS20a] I. Petrelli, L. F. Cugliandolo, G. Gonnella, and A. Suma. Effective temperatures in inhomogeneous passive and active bidimensional brownian particle systems. *Phys. Rev. E*, 102:012609, 2020.

[PCGS20b] I. Petrelli, L.F. Cugliandolo, G. Gonnella, and A. Suma. Effective temperatures in inhomogeneous passive and active bidimensional brownian particle systems. *Phys. Rev. E*, 102:012609, Jul 2020.

[PCY21] E. Pirhadi, X. Cheng, and X. Yong. Dependency of active pressure and equation of state on stiffness of wall. *Scientific Reports*, 11:22204, 2021.

[PD20] Siddharth Paliwal and Marjolein Dijkstra. Role of topological defects in the two-stage melting and elastic behavior of active brownian particles. *Phys. Rev. Res.*, 2(1):012013, 2020.

[PDB06a] F. Peruani, A. Deutsch, and M. Bär. Nonequilibrium clustering of self-propelled rods. *Phys. Rev. E*, 74:030904(R), 2006.

[PDB06b] Fernando Peruani, Andreas Deutsch, and Markus Bär. Nonequilibrium clustering of self-propelled rods. *Physical Review E*, 74(3):030904, 2006.

[PDC+18] I. Petrelli, P. Digregorio, L. F. Cugliandolo, G. Gonnella, and A. Suma. *Eur. Phys. J. E*, 41:128, 2018.

[Ped16] Timothy J Pedley. Spherical squirmers: models for swimming microorganisms. *IMA Journal of Applied Mathematics*, 81(3):488–521, 2016.

[PF01] I Pagonabarraga and D Frenkel. Dissipative particle dynamics for interacting systems. *The Journal of Chemical Physics*, 115(11):5015–5026, 2001.

[PL79] O Penrose and JL Lebowitz. Towards a rigorous theory of metastability. volume vii of studies in statistical mechanics, 1979.

[PL06] J.T. Padding and A.A. Louis. Hydrodynamic interactions and brownian forces in colloidal suspensions: Coarse-graining over time and length scales. *Phys. Rev. E*, 74:031402, Sep 2006.

[PL23] Anthony R Poggioli and David T Limmer. Emergent kelvin waves in chiral active matter. *arXiv preprint arXiv:2306.14984*, 2023.

[Poo02] W. C. K. Poon. The physics of a model colloid-polymer mixture. *J. Phys.: Condens. Matter*, 14:R859, 2002.

[PPFD17] Siddharth Paliwal, Vasileios Prymidis, Laura Filion, and Marjolein Dijkstra. Non-equilibrium surface tension of the vapour-liquid interface of active lennard-jones particles. *The Journal of chemical physics*, 147(8):084902, 2017.

[PS14] Oliver Pohl and Holger Stark. Dynamic clustering and chemotactic collapse of self-phoretic active particles. *Phys. Rev. Lett.*, 112(23):238303, 2014.

[PSF15] V. Prymidis, H. Sielcken, and L. Filion. Self-assembly of active attractive spheres. *Soft Matter*, 11:4158, 2015.

[PSS+13] Jeremie Palacci, Stefano Sacanna, Asher Preska Steinberg, David J Pine, and Paul M Chaikin. Living crystals of light-activated colloidal surfers. *Science*, 339(6122):936–940, 2013.

[PY58] Jerome K. Percus and George J. Yevick. Analysis of classical statistical mechanics by means of collective coordinates. *Phys. Rev.*, 110:1–13, Apr 1958.

[RBE+12] Pawel Romanczuk, Markus Bär, Werner Ebeling, Benjamin Lindner, and Lutz Schimansky-Geier. Active brownian particles. *Eur. Phys. J. Spec. Topics*, 202(1):1–162, 2012.

[RC75] V Raghavan and Morris Cohen. Solid-state phase transformations. In *Changes of State*, pages 67–127. Springer, 1975.

[RCB77] J.-P. Ryckaert, G. Ciccotti, and H. J. C. Berendsen. Numerical integration of the cartesian equations of motion of a system with constraints: molecular dynamics of n-alkanes. *J. Comp. Phys.*, 23:327, 1977.

[RCD+] C. P. Royall, P. Charbonneau, M. Dijkstra, J. Russo, F. Smallenburg, T. Speck, and C. Valeriani. Colloidal hard spheres: Triumphs, challenges and mysteries. arXiv:2305.02452.

[RHB90] Marzia Rovere, Dieter W Heermann, and Kurt Binder. The gas-liquid transition of the two-dimensional lennard-jones fluid. *Journal of Physics: Condensed Matter*, 2(33):7009, 1990.

[RHB13a] G. S. Redner, M. F. Hagan, and A. Baskaran. Structure and dynamics of a phase-separating active colloidal fluid. *Phys. Rev. Lett.*, 110:055701, 2013.

[RHB13b] G. S. Redner, M. F. Hagan, and A. Baskaran. Structure and dynamics of a phase-separating active colloidal fluid. *Phys. Rev. Lett.*, 110:055701, 2013.

[RHB13c] Gabriel S Redner, Michael F Hagan, and Aparna Baskaran. Structure and dynamics of a phase-separating active colloidal fluid. *Phys. Rev. Lett.*, 110(5):055701, 2013.

[RHB13d] Gabriel S. Redner, Michael F. Hagan, and Aparna Baskaran. Structure and Dynamics of a Phase-Separating Active Colloidal Fluid. *Phys. Rev. Lett.*, 110(5):055701, 2013.

[RL21] Ylann Rouzaire and Demian Levis. Defect superdiffusion and unbinding in a 2d xy model of self-driven rotors. *Physical Review Letters*, 127(8):088004, 2021.

[RMWG04] M. Ripoll, K. Mussawisade, R.G. Winkler, and G.Gompper. Low-reynolds-number hydrodynamics of complex fluids by multi-particle-collision dynamics. *Europhysics Letters (EPL)*, 68(1):106–112, oct 2004.

[RMWG05] M. Ripoll, K. Mussawisade, R.G. Winkler, and G. Gompper. Dynamic regimes of fluids simulated by multiparticle-collision dynamics. *Phys. Rev. E*, 72:016701, Jul 2005.

[SA17] D. Stauffer and A. Aharony. *Introduction To Percolation Theory: Second Edition*. Taylor & Francis, London, UK, 2017.

[SBM+19] Vishal Soni, Ephraim S Bililign, Sofia Magkiriadou, Stefano Sacanna, Denis Bartolo, Michael J Shelley, and William TM Irvine. The odd free surface flows of a colloidal chiral fluid. *Nature physics*, 15(11):1188–1194, 2019.

[SBML14] T. Speck, J. Bialké, A. M. Menzel, and H. Löwen. Effective cahn-hilliard equation for the phase separation of active brownian particles. *Phys. Rev. Lett.*, 112:218304, 2014.

[SCG16] Antonio Suma, Leticia F Cugliandolo, and Giuseppe Gonnella. Tracer motion in an active dumbbell fluid. *J. Stat. Mech.*, 2016(5):054029, 2016.

[SCT15] Alexandre P Solon, Hugues Chaté, and Julien Tailleur. From phase to microphase separation in flocking models: The essential role of nonequilibrium fluctuations. *Physical review letters*, 114(6):068101, 2015.

[SEP18] Christian Scholz, Michael Engel, and Thorsten Pöschel. Rotating robots move collectively and self-organize. *Nature communications*, 9(1):931, 2018.

[SF91] B Smit and D Frenkel. Vapor–liquid equilibria of the two-dimensional lennard-jones fluid (s). *The Journal of chemical physics*, 94(8):5663–5668, 1991.

[SFC+20] X. Shi, G. Fausti, H. Chaté, C. Nardini, and A. Solon. Self-organized critical coexistence phase in repulsive active particles. *Phys. Rev. Lett.*, 125:168001, 2020.

[SGL+14] A. Suma, G. Gonnella, G. Laghezza, A. Lamura, A. Mossa, and L. F. Cugliandolo. Dynamics of a homogeneous active dumbbell system. *Phys. Rev. E*, 90:052130, 2014.

[SH22] A. Solon and J. M. Horowitz. On the einstein relation between mobility and diffusion coefficient in an active bath. *J. Phys. A: Math. Theor.*, 55:184002, 2022.

[SLSV17] J. T. Siebert, J. Letz, T. Speck, and P. Virnau. Phase behavior of active brownian disks, spheres, and dumbbells. *Soft Matter*, 13:1020, 2017.

[SLVC+12a] J. Schwarz-Linek, C. Valeriani, A. Cacciuto, M. Cates, D. Marenduzzo, A. Morozov, and W. Poon. *Proc. Natl. Acad. Sci. U. S. A.*, 109:4052, 2012.

[SLVC+12b] J. Schwarz-Linek, C. Valeriani, A. Cacciuto, M. E. Cates, D. Marenduzzo, A. N. Morozov, and W. C. K. Poon. Phase separation and rotor self-assembly in active particle suspensions. *Proc. Nat. Acad. Sc.*, 109:4052, 2012.

[SMAC14a] J Stenhammar, D Marenduzzo, R J Allen, and M E Cates. Phase behaviour of active brownian particles: the role of dimensionality. *Soft Matter*, 10(10):1489, 2014.

[SMAC14b] Joakim Stenhammar, Davide Marenduzzo, Rosalind J Allen, and Michael E Cates. Phase behaviour of active brownian particles: the role of dimensionality. *Soft Matter*, 10(10):1489–1499, 2014.

[SMBL15] T. Speck, A. M. Menzel, J. Bialké, and H. Löwen. Dynamical mean-field theory and weakly non-linear analysis for the phase separation of active brownian particles. *J. Chem. Phys.*, 142:224109, 2015.

[SMGO14] A. Suma, D. Marenduzzo, G. Gonnella, and E. Orlandini. Motility-induced phase separation in an active dumbbell fluid. *EPL (Europhysics Letters)*, 108:56004, 2014.

[Smo16] M von Smoluchowski. Drei vortrage uber diffusion, brownsche bewegung und koagulation von kolloidteilchen. *Zeitschrift fur Physik*, 17:557–585, 1916.

[Sne16] Alexey Snezhko. Complex collective dynamics of active torque-driven colloids at interfaces. *Current opinion in colloid & interface science*, 21:65–75, 2016.

[SPJ+19] Haiyang Su, C-A Hurd Price, Lingyan Jing, Qiang Tian, Jian Liu, and Kun Qian. Janus particles: design, preparation, and biomedical applications. *Materials today bio*, 4:100033, 2019.

[SS78] T Schneider and E Stoll. Molecular-dynamics study of a three-dimensional one-component model for distortive phase transitions. *Physical Review B*, 17(3):1302, 1978.

[SSC+18a] Alexandre P Solon, Joakim Stenhammar, Michael E Cates, Yariv Kafri, and Julien Tailleur. Generalized thermodynamics of motility-induced phase separation: phase equilibria, laplace pressure, and change of ensembles. *New Journal of Physics*, 20(7):075001, 2018.

[SSC+18b] Alexandre P Solon, Joakim Stenhammar, Michael E Cates, Yariv Kafri, and Julien Tailleur. Generalized thermodynamics of phase equilibria in scalar active matter. *Phys. Rev. E*, 97(2):020602, 2018.

[SSLP22] Elena Sesé-Sansa, Demian Levis, and Ignacio Pagonabarraga. Microscopic field theory for structure formation in systems of self-propelled particles with generic torques. *The Journal of Chemical Physics*, 157(22):224905, 2022.

[SSW+15a] Alexandre P. Solon, Joakim Stenhammar, Raphael Wittkowski, Mehran Kardar, Yariv Kafri, Michael E. Cates, and Julien Tailleur. Pressure and phase equilibria in interacting active Brownian spheres. *Phys. Rev. Lett.*, 114(19):198301, 2015.

[SSW+15b] Alexandre P Solon, Joakim Stenhammar, Raphael Wittkowski, Mehran Kardar, Yariv Kafri, Michael E Cates, and Julien Tailleur. Pressure and phase equilibria in interacting active brownian spheres. *Physical review letters*, 114(19):198301, 2015.

[STA+13a] J. Stenhammar, A. Tiribocchi, R. J. Allen, D. Marenduzzo, and M. E. Cates. A continuum theory of phase separation kinetics for active brownian particles. *Phys. Rev. Lett.*, 111:145702, 2013.

[STA+13b] Joakim Stenhammar, Adriano Tiribocchi, Rosalind J Allen, Davide Marenduzzo, and Michael E Cates. Continuum theory of phase separation kinetics for active brownian particles. *Phys. Rev. Lett.*, 111(14):145702, 2013.

[SVLVB87] JH Sikkenk, JMJ Van Leeuwen, EO Vossnack, and AF Bakker. Simulation of a liquid-vapor interface in an external field. *Physica A: Statistical Mechanics and its Applications*, 146(3):622–633, 1987.

[SWMC15] J. Stenhammar, R. Wittkowski, D. Marenduzzo, and M.E. Cates. Activity-induced phase separation and self-assembly in mixtures of active and passive particles. *Phys. Rev. Lett.*, 114, 2015.

[SWW+20a] M Reza Shaebani, Adam Wysocki, Roland G Winkler, Gerhard Gompper, and Heiko Rieger. Computational models for active matter. *Nature Reviews Physics*, 2(4):181–199, 2020.

[SWW+20b] M Reza Shaebani, Adam Wysocki, Roland G Winkler, Gerhard Gompper, and Heiko Rieger. Computational models for active matter. *Nat. Rev. Phys.*, 2(4):181–199, 2020.

[TA99] Andrij Trokhymchuk and José Alejandre. Computer simulations of liquid/vapor interface in lennard-jones fluids: Some questions and answers. *The Journal of chemical physics*, 111(18):8510–8523, 1999.

[TAB+22] Aidan P Thompson, H Metin Aktulga, Richard Berger, Dan S Bolintineanu, W Michael Brown, Paul S Crozier, Pieter J in't Veld, Axel Kohlmeyer, Stan G Moore, Trung Dac Nguyen, et al. Lammps-a flexible simulation tool for particle-based materials modeling at the atomic, meso, and continuum scales. *Computer Physics Communications*, 271:108171, 2022.

[TC08] J Tailleur and M E Cates. Statistical mechanics of interacting run-and-tumble bacteria. *Phys. Rev. Lett.*, 100(21):218103, 2008.

[TCBP+12a] I Theurkauff, C Cottin-Bizonne, J Palacci, C Ybert, and L Bocquet. Dynamic clustering in active colloidal suspensions with chemical signaling. *Phys. Rev. Lett.*, 108(26):268303, 2012.

[TCBP+12b] Isaac Theurkauff, Cécile Cottin-Bizonne, Jérémie Palacci, Christophe Ybert, and Lydric Bocquet. Dynamic clustering in active colloidal suspensions with chemical signaling. *Physical review letters*, 108(26):268303, 2012.

[TCP18] Alessandro Tartaglia, Leticia F Cugliandolo, and Marco Picco. Coarsening and percolation in the kinetic 2d ising model with spin exchange updates and the voter model. *J. Stat. Mech.*, 2018(8):083202, 2018.

[TEQ+18] M. Theers, Westphal E, K. Qi, R.G. Winkler, and G. Gompper". Clustering of microswimmers: interplay of shape and hydrodynamics. *Soft Matter*, 14:8590–8603, 2018.

[THVC16] C. Tung, J. Harder, C. Valeriani, and A. Cacciuto. Micro-phase separation in two dimensional suspensions of self-propelled spheres and dumbbells. *Soft Matter*, 12:555, 2016.

[TIK06] E. Tüzel, T. Ihle, and D.M. Kroll. Dynamic correlations in stochastic rotation dynamics. *Phys. Rev. E*, 74:056702, Nov 2006.

[TNC18] E. Tjhung, C. Nardini, and M. E. Cates. Cluster phases and bubbly phase separation in active fluids: Reversal of the ostwald process. *Phys. Rev. X*, 8:031080, 2018.

[TSGL09] A. Tiribocchi, N. Stella, G. Gonnella, and A. Lamura. Hybrid lattice boltzmann model for binary fluid mixtures. *Phys. Rev. E*, 80:026701, 2009.

[TT95] J. Toner and Y. Tu. Long-range order in a two-dimensional dynamical xy model: How birds fly together. *Phys. Rev. Lett.*, 75:4326, 1995.

[TT98] J. Toner and Y. Tu. Flocks, herds, and schools: A quantitative theory of flocking. *Phys. Rev. E*, 58:4828–4858, 1998.

[TTR05] J. Toner, Y. Tu, and S. Ramaswamy. Hydrodynamics and phases of flocks. *Ann. Phys.*, 318:170, 2005.

[Tuc09] Mark Tuckerman. *Statistical Mechanics: Theory and Molecular Simulation*. Oxford Press, 2009.

[TW21] F. Turci and N. B. Wilding. Phase separation and multibody effects in three-dimensional active Brownian particles. *Phys. Rev. Lett.*, 126:038002, 2021.

[TWMC15] A. Tiribocchi, R. Wittkowski, D. Marenduzzo, and M.E. Cates. Active model h: Scalar active matter in a momentum-conserving fluid. *Phys. Rev. Lett.*, 115:188302, 2015.

[TWQ+18a] M. Theers, E. Westphal, K. Qi, R. G. Winkler, and G. Gompper. Clustering of microswimmers: interplay of shape and hydrodynamics. *Soft Matter*, 14:8590–8603, 2018.

[TWQ+18b] M. Theers, E. Westphal, K. Qi, R.G. Winkler, and G. Gompper. Clustering of microswimmers: interplay of shape and hydrodynamics. *Soft Matter*, 14:8590–8603, 2018.

[TYR+05] J-C Tsai, Fangfu Ye, Juan Rodriguez, Jerry P Gollub, and TC Lubensky. A chiral granular gas. *Physical review letters*, 94(21):214301, 2005.

[TZ12] V. Tamás and A. Zafeiris. Collective motion. *Physics Reports*, 517(3):71–140, 2012. Collective motion.

[VCBJ+95] T. Vicsek, A. Czirók, E. Ben-Jacob, I. Cohen, and O. Shochet. Novel type of phase transition in a system of self-driven particles. *Phys. Rev. Lett.*, 75:1226, 1995.

[vdLAAD19] M. N. van der Linden, L. C. Alexander, D. G. A. L. Aarts, and O. Dauchot. Interrupted motility induced phase separation in aligning active colloids. *Phys. Rev. Lett.*, 123:098001, 2019.

[vDRvRD19a] R. van Damme, J. Rodenburg, R. van Roij, and M. Dijkstra. Interparticle torques suppress motility-induced phase separation for rodlike particles. *J. Chem. Phys.*, 150:164501, 2019.

[vDRVRD19b] R. van Damme, J. Rodenburg, R. Van Roij, and M. Dijkstra. Interparticle torques suppress motility-induced phase separation for rodlike particles. *J. Chem. Phys.*, 150:164501, 2019.

[VHA+05] D. A. Vega, C. K. Harrison, D. E. Angelescu, M. L. Trawick, D. A. Huse, P. M. Chaikin, and R. A. Register. Ordering mechanisms in two-dimensional sphere-forming block copolymers. *Phys. Rev. E,*, 71:061803, 2005.

[VLP23] N. Venkatareddy, S.-T. Lin, and K. Prabal. Phase behavior of active and passive dumbbells. *Phys. Rev. E*, 107:034607, 2023.

[VRLCRR22] Francisco Vega Reyes, Miguel A López-Castaño, and Álvaro Rodríguez-Rivas. Diffusive regimes in a two-dimensional chiral fluid. *Communications Physics*, 5(1):256, 2022.

[Wag61] Carl Wagner. Theory of precipitate change by redissolution. *Z. Elektrochem.*, 65:581–591, 1961.

[Wes16] Fabian Westermeier. *Structure and Dynamics of highly charged colloidal suspensions*. 2016.

[Win16] Roland G. Winkler. Dynamics of flexible active Brownian dumbbells in the absence and the presence of shear flow. *Soft Matter*, 12(16):3737–3749, 2016.

[WM13] Andreas Walther and Axel HE Muller. Janus particles: synthesis, self-assembly, physical properties, and applications. *Chemical reviews*, 113(7):5194–5261, 2013.

[WRDD18] Marcel Workamp, Gustavo Ramirez, Karen E Daniels, and Joshua A Dijksman. Symmetry-reversals in chiral active matter. *Soft Matter*, 14(27):5572–5580, 2018.

[WSII14] Hiroshi Watanabe, Masaru Suzuki, Hajime Inaoka, and Nobuyasu Ito. Ostwald ripening in multiple-bubble nuclei. *J. Chem. Phys.*, 141(23):234703, 2014.

[WSS+16] Yingjie Wu, Tieyan Si, Jingxin Shao, Zhiguang Wu, and Qiang He. Near-infrared light-driven janus capsule motors: Fabrication, propulsion, and simulation. *Nano Research*, 9:3747–3756, 2016.

[WTS+14] Raphael Wittkowski, Adriano Tiribocchi, Joakim Stenhammar, Rosalind J Allen, Davide Marenduzzo, and Michael E Cates. Scalar φ 4 field theory for active-particle phase separation. *Nature Comm.*, 5(1):1–9, 2014.

[WWG14] A. Wysocki, R. G. Winkler, and G. Gompper. Cooperative motion of active Brownian spheres in three-dimensional dense suspensions. *EPL*, 105:48004, 2014.

[YDVK19] Y. I. Yaman, E. Demir, R. Vetter, and A. Kocabas. Emergence of active nematics in chaining bacterial biofilms. *Nature Comm.*, 10:2285, 2019.

[YMG10] Y. Yang, V. Marceau, and G. Gompper. Swarm behavior of self-propelled rods and swimming flagella. *Phys. Rev. E*, 82(3):031904, 2010.

[YRCZ20] Xiang Yang, Chenyang Ren, Kangjun Cheng, and HP Zhang. Robust boundary flow in chiral active fluid. *Physical Review E*, 101(2):022603, 2020.

[YSCP17] Paloma Yánez-Sedeño, Susana Campuzano, and JM Pingarrón. Janus particles for (bio) sensing. *Applied Materials Today*, 9:276–288, 2017.

[Zac07] E. Zaccarelli. Colloidal gels: equilibrium and non-equilibrium routes. *J. Phys.: Condens. Matter*, 19:323101, 2007.

[ZBFS10] He-Peng Zhang, Avraham Be'er, E-L Florin, and Harry L Swinney. Collective motion and density fluctuations in bacterial colonies. *Proceedings of the National Academy of Sciences*, 107(31):13626–13630, 2010.

[ZLC+08] E. Zaccarelli, P. J. Lu, F. Ciulla, D. A. Weitz, and F. Sciortino. Gelation as arrested phase separation in short-ranged attractive colloid-polymer mixtures. *J. Phys.: Condens. Matter*, 20:494242, 2008.

[ZS14] A. Zöttl and H. Stark. Hydrodynamics determines collective motion and phase behavior of active colloids in quasi-two-dimensional confinement. *Phys. Rev. Lett.*, 112:118101, Mar 2014.

List of Publications

Part II of this thesis is based on research published in collaboration with my research group during the PhD. The relevant publications are listed below.

1. Caporusso, C. B., Digregorio, P., Levis, D., Cugliandolo, L. F., Gonnella, G. (2020). Motility-induced microphase and macrophase separation in a two-dimensional active Brownian particle system. *Physical Review Letters*, 125(17), 178004.

2. Negro, G., Caporusso, C. B., Digregorio, P., Gonnella, G., Lamura, A., Suma, A. (2022). Hydrodynamic effects on the liquid-hexatic transition of active colloids. *The European Physical Journal E*, 45(9), 75.

3. Caporusso, C. B., Cugliandolo, L. F., Digregorio, P., Gonnella, G., Levis, D., Suma, A. (2023). Dynamics of Motility-Induced clusters: coarsening beyond Ostwald ripening. *Physical Review Letters*, 131(6), 068201.

4. Caporusso, C. B., Gonnella, G., Levis, D. (2023). Phase coexistence and edge currents in the chiral Lennard-Jones fluid. arXiv preprint arXiv:2307.03528 (in consideration for *Physical Review Letters*).

5. Caporusso, C. B., Negro, G., Suma, A., Digregorio, P., Carenza, L. N., Gonnella, G., Cugliandolo, L. (2024). Phase Behaviour and Dynamics of Three-Dimensional Active Dumbbell Systems. *Soft Matter*.

6. Caporusso, C. B., Digregorio, P., Cugliandolo, L. F., Gonnella, G., Suma, A., (2024). Phase Separation Kinetics and Cluster Dynamics in Two-Dimensional Active Dumbbell Systems. arXiv preprint arXiv:XXXX.XXXX (in consideration for *Soft Matter*).

Motility-Induced Microphase and Macrophase Separation in a Two-Dimensional Active Brownian Particle System

Claudio B. Caporusso,[1] Pasquale Digregorio,[2,1] Demian Levis,[3,4]
Leticia F. Cugliandolo,[5,6] and Giuseppe Gonnella[1]

[1]*Dipartimento di Fisica, Università degli Studi di Bari and INFN, Sezione di Bari, via Amendola 173, Bari I-70126, Italy*
[2]*CECAM Centre Européen de Calcul Atomique et Moléculaire, Ecole Polytechnique Fédérale de Lausanne, Batochimie, Avenue Forel 2, 1015 Lausanne, Switzerland*
[3]*Departement de Fisica de la Materia Condensada, Facultat de Fisica, Universitat de Barcelona, Martí i Franquès 1, E08028 Barcelona, Spain*
[4]*UBICS University of Barcelona Institute of Complex Systems, Martí i Franquès 1, E08028 Barcelona, Spain*
[5]*Sorbonne Université, Laboratoire de Physique Théorique et Hautes Energies, CNRS UMR 7589, 4 Place Jussieu, 75252 Paris Cedex 05, France*
[6]*Institut Universitaire de France, 1 rue Descartes, 75005 Paris, France*

(Received 14 May 2020; accepted 17 September 2020; published 23 October 2020)

As a result of nonequilibrium forces, purely repulsive self-propelled particles undergo macrophase separation between a dense and a dilute phase. We present a thorough study of the ordering kinetics of such motility-induced phase separation (MIPS) in active Brownian particles in two dimensions, and we show that it is generically accompanied by microphase separation. The growth of the dense phase follows a law akin to the one of liquid-gas phase separation. However, it is made of a mosaic of hexatic microdomains whose size does not coarsen indefinitely, leaving behind a network of extended topological defects from which microscopic dilute bubbles arise. The characteristic length of these finite-size structures increases with activity, independently of the choice of initial conditions.

DOI: 10.1103/PhysRevLett.125.178004

Active systems are ubiquitous in nature. Driven out of equilibrium by the consumption of energy from the environment, they cannot be described using the tools of equilibrium statistical physics, and present intriguing collective behavior [1,2]. One such peculiarity is that, at sufficiently high activity, their constituents cluster in the absence of attractive interactions. A steady state with a dense droplet immersed in a dilute background can thus be reached in systems of purely repulsive spherical particles by motility-induced phase separation (MIPS) [3].

Arguably, the simplest microscopic active matter model is one of self-propelled spheres undergoing rotational diffusion, and excluded volume interactions only. This is the active Brownian particles (ABPs) model that exhibits a very rich phase diagram, including MIPS, especially in two dimensions (2D) [4–16]. In particular, the special role played by hexatic order in these systems was discussed in Refs. [10–14], and the existence of a phase with such order was exhibited [11]. In parallel to particle based models, the large scale and long time behavior of systems exhibiting MIPS was addressed with adaptations of the Cahn-Hilliard approach [9,17–20].

While the nonequilibrium phase diagram of (hard) ABPs is well established [11], the dynamics across the various phase transitions, how the dense droplet is formed via MIPS, and which is its actual nature, still need clarification. A relevant question to ask is whether the hexatic ordering helps or interferes with the simple particle aggregation. Moreover, whether the droplet behaves as a 2D hexatic, liquid or else, featuring or not gas bubbles inside [20], are important issues that have to be elucidated.

In this Letter we address these points and in so doing we clarify the origin of the cavitation gas bubbles recently predicted with a continuum description [20]. Using extensive numerical simulations (more than 10^6 ABPs) we exhibit and characterize several dynamic regimes: multinucleation, condensation and aggregation, and coarsening fulfilling dynamic scaling, see movie 1 in the Supplemental Material (SM) [21]. Furthermore, we show that, asymptotically, the macrodroplet self-organizes into a mosaic of hexatic microdomains, see Fig. 1, differently from what happens in equilibrium coexistence. The hexatic domains do not coarsen to reach the droplet size but rather saturate to a microscopic though relatively large scale which can be directly controlled by self-propulsion. Different hexatic domains are delimited by clusters of topological defects, leaving behind regions of lower density from which microbubbles pop up. Devising generic mechanisms to control the spatiotemporal organization of active matter into structures that do not coarsen constitutes a central challenge of current research which has been tackled with self-propelled particles with chemotactic [24,25],

Eur. Phys. J. E (2022) 45:75
https://doi.org/10.1140/epje/s10189-022-00230-1

THE EUROPEAN PHYSICAL JOURNAL E

Regular Article - Flowing Matter

Hydrodynamic effects on the liquid-hexatic transition of active colloids

G. Negro[1], C. B. Caporusso[1,a], P. Digregorio[2], G. Gonnella[1], A. Lamura[3], and A. Suma[1]

[1] Dipartimento di Fisica, Università degli Studi di Bari and INFN, Sezione di Bari, via Amendola 173, Bari 70126, Italy
[2] Centre Européen de Calcul Atomique et Moléculaire (CECAM), Ecole Polytechnique Fédérale de Lausanne (EPFL), Batochimie, Avenue Forel 2, 1015 Lausanne, Switzerland
[3] Istituto Applicazioni Calcolo, CNR, Via Amendola 122/D, 70126 Bari, Italy

Received 25 January 2022 / Accepted 25 August 2022 / Published online 13 September 2022

Abstract We study numerically the role of hydrodynamics in the liquid-hexatic transition of active colloids at intermediate activity, where motility induced phase separation (MIPS) does not occur. We show that in the case of active Brownian particles (ABP), the critical density of the transition decreases upon increasing the particle's mass, enhancing ordering, while self-propulsion has the opposite effect in the activity regime considered. Active hydrodynamic particles (AHP), instead, undergo the liquid-hexatic transition at higher values of packing fraction ϕ than the corresponding ABP, suggesting that hydrodynamics have the net effect of disordering the system. At increasing densities, close to the hexatic-liquid transition, we found in the case of AHP the appearance of self-sustained organized motion with clusters of particles moving coherently.

1 Introduction

Self-propelled particles (SPP) are the fundamental units of a broad class of theoretical models for active matter. In the context of SPP models, injected energy from the environment fuels a persistent motion of the single constituents, driving the system out of thermal equilibrium. Simplified models of SPP [1–4] are of crucial importance, because they offer a minimal setup to explore some of the large variety of collective behaviours observed in nature for systems of motile living bodies at different length scales, from flocking of birds and fish [5], to swarming in bacterial colonies [6] and dynamics in cells' cytoskeleton [7].

Active Brownian Particles (ABP) models are very popular among SPP models [1,8,9]. Active colloids are usually spherical particles undergoing directed motion due to an active force, while both translational and rotational degrees of freedom are in contact with a stochastic thermal bath. Although the model is very simple, ABP show paradigmatic collective phenomena like motility-induced phase separation (MIPS) [1,10–13] and are therefore very interesting in order to characterize the fundamental principles governing active matter systems. Moreover, ABP are of primary use for comparisons with experimental systems of synthetic microswimmers [13,14], opening the perspectives for a systematic control of active systems and collective motion, with the purpose to exploit some of their unique features for technological uses, for instance in robotics [15–17], realisation of biological machines [18], or understanding of flocking intelligence [19,20].

Of particular interest is the characterization of ABP in the dense regime, see e.g. spontaneous flow [21] or glassy behaviour [22,23] in biological tissues, biofilms, cell mono-layers [24,25], and can be considered a target for the development of new materials [26]. In two dimensions (2D), ABP present ordering phase transitions when the density of the system is increased [8,9,27,28], which are connected to those encountered for passive hard colloids [29–31]. At intermediate values of the self-propelling force, a liquid-hexatic critical transition is followed by a hexatic-solid transition, where the solid phase has quasi-long-range (QLR) positional and long-range (LR) orientational order, the hexatic phase has short-range (SR) positional and QLR orientational order, while the liquid phase is homogeneous and has SR positional and orientational order. This scenario is very similar to the theoretical Kosterlitz, Thouless, Halperin, Nelson, and Young (KTHNY) two-step scenario [32–34]. If activity is high enough, instead, MIPS takes place, as a phase separation between a dense phase and a gaseous one [8].

The aforementioned features of the ABP phase diagram have been well established in the context of overdamped motion and without an explicit underlying thermo-hydrodynamic bath. At the same time, there

[a] e-mail: claudio.caporusso@ba.infn.it (corresponding author)

Dynamics of Motility-Induced Clusters: Coarsening beyond Ostwald Ripening

Claudio B. Caporusso,[1] Leticia F. Cugliandolo,[2,3] Pasquale Digregorio,[4,5,6] Giuseppe Gonnella,[1] Demian Levis,[5,6] and Antonio Suma[1]

[1]Dipartimento Interateneo di Fisica, Università degli Studi di Bari and INFN, Sezione di Bari, via Amendola 173, Bari, I-70126, Italy
[2]Sorbonne Université, Laboratoire de Physique Théorique et Hautes Energies, CNRS UMR 7589, 4 Place Jussieu, 75252 Paris Cedex 05, France
[3]Institut Universitaire de France, 1 rue Descartes, 75005 Paris France
[4]CECAM Centre Européen de Calcul Atomique et Moléculaire, Ecole Polytechnique Fédérale de Lausanne, Batochimie, Avenue Forel 2, 1015 Lausanne, Switzerland
[5]Departement de Fisica de la Materia Condensada, Facultat de Fisica, Universitat de Barcelona, Martí i Franquès 1, E08028 Barcelona, Spain
[6]UBICS University of Barcelona Institute of Complex Systems, Martí i Franquès 1, E08028 Barcelona, Spain

(Received 30 November 2022; accepted 6 July 2023; published 8 August 2023)

We study the dynamics of clusters of active Brownian disks generated by motility-induced phase separation, by applying an algorithm that we devised to track cluster trajectories. We identify an aggregation mechanism that goes beyond Ostwald ripening but also yields a dynamic exponent characterizing the cluster growth $z = 3$, in the timescales explored numerically. Clusters of mass M self-propel with enhanced diffusivity $D \sim \mathrm{Pe}^2/\sqrt{M}$. Their fast motion drives aggregation into large fractal structures, which are patchworks of diverse hexatic orders, and coexist with regular, orientationally uniform, smaller ones. To bring out the impact of activity, we perform a comparative study of a passive system that evidences major differences with the active case.

DOI: 10.1103/PhysRevLett.131.068201

A conservative system of attractive particles cooled across a condensation transition undergoes particle aggregation: dense clusters grow following Ostwald ripening at long times. The Lifshitz, Slyozov, and Wagner (LSW) theory of this process [1–3] predicts the $R(t) \sim t^{1/3}$ growth of the clusters' typical length.

Understanding the dynamics across phase transitions has been a central problem of condensed matter theory, partly due to the fact that it may allow one to define dynamic universality classes [4–6]. In the context of active matter [7–9], a key open question is how such universality classes, if any, are affected by nonequilibrium forces, e.g., self-propulsion.

Systems of repulsive self-propelled particles experience motility-induced phase separation (MIPS). This phenomenon bears analogies with the phase separation of attractive passive particles even though, being purely triggered by activity, arises under nonequilibrium conditions [10,11]. In the quest to identify universal properties of MIPS, much work has been devoted to the analysis of simple particle models, such as active Brownian particles (ABP) [8,12–23], as well as field theories in the spirit of the Hohenberg-Halperin classification [4,24–32]. The latter, albeit including time reversal symmetry breaking terms, predict the same growth law as in phase separation under conservative forces [24–26]: those terms turn out to be irrelevant in the renormalization group sense [31,32]. When we let the ABPs evolve at large activities from an initial homogeneous state, they progressively aggregate and, after a transient, enter a scaling regime in which structural measurements scale with a growing length compatible with $R(t) \sim t^{1/3}$ [14,15,17]. Hence, the MIPS kinetics was ascribed to Ostwald ripening, in line with universality.

Active colloids usually aggregate into dynamic clusters that break up and form again but do not clearly coarsen towards complete phase separation [33–36]. Experimentally, clustering might result from more involved mechanisms than the mere competition between self-propulsion and excluded volume; indeed, aggregation-fragmentation [35] and interrupted coarsening [36] have been exhibited, and both go beyond the LSW theory.

In this Letter, we elucidate the role played by cluster motion in the numerically accessible MIPS of large assemblies of ABPs. With the cluster tracking method that we conceived, we show that the mechanisms in action are not just Ostwald ripening. Cluster diffusion is a key player at these long and extended, though not yet asymptotic, scales and leads to aggregation. Clusters break up and recombine and, pushed by particles at their surface, are much more mobile than their passive counterparts. Enhanced motility is evidenced by a diffusion coefficient with anomalous mass dependence, $D \sim \mathrm{Pe}^2/\sqrt{M}$ for $M \lesssim 5 \times 10^4$, while clusters of passive attractive particles exhibit $D \sim 1/M$. Very rich cluster structures are thus built

Phase Coexistence and Edge Currents in the Chiral Lennard-Jones Fluid

Claudio B. Caporusso,[1,*] Giuseppe Gonnella,[1] and Demian Levis[2,3]

[1] *Dipartimento Interateneo di Fisica, Università degli Studi di Bari and INFN Sezione di Bari, via Amendola 173 Bari 70126 Italy*

[2] *Departament de Física de la Matèria Condensada, Universitat de Barcelona C. Martí Franquès, 1 08028 Barcelona Spain.*

[3] *UBICS University of Barcelona Institute of Complex Systems Martí i Franquès, 1 E08028 Barcelona Spain.*

(Dated: July 10, 2023)

We study a model chiral fluid in two dimensions composed of Brownian disks interacting via a Lennard-Jones potential and a non-conservative transverse force, mimicking colloids spinning at a rate ω. The system exhibits a phase separation between a chiral liquid and a dilute gas phase that can be characterized using a thermodynamic framework. We compute the equations of state and show that the surface tension controls interface corrections to the coexisting pressure predicted from the equal-area construction. Transverse forces increase surface tension and generate edge currents at the liquid-gas interface. The analysis of these currents shows that the rotational viscosity introduced in chiral hydrodynamics is consistent with microscopic bulk mechanical measurements. Chirality can also break the solid phase, giving rise to a dense fluid made of rotating hexatic patches. Our work paves the way for the development of the statistical mechanics of chiral particles assemblies.

Chiral fluids composed of interacting spinning particles break parity and time-reversal symmetry, defying our fundamental description of soft materials [1]. Salient examples include suspensions of magnetic colloids driven by an external rotating field [2–6], and chiral grains put into motion by an inner motor or a vibrated plate [7–11]. In all cases a common feature arises: transverse pairwise forces. In spinning colloids, they result from the advection of the flow field generated by their rotation [4, 12], while in dry systems, it is the friction between colliding grains that lead to them [13, 14]. As spinning colloids carry a permanent magnetic moment they self-assemble into clusters that eventually coarsen, and the resulting drops sustain steady edge currents at their surface [3, 4]. The dynamic properties of such chiral liquid interface have been described within hydrodynamic models, allowing to measure odd transport coefficients that capture the breakdown of parity symmetry in the constitutive equations [3, 15], akin odd viscosity in quantum Hall systems [16, 17]. The possibility to control edge states in soft matter has boosted the interest on these systems, both from experiments and theory [18]. Localized currents have been also observed in dry systems at the interface between two species with opposite chirality [7, 19] or at the boundaries of a confining wall [9, 20, 21], raising the question about the impact of transverse forces on the properties of matter. Despite recent progress, there is still much to understand about the nature of phase transitions in chiral particle systems, as well as the minimal ingredients needed to sustain such edge currents and their impact on the large-scale behaviour.

To address such question, we study a chiral extension of the Lennard-Jones model in two dimensions (2D) [22–25], with pairwise, non-conservative, transverse forces. Although dipolar interactions are responsible for the clustering of magnetic colloids [2, 4, 26, 27], here we consider a paradigmatic reference model incorporating attractive and excluded volume interactions to decipher the impact of self-spinning on general grounds. Using extensive numerical simulations we establish its phase behaviour, identifying a coexistence region between a dilute gas and a *chiral liquid* (G+CL), followed by a (homogeneous) chiral liquid (CL) and finally a *chiral solid* phase (S), see Fig. 1. Despite being out-of-equilibrium, we show that phase separation in this system can be well characterized

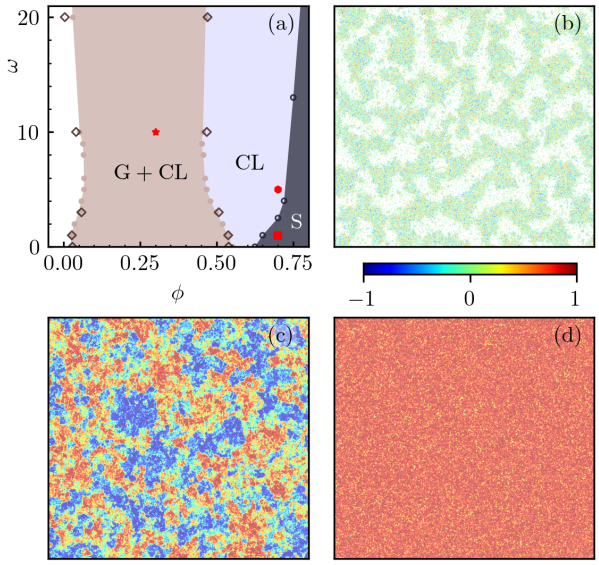

FIG. 1: (a) Phase diagram at $T = 0.47$ comprising a gas (white), chiral liquid (blue) and solid (grey) phases, and a coexistence region (brown). Filled symbols are obtained from density distributions while the empty ones from the pressure. Black circles come from the analysis of the hexatic order parameter. (b)-(d) Snapshots of the system corresponding to $(\phi, \omega) = (0.3, 10)$ (b), $(0.7, 5)$ (c) and $(0.7, 1)$ (d). Particles are colored according to the projection of the local hexatic order $\psi_6(r_i)$ on the global mean orientation.

Journal Name

ARTICLE TYPE

Cite this: DOI: 00.0000/xxxxxxxxxx

Phase Behaviour and Dynamics of Three-Dimensional Active Dumbbell Systems

C. B. Caporusso,[a†] G. Negro,[a*†] A. Suma,[a] P. Digregorio[b,c], L. N. Carenza[d,e], G. Gonnella[a] and L. F. Cugliandolo[f,g]

Received Date
Accepted Date

DOI: 00.0000/xxxxxxxxxx

We present a comprehensive numerical study of the phase behavior and dynamics of a three-dimensional active dumbbell system with attractive interactions. We demonstrate that attraction is essential for the system to exhibit nontrivial phases. We construct a detailed phase diagram by exploring the effects of the system's activity, density, and attraction strength. We identify several distinct phases, including a disordered, a gel, and a completely phase-separated phase. Additionally, we discover a novel dynamical phase, that we name percolating network, which is characterized by the presence of a spanning network of connected dumbbells. In the phase-separated phase we characterize numerically and describe analytically the helical motion of the dense cluster.

1 Introduction

Active systems are a striking class of soft matter which employs internal energy stored in some kind of reservoir and converts it into motion [1–4]. Active systems greatly vary in their extension, ranging from macroscopic to microscopic assemblies of active constituents, and a multitude of different realizations. Focusing on the microscopic world, active systems can either have synthetic origin (*e.g.* Janus particles [5–7]) or biological origin. In this latter case, cytoskeletal suspensions [8] and cellular cultures [9–12] are examples of *in vitro* systems which are often employed to study active behaviors in a controlled environment, but more complex living organisms, such as developing embryos or living tissues [13–15] have recently been considered for their promising implications in understanding a variety of different biological phenomena from morphogenesis to cancer progression and spreading of infections in living organisms. Regardless of their particular realization, active systems can exploit energy to interact with the surrounding environment and perform autonomous motion, leading to a plethora of collective behaviors.

In the past two decades much effort has been spent to identify the physical rules underlying the behavior of living and active systems [1,16–18], with important repercussions on our understanding of their non-equilibrium dynamics. Among others, bacteria have gained the attention of the physics community as they represent a simple natural realization of self-propelled particles, by virtue of their biological simplicity and limited ability in interacting with both the environment and other units. Therefore, bacterial systems provide an elementary yet relevant example of how the dynamics of active constituents may lead to self-assembly [19–21]. Indeed bacteria exhibit noteworthy chemotactic properties which allow them to respond to external stimuli such as variations of temperature, nutrient availability, oxygen concentration, *etc.* to develop different kinds of colonies, ranging from biofilms to fluidic suspensions, often characterized by the emergence of elaborate patterns, even in absence of guidance and only because of the uncoordinated evolution of the separate units [22].

The chemotactic properties of bacteria are often exploited in experiments to trigger a particular response. For instance, most bacteria preferentially reproduce at room temperature – process during which they mostly remain motionless [23,24]– while at higher temperatures they can either develop biofilms if the growing substrate is dry or become motile by growing flagella –a proteic protrusion which is used by some bacterial species to swarm and swim in wet environments. In this latter case, oxygen availability or light intensity determines the dynamical response of the system and can be used in experiments as a control parameter to tune the typical speed of migration. When this is large enough, dense suspensions of flagellate bacteria in a fluidic environment arrange in a liquid crystalline fashion [22] and develop

[a] *Dipartimento Interateneo di Fisica, Università degli Studi di Bari and INFN, Sezione di Bari, via Amendola 173, Bari, I-70126, Italy*
[b] *Departement de Fisica de la Materia Condensada, Facultat de Fisica, Universitat de Barcelona, Martí i Franquès 1, E08028 Barcelona, Spain*
[c] *UBICS University of Barcelona Institute of Complex Systems, Martí i Franquès 1, E08028 Barcelona, Spain*
[d] *Instituut-Lorentz, Universiteit Leiden, P.O. Box 9506, 2300 RA Leiden, Netherlands*
[e] *Department of Physics, Koç University, Rumelifeneri Yolu, 34450 Sarıyer, Istanbul, Türkiye*
[f] *Sorbonne Université, CNRS, Laboratoire de Physique Théorique et Hautes Energies, LPTHE, F-75005 Paris, France*
[g] *Institut Universitaire de France, 1 rue Descartes, 75231 Paris Cedex 05, France*
† These authors contributed equally to this work.
∗ giuseppe.negro@ba.infn.it

Phase Separation Kinetics and Cluster Dynamics in Two-Dimensional Active Dumbbell Systems

C. B. Caporusso[1], L. F. Cugliandolo[2,3] P. Digregorio[4,5], G. Gonnella[1], A. Suma[1],
[1] *Dipartimento Interateneo di Fisica, Universitá degli Studi di Bari and INFN, Sezione di Bari, via Amendola 173, Bari, I-70126, Italy,*
[2] *Sorbonne Université, Laboratoire de Physique Théorique et Hautes Energies, CNRS UMR 7589, 4 Place Jussieu, 75252 Paris Cedex 05, France*
[3] *Institut Universitaire de France, 1 rue Descartes, 75231 Paris Cedex 05, France,*
[4] *Departement de Fisica de la Materia Condensada, Facultat de Fisica, Universitat de Barcelona, Martí i Franquès 1, E08028 Barcelona, Spain,*
[5] *UBICS University of Barcelona Institute of Complex Systems, Martí i Franquès 1, E08028 Barcelona, Spain*

Molecular dynamics simulations were employed to investigate the phase separation process of a two-dimensional active Brownian dumbbell model. We evaluated the time dependence of the typical size of the dense component using the scaling properties of the structure factor, along with the averaged number of clusters and their radii of gyration. The growth observed is faster than in active particle (disk) models, and this effect is further enhanced under stronger activity. Next, we focused on studying the hexatic order of the clusters. The length associated to the orientational order grows algebraically and faster than for active Brownian particles. Under weak active forces, most clusters exhibit a uniform internal orientational order. However, under strong forcing, large clusters consist of domains with different orientational orders. We demonstrated that the latter configurations are not stable, and given sufficient time to evolve, they eventually reach homogeneous configurations as well. No gas bubbles are formed within the clusters, even when there are patches of different hexatic order. Finally, attention was directed towards the geometry and motion of the clusters themselves. By employing a tracking algorithm, we showed that clusters smaller than the typical size at the observation time exhibit regular shapes, while larger ones display fractal characteristics. In between collisions or break-ups, the clusters behave as solid bodies. Their centers of mass undergo circular motion, with radii increasing with the cluster size. The center of mass angular velocity equals that of the constituents with respect to their center of mass. These observations were rationalised with a simple mechanical model.

CONTENTS

I. INTRODUCTION

Active matter refers to a class of systems composed of entities that can convert stored or ambient energy into directed motion [1–8]. These particles or agents can exhibit self-propulsion or autonomous motion. Active matter systems can exhibit complex dynamic behaviors [8–23] due to the internal energy conversion processes of their constituents. Examples are varied and cover natural and artificial systems at very different scales, including motor proteins in cells [24] and flocks of birds [25]